

BF₂-25-oxasmaragdyrin based systems for Near Infra-Red Fluorescence (NIRF) Imaging and Photothermal Therapy (PTT) for Cancer Treatment

Submitted in partial fulfillment of the requirements
of the degree of

Doctor of Philosophy

of the
Indian Institute of Technology Bombay, India
and
Monash University, Australia

by
Kandala Laxman Vamshi Krishna

Supervisors:

Prof. M. Ravikanth (IIT Bombay)

Prof. Andrea Robinson (Monash University)



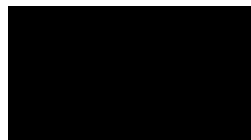
*The course of study for this award was developed jointly by
Monash University, Australia and the Indian Institute of Technology Bombay, India
and was given academic recognition by each of them.*

The programme was administrated by The IITB-Monash Research Academy

(Year 2020)

Approval Sheet

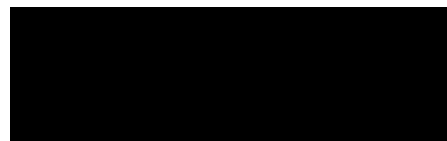
The thesis entitled “**BF₂-25-oxasmaragdyrin based systems for Near Infra-Red Fluorescence (NIRF) Imaging and Photothermal Therapy (PTT) for Cancer Treatment**” by **Kandala Laxman Vamshi Krishna** is approved for the degree of **Doctor of Philosophy**.



(Prof. A. Srinivasan)
External Examiner



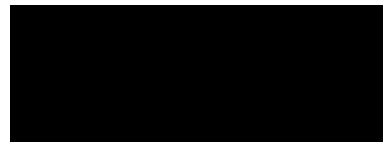
(Prof. Nandita Madhavan)
Internal Examiner



(Prof. M. Ravikanth)
IITB Supervisor



(Prof. Andrea Robinson)
Monash Supervisor



(Prof. P. V. Balaji)
Chairperson

Date: 08-07-2020
Place: IIT Bombay

Declaration

I declare that this written submission represents my ideas in my own words and where others' ideas or words have been included, I have adequately cited and referenced the original sources. I also declare that I have adhered to all principles of academic honesty and integrity and have not misrepresented or fabricated or falsified any idea/data/fact/source in my submission. I understand that any violation of the above will be cause for disciplinary action by the Institute and can also evoke penal action from the sources which have thus not been properly cited or from whom proper permission has not been taken when needed.



Kandala Laxman Vamshi Krishna

154034004

Date: 8th July 2020

INDIAN INSTITUTE OF TECHNOLOGY BOMBAY

CERTIFICATE OF COURSE WORK

This is to certify that Mr. Kandala Laxman Vamshi Krishna was admitted to the candidacy of the Ph.D. degree on 16th of July, 2015 after successfully completing all the courses required for the Ph.D. degree programme. The details of the course work done are given below.

Sl. No.	Course No.	Course Name	Course Credits
1	CHS802	Seminar	4.0
2	CH 818	Single Molecule Fluorescence Spectroscopy	6.0
3	HS 791	Communication Skills -I	2.0
4	CH 831	Advanced Laboratory Techniques	8.0
5	CH 827	Inorganic Complexes	6.0
6	CH 821	Topics in Chemistry I	6.0
7	CH 807	Organic Synthesis	6.0
8	CH 792	Communication Skills -II	4.0
9	CH 521	Interpretative Molecular Spectroscopy	6.0

I. I. T. Bombay

Date :

Dy. Registrar (Academic)

Dedicated
to my
Beloved Parents

Table of Contents

List of Abbreviations	v
Chapter 1: General Introduction	1
1.1 NIR fluorescent dyes	4
1.1.1 Cyanine dyes	4
1.1.2 Xanthenes	5
1.1.3 Squaraines.....	6
1.1.4 Benzo[<i>c</i>]heterocycles	6
1.1.5 BODIPYs and Aza-BODIPYs.....	7
1.1.6 Porphyrins and Phthalocyanines.....	8
1.1.7 Expanded porphyrins and NIR fluorescence	9
1.2 Cancer and anticancer therapy	12
1.2.1 Surgery and Radiotherapy	12
1.2.2 Chemotherapy.....	13
1.2.3 Immunotherapy.....	15
1.2.4 Photodynamic therapy	15
1.2.5 Hyperthermia.....	16
1.3 Scope of the thesis	17
1.4 References	20
Chapter 2: General Experimental.....	29
2.1. Chemicals for syntheses	31
2.2. Solvents employed for spectroscopic and microscopic analysis.....	31
2.3. Synthesis of precursor compounds.....	32
2.4. Characterization techniques	35
2.4.1 Fluorescence analysis	37

2.4.2 <i>In vitro</i> studies	38
2.4.3 <i>In vivo</i> studies	40
2.5 References	40
Chapter 3: Synthesis of Oxasmaragdyrin-Amino Acid Conjugates	41
3.1. Introduction	43
3.2. Results and Discussion.....	44
3.2.1 Synthesis and Characterization.....	44
3.3. Conclusions	51
3.4. Experimental	51
3.5. References	58
Chapter 4: Glucosamine conjugated BF₂-oxasmaragdyrin as NIR Fluorescence Imaging Agent	63
4.1. Introduction	65
4.2. Results and Discussion.....	66
4.2.1 Synthesis and Characterization.....	66
4.2.2 Photophysical and Electrochemical properties.....	68
4.2.3 <i>In vitro</i> studies	69
<i>Biocompatibility</i>	69
<i>Cellular uptake</i>	71
4.3. Conclusions	72
4.4. Experimental	73
4.5. References	76
Chapter 5: L,L-Diphenylalanine Conjugated BF₂-oxasmaragdyrin Self-Assemblies as NIR Photothermal Therapeutic Agents for Cancer Therapy	79
5.1. Introduction	81
5.2. Results and Discussion.....	82
5.2.1 Synthesis and Characterization.....	82

5.2.2 Formation of self-assemblies.....	84
5.2.3 Stability studies	85
<i>pH stability</i>	85
<i>Lyophilization</i>	86
5.2.4 Photo-thermal transduction studies	87
5.2.5 <i>In vitro</i> studies	89
<i>Biocompatibility</i>	89
<i>Cellular uptake</i>	90
<i>In vitro photothermal efficacy</i>	90
<i>Hemocompatibility study</i>	91
5.2.6 <i>In vivo</i> studies	91
5.3. Conclusions	93
5.4. Experimental	93
5.5. References	105
Chapter 6: BF₂-Oxasmaragdyrin based Quantum Dots as theragnostic agent for cancer therapy	113
6.1. Introduction	115
6.2. Results and Discussion.....	116
6.2.1 Synthesis and characterization of TBSQDs.	116
6.2.2 Photophysical properties	118
6.2.3 Photothermal properties.....	120
6.2.3 <i>In vitro</i> studies	122
<i>Biocompatibility</i>	122
<i>Cellular uptake</i>	122
<i>In vitro photothermal efficacy</i>	123
<i>Hemocompatibility study</i>	123

6.2.3 <i>In vivo</i> studies	124
6.3. Conclusions	126
6.4. Experimental	127
6.5. References	134
Chapter 7: Cell Penetrating Peptide Conjugated BF₂-Oxasmaragdyrin As NIR Imaging and Photothermal Therapeutic Agents	141
7.1. Introduction	143
7.2. Results and Discussion.....	144
7.2.1 Synthesis and Characterization.....	144
7.2.2 Photophysical characterization.....	146
7.2.3 <i>In vitro</i> studies	147
<i>Biocompatibility</i>	147
<i>Cellular uptake</i>	149
7.2.4 Photothermal properties.....	149
7.3. Conclusions	151
7.4. Experimental	152
7.5. References	159
Chapter 8: Summary	165
List of Publications	189
List of Patents.....	191
Acknowledgements	193

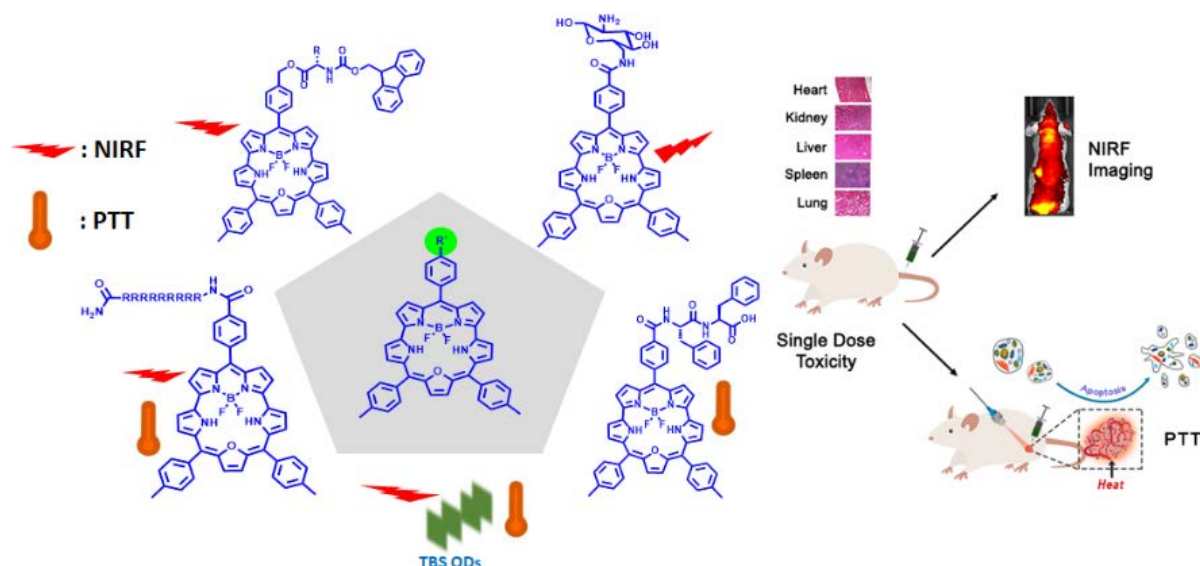
List of Abbreviations

Å	Angstrom
Ar	Aryl
Ph	Phenyl
NMR	Nuclear Magnetic Resonance
Hz	Hertz
MHz	MegaHertz
CDCl ₃	Deuterated Chloroform
COSY	Correlation Spectroscopy
NOESY	Nuclear Overhauser Spectroscopy
CV	Cyclic Voltammetry
Calcd.	Calculated
DMF	<i>N,N</i> -Dimethylformamide
DPV	Differential Pulse Voltammetry
DMSO	Dimethyl Sulphoxide
DDQ	2,3-Dichloro-5,6-Dicyanobenzoquinone
ESI-MS	Electrospray Ionization Mass Spectrometry
TOF	Time of flight
Nm	Nanometer
eV	Electron Volt
ε	Molar extinction co-efficient
RT	Room Temperature
Eq.	Equivalent
ppm	Parts per million
mmol	milli molar
TFA	Trifluoroacetic acid
TEA	Triethylamine
TBAP	Tetrabutylammoniumperchlorate
HATU	1-[Bis(dimethylamino)methylene]-1H-1,2,3-triazolo[4,5-b]pyridinium 3-oxide hexafluorophosphate
HBTU	2-(1H-benzotriazol-1-yl)-1,1,3,3-tetramethyluronium hexafluorophosphate
HCTU	O-(1H-6-Chlorobenzotriazole-1-yl)-1,1,3,3-tetramethyluronium hexafluorophosphate

DIEA	N,N-diisopropylamine
TMEDA	<i>N,N,N',N'</i> -Tetramethylethylenediamine
HOBt	Hydroxybenzotriazole
EDC.HCl	1-Ethyl-3-(3-dimethylaminopropyl)carbodiimide hydrochloride
TLC	Thin Layer Chromatography
THF	Tetrahydrofuran
UV	Ultraviolet
NIR	Near Infra-red
mW	Milli Watt

Abstract

Photothermal therapy (PTT) has gained huge interest in cancer treatment, and the quest for potential organic photothermal agents is underway owing to the nonbiodegradable nature and chronic toxicity of the existing inorganic nanomaterials. Organic material based nano formulations with good photothermal and fluorescence properties in the NIR-I window are scarce. However, porphyrins are one such biocompatible systems which are advantageous for photothermal therapy but are currently based in visible region causing limited depth of tissue penetration leading to compromised photothermal and NIR fluorescence imaging applications. To overcome these limitations, we utilized an expanded porphyrin; BF₂-oxamsmaragdyrin which is a 22 π electronic aromatic macrocycle absorbs in visible-NIR (~400-700 nm) and emits in NIR (~710 nm) region. We synthesized a series of BF₂-oxamsmaragdyrin based systems such as covalent conjugates of BF₂-oxamsmaragdyrin from amino acids, glucosamine, peptides



(FF, CRGDK & R₉) and BF₂-oxamsmaragdyrin based quantum dots (TBSQDs). All the materials were thoroughly characterized by different analytical/spectroscopic techniques and were biocompatible with excellent cellular internalization. Though the amino acid conjugated BF₂-oxamsmaragdyrin possessed excellent fluorescence but was not appropriate for cellular imaging due to its hydrophobic nature. Hence, glucosamine conjugated BF₂-oxamsmaragdyrin was synthesized and showed efficient cellular imaging capacity in NIR-I window when solubilized in DMSO (<1%). Further refining to biologically appealing water-soluble systems, peptide (FF, CRGDK & R₉) conjugated BF₂-oxamsmaragdyrin, and TBSQDs were prepared which exhibited excellent NIR fluorescence imaging as well as NIR triggered photothermal tumor ablation efficacy in preclinical settings. These systems seem to be ideal candidates for image guided theranostic applications for clinical translation.

Chapter 1

General Introduction

Optical imaging is an emerging technology with great potential for improving disease prevention, diagnosis, and treatment.¹ Optical imaging is advantageous over existing radiological imaging techniques such as (a) use of non-ionizing radiation in optical imaging reduces the radiation exposure times which allows for repeated studies over time; (b) optical imaging could potentially differentiate between soft tissues and tissue labelled with contrast media with the help of different photon absorption/scattering profiles at different wavelengths and (c) optical imaging could be employed simultaneously/integrated with other imaging techniques to improve resolution and information obtained which is called as multimodal imaging.

Over the past few decades, several types of dyes have been synthesised which absorb and fluoresce in visible region such as BODIPYs, rhodamines, coumarins, porphyrins etc. Though these dyes have numerous advantages, they all absorb and emit in visible region. Dyes which fluoresce in visible region are disadvantageous as they could not be used to image mammalian cells/tissues because of the absorption and higher auto-fluorescence by the mammalian cells.

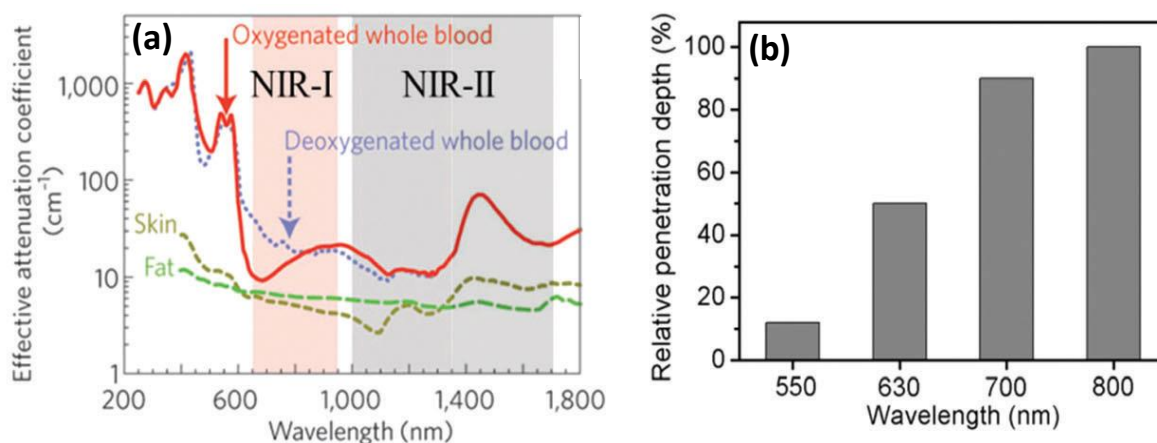


Figure 1: (a) Absorption spectra of O₂-Hb, Hb, skin and fat (b) relative penetration depth of different wavelengths of light. Reproduced from Ref. 2 with permission from The Royal Society of Chemistry.

Mammalian cells are found to be more transparent in the window of 700-900 nm (designated as NIR I region) and 1000-1700 nm (designated as NIR II region) as shown in figure 1. Hence dyes which absorb and emit in these regions are very advantageous as lower tissue auto-fluorescence and less fluorescence extinction enhance deep tissue penetration with minimal background interference.²⁻⁴ NIR light is known to travel at least 10 cm through breast tissue and 4 cm through skull/brain tissue and deep muscle tissue by usage of microwatt laser

sources (FDA class 1). At higher power levels (FDA class 3) has shown to penetrate through 7 cm of muscle and skull/brain.⁵ Though Near-IR Fluorescence (NIRF) imaging is advantageous, there are only handful of dyes that fluoresce in this region such as cyanine dyes,^{6,7} xanthenes/rhodamines,⁸ squaraine dyes,^{9–12} benzo[c]heterocycles,¹³ BODIPY analogs,^{14–17} phthalocyanines and a small selection of porphyrin derivatives.^{18–20} Though there is vast literature present on general synthetic strategies of these dyes, we will limit the discussion to the dye molecules which have been used for bioimaging and biomedical applications.

1.1 NIR fluorescent dyes

1.1.1 Cyanine dyes

Cyanine dyes were first reported by Williams in 1856. A typical cyanine dye contains two nitrogen containing heterocycles as charged chromophores, each conjugated to the end of a polymethine that comprises of odd number of carbons as shown in figure 2. Cyanine dyes display narrow absorption band with high extinction coefficients. Indocyanine green (ICG) **1** is a tricarbocyanine dye which fluoresce in green region of visible spectrum has been used extensively for biomedical applications over past few decades.²¹ Few cyanines such as **2** (Cy5), **3** (Cy7) and **4** (IR780) which absorb and emit in NIR region with relatively high extinction coefficients and strong fluorescence.^{21–23} It has been observed that the elongation of polymethine bridges (vinylene bond) results in approximately ~100 nm of redshift while an extension in nitrogen containing heterocycles gives ~20 nm of redshift.²³ Though the properties are easily tuneable, these dyes have poor photostability, lower quantum yields in aqueous solutions and have a tendency to aggregate in water.

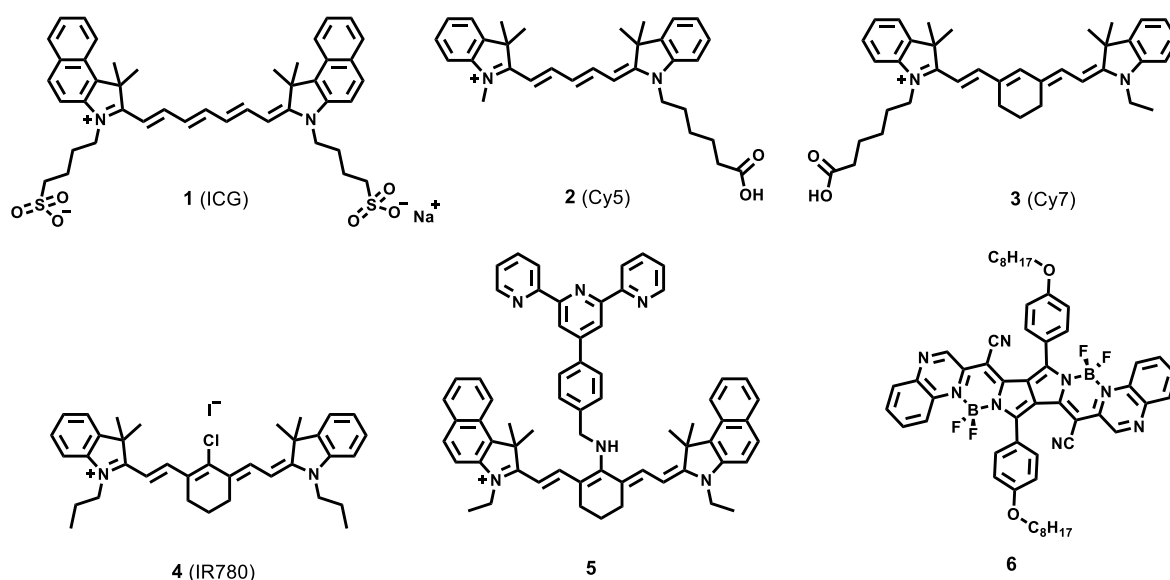


Figure 2: Structures of different cyanine dyes.

Research in past few years led to the development of more NIRF cyanine dyes with subtle modifications.^{24,25} Pandey and coworkers have developed heptamethine carbocyanine IR-783 with a cyclic chloro-cyclohexene moiety which is a minor modification to **4** where alkyl chains have terminal sulphonate groups.²⁶ Later Tan et.al constructed multifunctional NIRF heptamethine cyanine dye **4** (IR780) and a pentacyclic modification in place of hexacyclic in **4** leading to IR808 dye.²⁷ Both IR 780 and IR 808 have good photophysical properties, biocompatibility and targets cancer cells. Tang et al. appended a terpyridine moiety to a tricarbocyanine dye to afford a water-soluble fluorophore **5**. Further a new type of NIR dyes called as pyrrolopyrrole cyanine (PPCy) dyes **6** have been explored.²⁵ Zumbusch and coworkers have synthesised a series of PPCy dyes by varying the aryl groups bonded to BF₂ moieties which led to changes in absorption and fluorescence maximas with good quantum yields ($\phi_f = 0.3-0.6$).

1.1.2 Xanthenes

Fluorescein and Rhodamines **7** are most common dyes which fall in the family of xanthene based dyes as shown in figure 3. Most of these dyes are not NIR active; absorb and emit in visible region. Strongin and co-worker have developed a series of seminaphthafluorones **8** dyes on the xanthene backbone which are water soluble, emit in NIR with moderate quantum yields and large stokes shift (~ 200 nm).²⁸ These seminaphthafluorones **8** are highly stable, very low photobleachable and used for bioimaging. Wang and coworkers have developed xanthene based NIR fluorescent probe **9** which detects hydrazine at a concentration limit of 5.4 ppb and its use in biomedical applications.²⁹ Liu and coworkers have

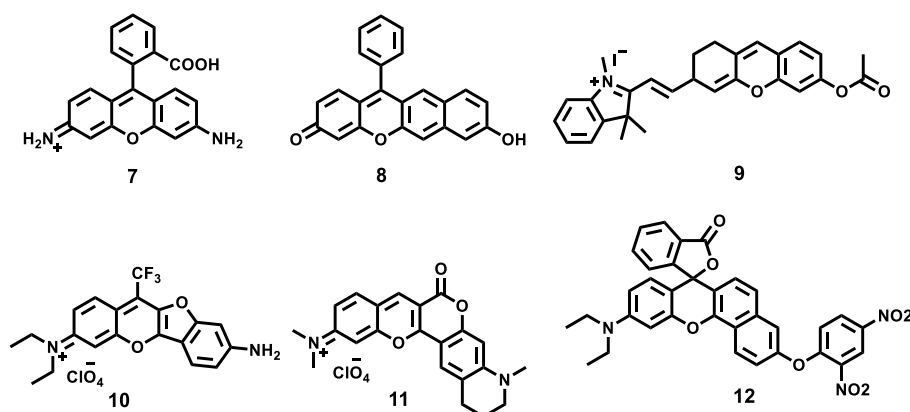


Figure 3: Structures of Xanthene based dyes

prepared deep-red and NIR xanthene dyes **10** and **11** for rapid cell imaging.³⁰ Dye **10** emits at 660 nm which bathochromatically shifts to ~ 720 nm as hydrogen at 9-position of xanthene is

replaced by the electron withdrawing CF_3 group to give dye **11**. Furthermore, Zhu and coworkers developed NIR fluorescent xanthene-based dye **12** which selectively detects presence of thiophenol and studied its applications in bioimaging.³¹

1.1.3 Squaraines

Treibs and Jacob first developed squaraine/squarylium dyes **13** which consists of central ring-based core and a zwitterionic structure as shown in figure 4.³² The oxocyclobutenolate core is linked by aromatic or heterocyclic components at both ends leading to a donor-acceptor-donor motif which typically emit in red to NIR region. Delcamp and coworkers developed Indolizine-squaraines **14** which are NIR fluorescent and stokes shift could be molecularly engineered by appropriately changing the substitutions on indole moiety.³³ Nithyanandan and coworkers prepared unsymmetrical heterotriangulene based squaraine dyes **15** and used them as dyes in DSSC where an efficiency of 2-8% was achieved.³⁴

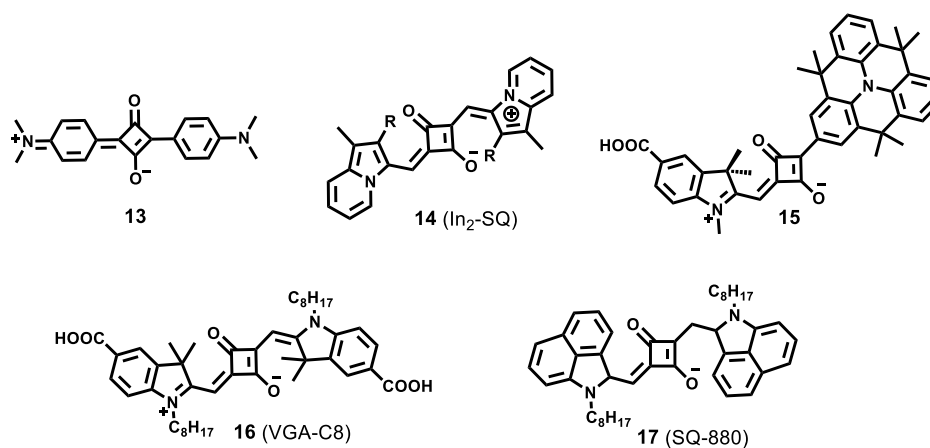


Figure 4: Structures of Squaraine dyes

Paterno and coworkers have developed single squaraine dye **16** which aggregates to form a thin film and absorbs in the range 650 nm to 800 nm depending upon the size of the aggregation.³⁵ Hany and coworkers have synthesised squaraine dye **17** (SQ880) with benz[*cd*]indolium heterocycle moiety absorb in 700-1100 nm region and was used to construct transparent upconversion device.³⁶ Synthesis of these dyes at large scale and hydrophobicity of the dyes are of grave concern for biological applications.

1.1.4 Benzo[*c*]heterocycles

The simplest dyes that are NIR fluorescent are benzo[*c*]heterocycles as shown in figure 5. Swager and coworkers have developed fluorophores containing benzo[*c*]heterocycles **18** and **19**.¹³ The authors have shown that the appropriate choice of donor moieties on the skeleton of

dyes **18** and **19** could tune the absorption and fluorescence from visible to NIR. The highest red shift (emission at 785 nm) was observed in case of dye **19** with *N,N*-dimethylamine as donating moiety. Though these molecules have good photophysical properties, they have not been explored for imaging and other applications.

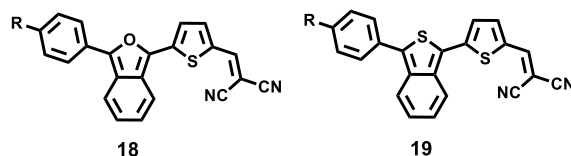


Figure 5: Structures of Benzo[c]heterocycles.

1.1.5 BODIPYs and Aza-BODIPYs

4,4-Difluoro-4-bora-3a,4a-diaza-*s*-indacene, commonly known as BODIPYs **19** have emerged as a fascinating class of dyes with wide range of applications as biomolecular labels, drug delivery agents, fluorescent switches, electroluminescent films, laser dyes, light harvesters and solar cells.³⁷ Treibs and Kreuzer are the first to report the synthesis of these dyes in 1968.³⁸ These dyes are robust, have high absorption coefficients and high fluorescence quantum yields. Though these have numerous advantages, until recently the research was mostly focussed on BODIPYs which are fluorescent in visible region. Ziessel and coworkers

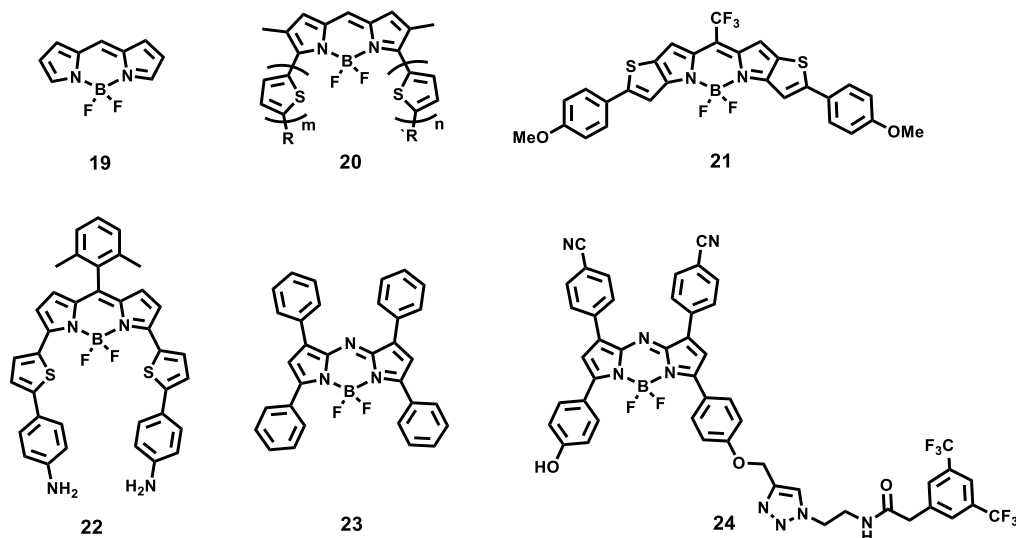


Figure 6: Structures of BODIPYs and aza-BODIPYs

have synthesised oligothiophenyl-BODIPYs **20** which are fluorescent in red to NIR region.³⁸ Authors found that the increasing number of thiophene rings on the BODIPY has shifted the absorption and emission bathochromically with reduction in quantum yield. Later, You and coworkers have achieved the NIR fluorescence in BODIPYs by synthesizing thieno-pyrrole fused BODIPYs **21** based systems.³⁹ By changing appropriate aryl groups the absorption was

tuned from 520 nm to 850 nm and fluorescence from 560 nm to 860 nm. Recently Yamada and coworkers have devised the strategy to tune BODIPYs to NIR region by Suzuki-Miyaura cross coupling of BODIPYs with 2-aryl substituted thiophenes to give BODIPYs **22**.⁴⁰ All these strategies involve extending the π -conjugation in the molecule by fusion or coupling with heterocyclic rings.

Other way of achieving it is by replacing the *meso* carbon of BODIPY by nitrogen atom to give rise to aza-BODIPYs **23** which have bathochromically shifted absorption and fluorescence bands compared to BODIPYs, thereby making aza-BODIPYs NIR absorbing and emitting materials.⁴¹ Borisov and coworkers have synthesised aza-BODIPY dyes for sensing and imaging of pH from neutral to highly alkaline range by drop in the fluorescence of dyes as pH is increased.⁴² Zhau, Chen and coworkers have developed fluorinated aza-BODIPY derivatives **24** for NIR fluorescence, photoacoustic and ¹⁹F trimodality *in vivo* imaging.⁴³

1.1.6 Porphyrins and Phthalocyanines

Porphyrins **25** are 18π electron macrocyclic systems in which four pyrroles are connected in a cyclic fashion through methine bridges.⁴⁴ Porphyrins have gained a lot of interest due to their presence in biological systems such as chlorophyll in PS-I and PS-II, as prosthetic group of heme in haemoglobin and myoglobin, as chlorin in vitamin B₁₂. It is reported that the porphyrin and its analogs conjugated with peptides can be used as PDT agents, artificial hemes, cellular imaging and anti-tumour agents. Porphyrins in general absorb in visible region and emit in far red with moderate quantum yields. Porphyrins are particularly advantageous in biomedical applications as they are highly biocompatible/less toxic, easily degraded by cellular mechanisms. Photofrin is the only porphyrin based drug in the market which is approved by FDA for the treatment for cancer.^{45,46} Photophysical properties of porphyrins can be easily altered by changing the *meso*-aryl groups, substitutions on β -pyrrolic positions and replacing the pyrrole with other heterocycles such as furan, thiophene, selenophene, tellurophene etc.⁴⁷ For example, Dong and coworkers introduced alkyne substituents at *meso* positions to give porphyrin **26** which has last absorption Q-band at 700 nm with fluorescence at 730 nm.⁴⁸ Furthermore, authors have shown that the nanoparticles made from porphyrin **26** could be used as NIR fluorescence imaging and cancer photodynamic therapy. Alternatively, this could be achieved by covalently conjugating different porphyrins to form arrays. Therien and coworkers have synthesised porphyrin arrays with Zn-porphyrin subunits with accepting and donor aryl systems at *meso*-positions alternatively to lead to an exceptional NIR fluorescence with moderate quantum yields.⁴⁹

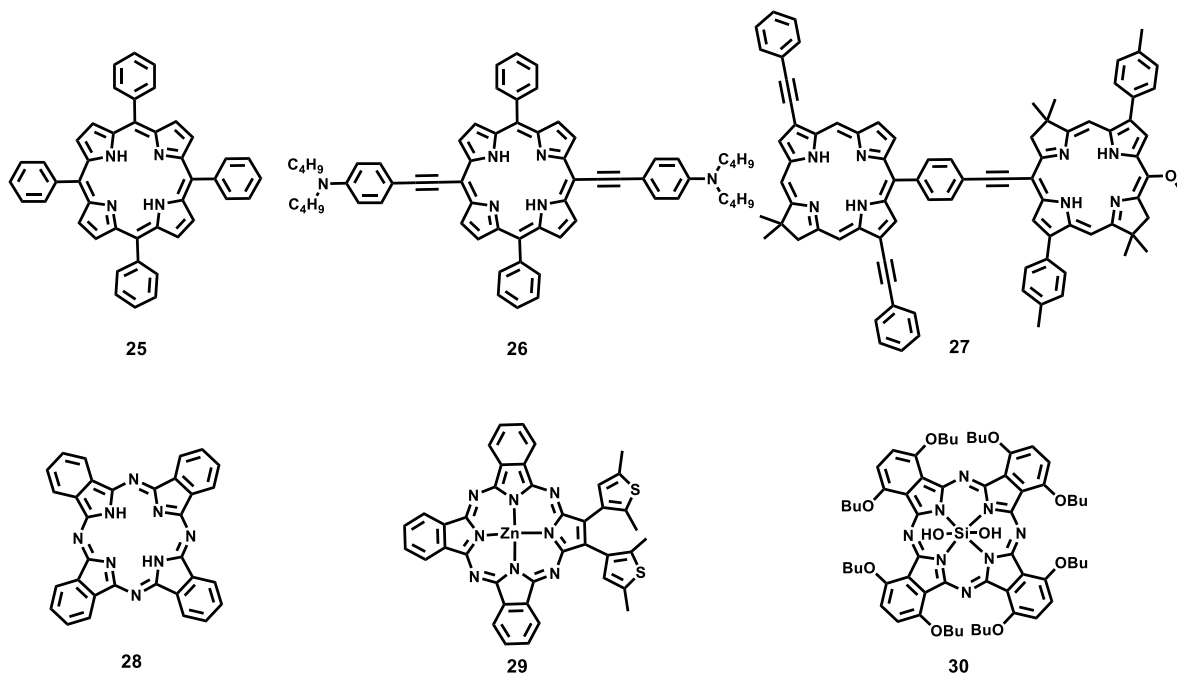


Figure 7: Structures of few Porphyrins and Phthalocyanines.

Phthalocyanines **28** are analogs of porphyrins where *meso* carbon atoms are replaced by nitrogens.⁵⁰ Phthalocyanines are also 18 π electron macrocyclic systems which are aromatic, absorb and emit in NIR region. Typical phthalocyanine **28** has an absorption band at 698 nm and emission at 701 nm. Tian and coworkers had synthesised 2,3-bis(2,5-dimethyl-3-thienyl) unsymmetrical-phthalocyanines **29** which behaves as reversible NIR fluorescence switch.⁵¹ Similarly, Arnaut and coworkers have synthesised dihydroxy silicon complex of phthalocyanine **30** which showed absorption at 743 nm and emission at 759 nm with decent quantum yield ($\phi_f = 0.22$). Furthermore, authors have used phthalocyanine **30** as labels for NIR fluorescence imaging of solid tumors.⁵²

1.1.7 Expanded porphyrins and NIR fluorescence

NIR absorption in porphyrins can also be achieved by the expansion of the core ring of the porphyrin by introducing more pyrrole rings and *meso* carbons which are called as expanded porphyrins.⁵³ When a pyrrole ring and a *meso* carbon is added to porphyrin **25** as shown in figure 8, we obtain an expanded porphyrin named as pentaphyrin **31** as shown in figure 8. When one *meso* carbon is removed from the pentaphyrin **31** and have one direct pyrrole–pyrrole bond, we obtain sapphyrin. Similarly, when two *meso* carbons are removed from the pentaphyrin **31** and make two direct pyrrole-pyrrole bonds, we end up having smaragdyrin **33**.^{53,54} Names for these macrocycles were given by R. B. Woodward, as colour of sapphyrin is red which matches with sapphire and that of smaragdyrin is green which

matches with smarald/emrald. These are the only two expanded porphyrins; sapphyrin and smaragdyrin which are fluorescent.

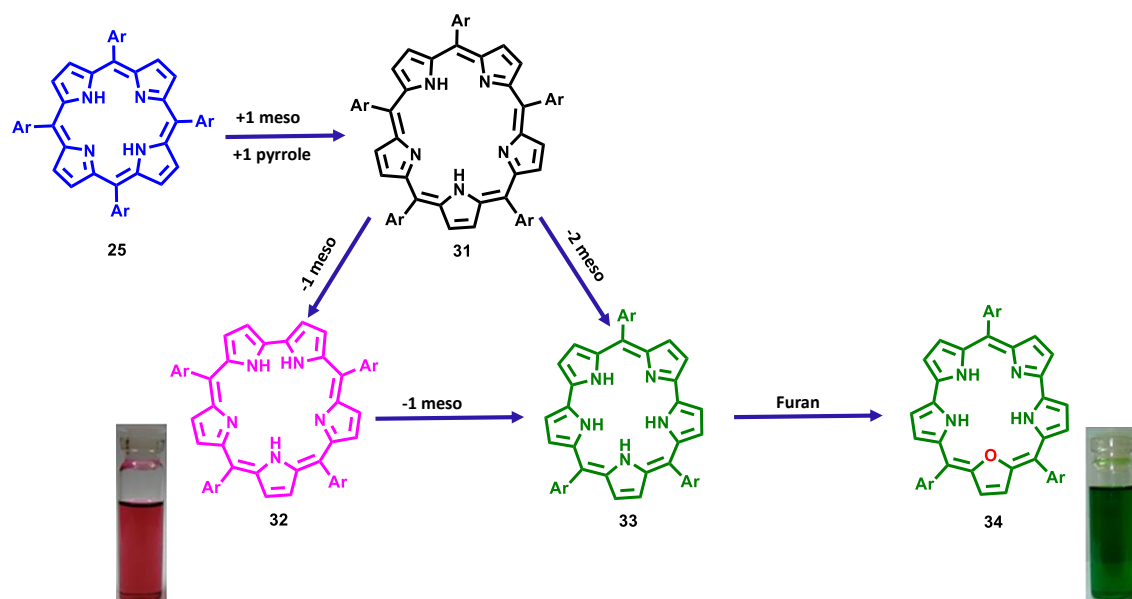
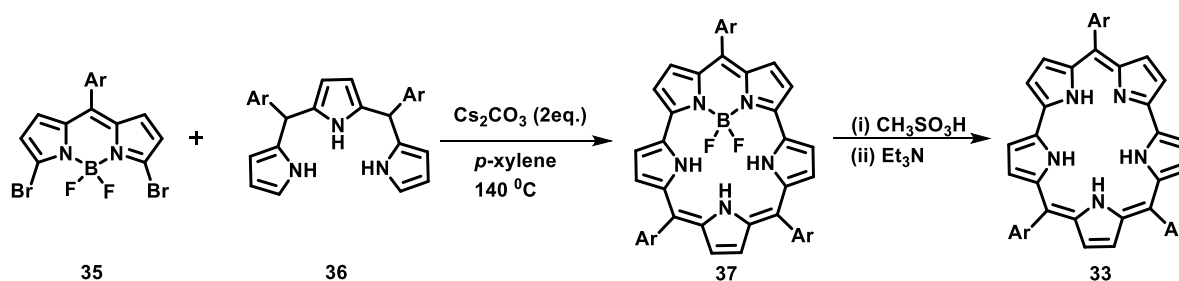


Figure 8: Schematic representation of different expanded porphyrins

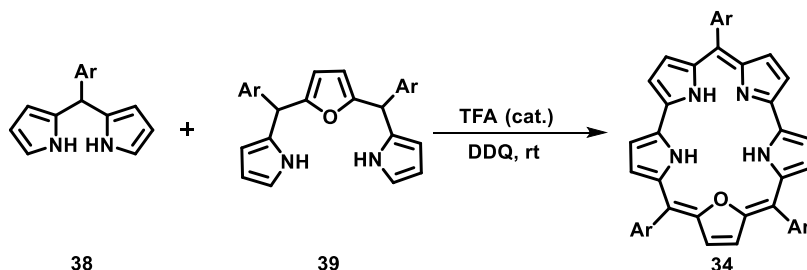
Smaragdyrins are 22π electron pentapyrrolic system in which five pyrroles are connected in a circular fashion with three methine bridges and two direct pyrrole-pyrrole bonds. Due to the presence of two direct pyrrole-pyrrole bonds, the macrocycle core becomes rigid leading to fluorescence which is absent in other expanded porphyrin systems. Though the molecule has excellent photophysical properties, synthesis of pentaazasmaragdyrin was elusive until recently because of its inherent instability. Song and coworkers have developed the synthesis of *meso*-triarylsmaragdyrins **33** as shown in scheme 1.⁵⁵ Brominated BODIPY **35** was treated with azatripyrrane **36** in presence of Cs_2CO_3 under reflux conditions to give BF_2 -azasmaragdyrin **37** which underwent decomplexation in acidic conditions to give *meso*-triarylsmaragdyrins **33**. The *meso*-triarylsmaragdyrins **33** easily oxidises in presence of air to



Scheme 1: Synthesis of pentaazasmaragdyrin.

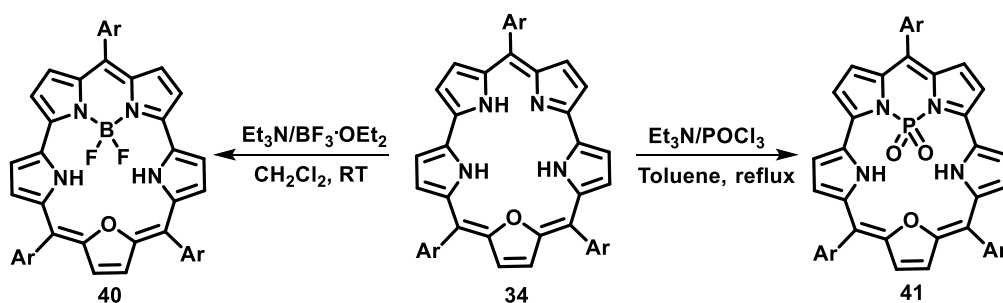
give oxidised form which is anti-aromatic in nature. Chandrasekhar and coworkers devised a method to stabilise smaragdyrin macrocycle in free base form by replacing one of the pyrrole

rings with furan to give rise to oxasmaragdyrins **34**.^{53,54,56} Authors achieved this by following [3+2] MacDonald condensation between appropriate dipyrromethanes **38** and oxatripyrranes **39** under acid catalysed conditions at room temperature followed by oxidation with DDQ to give oxasmaragdyrins in decent yields. Oxasmaragdyrins are quite stable, absorb in visible-NIR region and emit in NIR region with low quantum yields ($\phi_f = 0.04$). The stability of these macrocycles was further enhanced by forming BF₂ **40** and PO₂ **41** complexes of these



Scheme 2: Synthesis of 25-oxasmaragdyrin.

macrocycles as shown in the scheme 3.^{57,58} The oxasmaragdyrin **34** was treated with BF₃·OEt₂ in presence of triethylamine to give BF₂-oxasmaragdyrin **40** in 70-80% yields. Similarly, the oxasmaragdyrin **34** was treated with POCl₃ in presence of triethylamine to give PO₂-oxasmaragdyrin **41** in 50-60% yields. Upon BF₂ and PO₂ complexation of oxasmaragdyrin, a bathochromic shift of 5 nm in absorption band was observed with a significant increase in molar absorptivity. Furthermore, a bathochromic shift of 10 nm in fluorescence with threefold increase in quantum yield ($\phi_f = 0.15$) was observed upon BF₂ and PO₂ complexation. BF₂-oxasmaragdyrins and PO₂ oxasmaragdyrins are highly stable with excellent photophysical and electrochemical properties which makes these molecules very useful for various applications. Ravikanth and coworkers have further explored the chemistry of oxasmaragdyrin macrocycles by synthesizing B(OH)₂ and B(OR)₂ complexes of oxasmaragdyrin, *meso* free oxasmaragdyrin, *meso* functionalised oxasmaragdyrin and so on which showed excellent photophysical and electrochemical properties.^{57,59–61} Hung and coworkers have used BF₂-oxasmaragdyrin **40** for DSSC applications.⁶² Though these molecules have excellent absorption and fluorescence in NIR region and have relatively higher stability, the biomedical applications of these dyes have not been explored.



Scheme 3: Synthesis of BF_2 and PO_2 complexes of oxasmaragdyrin.

Though NIR fluorophores are intended primarily for NIR fluorescence imaging to enhance the imaging resolution in mammalian tissues, the research in past few years has led to the use these NIR fluorescent molecules as diagnosis and thernostic agents especially as anticancer agents.

1.2 Cancer and anticancer therapy

Cancer has become a major cause of deaths worldwide for past few decades. The treatment for cancer is not straight-forward as it doesn't have a single specific cause unlike other diseases.^{63,64} The Cancer Society of Finland roughly divides the causes of cancer as follows, (a) biological/internal factors such as age, gender, inherited genetic defects and skin type; (b) environmental exposure such as radon/UV radiation, small particulate matter, polymer materials; (c) occupational factors which includes carcinogens such as radioactive materials, chemicals; (d) lifestyle-related factors such as tobacco, alcohol, UV radiation from sunlight and some foods which generate excess nitrites and polyaromatic hydrocarbons (PAHs). Each cancer operates differently at the cellular level which is posing great challenges to the researchers working on anticancer therapies around the world.⁶⁵ In spite of the difficulties posed by vast number of causes and mechanisms, we now have various ways to treat cancer which include surgery, radiotherapy, chemotherapy, hormone therapy, photodynamic therapy (PDT) and photothermal therapy (PTT). Cancer therapy is personalised which make the treatments vary depending upon the location of tumor, distribution, cell type and the patient's overall condition. Here we will discuss about each type of therapy used, few molecules/materials which are in clinical stage and commercialisation.

1.2.1 Surgery and Radiotherapy

Surgery was the oldest treatment where the solid cancers were removed by surgical treatment. The discovery of X-rays and radiation by Becquerel and Rontgen in the late 19th century was the primary step towards radiation treatment. Marie Curie's work has immensely

contributed for the development of radiotherapy. The first cancer case cured exclusively by radiation occurred in 1898. The technological progress after World War II allowed charged particles to be propelled through a vacuum tunnel named as ‘linac, or linear accelerator’. In 1960, Ginzton and Kaplan started using a rotational linac radiotherapy called “Clinac 6”, which was used to concentrate X-rays more deeply thereby not affecting the skin to large extent. Surgery and radiotherapy were the treatments mainly followed for solid tumor treatment into the 1960s. The curability rates were low due to uncontrolled micrometastases. There were some promising publications about the use of chemotherapy after radiotherapy or surgery in curing patients with advanced cancer. Breast cancer was the first type of disease in which positive results were obtained with adjuvant therapy, and the first example of multimodality treatment, a strategy currently employed for treatment of numerous types of tumors. In the late 1960s, the use of adjuvant chemotherapy changed the concept of localized treatment.

The development of modern computers enabled three-dimensional X-ray therapy, such as intensity-modulated radiation therapy (IMRT) using mapping information from Computed Tomography (CT) scans. This provides a three-dimensional reconstruction, which helps avoid toxicity since the contours of the tumor are targeted and separated from healthy tissues. In 2003, a specific type of IMRT was developed called the TomoTherapy® system.⁶⁶ This treatment uses CT-guided IMRT technology that directs the radiation source by rotating it around the patient, which makes the morphological limits of a tumor easier to trace with the beam. Another significant trend is the use of charged particle radiotherapy with proton or helium ions for specific types of patients with melanoma of the uveal tract. It is also used as adjuvant therapy for skull base chondroma, chondrosarcoma and spine (usually cervical). In summary, the lines of development have been fractionated dose delivery, technological advances in X-ray production and delivery and improvement of computer-based treatment planning.

1.2.2 Chemotherapy

Chemotherapy is a common and widely used technique for treating cancer. The term ‘chemotherapy’ was coined by the German scientist Paul Ehrlich. The history of chemotherapy leads back to 1930s. Chemotherapy involves usage of chemical molecules to kill the cancerous cells by attacking various cellular processes. These include plant alkaloids, alkylating agents, antimetabolites, antitumor antibiotics, topoisomerase inhibitors and antineoplastics. Alkylating agents are most active in the resting phase of the cells. The first cancer to be cured with

chemotherapy, choriocarcinoma, was reported in 1958.⁶⁷ Later during the 1960s, the main targets were hematologic cancers. The most commonly used drugs for chemotherapy include Cisplatin **42** and Taxol.^{68,69} Better treatments were developed, with alkaloids from vinca **43** and ibenzmethylin (procarbazine) **44**, successfully applied to leukemia and Hodgkin's disease.^{70,71} Advanced Hodgkin's disease was made curable with chemotherapy in 1970s using the MOMP protocol which combined nitrogen mustard with vincristine, methotrexate and prednisone, and the MOPP protocol containing procarbazine but no methotrexate. Patients with diffused large B-cell lymphoma were treated with the same therapy and a cure for advanced diffused large B-cell lymphoma was reported using protocol C-MOPP, which substituted cyclophosphamide for nitrogen mustard was reported in 1975. A significant progress was made

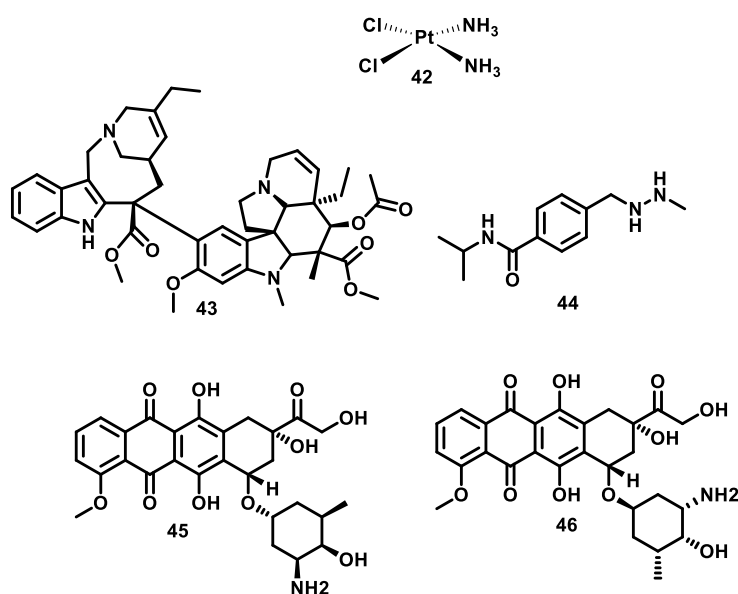


Figure 9: Structures of various chemotherapeutic drugs

in late 1970s where the higher cure rates were achieved by combining cisplatin, bleomycin and vinblastine.⁶⁹ This practice of polychemotherapy in hematologic has led to the concept that different drugs act against tumor cells at different phases of their cell cycle. One of these drugs CMF (Cytosan, methotrexate and fluorouracil) was a standard therapy for breast cancer for over 30 years. Understanding the effects at molecular level in the cells, number of drugs with various mechanisms of action were described. Consequently, the advances and developments led to liposomal therapy, which incorporates drugs inside liposomes (vesicles made of lipid bilayers), led to decrease some of the side effects of chemotherapy such as cardiotoxicity.⁷² Few examples of liposomal drugs such as liposomal doxorubicin **45** and daunorubicin **46**, are first steps in nanotechnology-based approaches.

1.2.3 Immunotherapy

Immunotherapy uses components of immune system such as antibodies, cytokines and dendritic cells to treat various diseases.⁷³ Although immunotherapy is used to cure several illnesses, in case of cancers it aims at helping patient's immune system to destroy tumors. Rituximab is the first monoclonal antibody approved by FDA for non-hodgkin's lymphoma. Since then the immunotherapy has entered for the treatment of breast cancer breast cancer (trastuzumab), acute myeloid leukemia (gemtuzumab Ozogamicin), chronic lymphocytic leukemia (alemtuzumab), and colorectal tumor (cetuximab). The new development in this field of immunotherapy has been making immunoconjugates. Immunoconjugates include antibodies linked to the anti-cancer agents such as drugs, cytokines, toxins and radioisotopes. The antibody in the immunoconjugates act as a transporter for the cancer-killing agents to concentrate at the cancer cells and have minimal damage to healthy cells.

1.2.4 Photodynamic therapy

Photodynamic therapy (PDT) uses a photosensitizer which activates upon exposure to visible/NIR radiation and transfers energy to molecular oxygen thereby generating reactive oxygen species (ROS) such as singlet oxygen, free radicals, and peroxides as shown in figure 10.⁷⁴ ROS oxidises lipids, amino acids, and proteins to induce cell death. Number of PDT agents have been reported over the years for efficient cancer therapy. Most of the FDA-approved photosensitisers absorb in the visible region where cell penetration is only few millimetres as previously discussed. Hence, PDT is limited to treatment of certain types of skin cancers.

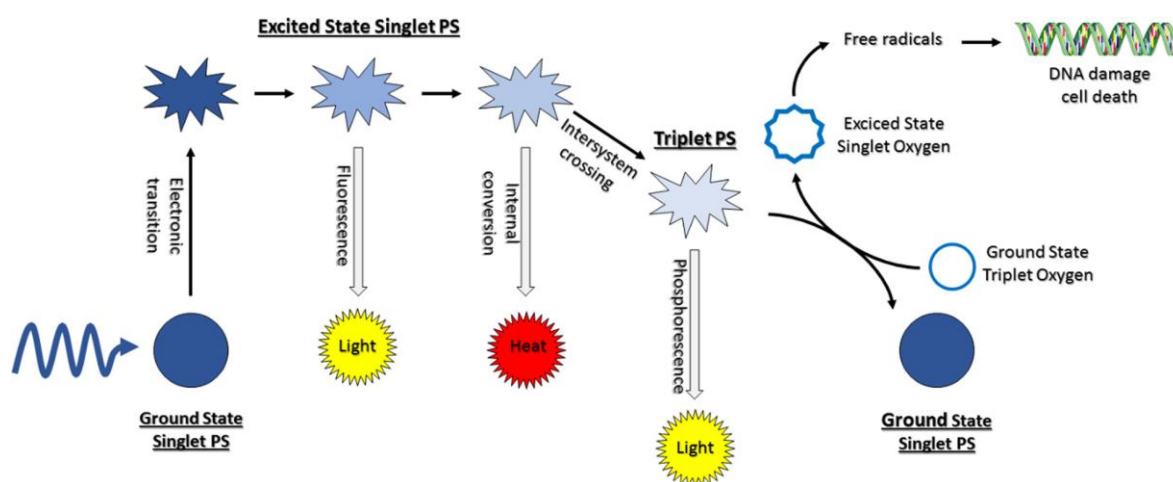


Figure 10: Mechanism for Photodynamic reaction. Reproduced from ref. 74 Copyright © 2018 Elsevier Masson SAS. All rights reserved.

1.2.5 Hyperthermia

Hyperthermia is an anticancer therapy which consists of heating a tumor to inhibit proliferation of cancer cells to destroy or making them more sensitive to the effects of radiation and chemotherapy.⁷⁵ Hyperthermia is currently used as an adjunct therapy to radiotherapy and chemotherapy. Hyperthermia uses the fact that when cells are heated beyond the normal temperatures normally 43 °C, the cells undergo irreparable damage which results in cell death commonly known as thermal ablation. A typical hyperthermia treatment uses microwaves, ultrasound and radiofrequency which can be focussed on a target local tumor. The therapy is non-invasive, mild heat generated increases the blood flow to the tumor tissue whereby increasing the effect of chemotherapy. Integration of hyperthermia with imaging technologies such as non-invasive MR-based thermometry or NIR fluorescence will help to achieve full potential of hyperthermia in cancer treatment.

Nanotechnology offers an opportunity to improve heat delivery. Magnetic Fluid Hyperthermia (MPH) uses iron oxide nanoparticles as a heating source due to their excellent magnetic properties.⁷⁶ MPH is broadly classified into two types depending on the route of administration; arterial embolization hyperthermia and direct intratumoral injection hyperthermia. Magnetic nanoparticles have an added advantage of achieving site-specific tumor targeting which could be achieved by external magnetic field. The particles can simultaneously be traced by MRI. Magnetic energy dissipation from nanoparticles induces heating which give rise to cell death at temperatures above 43 °C. MPH is in Phase I and Phase II clinical trials in treating prostate carcinoma and glioblastoma multiforme by using magnetic nanoparticles. The minor limiting factors have been reported in use of MPH such as patient discomfort at high magnetic fields and irregular intratumoral heat distribution. Purushotham *et. al.* have developed magnetic nanoparticles with a thermoresponsive polymer embedded with doxorubicin.⁷⁷ These nanoparticles have been used as simultaneous hyperthermia and release of doxorubicin at hyperthermia temperatures to cure cancer in *in vitro* and *in vivo* rat models.

NIR absorbing nanoparticles have entered hyperthermia treatment in recent years. These nanoparticles absorb or scatter light whereby producing heat which increase the temperature of the tissue where nanoparticles are embedded. This phenomena of using light to heat conversion is generally called as Photothermal Therapy (PTT).⁵ NIR region of electromagnetic spectrum is very advantageous as there is minimal absorption by water and biological chromophores as discussed previously.

Halas and coworkers developed SiO₂/Au nanoshells as NIR absorbing tags have been considered for the photothermal ablation of solid tumors.⁷⁷ Furthermore, West and coworkers demonstrated Au/AuS NIR-absorbing particles (35-55nm) which have higher absorption than nanoshells as well as potentially better tumor penetration.⁷⁸ Bhatia and coworkers have shown that the PEG-protected gold nanorods exhibit superior spectral bandwidth, higher photothermal heat generation and longer circulation half-life compared to gold nanoshells.⁷⁹ Recent works in the field, led to various inorganic nanoparticles such as graphene and graphene oxide, black phosphorus quantum dots and nanosheets, gold nanoparticles, palladium nanosheets, copper sulphide, copper selenide, and molybdenum oxide nanomaterials have been studied as PTT agents.⁷⁹ Inorganic nanoparticles have inherent disadvantages which include structural instability, non-biodegradability and long term toxicity. Newer organic polymer based PTT agents were developed to counter the disadvantages of inorganic nanoparticles.^{80,81} Organic polymer based PTT agents are restricted for applications as they are often encumbered with lengthy synthetic procedures and undergo complicated processing techniques. In recent years, organic dye-based nanoparticles and C-dot based materials have emerged as promising PTT agents. Qiu and coworkers, have synthesised porphyrin immobilized on nanographene oxide and used it for targeted photothermal therapy of brain cancer.⁸² Yan and coworkers, have synthesised porphyrin diphenylalanine conjugates and self-assembled into spherical nanoparticles.⁸³ These particles have been used as photothermal thermal agents with very high photothermal efficacy (~56%) to for cancer treatment.

1.3 Scope of the thesis

In the previous sections we have briefly discussed about the NIR fluorescence imaging, existing NIR fluorophores, expanded porphyrins as NIR fluorophores, various treatments of cancer, role of hyperthermia in cancer treatment, various hyperthermia agents available. We have also discussed with the limited literature available on incorporation of NIR fluorophores towards the hyperthermia and their use as imaging as well as therapeutic agents. There is a lot of scope for synthesis of stable NIR fluorophores and their use in imaging and hyperthermia. In this thesis we have explored some of those properties by using an expanded porphyrin, BF₂-25-oxasmaragdyrin as a highly stable NIR fluorophore.

In chapter 3, we synthesised a series of amino acid conjugated oxasmaragdyrins and BF₂-oxasmaragdyrins (Figure 11) to study the changes in the photophysical and electrochemical properties. The target amino acid conjugates were achieved by synthesising

the precursor *meso*-(4-hydroxymethylphenyl) oxasmaragdyrin which was then conjugated with various *fmoc*-protected amino acids under standard conditions. The photophysical and electrochemical studies indicated that there were no significant changes in photophysical properties of the conjugates of oxasmaragdyrin and BF₂-oxasmaragdyrin compared to their precursor oxasmaragdyrin/BF₂-oxasmaragdyrin.

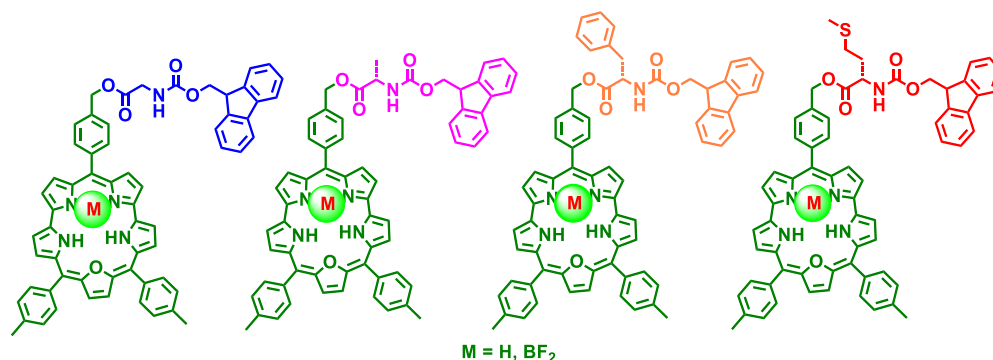


Figure 11: Oxasmaragdyrin-amino acid conjugates and their corresponding BF₂ complexes.

In chapter 4, we described the synthesis of glucosamine conjugated BF₂-oxasmaragdyrin using *meso*-(4-carboxyphenyl) oxasmaragdyrin as a precursor (Figure 12). The glucosamine conjugated BF₂-oxasmaragdyrin was characterised thoroughly by 1D, 2D NMR, HRMS. The synthesised conjugate is stable and have retained the photophysical, electrochemical properties as that of the BF₂-oxasmaragdyrin. Glucosamine conjugated BF₂-oxasmaragdyrins were tested for *in vitro* biocompatibility and cellular uptake in L929 cells.

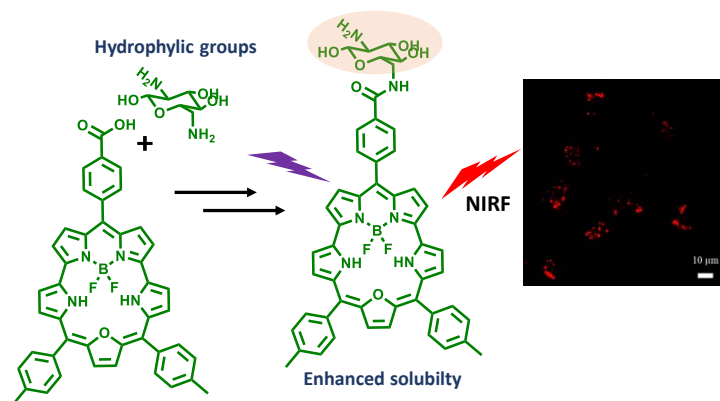


Figure 12: Glucosamine conjugated BF₂-oxasmaragdyrin as NIR fluorescence imaging agent.

In chapter 5, we described the synthesis of L,L-Diphenylalanine conjugated BF₂-oxasmaragdyrin by using *meso*-(4-carboxyphenyl) oxasmaragdyrin as a precursor molecule under standard conditions (Figure 13). The L,L-Diphenylalanine conjugated BF₂-oxasmaragdyrin easily self assembles to spherical nanoparticles (~100 nm) in water which were characterised by SEM, TEM and DLS. The L,L-Diphenylalanine conjugated BF₂-oxasmaragdyrin self-assemblies were assessed for physiological pH stability (5.5, 6.5, 7.4)

and lyophilisation stability. The L,L-Diphenylalanine conjugated BF₂-oxasmaragdyrin self-assemblies are non-fluorescent and shows photothermal property (PTT) i.e., convert light to heat when irradiated with 750 nm laser. Furthermore, we have used L,L-Diphenylalanine conjugated BF₂-oxasmaragdyrin self-assemblies for *in vitro* and *in vivo* photothermal therapy.

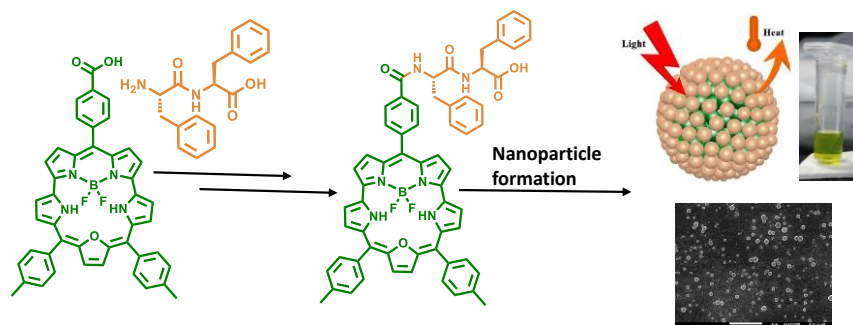


Figure 13: Schematic representation to synthesise L,L-Diphenylalanine conjugated BF₂-oxasmaragdyrin self-assemblies.

In chapter 6, we described the synthesis of *meso*-Tritolyl-BF₂-oxasmaragdyrin quantum dots (TBSQDs) by using high pressure homogenises on *meso*-tritolyl-BF₂-oxasmaragdyrin in presence of lipid S75. Formation of TBSQDs were observed by Surface Enhanced Raman Spectroscopy (SERS) and confirmed by TEM (Transmission Electron Microscopy) analysis. The synthesised TBSQDs are fluorescent in NIR with a quantum yield of 9% and shows photothermal property (PTT) i.e., convert light to heat when irradiated with 750 nm laser. Furthermore, we have used TBSQDs as theragnostic agents for NIR Fluorescence imaging as well as photothermal therapy *in vitro* and *in vivo* systems.

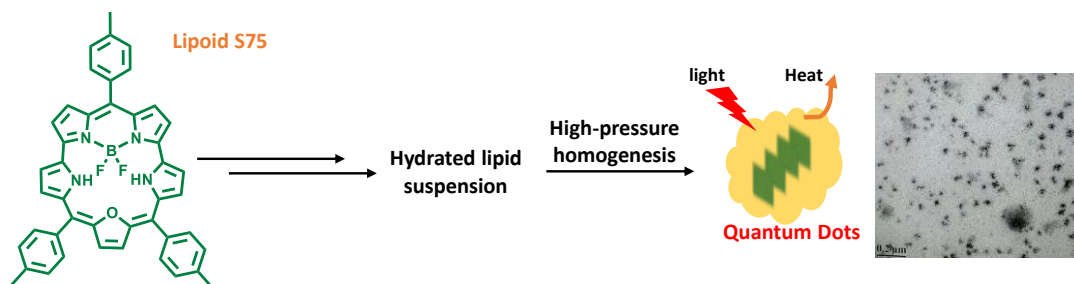


Figure 14: Schematic representation for formation of TBSQDs.

In chapter 7, we have synthesised Cell Penetrating Peptide (CPP) conjugated BF₂-oxasmaragdyrin by using *meso*-(4-carboxyphenyl)BF₂-oxasmaragdyrin as a precursor molecule and CRGDK, R₉ peptides under Solid Phase Peptide Synthesis (SPPS) conditions. CRGDK, R₉ conjugated BF₂-oxasmaragdyrin was purified by RP-HPLC and characterised by HRMS. The photophysical properties of synthesized compounds were thoroughly evaluated

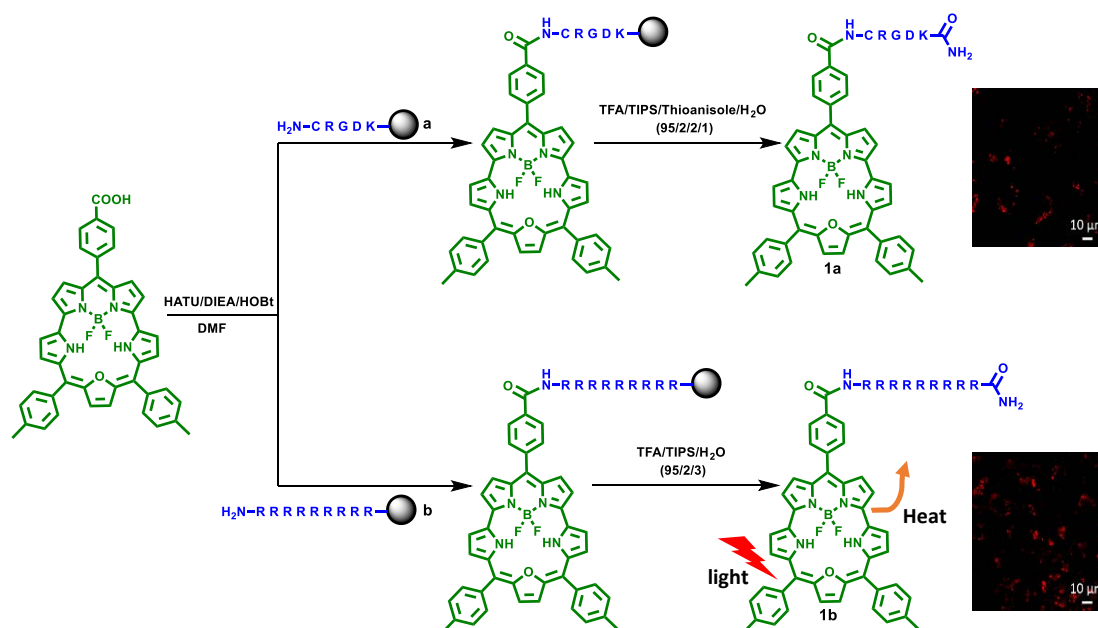


Figure 15: Schematic representation for synthesis of peptide conjugated BF₂-oxasmaragdyrins.

and found that both the conjugates were stable, absorb in the UV-Vis and emit in the NIR region with moderate quantum yields and singlet state lifetimes. CLSM experiments also revealed that both the conjugates were internalized into the MDA-MB-231 within 24 hours and emitting strong NIR fluorescence from within the cells. Furthermore, R₉ conjugated BF₂-oxasmaragdyrin has photothermal property when irradiated with 750 nm laser. The R₉ conjugated BF₂-oxasmaragdyrin could be used as theragnostic agents for *in vivo* whole-body or site-specific imaging as well as therapy in future.

1.4 References:

- (1) Hani, A. F. M.; Kumar, D. *Optical Imaging for Biomedical and Clinical Applications*, 1st ed.; CRC Press, 2017.
- (2) Zhao, J.; Zhong, D.; Zhou, S. NIR-I-to-NIR-II Fluorescent Nanomaterials for Biomedical Imaging and Cancer Therapy. *J. Mater. Chem. B* **2018**, 6, 349–365.
- (3) Yi, X.; Wang, F.; Qin, W.; Yang, X.; Yuan, J. Near-Infrared Fluorescent Probes in Cancer Imaging and Therapy: An Emerging Field. *Int J Nanomedicine* **2014**, 9, 1347–1365.
- (4) Escobedo, J. O.; Rusin, O.; Lim, S.; Strongin, R. M. NIR Dyes for Bioimaging

- Applications. *Current Opinion in Chemical Biology*. February 2010, pp 64–70.
- (5) Khot, M. I.; Andrew, H.; Svavarsdottir, H. S.; Armstrong, G.; Quyn, A. J.; Jayne, D. G. A Review on the Scope of Photothermal Therapy–Based Nanomedicines in Preclinical Models of Colorectal Cancer. *Clinical Colorectal Cancer*. Elsevier Inc. June 1, 2019, pp e200–e209.
 - (6) Pham, W.; Cassell, L.; Gillman, A.; Koktysh, D.; Gore, J. C. A Near-Infrared Dye for Multichannel Imaging. *Chem. Commun.* **2008**, No. 16, 1895–1897.
 - (7) Fischer, G. M.; Isomäki-Krondahl, M.; Göttker-Schnetmann, I.; Daltrozzo, E.; Zumbusch, A. Pyrrolopyrrole Cyanine Dyes: A New Class of Near-Infrared Dyes and Fluorophores. *Chem. – A Eur. J.* **2009**, *15*, 4857–4864.
 - (8) Yang, Y.; Lowry, M.; Xu, X.; Escobedo, J. O.; Sibrian-Vazquez, M.; Wong, L.; Schowalter, C. M.; Jensen, T. J.; Fronczek, F. R.; Warner, I. M.; et al. Seminaphthofluorones Are a Family of Water-Soluble, Low Molecular Weight, NIR-Emitting Fluorophores. *Proc. Natl. Acad. Sci.* **2008**, *105*, 8829.
 - (9) Arunkumar, E.; Forbes, C. C.; Noll, B. C.; Smith, B. D. Squaraine-Derived Rotaxanes: Sterically Protected Fluorescent Near-IR Dyes. *J. Am. Chem. Soc.* **2005**, *127*, 3288–3289.
 - (10) Johnson, J. R.; Fu, N.; Arunkumar, E.; Leevy, W. M.; Gammon, S. T.; Piwnica-Worms, D.; Smith, B. D. Squaraine Rotaxanes: Superior Substitutes for Cy-5 in Molecular Probes for near-Infrared Fluorescence Cell Imaging. *Angew. Chem. Int. Ed.* **2007**, *46*, 5528–5531.
 - (11) Umezawa, K.; Citterio, D.; Suzuki, K. Water-Soluble NIR Fluorescent Probes Based on Squaraine and Their Application for Protein Labeling. *Anal. Sci.* **2008**, *24*, 213–217.
 - (12) Fu, N.; Gassensmith, J. J.; Smith, B. D. Effect of Stopper Size on Squaraine Rotaxane Stability. *Supramol. Chem.* **2009**, *21*, 118–124.
 - (13) Meek, S. T.; Nesterov, E. E.; Swager, T. M. Near-Infrared Fluorophores Containing Benzo[c]Heterocycle Subunits. *Org. Lett.* **2008**, *10*, 2991–2993.
 - (14) Feng, G.; Liu, J.; Geng, J.; Liu, B. Conjugated Polymer Microparticles for Selective Cancer Cell Image-Guided Photothermal Therapy. *J. Mater. Chem. B* **2015**, *3*, 1135–

- 1141.
- (15) Loudet, A.; Bandichhor, R.; Burgess, K.; Palma, A.; McDonnell, S. O.; Hall, M. J.; O'Shea, D. F. B,O-Chelated Azadipyrromethenes as Near-IR Probes. *Org. Lett.* **2008**, *10*, 4771–4774.
- (16) Umezawa, K.; Nakamura, Y.; Makino, H.; Citterio, D.; Suzuki, K. Bright, Color-Tunable Fluorescent Dyes in the Visible–Near-Infrared Region. *J. Am. Chem. Soc.* **2008**, *130*, 1550–1551.
- (17) Umezawa, K.; Matsui, A.; Nakamura, Y.; Citterio, D.; Suzuki, K. Bright, Color-Tunable Fluorescent Dyes in the Vis/NIR Region: Establishment of New “Tailor-Made” Multicolor Fluorophores Based on Borondipyrromethene. *Chem. – A Eur. J.* **2009**, *15*, 1096–1106.
- (18) Nesterova, I. V; Verdree, V. T.; Pakhomov, S.; Strickler, K. L.; Allen, M. W.; Hammer, R. P.; Soper, S. A. Metallo-Phthalocyanine Near-IR Fluorophores: Oligonucleotide Conjugates and Their Applications in PCR Assays. *Bioconjug. Chem.* **2007**, *18*, 2159–2168.
- (19) Kee, H. L.; Nothdurft, R.; Muthiah, C.; Diers, J. R.; Fan, D.; Ptaszek, M.; Bocian, D. F.; Lindsey, J. S.; Culver, J. P.; Holten, D. Examination of Chlorin-Bacteriochlorin Energy-Transfer Dyads as Prototypes for near-Infrared Molecular Imaging Probes. *Photochem. Photobiol.* **2008**, *84*, 1061–1072.
- (20) Kuimova, M. K.; Collins, H. A.; Balaz, M.; Dahlstedt, E.; Levitt, J. A.; Sergent, N.; Suhling, K.; Drobizhev, M.; Makarov, N. S.; Rebane, A.; et al. Photophysical Properties and Intracellular Imaging of Water-Soluble Porphyrin Dimers for Two-Photon Excited Photodynamic Therapy. *Org. Biomol. Chem.* **2009**, *7*, 889–896.
- (21) Barnes, K. D.; Shafirstein, G.; Webber, J. S.; Koonce, N. A.; Harris, Z.; Griffin, R. J. Hyperthermia-Enhanced Indocyanine Green Delivery for Laser-Induced Thermal Ablation of Carcinomas. *Int. J. Hyperth.* **2013**, *29*, 474–479.
- (22) Lavis, L. D.; Raines, R. T. Bright Ideas for Chemical Biology. *ACS Chem. Biol.* **2008**, *3*, 142–155.
- (23) Yuan, L.; Lin, W.; Zheng, K.; He, L.; Huang, W. Far-Red to near Infrared Analyte-Responsive Fluorescent Probes Based on Organic Fluorophore Platforms for

- Fluorescence Imaging. *Chemical Society Reviews*. **2013**, 622–661.
- (24) Wang, S.; Fan, Y.; Li, D.; Sun, C.; Lei, Z.; Lu, L.; Wang, T.; Zhang, F. Anti-Quenching NIR-II Molecular Fluorophores for in Vivo High-Contrast Imaging and PH Sensing. *Nat Commun* **2019**, *10*, 1058–1069.
- (25) Fischer, G. M.; Isomäki-Krondahl, M.; Göttker-Schnetmann, I.; Daltrozzo, E.; Zumbusch, A. Pyrrolopyrrole Cyanine Dyes: A New Class of Near-Infrared Dyes and Fluorophores. *Chem. - A Eur. J.* **2009**, *15*, 4857–4864.
- (26) James, N. S.; Chen, Y.; Joshi, P.; Ohulchanskyy, T. Y.; Ethirajan, M.; Henary, M.; Streckowski, L.; Pandey, R. K. Evaluation of Polymethine Dyes as Potential Probes for near Infrared Fluorescence Imaging of Tumors: Part - 1. *Theranostics* **2013**, *3*, 692–702.
- (27) Tan, X.; Luo, S.; Wang, D.; Su, Y.; Cheng, T.; Shi, C. A NIR Heptamethine Dye with Intrinsic Cancer Targeting, Imaging and Photosensitizing Properties. *Biomaterials* **2012**, *33*, 2230–2239.
- (28) Yang, Y.; Lowry, M.; Xu, X.; Escobedo, J. O.; Sibrian-Vazquez, M.; Wong, L.; Schowalter, C. M.; Jensen, T. J.; Fronczek, F. R.; Warner, I. M.; et al. Seminaphthofluorones Are a Family of Water-Soluble, Low Molecular Weight, NIR-Emitting Fluorophores. *Proc. Natl. Acad. Sci. U. S. A.* **2008**, *105*, 8829–8834.
- (29) Zhou, M.; Li, J.; Liang, S.; Sood, A. K.; Liang, D.; Li, C. CuS Nanodots with Ultrahigh Efficient Renal Clearance for Positron Emission Tomography Imaging and Image-Guided Photothermal Therapy. *ACS Nano* **2015**, *9*, 7085–7096.
- (30) Niu, G.; Liu, W.; Zhou, B.; Xiao, H.; Zhang, H.; Wu, J.; Ge, J.; Wang, P. Deep-Red and Near-Infrared Xanthene Dyes for Rapid Live Cell Imaging. *J. Org. Chem.* **2016**, *81*, 7393–7399.
- (31) Guo, S. H.; Leng, T. H.; Wang, K.; Wang, C. Y.; Shen, Y. J.; Zhu, W. H. A Colorimetric and Turn-on NIR Fluorescent Probe Based on Xanthene System for Sensitive Detection of Thiophenol and Its Application in Bioimaging. *Talanta* **2018**, *185*, 359–364.
- (32) Treibs, A.; Jacob, K. Cyclobutenderivate Der Pyrrolreihe, II1) Über Vierring-Trimethin-Farbstoffe. *Justus Liebigs Ann. Chem.* **1968**, *712*, 123–137.
- (33) McNamara, L. E.; Rill, T. A.; Huckaba, A. J.; Ganeshraj, V.; Gayton, J.; Nelson, R. A.;

- Sharpe, E. A.; Dass, A.; Hammer, N. I.; Delcamp, J. H. Indolizine-Squaraines: NIR Fluorescent Materials with Molecularly Engineered Stokes Shifts. *Chem. - A Eur. J.* **2017**, *23*, 12494–12501.
- (34) Karjule, N.; Munavvar, M. F.; Nithyanandhan, J. Heterotriangulene-Based Unsymmetrical Squaraine Dyes: Synergistic Effects of Donor Moieties and out-of-Plane Branched Alkyl Chains on Dye Cell Performance. *J. Mater. Chem. A* **2016**, *4*, 18910–18921.
- (35) Paternò, G. M.; Moretti, L.; Barker, A. J.; D'Andrea, C.; Luzio, A.; Barbero, N.; Galliano, S.; Barolo, C.; Lanzani, G.; Scotognella, F. Near-Infrared Emitting Single Squaraine Dye Aggregates with Large Stokes Shifts. *J. Mater. Chem. C* **2017**, *5*, 7732–7738.
- (36) Strassel, K.; Kaiser, A.; Jenatsch, S.; Véron, A. C.; Anantharaman, S. B.; Hack, E.; Diethelm, M.; Nüesch, F.; Aderne, R.; Legnani, C.; et al. Squaraine Dye for a Visibly Transparent All-Organic Optical Upconversion Device with Sensitivity at 1000 Nm. *ACS Appl. Mater. Interfaces* **2018**, *10*, 11063–11069.
- (37) Boens, N.; Leen, V.; Dehaen, W. Fluorescent Indicators Based on BODIPY. *Chem. Soc. Rev.* **2012**, *41*, 1130–1172.
- (38) Treibs, A.; Kreuzer, F.-H. Difluoroboryl-Komplexe von Di- Und Tripyrrylmethenen. *Justus Liebigs Ann. Chem.* **1968**, *718*, 208–223.
- (39) Awuah, S. G.; Das, S. K.; D'Souza, F.; You, Y. Thieno-Pyrrole-Fused BODIPY Intermediate as a Platform to Multifunctional NIR Agents. *Chem. - An Asian J.* **2013**, *8*, 3123–3132.
- (40) Li, G.; Otsuka, Y.; Matsumiya, T.; Suzuki, T.; Li, J.; Takahashi, M.; Yamada, K. A Straightforward Substitution Strategy to Tune BODIPY Dyes Spanning the Near-Infrared Region via Suzuki(-)Miyaura Cross-Coupling. *Materials (Basel)*. **2018**, *11*, 1297–1298.
- (41) Jiang, X.-D.; Li, S.; Guan, J.; Fang, T.; Liu, X.; Xiao, L.-J. Recent Advances of the Near-Infrared Fluorescent Aza-BODIPY Dyes. *Curr. Org. Chem.* **2016**, *20*, 1736–1744.
- (42) Staudinger, C.; Breining, J.; Klimant, I.; Borisov, S. M. Near-Infrared Fluorescent Aza-BODIPY Dyes for Sensing and Imaging of PH from the Neutral to Highly Alkaline

- Range. *Analyst* **2019**, *144*, 2393–2402.
- (43) Liu, L.; Yuan, Y.; Yang, Y.; McMahon, M. T.; Chen, S.; Zhou, X. A Fluorinated Aza-BODIPY Derivative for NIR Fluorescence/PA/(19)F MR Tri-Modality in Vivo Imaging. *Chem. Commun. (Camb)*. **2019**, *55*, 5851–5854.
 - (44) Kadish, K. M.; Smith, K. M.; Guillard, R. *The Porphyrin Handbook*; Academic Press, 2000.
 - (45) Dougherty, T. J.; Gomer, C. J.; Henderson, B. W.; Jori, G.; Kessel, D.; Korbely, M.; Moan, J.; Peng, Q. Photodynamic Therapy. *Journal of the National Cancer Institute*. **1998**, 889–905.
 - (46) Sun, B.; Li, W.; Liu, N. Curative Effect of the Recent Photofrin Photodynamic Adjuvant Treatment on Young Patients with Advanced Colorectal Cancer. *Oncol. Lett.* **2016**, *11*, 2071–2074.
 - (47) Chatterjee, T.; Shetti, V.; Sharma, R.; Ravikanth, M. Heteroatom-Containing Porphyrin Analogues. *Chem. Rev.* **2017**, *117*, 3254–3328.
 - (48) Pan, D.; Liang, P.; Zhong, X.; Wang, D.; Cao, H.; Wang, W.; He, W.; Yang, Z.; Dong, X. Self-Assembled Porphyrin-Based Nanoparticles with Enhanced Near-Infrared Absorbance for Fluorescence Imaging and Cancer Photodynamic Therapy. *ACS Appl. Bio Mater.* **2019**, *2*, 999–1005.
 - (49) Duncan, T. V.; Susumu, K.; Sinks, L. E.; Therien, M. J. Exceptional Near-Infrared Fluorescence Quantum Yields and Excited-State Absorptivity of Highly Conjugated Porphyrin Arrays. *J. Am. Chem. Soc.* **2006**, *128*, 9000–9001.
 - (50) Claessens, C. G.; Hahn, U.; Torres, T. Phthalocyanines: From Outstanding Electronic Properties to Emerging Applications. *Chem. Rec.* **2008**, *8*, 75–97.
 - (51) Chen, B.; Wang, M.; Wu, Y.; Tian, H. Reversible Near-Infrared Fluorescence Switch by Novel Photochromic Unsymmetrical-Phthalocyanine Hybrids Based on BisthiényleneElectronic Supplementary Information (ESI) Available: Experimental Details, Synthetic and Spectroscopic Data. See [Http://Www.R.](http://www.rsc.org/chemcomm) *Chem. Commun.* **2002**, 38, 1060–1061.
 - (52) Lobo, A. C.; Silva, A. D.; Tome, V. A.; Pinto, S. M.; Silva, E. F.; Calvete, M. J.; Gomes,

- C. M.; Pereira, M. M.; Arnaut, L. G. Phthalocyanine Labels for Near-Infrared Fluorescence Imaging of Solid Tumors. *J. Med. Chem.* **2016**, *59*, 4688–4696.
- (53) Pareek, Y.; Ravikanth, M.; Chandrashekar, T. K. Smaragdyrins: Emeralds of Expanded Porphyrin Family. *Acc. Chem. Res.* **2012**, *45*, 1801–1816.
- (54) Chatterjee, T.; Srinivasan, A.; Ravikanth, M.; Chandrashekar, T. K. Smaragdyrins and Sapphyrins Analogues. *Chem. Rev.* **2017**, *117*, 3329–3376.
- (55) Xie, D.; Liu, Y.; Rao, Y.; Kim, G.; Zhou, M.; Yu, D.; Xu, L.; Yin, B.; Liu, S.; Tanaka, T.; et al. Meso-Triaryl-Substituted Smaragdyrins: Facile Aromaticity Switching. *J. Am. Chem. Soc.* **2018**, *140*, 16553–16559.
- (56) Narayanan, S. J.; Sridevi, B.; Chandrashekar, T. K.; Englich, U.; Ruhlandt-Senge, K. Core-Modified Smaragdyrins: First Examples of Stable Meso-Substituted Expanded Corrole. *Org. Lett.* **1999**, *1*, 587–590.
- (57) Rajeswara Rao, M.; Ravikanth, M. Boron Complexes of Oxasmaragdyrin, a Core-Modified Expanded Porphyrin. *J. Org. Chem.* **2011**, *76*, 3582–3587.
- (58) Kalita, H.; Lee, W.-Z.; Ravikanth, M. Phosphorus Complexes of Meso-Triaryl-25-Oxasmaragdyrins. *Inorg. Chem.* **2014**, *53*, 9431–9438.
- (59) Kalita, H.; Lee, W.-Z.; Theophall, G. G.; Lakshmi, K. V.; Ravikanth, M. A Stable Seven-Membered Heterocycle, Containing B, C, N, O, and P Atoms, inside a Smaragdyrin Macrocycle. *Chem. - A Eur. J.* **2015**, *21*, 11315–11319.
- (60) Kalita, H.; Lee, W.-Z.; Ravikanth, M. Synthesis and Functionalization of BF₂ - Complexes of Meso-Free 25-Oxasmaragdyrin. *J. Org. Chem.* **2013**, *78*, 6285–6290.
- (61) Kalita, H.; Lee, W. Z.; Ravikanth, M. Synthesis, Structure, Spectral and Electrochemical Properties of B(OR)₂-Smaragdyrin Complexes. *Dalt. Trans.* **2013**, *42*, 14537–14544.
- (62) Mane, S. B.; Hu, J.-Y.; Chang, Y.-C.; Luo, L.; Diao, E. W.-G.; Hung, C.-H. Novel Expanded Porphyrin Sensitized Solar Cells Using Boryl Oxasmaragdyrin as the Sensitizer. *Chem. Commun.* **2013**, *49*, 6882–6884.
- (63) Siegel, R. L.; Miller, K. D.; Jemal, A. Cancer Statistics, 2019 (US Statistics). *CA. Cancer J. Clin.* **2019**, *69*, 7–34.
- (64) Vines, J. B.; Yoon, J. H.; Ryu, N. E.; Lim, D. J.; Park, H. Gold Nanoparticles for

- Photothermal Cancer Therapy. *Front. Chem.* **2019**, 7, 167.
- (65) Arruebo, M.; Vilaboa, N.; Sáez-Gutierrez, B.; Lambea, J.; Tres, A.; Valladares, M.; González-Fernández, Á. Assessment of the Evolution of Cancer Treatment Therapies. *Cancers (Basel)*. **2011**, 3, 3279–3330.
- (66) Hall, E. J. Intensity-Modulated Radiation Therapy, Protons, and the Risk of Second Cancers. *International Journal of Radiation Oncology Biology Physics*. **2006**, 1–7.
- (67) LI, M. C.; HERTZ, R.; BERGENSTAL, D. M. Therapy of Choriocarcinoma and Related Trophoblastic Tumors with Folic Acid and Purine Antagonists. *N. Engl. J. Med.* **1958**, 259, 66–74.
- (68) Einhorn, L. H. Testicular Cancer as a Model for a Curable Neoplasm: The Richard and Hinda Rosenthal Foundation Award Lecture. *Cancer Res.* **1981**, 41, 3275–3280.
- (69) Einhorn, L. H.; Donohue, J. Cis-Diamminedichloroplatinum, Vinblastine, and Bleomycin Combination Chemotherapy in Disseminated Testicular Cancer. *Ann. Intern. Med.* **1977**, 87, 293–298.
- (70) Brunner, K. W.; Young, C. W. A Methylhydrazine Derivative In Hodgkin's Disease And Other Malignant Neoplasms. Therapeutic And Toxic Effects Studied In 51 Patients. *Ann. Intern. Med.* **1965**, 63, 69–86.
- (71) DeVita, V. T.; Serpick, A.; Carbone, P. P. Preliminary Clinical Studies with Ibenzmethyzin. *Clin. Pharmacol. Ther.* **1966**, 7, 542–546.
- (72) Gullotti, E.; Yeo, Y. Extracellularly Activated Nanocarriers: A New Paradigm of Tumor Targeted Drug Delivery. *Mol. Pharm.* **2009**, 6, 1041–1051.
- (73) Kruger, S.; Imer, M.; Kobold, S.; Cadilha, B. L.; Endres, S.; Ormanns, S.; Schuebbe, G.; Renz, B. W.; D'Haese, J. G.; Schloesser, H. Advances in Cancer Immunotherapy 2019 - Latest Trends. *Journal of Experimental and Clinical Cancer Research*. BioMed Central Ltd., 2019.
- (74) Kwiatkowski, S.; Knap, B.; Przystupski, D.; Saczko, J.; Kędzierska, E.; Knap-Czop, K.; Kotlińska, J.; Michel, O.; Kotowski, K.; Kulbacka, J. Photodynamic Therapy – Mechanisms, Photosensitizers and Combinations. *Biomedicine and Pharmacotherapy*. **2018**, 1098–1107.

- (75) Griffin, R. J.; Dings, R. P. M.; Jamshidi-Parsian, A.; Song, C. W. Mild Temperature Hyperthermia and Radiation Therapy: Role of Tumour Vascular Thermotolerance and Relevant Physiological Factors. *Int. J. Hyperth.* **2010**, *26*, 256–263.
- (76) Sanvicens, N.; Marco, M. P. Multifunctional Nanoparticles - Properties and Prospects for Their Use in Human Medicine. *Trends in Biotechnology.* **2008**, 425–433.
- (77) Purushotham, S.; Chang, P. E. J.; Rumpel, H.; Kee, I. H. C.; Ng, R. T. H.; Chow, P. K. H.; Tan, C. K.; Ramanujan, R. V. Thermoresponsive Core-Shell Magnetic Nanoparticles for Combined Modalities of Cancer Therapy. *Nanotechnology* **2009**, *20*.
- (78) Gobin, A. M.; Watkins, E. M.; Quevedo, E.; Colvin, V. L.; West, J. L. Near-Infrared-Resonant Gold/Gold Sulfide Nanoparticles as a Photothermal Cancer Therapeutic Agent. *Small* **2010**, *6*, 745–752.
- (79) Von Maltzahn, G.; Park, J. H.; Agrawal, A.; Bandaru, N. K.; Das, S. K.; Sailor, M. J.; Bhatia, S. N. Computationally Guided Photothermal Tumor Therapy Using Long-Circulating Gold Nanorod Antennas. *Cancer Res.* **2009**, *69*, 3892–3900.
- (80) Men, X.; Yuan, Z. Multifunctional Conjugated Polymer Nanoparticles for Photoacoustic-Based Multimodal Imaging and Cancer Photothermal Therapy. *J. Innov. Opt. Health Sci.* **2019**, *12*, 1930001.
- (81) Ou, H.; Li, J.; Chen, C.; Gao, H.; Xue, X.; Ding, D. Organic/Polymer Photothermal Nanoagents for Photoacoustic Imaging and Photothermal Therapy in Vivo. *Science China Materials.* Science China Press, **2019**, 1740–1758.
- (82) Su, S.; Wang, J.; Vargas, E.; Wei, J.; Martínez-Zaguilán, R.; Sennoune, S. R.; Pantoya, M. L.; Wang, S.; Chaudhuri, J.; Qiu, J. Porphyrin Immobilized Nanographene Oxide for Enhanced and Targeted Photothermal Therapy of Brain Cancer. *ACS Biomater. Sci. Eng.* **2016**, *2*, 1357–1366.
- (83) Zou, Q.; Abbas, M.; Zhao, L.; Li, S.; Shen, G.; Yan, X. Biological Photothermal Nanodots Based on Self-Assembly of Peptide–Porphyrin Conjugates for Antitumor Therapy. *J. Am. Chem. Soc.* **2017**, *139*, 1921–1927.

Chapter 2

General Experimental

In this Chapter, the general materials employed at different stages of the investigation are presented. A description of the synthetic methodology of the various precursor compounds used for the synthesis of BF₂-oxasmaragdyrins and their conjugates are described in this thesis and purification procedure of all the chemicals and solvents are also given. This Chapter concluded with the brief description of the various instruments used and methods for the calculation of various parameters studied in this thesis.

2.1. Chemicals for syntheses

Reactions were carried out under nitrogen atmosphere using standard schlenk techniques. Common solvents for syntheses were purified by standard procedures and were freshly distilled prior to use. All general chemicals such as *N,N,N',N'*-tetramethyl ethylenediamine, *n*-butyllithium (15% in hexane), sodium sulphate, sodium bicarbonate, potassium hydroxide, ammonium chloride, sodium chloride, calcium chloride, and BF₃·O(Et)₂ were obtained from Qualigens and S.D. Fine chemicals, India. Pyrrole and furan, were procured from Aldrich chemicals, USA and were distilled before use. *p*-tolualdehyde, 4-hydroxybenzaldehyde, 4-nitrobenzaldehyde, 2,3-dichloro-5,6-dicyano-1,4-benzoquinone (DDQ) were procured from Lancaster, UK and used as recieved. *Fmoc*- protected aminoacids were procured from Aldrich, USA. All other chemicals used for the synthesis were reagent grade unless otherwise specified. Column chromatography was performed using 60-120 mesh silical gel and aluminium oxide (neutral and basic) obtained from Sisco Research Laboratories, India.

2.2. Solvents employed for spectroscopic and microscopic analysis

- (a) Chloroform (HPLC grade) from Qualigens fine chemicals, India was used without further purification.
- (b) Acetonitrile (HPLC grade) from Qualigens fine chemicals, India was used without further purification.
- (c) Tetrahydrofuran (L. R. grade) procured from Spectrochem, India was passed through a neutral alumina column, kept over in potassium hydroxide overnight and distilled, stored over sodium wire. This again redistilled before use.
- (d) Toluene (L. R. grade) from Qualigens fine chemicals, India was passed through a neutral alumina column and stored over sodium wire and distilled before use.
- (e) Dichloromethane (L. R. grade) from S. D. Fine-chemicals, India was washed twice with 10% aqueous Na₂CO₃ solution, twice with water, dried over anhydrous calcium

chloride overnight, distilled over anhydrous P_2O_5 and stored over molecular sieves (4 Å).

- (f) *n*-Hexane (L. R. grade) from S. D. Fine-chemicals, India was passed through a neutral alumina column and stored over sodium wire and distilled before use.
- (g) Benzene (L. R. grade) from Qualigens fine chemicals, India was passed through a neutral alumina column and stored over sodium wire and distilled before use.
- (h) Triethylamine (L. R. grade) from S. D. Fine-chemicals, India was distilled under inert atmosphere over calcium hydride prior to use.
- (i) Ethyl acetate (L. R. grade) from S. D. Fine-chemicals, India was distilled over calcium chloride before use.
- (j) Methanol (L. R. grade) Qualigens fine chemicals, India used after distillation.
- (k) Diethyl ether (L. R. grade) procured from Ranbaxy, India was passed through a neutral alumina column and stored over sodium wire. This was distilled under inert atmosphere prior to use.

Deuterated solvents such as $CDCl_3$, C_6D_6 , CD_3OD , CD_3CN and $DMSO-D_6$ were obtained from Aldrich, USA and were used as received.

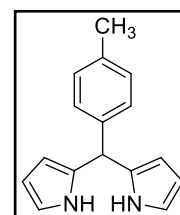
2.3. Synthesis of precursor compounds

General procedure for preparation of *meso*-(aryl)dipyrromethanes¹

Pyrrole (25 equiv.) and the arylaldehyde (1.0 equiv.) were added to a dry round-bottom flask and degassed with a stream of nitrogen for 5 min. TFA (0.1 equiv.) was then added, and the solution was stirred under nitrogen at room temperature for 10 min. The reaction mixture was quenched with 0.1 M NaOH and worked up with ethylacetate (3×20 mL). The combined organic layer was dried over anhydrous Na_2SO_4 and the solvent was removed under vacuum to afford crude product as orange oil. The crude product was purified by silica gel column chromatography to give pure *meso*-(aryl)dipyrromethanes.

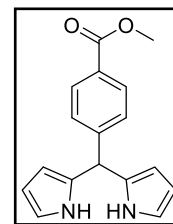
5-(4-Tolyl) dipyrromethene (1)

Yield 76%. M.p. 110-111 °C; 1H NMR (400 MHz, $CDCl_3$, δ in ppm) 2.33 (s, 3 H, -CH₃) 5.45 (s, 1 H, CH) 5.91-5.92 (m, 2 H, Py) 6.15-6.16 (m, 2 H, Py) 6.68-6.69 (m, 2 H, Py) 7.12 (d, $J=7.9$ Hz, 2 H, Ar) 7.38 (d, $J=7.9$ Hz, 2 H, Ar) 7.91 (br. s, 2 H, NH); ES-MS: Calcd. for $C_{16}H_{16}N_2$ is 236.1, found m/z 236.1 $[M]^+$.

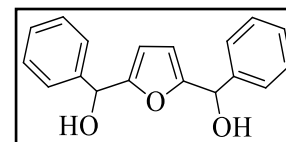


5-(4-carboxymethyl phenyl) dipyrromethene (2)

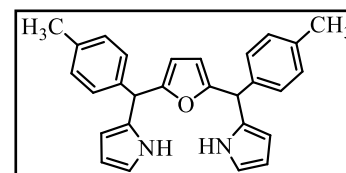
Yield 37%. M. p 160°C; ^1H NMR (CDCl_3) δ 3.90 (s, 3H, CH_3), 5.25 (s, 1H, *meso*-H), 5.89 (s, 2H, Py), 6.16 (q, 2H, Py), 6.71 (q, 2H, Py), 7.28 (d, 2H, Ar), 7.96 (m, 4H, Ar and NH). ES-MS: Calcd. for $\text{C}_{17}\text{H}_{16}\text{N}_2\text{O}_2$ is 280.1, found m/z 280.2 $[\text{M}]^+$.

**2,5-Bis(phenylhydroxymethyl)furan (3)²**

The 2,5-dilithiofuran was prepared by treating furan (1.0 mL, 13.75 mmol) with *n*-butyllithium (21.6 mL, of ca. 1.6 M solution in hexane) in the presence of N,N,N',N'-Tetramethylethylenediamine (4.5 mL, 29.54 mmol) in dry *n*-hexane (40 mL) as described for the compound **2**. Benzaldehyde (3.32 mL, 29.54 mmol) in dry THF (30 mL) at 0 °C was added followed by the similar work-up mentioned for previous compound **2**. The crude product was recrystallized from toluene and afforded the pure diol **3** as a white solid in 65% yield. Mp ≥ 81 °C. IR (KBr film): $\nu = 3299$ (OH) cm^{-1} . ^1H NMR (400 MHz, CDCl_3 , 25 °C): $\delta = 4.85$ (br s, 2H, OH), 5.78 (s, 2H, CH), 6.03 (d, $J = 4.3$ Hz, 2H, furan), 7.41 (m, 10H, Ar) ppm. ES-MS: $\text{C}_{18}\text{H}_{16}\text{O}_3$, Calcd. av.mass 280.1, obsd. m/z 273.4 $[\text{M}-\text{OH}]^+$ (100%). Anal. calcd.: C, 77.12; H, 5.75. Found: C, 77.13; H, 5.72.

**26 5,10-Di(*p*-tolyl)-16-oxa-15,17-dihydrotripyrane (4)²**

The compound was prepared by adding $\text{BF}_3 \cdot \text{Et}_2\text{O}$ (0.41 mL, 3.70 mmol) to the solution of 2,5-bis[*p*-tolylhydroxymethyl]furan **22** (1.1 g, 3.23 mmol) and pyrrole (9.3 mL, 148.0 mmol) as described for the compound **25**. The crude compound was purified by silica



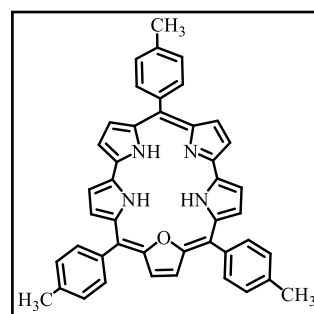
gel column chromatography using petroleum ether/ethyl acetate (92:8). The evaporation of solvent on rotary evaporator under reduced pressure gave the desired compound **26** as orange oil in 66% yield. ^1H NMR (400 MHz, CDCl_3 , δ in ppm): 2.28 (s, 6H; Ar- CH_3), 5.42 (s, 2H; CH), 5.86-5.88 (m, 2H; py), 6.08-6.11 (m, 2H; py), 6.56-6.58 (m, 4H; py+Fur), 7.10-7.14 (m, 8H; Ar), 7.83 (s, 2H; NH); ES-MS: Calcd for $\text{C}_{28}\text{H}_{26}\text{N}_2\text{O}$ 406.5, found m/z 406.6 $[\text{M}]^+$. Anal.calcd: C, 82.73; H, 6.45; N, 6.89. Found: C, 82.79; H, 6.49; N, 6.91.

General Procedure for the synthesis of 25-oxasmaragdyrins³⁻⁵

Samples of *meso*-aryldipyrromethane (1 equiv) and 16-oxatripyrrane **4** (430 mg, 1.06 mmol) were dissolved in 500 mL of dry dichloromethane and stirred under nitrogen atmosphere for 5 min. The reaction was initiated by adding TFA (7.5 μ l, 0.10 mmol) and the stirring was continued for 90 min. DDQ (725 mg, 3.18 mmol) was then added, and the reaction mixture was stirred in open air for an additional 90 min. The solvent was removed on rotary evaporator under vacuum and the crude compound was subjected to basic alumina column chromatographic purification. The required product was collected with petroleum ether/dichloromethane (4:1) to afford 25-oxasmaragdyrin building blocks as a green solid.

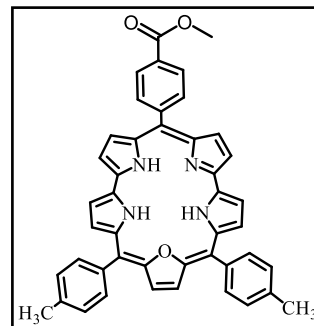
5,10,19-tri(*p*-tolyl)-25-oxasmaragdyrin (**5a**)

(170 mg, 25%). M.p. > 300 °C; ¹H NMR (400 MHz, CDCl₃, δ in ppm): 2.73 (s, 9H; CH₃), 7.59 (d, 4H, ³*J*(H, H) = 7.9 Hz; Ar), 8.07 (m, 6H; Ar), 8.18 (d, 2H, ³*J*(H, H) = 8.0 Hz; Ar), 8.45 (d, 2H, ³*J*(H, H) = 4.27 Hz; Py), 8.80 (s, 2H; Fur), 8.91 (d, 2H, ³*J*(H, H) = 4.27 Hz; Py), 9.38 (d, 2H, ³*J*(H, H) = 4.27 Hz; Py), 9.46 (d, 2H, ³*J*(H, H) = 4.27 Hz; Py); ES-MS: Calcd. for C₄₄H₃₄N₄O 634.7, found 635.3 [M+1]⁺.



19-(4-Methoxycarbonylphenyl)-5,10-di(*p*-tolyl)-25-oxasmaragdyrin (**5b**)

(360 mg, 26%). M.p. > 300 °C ; ¹H NMR (400 MHz, CDCl₃, δ in ppm): 2.72 (s, 6H; -CH₃), 4.12 (s, 3H; -OCH₃), 7.62 (d, 4H, *J* = 7.76 Hz; Ph), 8.10 (d, 4H, *J* = 7.8 Hz; Ph), 8.49 (m, 6H; Ph and β -pyrr), 8.83 (s, 2H; β -fur), 8.95 (d, 2H, *J* = 4.32 Hz, β -pyrr), 9.43 (d, 2H, *J* = 4.28 Hz; β -pyrr), 9.52 (d, 2H, *J* = 4.28 Hz; β -pyrr); ES-MS: *m/z* calcd for C₄₅H₃₅N₄O₃ : 679.2709, found 679.2708 [M+H]⁺.



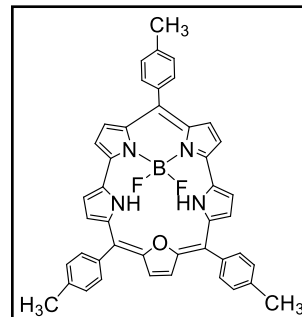
General Procedure for the synthesis of BF₂-smaragdyrins (**6a-b**)^{3,5}

Sample of smaragdyrin **5a-b** (0.157 mmol) was taken in CH₂Cl₂ (30 mL) and triethylamine (6.28 mmol) was added at room temperature. After 5 min. BF₃ Et₂O (7.85 mmol) was added, and continued stirring at room temperature for 30 min. The reaction mixture was diluted with CH₂Cl₂ and washed thoroughly with 0.1 M NaOH solution and water. The organic layers were combined, dried over Na₂SO₄, filtered, and solvent was removed on rotary evaporator under

vacuum. The resulted crude product was purified by column chromatography on alumina, using petroleum ether/dichloromethane (70:30) and afforded pure compound **6a-b** as a green powder.

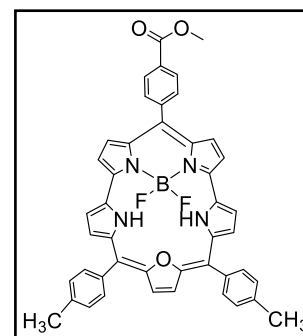
BF₂-[5,10,19-tri(*p*-tolyl)-25-oxasmaragdyrin] (6a)

(81 mg, 76%). M.p. >300 °C, ¹H NMR (400 MHz, CDCl₃, δ in ppm): -3.60 (t, 2H; -NH), 2.76 (s, 9H; Tol), 7.66 (d, 4H, ³*J*(H, H) = 7.0 Hz; Ar), 7.75 (d, 2H, ³*J*(H, H) = 7.0 Hz; Ar), 8.26 (d, 4H, ³*J*(H, H) = 6.7 Hz; Ar), 8.46 (d, 2H, ³*J*(H, H) = 6.7 Hz; Ar), 8.92 (dd, 2H, ³*J*(H, H) = 4.4 Hz, ⁴*J*(H, H) = 1.4 Hz; β-py), 9.41 (s, 2H; β-fur), 9.52 (d, 2H, ³*J*(H, H) = 7.0 Hz; β-py), 10.15 (dd, 2H, ³*J*(H, H) = 4.4 Hz, ⁴*J*(H, H) = 1.4 Hz; β-py), 10.20 (d, 2H, ³*J*(H, H) = 7.0 Hz; β-py); ¹⁹F NMR (282.2 MHz, CDCl₃, δ in ppm): -149.6 (br s); ¹¹B NMR (96.3 MHz, CDCl₃, δ in ppm): -12.04 (br s); ¹³C NMR (100 MHz, CDCl₃, δ in ppm): 21.7, 21.8, 107.0, 120.1, 120.5, 121.7, 123.7, 124.8, 125.0, 128.4, 129.4, 130.7, 131.1, 132.0, 134.4, 134.8, 136.2, 138.0, 138.1, 139.7, 149.9; HRMS calcd for C₄₄H₃₃BF₂N₄O 682.2715, found 682.2682.



meso-(4-Carboxy methyl ester phenyl) BF₂-oxasmaragdyrin (6b)

(95 mg, 75%). M.p. >300 °C, ¹H NMR (400 MHz, CDCl₃) δ 10.26 (d, *J* = 4.5 Hz, 2H), 10.17 (dd, *J* = 4.5, 2.0 Hz, 2H), 9.50 (d, *J* = 4.4 Hz, 2H), 9.44 (s, 2H), 8.96 (dd, *J* = 4.5, 1.8 Hz, 2H), 8.63 (d, *J* = 8.3 Hz, 2H), 8.57 (d, *J* = 8.3 Hz, 2H), 8.22 (d, *J* = 7.9 Hz, 4H), 7.63 (d, *J* = 7.6 Hz, 4H), 4.09 (s, 3H), 2.72 (s, 6H), -4.04 (t, *J* = 10.2 Hz, 2H). ¹³C NMR (101 MHz, CDCl₃) δ 167.6, 150.0, 144.2, 139.7, 138.1, 135.0, 134.5, 130.9, 129.8, 129.7, 128.5, 125.2, 124.1, 124.0, 122.3, 121.1, 120.6, 107.3, 52.6, 21.8. ¹¹B NMR (128 MHz, CDCl₃) δ -12.6. ¹⁹F NMR (377 MHz, CDCl₃) δ -149.2.



2.4 Characterization techniques

The details of the instruments employed for the characterization and evaluation of the spectroscopic data are presented below.

Melting points were recorded on Veego melting point apparatus and are uncorrected. Boiling points refer to bath temperatures. Infrared spectra were recorded on Nicolet Impact-400 FTIR spectrometer. Solid samples were recorded as KBr wafers and the liquid films were made on CsBr or NaCl plates and analyzed. ¹H and ¹³C NMR spectra were generally recorded on

Varian 400 and Bruker (400 and 500 MHz) spectrometers. ^{19}F , ^{11}B , and ^{31}P NMR spectra were recorded on Bruker (400 and 500 MHz) spectrometers. NMR samples were generally made in chloroform-*d* solvent and the chemical shifts were reported in δ scale using tetramethylsilane (TMS or SiMe_4) as an internal reference. The standard abbreviations s, d, t, q, m, bs, dd refer to singlet, doublet, triplet, quartet, multiplet, broad singlet and doublet of doublet respectively. Coupling constant (J) values are reported in Hertz. Absorption spectra were obtained with Perkin–Elmer Lambda-35, Varian Cary 100 Bio UV-Vis, Cary 5000 UV-Vis-Nir instruments. Steady state fluorescence spectra were obtained with PC1 photon counting spectrofluorometer manufactured by ISS, USA and Varian-Cary-Eclipse fluorescence spectrometer instruments. The fluorescence lifetimes of the smaragdyrin and corrole compounds were carried out at magic angle (54.6°) using a picoseconds diode laser based TCSPC fluorescence spectrometer from IBH, UK. An iterative fitting program provided by IBH analyzed the fluorescence decay curves. Elemental analyses were conducted by Thermo Finnigan Flash EA 1112 analyzer and reported.

Electro-spray mass spectra (ES-MS) were recorded at room temperature on Bruker maXis Impact and Q-ToF micro mass (YA-105) spectrometer instruments. Mass spectra were obtained with a Platform II single quadrupole mass spectrometer (Micromass, Altrincham, UK) using a dichloromethane and acetonitrile (otherwise mentioned separately) mobile phase. A Harvard 22 syringe pump delivered the solutions to the vaporization nozzle of the electro spray ion source at a flow rate of $10\ \mu\text{L min}^{-1}$. Nitrogen was used both as a drying gas and for nebulization with flow rates of approximately 200 and 20 ml min^{-1} , respectively. Pressure in the mass analyzer region was usually about 4×10^{-5} mbar.

Cyclic voltammetric (CV) and differential pulse voltammetric (DPV) studies were carried out with BAS electrochemical system utilizing the three-electrode configuration consisting of a glassy carbon (working electrode), platinum wire (auxiliary electrode) and saturated calomel (reference electrode) electrodes in dry dichloromethane using 0.1 M tetrabutylammonium perchlorate as supporting electrolyte. Under these conditions, ferrocene shows a reversible one electron oxidation wave ($E_{1/2} = 0.42\ \text{V}$).¹⁴ The solution was deaerated by bubbling argon gas, and during the acquisition argon was slowly flowed above the solution.

2.4.1 Fluorescence analysis

Steady state Fluorescence Quantum yield⁶

Fluorescence quantum yield, Φ_f of various new porphyrins synthesized were calculated from the emission and absorption spectra by a comparative method using the following equation

$$\Phi_f = \phi_f(\text{standard}) \times \frac{[F(\text{porphyrin})][A(\text{standard})]}{[A(\text{porphyrin})][F(\text{standard})]}$$

where, $[F(\text{porphyrin})]$ and $[F(\text{standard})]$ are the integrated fluorescence intensity of the corresponding porphyrin and standard respectively and $[A(\text{porphyrin})]$ and $[A(\text{standard})]$ are the absorbance of porphyrin and standard respectively, at the excitation wavelengths and $\phi_f(\text{standard})$ represents the quantum yield of the standard sample. Free base tetraphenylporphyrin (H_2TPP , $\Phi_f = 0.11$) was used as the standard for free base porphyrins and zinc(II)tetraphenylporphyrin (ZnTPP) was used as standard ($\Phi_f = 0.033$) for the Zn^{2+} derivative of *meso*-substituted porphyrins.⁷ Fluorescence lifetimes of the representative porphyrins were carried out at magic angle (54.6°) using a picosecond diode laser based TCSPC fluorescence spectrometer from IBH, UK. An iterative fitting program provided by IBH analyzed the fluorescence decay curves.

Time-resolved spectroscopy

Time-correlated single photon counting: Nanosecond lifetime is measured using time-correlated single photon counting (TCSPC) spectrometer from IBH Horiba Jobin Yvon (FluoroCube). The samples are excited with 375 nm diode laser (Horiba NanoLED) with a repetition rate of 1 MHz. The decays are collected at magic angle (54.7°) polarization with respect to vertically polarized excitation light to eliminate rotational anisotropy. The full width at half maximum (FWHM) of the instrument response function (IRF) is around 250 ps.

2.7.2. Data analysis. The decays were fitted to one or more exponential function by iterative deconvolution using IBH DAS 6.2 software.

$$I(t) = \sum_i A_i \cdot \exp\left(-\frac{t}{\tau_i}\right) + B$$

where, τ_i and A_i are the lifetime and amplitude of the i -th component making $\sum_i A_i = 1$. B is the background signal.

The goodness of fit is judged by χ^2 .

$$\chi^2 = \sum_{k=1}^n \left(\frac{N_k - N_k^C}{\sigma_k} \right)^2 = \sum_{k=1}^n \frac{(N_k - N_k^C)^2}{N_k}$$

where N_k and N_k^C are measured and calculated (fitted) data at the k^{th} channel. σ_k the standard deviation at the k^{th} channel. For a Poisson distribution $\sigma_k = \sqrt{N_k}$. N_k is the photon count at the k^{th} channel.

Since χ^2 is dependent on the number of channels (data points) it is defined in a reduced form

$$\chi_{red}^2 = \frac{\chi^2}{\nu} = \frac{\chi^2}{n - p}$$

Where ν is the degrees of freedom and is equal to $n - p$ which are number of data points and number of floating parameters respectively.

The reduced χ^2 (χ_{red}^2) has theoretical limit of 1.0 and value within 1.0 to 1.2 is accepted as good fit.

2.4.2 *In vitro*

In vitro studies were carried out in collaboration with Prof. Rohit Srivastava and Mr. B. Pradeep Kumar Reddy, Department of Biosciences and Bioengineering, IIT Bombay.

Mouse fibroblast cells (L929) and human breast cancer cell line, MDA MB 231 were procured from National Centre for Cell Sciences, Pune, India. Phosphate buffer saline (PBS), antibiotic-antimycotic solution, Dulbecco's Modified Eagle Medium (DMEM), and fetal bovine serum (FBS) were purchased from HiMedia Laboratories Pvt. Ltd India.

Cell Culture: DMEM supplemented with 10% v/v FBS and 1% v/v antibiotic-antimycotic solution was used for culturing and maintaining L929 and MDA MB 231 cells. The cells were incubated at 37 °C and 5% CO₂ during culture and experimentation.

Biocompatibility Study: *In vitro* biocompatibility assessment of Compound **1** was carried out in L929 cells. Briefly, L929 cells were seeded in a 96 well plate at a density of ~ 6000 cells/well and were incubated for 24 h to adhere and attain morphology. Compound **1** dissolved in DMSO, was diluted in complete media to attain different concentrations in the range 10 to 150 µg/mL. Further, the media was replaced with varying concentrations of compound **1**, positive control being 1 % Triton X-100, negative control being complete media. The cells were

incubated for 24 hours, the contents of wells removed, washed with PBS, followed by addition of alamar blue at a concentration of 10 µg/well. The cells were incubated for 4 h, followed by recording the fluorescence with excitation and emission wavelengths being 560 and 590 nm respectively (TECAN Infinite 200 Pro series). Percentage cell viability was calculated based on the following equation

$$\text{Cell viability (\%)} = \frac{\text{Intensity of treated sample}}{\text{Intensity of negative control}} \times 100$$

Cellular uptake:

Cellular uptake by confocal laser scanning microscopy (CLSM):

CLSM was performed to evaluate the cellular uptake in L929/MDA MB 231/4T1 cells. Briefly, the cells were seeded on sterile coverslips in a 12-well plate at a density of 25000 cells/well and incubated for 24 hours. Compounds dissolved in solvent (DMSO or H₂O) was diluted appropriately and added to each well such that the final amount of compound in each well is 10 µg/well. The cells were incubated for 24 h, followed careful washing with PBS and fixation. The fixation was carried out with 4% paraformaldehyde (15 min) at room temperature, followed by PBS wash. CLSM imaging was performed on fixed cells by using 488 nm excitation and 680-740 nm emission filter respectively.

Cell Internalization by Flow Cytometry (FACS):

MDA-MB-231/4T1 cells were employed to investigate the cell internalization of Dyes. MDA-MB-231/4T1 cells were cultured in Dulbecco's Modified Eagle's Medium (DMEM) supplemented with 10% fetal bovine serum and 1% penicillin/streptomycin and were sub-cultured at regular intervals. Briefly, cells were seeded at a density of 1×10⁶ cells per 60 mm dish and incubated at 5% CO₂ and 37 °C for 24 hours under humidified conditions. Freshly prepared sample (10 µg/mL) was incubated with cells for different time periods i.e. 1h, 3h, 12h and 24h. After the incubation period, the media was removed, washed with Dulbecco's Phosphate Buffered Saline (DPBS), and trypsinized. Cells were centrifuged and were redispersed in 0.5 mL DPBS and internalization was quantified using flow cytometer. The excitation wavelength was 488 nm (blue) laser and emission was captured employing PerCP-Cy5.5 (695/40) channel and minimum of 10000 events were recorded. Gating was carried out to remove any debris, free nanoparticles, or dead cells and a shift in the fluorescence peaks from that of the negative control indicates cellular uptake.

2.4.3 *In vivo*

In vivo studies were carried out in collaboration with Dr. Abhijit De and Mr. Sumit Mishra, Advanced Centre for Treatment, Research and Education in Cancer (ACTREC), Tata Memorial Centre, Kharghar, Navi Mumbai.

The general methods for *in vivo* are incorporated in the chapters where *in vivo* studies were performed.

2.5 References

- (1) Laha, J. K.; Dhanalekshmi, S.; Taniguchi, M.; Ambroise, A.; Lindsey, J. S. A Scalable Synthesis of Meso-Substituted Dipyrrromethanes. *Org. Process Res. Dev.* **2003**, *7*, 799–812.
- (2) Heo, Y.-H.; Lee, C.-H. Facile Syntheses of Modified Tripyrranes and Their Application to the Syntheses of Regioisomerically Pure Porphyrin Derivatives. *Bull. Korean Chem. Soc.* **1996**, *17*, 515–520.
- (3) Rajeswara Rao, M.; Ravikanth, M. Boron Complexes of Oxasmaragdyrin, a Core-Modified Expanded Porphyrin. *J. Org. Chem.* **2011**, *76*, 3582–3587.
- (4) Narayanan, S. J.; Sridevi, B.; Chandrashekar, T. K.; Englich, U.; Ruhlandt-Senge, K. Core-Modified Smaragdyrins: First Examples of Stable Meso-Substituted Expanded Corrole. *Org. Lett.* **1999**, *1*, 587–590.
- (5) Chatterjee, T.; Srinivasan, A.; Ravikanth, M.; Chandrashekar, T. K. Smaragdyrins and Sapphyrins Analogues. *Chem. Rev.* **2017**, *117*, 3329–3376.
- (6) Brouwer, A. M. Standards for Photoluminescence Quantum Yield Measurements in Solution. *Pure Appl. Chem.* 2011, pp 2213–2228.
- (7) Gouterman, M. Electronic Spectra. *The Porphyrins* **1978**, *3*, 1–156.

Chapter 3

Synthesis of Oxasmaragdyrin-Amino Acid Conjugates

3.1 Introduction

Smaragdyrins **I** are 22π aromatic expanded pentapyrrolic macrocycles in which the five pyrroles are connected via three *meso*-carbons and two direct pyrrole-pyrrole bonds.¹ Because of the presence of two direct pyrrole-pyrrole bonds, the smaragdyrin macrocycle is highly strained and not stable for further studies. Thus, to the best of our knowledge, there are no reports available on synthesis of stable smaragdyrin macrocycles containing five pyrrole rings. However, Chandrasekhar and co-workers reported few years back the synthesis of *meso*-triaryl 25-oxasmaragdyrins **II** which are stable and exhibit interesting spectral and electrochemical properties.²⁻⁴ The 25-oxasmaragdyrins were resulted by replacing one of the pyrrole groups of smaragdyrin with furan ring and these macrocycles absorb and emit in 400-800 nm region with decent quantum yields and singlet state lifetimes. The spectral and electrochemical properties of 25-oxasmaragdyrins were further enhanced by BF_2 -complexation of 25-oxasmaragdyrins.⁵ For example, the BF_2 -oxasmaragdyrins **III** showed a strong band at 710 nm that is three times more intense than the absorption band of free base 25-oxasmaragdyrin and also the BF_2 -oxasmaragdyrins are more fluorescent than free base oxasmaragdyrins with decent quantum yields and singlet state lifetimes. Thus, 25-oxasmaragdyrins and their BF_2 -complexes are fluorescent expanded porphyrinoids unlike many other reported expanded porphyrinoids which are generally non-fluorescent.⁶⁻⁸

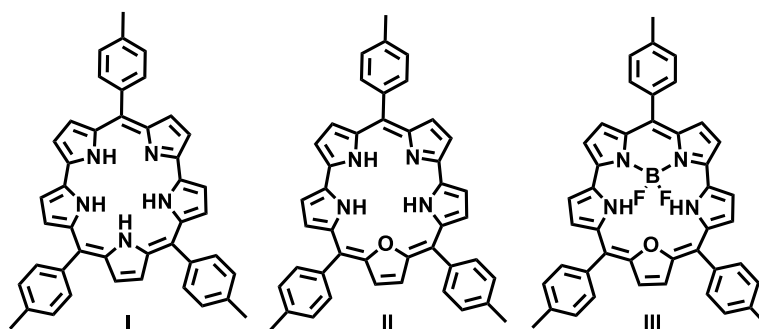


Chart 3.1: Structures of smaragdyrin analogues

Porphyrins, corroles and their peptide conjugates were previously used in various applications such as cellular imaging, PDT agents,⁹⁻¹¹ DSSC^{12, 13} due to their photophysical properties. As these molecules are fluorescent in the visible region, the signal to noise ratio of fluorescent signal in case of mammalian cells is very less due to auto fluorescence and scattering. It is known that the mammalian cells are quite transparent in the region of 650 nm to 900 nm. Therefore, the dyes in this region are very useful for Near Infrared Fluorescence Imaging (NIRF). Thus, there is a need for the dyes that can be easily prepared and absorbs and

emits strongly in NIR region. However, to best of our knowledge, there are only handful of dyes which are fluorescent in this region like cyanine dyes,¹⁴⁻¹⁶ squaraine dyes,¹⁷⁻²⁰ BODIPY analogues,²¹⁻²³ benzo[c]heterocycles,^{24, 25} xanthenes,²⁶ phthalocyanines and few porphyrin derivatives.^{9, 27-29} Although extensive literature is presently available on porphyrin-amino acid/peptide/protein conjugates,³⁰⁻³⁴ only limited reports on contracted porphyrinoids such as corrole-amino acid conjugates,³⁵ and very few reports on expanded porphyrins³⁶ where the expanded porphyrins were linked to amino acids, peptides and proteins to form covalent conjugates which can be used for biological applications. We thought of using the fluorescent oxasmaragdyrins and their BF₂ complexes to link covalently with various amino acids to synthesize conjugates which can be used for NIR fluorescence imaging studies and other applications. With this idea in mind, we attempted to synthesize oxasmaragdyrin/BF₂-oxasmaragdyrin-amino acid conjugates using readily available precursors under simple reaction conditions. Herein, we report the synthesis of first examples of covalently linked *meso*-triaryl 25-oxasmaragdyrin-amino acid conjugates **1a-1d** and their BF₂ complexes **2a-2d** (Chart 3.2) and studied their photophysical and electrochemical properties. The studies indicated that the conjugates absorb and emit strongly in visible-NIR region with decent quantum yields and singlet state lifetimes and exhibit reversible oxidation and reduction under electrochemical redox conditions.

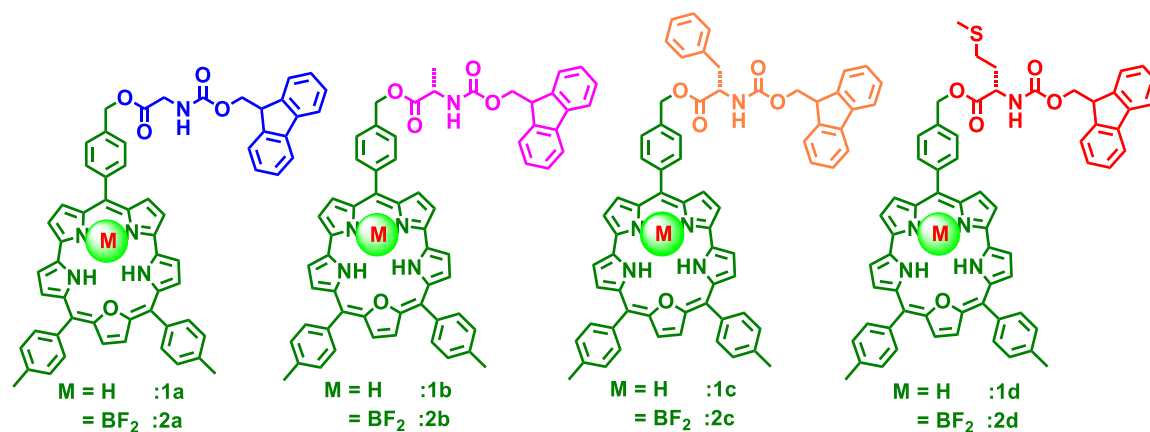


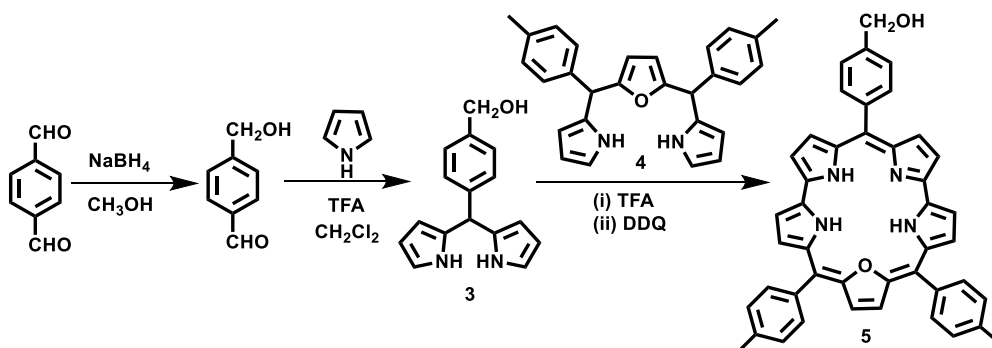
Chart 3.2: Oxasmaragdyrin-amino acid conjugates and their corresponding BF₂ complexes.

3.2 Results and Discussion

3.2.1 Synthesis and Characterization

The required *meso*-(4-hydroxymethyl)phenyl dipyrromethane **3** was synthesized in two steps starting from commercially available 1,4-terephthalaldehyde as shown in Scheme 3.1. The 1,4-terephthalaldehyde was selectively reduced by treating with 0.25 equivalent of NaBH₄

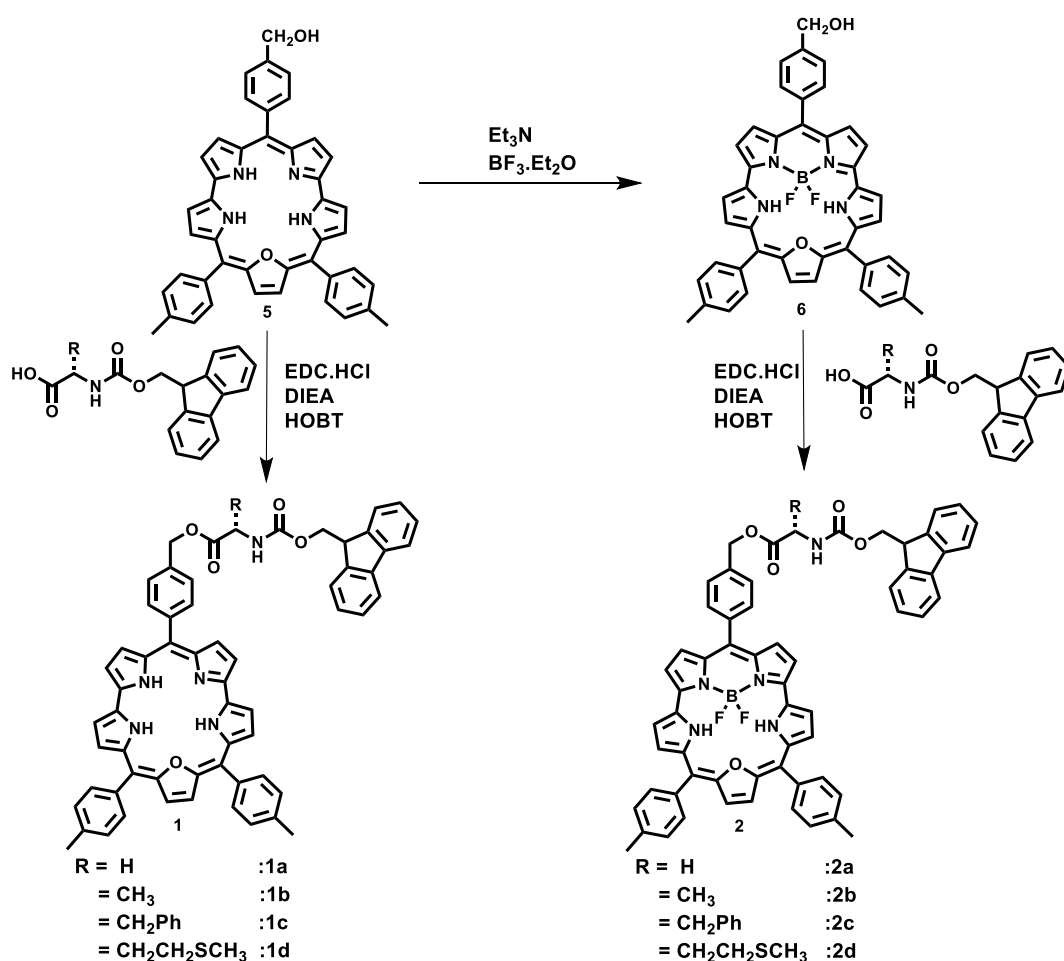
in CH₃OH to afford 4-(hydroxymethyl)benzaldehyde in 80% yield. The 4-(hydroxymethyl)benzaldehyde was reacted with excess of pyrrole in the presence of catalytic amount of TFA in CH₂Cl₂ followed by work-up and column chromatographic purification afforded *meso*-(4-hydroxymethyl)phenyl dipyrromethane as white solid in 40% yield.³⁷ The other desired 16-oxatripyrrane **4** was synthesized by following the reported procedure.³⁸ The 25-oxasmaragdyrin **5** containing benzyloxy group at one of the *meso* positions was synthesized by condensing one equivalent of dipyrromethane **3** with one equivalent of 16-oxatripyrrane **4** in CH₂Cl₂ in the presence of catalytic amount of TFA for 1 h under inert atmosphere followed by oxidation with DDQ in open air for additional 1 h. The formation of the 25-oxasmaragdyrin **5** was followed by tlc analysis and absorption spectroscopy. The crude compound was purified by basic alumina column chromatography and afforded the desired functionalized 25-oxasmaragdyrin **5** in 25% yield. The formation of 25-oxasmaragdyrin **5** was confirmed by HR-MS and NMR spectroscopy. The compound **5** was treated with excess BF₃·OEt₂ in CH₂Cl₂ in the presence of triethylamine for 15 min and purified the crude compound by basic alumina column chromatography to afford pure BF₂ complex of functionalized 25-oxasmaragdyrin **6** as green crystalline solid in 80% yield. The BF₂-oxasmaragdyrin complex **6** was confirmed by HR-MS, ¹H, ¹⁹F and ¹¹B NMR spectroscopy.



Scheme 3.1: Synthesis of oxasmaragdyrin **5**.

The oxasmaragdyrin-amino acid **1** as well as BF₂-oxasmaragdyrin-amino acid **2** conjugates were synthesized as shown in the Scheme 3.2. The oxasmaragdyrin **5** or its BF₂ complex **6** was reacted with appropriate Fmoc (Fluorenylmethyloxycarbonyl)-protected amino acid in CH₂Cl₂ in the presence of 1 equivalent of EDC.HCl (1-Ethyl-3-(3-dimethylaminopropyl)carbodiimide Hydrochloride), 0.1 equivalent HOBt (Hydroxybenzotriazole) and 1 equivalent DIEA (diisopropylethylamine) at room temperature for 3 h. The tlc analysis showed the disappearance of the more polar spot corresponding to the starting material **5** or **6** and appearance of less polar spot corresponding to the desired

conjugate. The crude mixture after standard work-up was purified by silica gel column chromatography and afforded the desired oxasmaragdyrin-amino acid conjugates in 25% yields and BF_2 -oxasmaragdyrin-amino acid conjugates in 30% yields. The conjugates **1** and **2** are freely soluble in all common organic solvents and their identities were confirmed by corresponding molecular ion peak in HR-MS. The conjugates **1** and **2** were characterized in detail by 1D and 2D NMR spectroscopy, absorption, fluorescence and electrochemical techniques. The representative ^1H NMR and ^1H - ^1H COSY spectra of **2c** are presented in Figure 3.1.



Scheme 3.2: Synthesis of oxasmaragdyrin-amino acid conjugates **1a-d** and BF_2 complex of oxasmaragdyrin-amino acid conjugates **2a-d**.

In general, covalently linked oxasmaragdyrin-amino acid conjugates showed five sets of resonances for 10 protons corresponding to eight pyrrole and two furan protons in the region of 9 – 10.5 ppm which were identified by their location, integration, coupling constant and cross-peak connectivity in ^1H - ^1H COSY NMR. The protons corresponding to amino acid moiety appeared in the region of 1.5 – 6 ppm which were also easily identified based on their

cross peak correlations in COSY spectra. The inner NH protons of BF₂-oxasmaragdyrin-amino acid conjugates **2** were appeared at upfield region of -3.5 ppm which were not observed in oxasmaragdyrin-amino acid conjugates due to their involvement in rapid tautomerism. The conjugates **2** were also characterized by ¹⁹F and ¹¹B NMR spectroscopy.

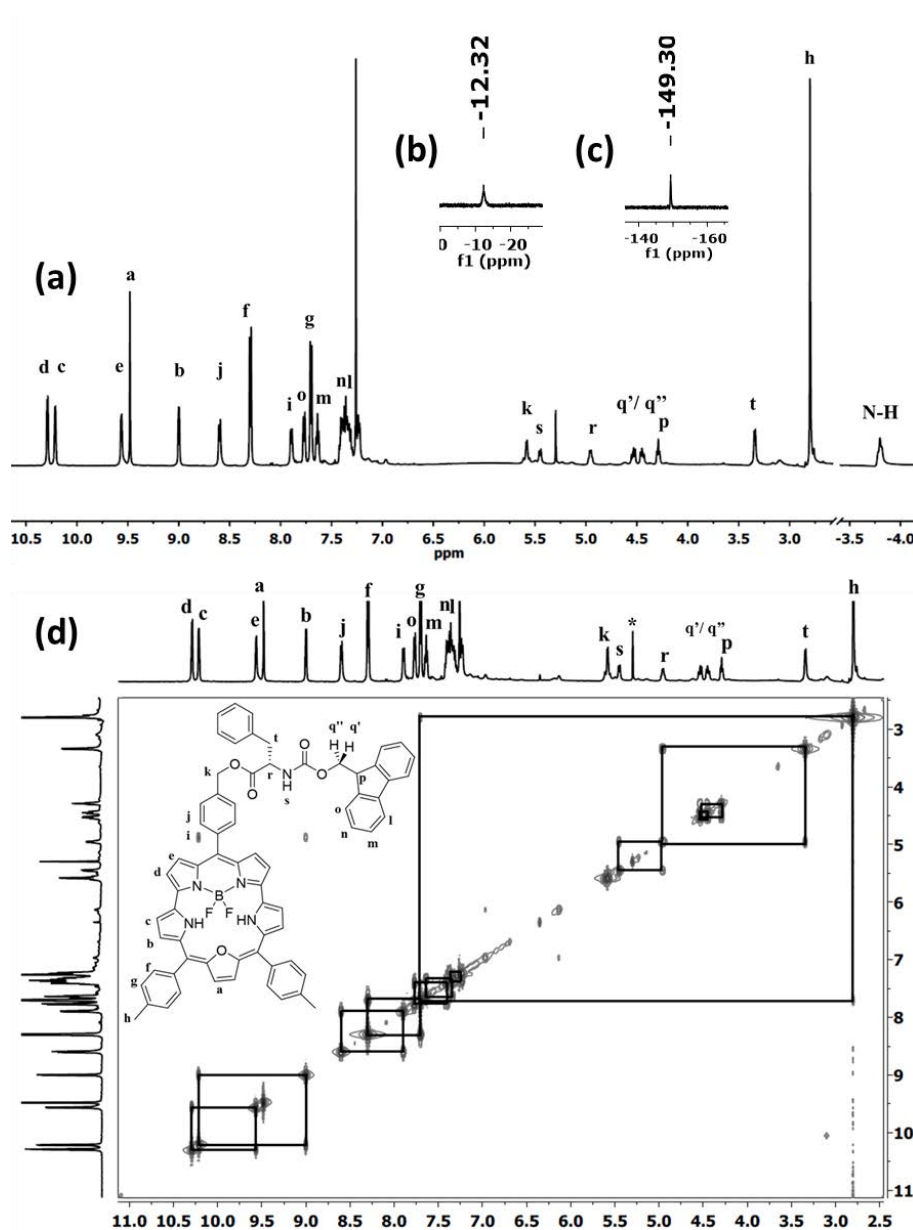


Figure 3.1: (a) ¹H, (b) ¹¹B, (c) ¹⁹F, (d) ¹H-¹H COSY NMR of **2c** recorded in CDCl₃.

The absorption, fluorescence and electrochemical properties of free base/BF₂-oxasmaragdyrin-amino acid conjugates **1/2** were studied and relevant data is tabulated in Table 3.1 and Table 3.2. The comparison of absorption spectra of oxasmaragdyrin- phenylalanine conjugate **1c** with *meso*-triaryl oxasmaragdyrin **5** is presented in Figure 3.2a and comparison of their corresponding BF₂- complexes is presented in Figure 3.2b. As clear from Figures 3.2a

& 3.2b, the conjugates showed similar absorption features like oxasmaragdyrin precursors **5** & **6** with almost no shifts in their peak maxima. However, the extinction coefficients of absorption bands of conjugates were slightly altered compared to corresponding precursors **5** & **6**. The comparison of fluorescence spectra of oxasmaragdyrin and conjugate shown as an inset in Figure 3.2a and comparison of fluorescence spectra of BF₂-oxasmaragdyrin and conjugate shown as inset in Figure 3.2b also indicate that the linking of amino acids to oxasmaragdyrin/BF₂-oxasmaragdyrin did not modify the fluorescence properties of oxasmaragdyrin/BF₂-oxasmaragdyrin moiety supporting weak interaction between the oxasmaragdyrin/BF₂-oxasmaragdyrin and amino acid moieties in conjugates.

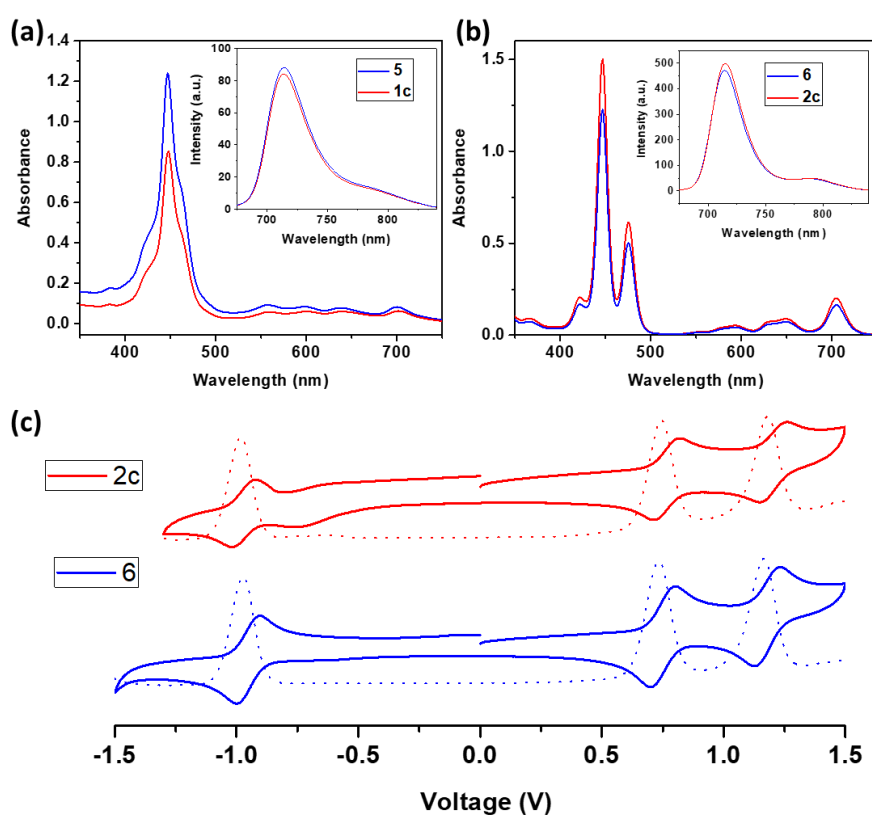


Figure 3.2: (a) Comparison of absorption and fluorescence (inset) spectra of **1c** and **5** recorded in CHCl₃; (b) Comparison of absorption and fluorescence (inset) spectra of **2c** and **6** recorded in CHCl₃; (c) Comparison of cyclic Voltammograms and Differential Pulse Voltammograms of **2c** and **6** in CH₂Cl₂ containing 0.1M TBAP as supporting electrolyte using scan rate of 50 mV/sec.

Table 3.1: Absorption and fluorescence data of oxasmaragdyrin, BF₂ complexed oxasmargdyrin and their amino acid conjugates recorded in CHCl₃.

Compound			Wavelength (nm) ϵ (mol ⁻¹ L ⁻¹ cm ⁻¹)				λ_f (nm)	Φ_f	τ (ns)
5	447	--	558	599	638	700	714	0.029	--
	(123600)		(9200)	(8321)	(7708)	(8177)			
1a	447	--	558	599	638	700	714	0.015	--
	(71900)		(5300)	(5251)	(5066)	(5363)			
1b	447	--	558	599	638	700	714	0.015	--
	(71900)		(5300)	(5251)	(5066)	(5363)			
1c	447	--	558	599	638	700	714	0.026	--
	(85100)		(5700)	(5967)	(5945)	(6164)			
1d	447	--	558	599	638	700	714	0.018	--
	(71400)		(5500)	(5416)	(5267)	(5424)			
6	447	475	592	631	649	705	714	0.143	4.059
	(284700)	(127000)	(11300)	(15500)	(18300)	(39900)			
2a	447	475	592	631	649	705	716	0.156	4.030
	(175600)	(75600)	(5890)	(8730)	(10350)	(23400)			
2b	447	475	592	631	649	705	714	0.165	4.028
	(175645)	(75652)	(6000)	(9000)	(11200)	(24400)			
2c	447	475	592	631	649	705	715	0.167	4.102
	(299200)	(122400)	(105200)	(14800)	(17800)	(40400)			
2d	447	475	592	631	649	705	714	0.159	4.116
	(244200)	(100200)	(83000)	(12000)	(14400)	(32800)			

Table 3.2: Cyclic voltammogram data of oxasmaragdyrin, BF₂ complexed oxasmaragdyrin and their amino acid conjugates recorded in CH₂Cl₂ containing 0.1M TBAP as supporting electrolyte using scan rate of 50 mV/sec with BAS electrochemical system utilizing the three electrode configuration consisting of a glassy carbon (working electrode), platinum wire (auxilliary electrode) and saturated calomel (reference electrode) electrodes. All potentials were calibrated versus saturated calomel electrode by the addition of ferrocene as an internal standard, taking E1/2 (Fc/Fc⁺) = 0.42 V vs SCE.

Compound	Reduction (V)		Oxidation (V)	
	I	II	I	II
5	-1.32	-1.66	0.49	0.82
1a	-1.29	-1.64	0.45	0.77
1b	-1.27	-1.64	0.46	0.77
1c	-1.27	-1.64	0.46	0.77
1d	-1.28	-1.64	0.46	0.77
6	- 0.97	--	0.73	1.16
2a	-0.97	--	0.74	1.18
2b	-0.97	--	0.74	1.18
2c	-0.98	--	0.74	1.18
2d	-0.97	--	0.74	1.17

The electrochemical properties of conjugates **1** and **2** along with their corresponding precursors were studied in CH₂Cl₂ by cyclic voltammetry at a scan rate of 50 mV/s using tetrabutylammonium perchlorate (TBAP) as the supporting electrolyte. The conjugates **1** and **2** also showed two reversible oxidations and one or two reversible/irreversible reduction(s) like their precursor oxasmaragdyrin **5** and BF₂-oxasmaragdyrin **6** with negligible shifts in their peak potentials indicating that the rich redox chemistry of oxasmaragdyrin/BF₂-oxasmaragdyrin did not alter significantly by linking them with various amino acids. Thus, the spectral and electrochemical properties indicate that the oxasmaragdyrin/BF₂-oxasmaragdyrin and amino

acid moieties did not interact strongly and the individual properties of the moieties retained in conjugates.

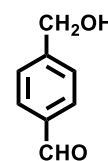
3.3 Conclusions

In summary, we successfully synthesized a series oxasmaragdyrin-amino acid conjugates and BF₂-oxasmaragdyrin-amino acid conjugates using readily available building blocks under simple reaction conditions. The conjugates were easily isolated by column chromatography and characterized in detail by HR-MS, 1D and 2D NMR spectroscopy. The spectral and electrochemical properties indicated that the conjugates showed similar rich spectral and redox properties like unconjugated oxasmaragdyrins/BF₂-oxasmaragdyrins without significant alteration which are very useful for their potential applications as NIR fluorescent probes in biology and medicine. The biological studies on these conjugates are currently under investigation in our laboratory.

3.4 Experimental

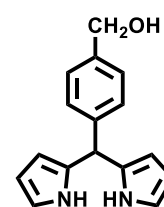
Synthesis of 4-(hydroxymethyl)benzaldehyde:

To 1,4-terephthalaldehyde (1.0 g, 7.46 mmol) in methanol, sodiumborohydride (70.51 mg, 1.86 mmol) was added at 0 °C and the reaction mixture was stirred at room temperature for 3 hours. The completion of the reaction was monitored by the formation of more polar spot on TLC. After the completion of reaction, the solvent was evaporated to get crude solid. The crude solid was extracted in dichloromethane and organic layer was washed with water (3 × 25 mL). The organic layer was dried over anhydrous sodium sulphate and evaporated to give product as colourless liquid in 80% yield.



Synthesis of compound 3:

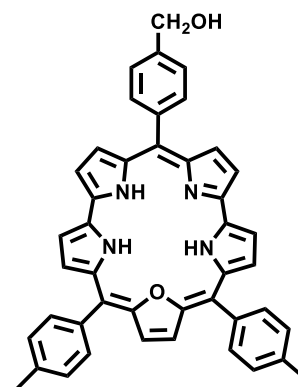
To a mixture of 4-(hydroxymethyl) benzaldehyde (1.0 g, 7.34 mmol) and pyrrole (10 mL, 146.90 mmol) in dichloromethane under nitrogen atmosphere, TFA (73 μL, 0.73 mmol) was added. The resulting mixture was stirred for 10 min at room temperature and the mixture was quenched by 10% aqueous NaOH solution. The organic layer was washed with water (3 × 50 mL), dried over anhydrous sodium sulphate and evaporated under reduced pressure to give crude product which was further purified by silica gel column chromatography (petroleum ether/ethyl acetate) to give pure compound as crystalline solid (0.750 g) in 40% yield. ¹H NMR (500 MHz, Chloroform-d) δ 7.98 (s, 2H), 7.31 (d, *J* = 7.9 Hz, 2H), 7.21 (d, *J* = 8.1 Hz, 2H), 6.68 (d, *J* = 1.5 Hz, 1H), 6.16



(d, $J = 3.0$ Hz, 1H), 5.91 (d, $J = 1.0$ Hz, 1H), 5.46 (s, 1H), 4.66 (s, 2H). ^{13}C NMR (126 MHz, CDCl_3) δ 141.8, 139.6, 132.5, 128.7, 127.5, 117.4, 108.5, 107.3, 65.2, 43.8.

Synthesis of compound 5:

To a mixture of *meso*-(4-hydroxymethyl)phenyl dipyrromethane **3** (0.310 g, 1.23 mmol), oxatripyrrane **4** (0.500 g, 1.23 mmol) in dichloromethane solvent, 0.1 equivalents of TFA (10 μL , 0.123 mmol) was added and stirred at room temperature for 1.5 hours. Then DDQ (0.836 g, 3.69 mmol) was added to above mixture and stirred for further 1.5 hours. The reaction mixture was evaporated under reduced pressure and the crude solid was subjected to basic-alumina column chromatography using dichloromethane/petroleum ether as



solvent to give pure compound as dark green solid in 25% yield. ^1H NMR (400 MHz, Chloroform- d) δ 9.41 (d, $J = 4.2$ Hz, 2H), 9.34 (d, $J = 4.3$ Hz, 2H), 8.91 (d, $J = 4.3$ Hz, 2H), 8.75 (s, 2H), 8.40 (d, $J = 4.2$ Hz, 2H), 8.33 (d, $J = 7.7$ Hz, 2H), 8.08 (d, $J = 7.8$ Hz, 4H), 7.77 – 7.64 (d, $J = 7.7$ Hz, 2H), 7.60 (d, $J = 7.7$ Hz, 4H), 4.86 (s, 2H), 2.72 (s, 6H). ^{13}C NMR (126 MHz, CDCl_3) δ 149.2, 143.7, 139.6, 138.1, 137.8, 136.0, 134.7, 133.8, 131.0, 129.9, 129.3, 128.9, 128.5, 128.3, 127.9, 126.5, 126.3, 126.0, 125.2, 124.4, 119.5, 118.6, 117.7, 115.5, 108.2, 105.5, 65.1, 21.7. IR (ν cm^{-1} , CHCl_3) 3393, 2918, 2861, 1715, 1600, 1512, 1463, 1463, 1271, 1044, 785, 756. UV/Vis (Chloroform) (λ_{max} /nm, ϵ $\text{mol}^{-1}\text{dm}^3\text{cm}^{-1}$) 447 (123600), 558 (9200), 599 (8321), 638 (7708), 700 (8177). Fluorescence (in chloroform) λ_f (Φ_f) 714 nm (0.029) Calculated mass: $m/z = 651.2755$, measured mass: $m/z = 651.2756$ $[\text{M}+\text{H}]^+$.

Synthesis of compound 1:

To the mixture of (4-(methylhydroxy)phenyl) oxasmaragdyrin **5** (50 mg, 0.077 mmol) and N-Fmoc protected amino acid (0.23 mmol) in dry CH_2Cl_2 , diisopropylethylamine (60 μL , 0.346 mmol) and HOBT (37.4 mg, 0.277 mmol) were added under nitrogen atmosphere, followed by addition of EDC.HCl (54 mg, 0.277 mmol) at 0 $^\circ\text{C}$. The mixture was stirred for 12 hr. The reaction was monitored by thin layer chromatography which showed formation of less polar spot. Upon completion of reaction, the mixture was washed with 10% NaHCO_3 (3×50 mL). The organic layer was collected, dried over anhydrous Na_2SO_4 and the solvent was evaporated to give crude product. The crude product was purified using silica gel column chromatography by EtOAc/Petroleum ether (15%) as eluent to give amino acid conjugate as green solid in 20-25% yield.

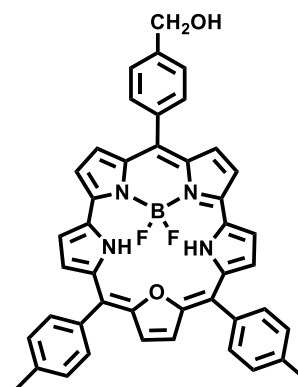
The chemical structure shows a central macrocyclic core, likely a porphyrin or phthalocyanine derivative, with four nitrogen atoms (NH) and one oxygen atom in the ring. It is substituted with several side chains: a 4-phenylphenyl group, a 4-phenylphenyl group, a 4-phenylphenyl group, and a 4-phenylphenyl group. Additionally, there is a side chain with a benzyl group and a carbonyl group, and another side chain with a benzyl group and a carbonyl group.

[illegible]

(Chloroform) ($\lambda_{\text{max}}/\text{nm}$, $\epsilon \text{ mol}^{-1}\text{dm}^3\text{cm}^{-1}$) 447 (71400), 558 (5500), 599 (5416), 638 (5267), 700 (5424). Fluorescence (in chloroform) λ_f (Φ_f) 714 nm (0.018).

Synthesis of compound 6:

To a mixture of oxasmaragdyrin **5** (100 mg, 0.153 mmol) and triethylamine (0.850 ml, 6.15 mmol) in dichloromethane solvent, $\text{BF}_3\cdot\text{OEt}_2$ (1.1 ml, 8.0 mmol) was added and stirred for 30 minutes. The formation of product was checked through TLC. Upon completion of reaction, the solvent was evaporated and crude solid was subjected to basic-alumina column chromatography using dichloromethane/petroleum ether as solvent to give pure compound as light green solid in 80% yield. ^1H NMR (500 MHz, Chloroform-



δ 10.30 (d, $J = 4.4$ Hz, 2H), 10.21 (dd, $J = 4.4$, 1.9 Hz, 2H), 9.59 (d, $J = 4.4$ Hz, 2H), 9.48 (s, 2H), 9.00 (d, $J = 3.7$ Hz, 2H), 8.63 (d, $J = 7.6$ Hz, 2H), 8.32 (d, $J = 7.7$ Hz, 4H), 8.00 (d, $J = 7.7$ Hz, 2H), 7.72 (d, $J = 7.6$ Hz, 4H), 5.16 (s, 2H), 2.82 (s, 6H), -3.70 (s, 2H). ^{13}C NMR (126 MHz, CDCl_3) δ 149.9, 147.3, 144.2, 143.9, 140.8, 139.7, 138.6, 138.0, 135.1, 134.4, 133.1, 131.9, 131.6, 130.9, 130.7, 128.4, 127.1, 126.8, 125.1, 124.5, 123.7, 121.9, 120.7, 120.3, 119.0, 118.7, 107.0, 65.5, 64.7, 29.8, 21.8. ^{11}B NMR (160 MHz, CDCl_3) δ -12.39. ^{19}F NMR (471 MHz, CDCl_3) δ -149.43. IR ($\nu \text{ cm}^{-1}$, CHCl_3) 3430, 2925, 2857, 1727, 1574, 1471, 1457, 1413, 1390, 1263, 1114, 1075, 1031, 760, 715, 666. UV/Vis (Chloroform) ($\lambda_{\text{max}}/\text{nm}$, $\epsilon \text{ mol}^{-1}\text{dm}^3\text{cm}^{-1}$) 447 (284700), 475 (127000), 592 (11300), 631 (15500), 649 (18300), 705 (39900). Fluorescence (in chloroform) λ_f (Φ_f) 714 nm (0.143). Calculated mass: $m/z = 698.2667$, measured mass: m/z : 698.2695 [M^+].

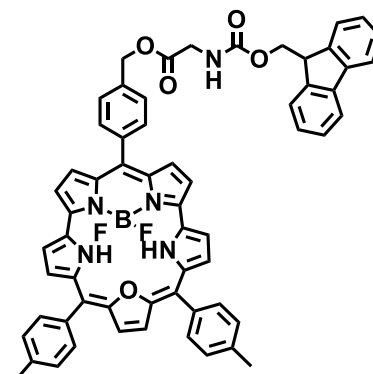
Synthesis of compound 2:

To the mixture of BF_2 -(4-(methylhydroxy)phenyl) oxasmaragdyrin **6** (30 mg, 0.04 mmol) and N-Fmoc protected amino acid (0.126 mmol) in dry CH_2Cl_2 , diisopropylethylamine (33 μL , 0.19 mmol) and HOBt (20.5 mg, 0.152 mmol) was added under nitrogen atmosphere. Followed by addition of EDC.HCl (29 mg, 0.152 mmol) was added at 0 $^\circ\text{C}$. The mixture was stirred for 12 hr. The reaction was monitored by thin layer chromatography which showed formation of less polar spot. Upon completion of reaction, the mixture was washed with 10% NaHCO_3 ($3 \times 50 \text{ mL}$). The organic layer was collected, dried over anhydrous Na_2SO_4 and the solvent was evaporated to give crude product. The crude product was purified using silica gel

column chromatography by EtOAc/Petroleum ether (15%) as eluent to give amino acid conjugate as green solid in 25-30% yield.

Compound 2a:

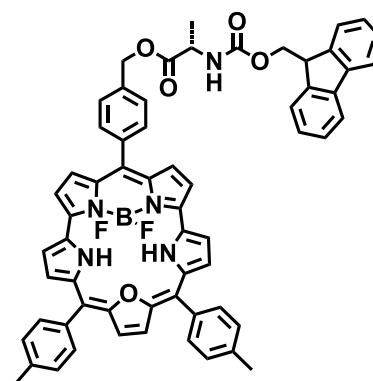
Yield = 28%; ^1H NMR (400 MHz, Chloroform- d) δ 10.28 (d, J = 4.5 Hz, 2H), 10.21 (dd, J = 4.5, 2.0 Hz, 2H), 9.56 (d, J = 4.5 Hz, 2H), 9.48 (s, 2H), 9.00 (dd, J = 4.5, 1.8 Hz, 2H), 8.60 (d, J = 8.0 Hz, 2H), 8.30 (d, J = 8.0 Hz, 4H), 7.95 (d, J = 7.7 Hz, 2H), 7.78 (d, J = 7.5 Hz, 2H), 7.69 (t, J = 8.5 Hz, 6H), 7.41 (dd, J = 7.5, 1.2 Hz, 2H), 7.37 (dd, J = 7.4, 1.3 Hz, 2H), 5.62 (s, 2H), 5.45 (s, 1H), 4.52 (d, J = 7.1 Hz, 2H), 4.33 (t, J = 7.2 Hz, 1H), 4.27 (d, J = 5.6 Hz, 2H), 2.80 (s, 6H), -3.79 (s, 2H). ^{13}C NMR (126



MHz, CDCl_3) δ 171.0, 149.9, 143.8, 143.8, 141.5, 139.7, 138.0, 135.4, 134.4, 131.9, 130.9, 130.7, 128.9, 128.4, 128.0, 127.4, 127.2, 125.2, 125.1, 124.5, 123.7, 121.9, 121.1, 120.6, 120.3, 120.2, 120.1, 119.9, 118.8, 107.0, 67.6, 58.5, 47.3, 45.9, 29.8, 29.5, 21.8, 18.2, 8.8, 8.3. ^{11}B NMR (160 MHz, CDCl_3) δ -12.28. ^{19}F NMR (471 MHz, CDCl_3) δ -149.32. IR (ν cm^{-1} , CHCl_3) 2922, 2406, 2315, 1725, 1515, 1454, 1380, 1276, 1181, 1053, 907, 780, 760, 732, 616. UV/Vis (Chloroform) (λ_{max} /nm, ϵ $\text{mol}^{-1}\text{dm}^3\text{cm}^{-1}$) 447 (175600), 475 (75600), 592 (5890), 631 (8730), 649 (10350), 705 (23400). Fluorescence (in chloroform) λ_f (Φ_f) 716 nm (0.156). Calculated mass: m/z = 977.3565, measured mass: m/z = 977.3566 [M^+].

Compound 2b

Yield = 27%; ^1H NMR (500 MHz, Chloroform- d) δ 10.31 (d, J = 4.4 Hz, 2H), 10.23 (dd, J = 4.4, 2.0 Hz, 2H), 9.58 (d, J = 4.4 Hz, 2H), 9.50 (s, 2H), 9.02 (s, 2H), 8.63 (d, J = 7.7 Hz, 2H), 8.32 (d, J = 7.8 Hz, 4H), 7.97 (d, J = 7.6 Hz, 2H), 7.78 (dd, J = 7.6, 3.8 Hz, 2H), 7.69 (d, J = 7.4 Hz, 2H), 7.39 (d, J = 7.0 Hz, 4H), 5.65 (s, 2H), 5.55 (d, J = 7.9 Hz, 1H), 4.79 – 4.62 (m, 1H), 4.51 (dt, J = 17.9, 9.0 Hz, 2H), 4.34 (t, J = 7.0 Hz, 1H), 2.82 (s, 6H), 1.69 (d, J = 7.2 Hz, 3H). ^{13}C NMR (126 MHz, CDCl_3) δ

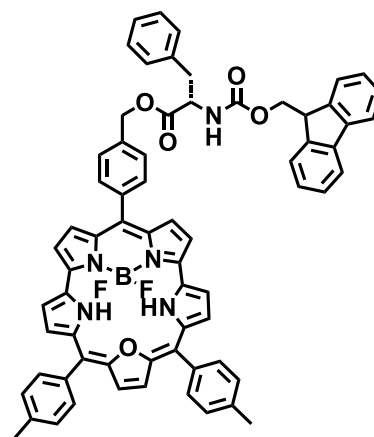


171.0, 149.9, 143.8, 143.8, 141.5, 139.7, 138.0, 135.4, 134.4, 131.9, 130.9, 130.7, 128.9, 128.4, 128.0, 127.4, 127.2, 125.2, 125.1, 124.5, 123.7, 121.9, 121.1, 120.6, 120.3, 120.2, 120.1, 119.9, 118.8, 107.0, 67.6, 58.5, 47.3, 45.9, 29.8, 29.5, 21.8, 18.2, 8.8, 8.3. ^{11}B NMR (160 MHz, CDCl_3) δ -12.29. ^{19}F NMR (471 MHz, CDCl_3) δ -149.45. IR (ν cm^{-1} , CHCl_3) 2922, 2857, 1690,

1601, 1523, 1513, 1454, 1378, 1344, 1290, 1249, 1183, 1092, 1066, 1017, 997, 927, 909, 782, 732. UV/Vis (Chloroform) (λ_{\max}/nm , $\epsilon \text{ mol}^{-1}\text{dm}^3\text{cm}^{-1}$) 447 (175645), 475 (75652), 592 (6000), 631 (9000), 649 (11200), 705 (24400). Fluorescence (in chloroform) λ_f (Φ_f) 714 nm (0.165). Calculated mass: $m/z = 943.3728$, measured mass: $m/z = 943.3725 [M^+]$.

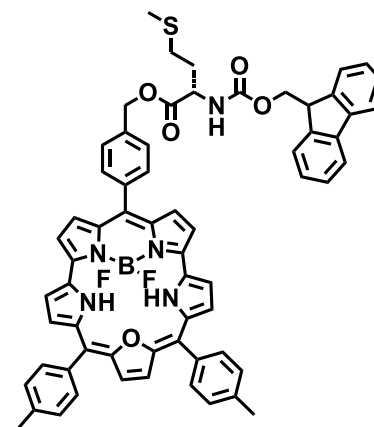
Compound 2c

Yield = 30%; ^1H NMR (500 MHz, Chloroform-*d*) δ 10.29 (d, $J = 4.4$ Hz, 2H), 10.21 (dd, $J = 4.5, 2.0$ Hz, 2H), 9.56 (d, $J = 4.4$ Hz, 2H), 9.48 (s, 2H), 9.00 (dd, $J = 4.4, 1.9$ Hz, 2H), 8.60 (d, $J = 7.6$ Hz, 2H), 8.30 (d, $J = 7.5$ Hz, 4H), 7.89 (d, $J = 7.5$ Hz, 2H), 7.77 (d, $J = 7.5$ Hz, 2H), 7.70 (d, $J = 7.5$ Hz, 4H), 7.64 (t, $J = 6.8$ Hz, 2H), 7.46 – 7.32 (m, 8H), 7.26 (s, 2H), 5.58 (d, $J = 5.1$ Hz, 2H), 5.45 (d, $J = 8.3$ Hz, 1H), 4.96 (d, $J = 7.3$ Hz, 1H), 4.53 (dd, $J = 10.7, 7.2$ Hz, 1H), 4.45 (dd, $J = 10.7, 7.0$ Hz, 1H), 4.29 (t, $J = 7.0$ Hz, 2H), 3.34 (d, $J = 5.9$ Hz, 2H), 2.80 (s, 6H), -3.81 (d, $J = 10.2$ Hz, 2H). ^{13}C NMR (101 MHz, CDCl_3) δ 171.6, 155.7, 149.8, 143.7, 141.3, 139.5, 137.9, 134.9, 134.2, 131.6, 130.6, 129.5, 128.7, 128.5, 128.3, 127.7, 127.3, 127.1, 125.1, 124.9, 124.2, 123.6, 121.8, 120.6, 120.2, 120.0, 106.9, 67.3, 67.1, 55.0, 47.2, 38.4, 21.6. ^{11}B NMR (160 MHz, CDCl_3) δ -12.32. ^{19}F NMR (471 MHz, CDCl_3) δ -149.30. IR ($\nu \text{ cm}^{-1}$, CHCl_3) 2928, 2854, 2355, 2325, 1725, 1515, 1454, 1378, 1349, 1276, 1254, 1185, 1095, 1053, 1022, 780, 758, 739, 580. UV/Vis (Chloroform) (λ_{\max}/nm , $\epsilon \text{ mol}^{-1}\text{dm}^3\text{cm}^{-1}$) 447 (299200), 475 (122400), 592 (105200), 631 (14800), 649 (17800), 705 (40400). Fluorescence (in chloroform) λ_f (Φ_f) 715 nm (0.167). Calculated mass: $m/z = 1067.4035$, measured mass: $m/z = 1067.4037 [M^+]$.



Compound 2d:

Yield = 25%; ^1H NMR (400 MHz, Chloroform-*d*) δ 10.29 (d, $J = 4.4$ Hz, 2H), 10.21 (dd, $J = 4.4, 1.9$ Hz, 2H), 9.56 (d, $J = 4.5$ Hz, 2H), 9.48 (s, 2H), 9.00 (dd, $J = 4.4, 1.8$ Hz, 2H), 8.60 (d, $J = 7.8$ Hz, 2H), 8.30 (d, $J = 7.9$ Hz, 4H), 7.95 (d, $J = 7.6$ Hz, 4H), 7.76 (d, $J = 5.7$ Hz, 2H), 7.72 – 7.65 (m, 6H), 7.46 – 7.32 (m, 4H), 5.99 (d, $J = 8.0$ Hz, 1H), 5.62 (s, 2H), 4.79 (d, $J = 6.4$ Hz, 1H), 4.52 (d, $J = 7.0$ Hz, 2H), 4.31 (t, $J = 6.7$ Hz, 1H), 2.80 (s, 6H), 2.19 (s, 3H), 1.26 (d, $J = 1.3$ Hz, 2H), 0.89 (s, 2H), -3.82 (s, 2H). ^{13}C NMR (126 MHz, CDCl_3) δ 172.3, 156.2, 150.0, 144.0, 143.8,



141.5, 139.7, 138.1, 137.6, 135.1, 134.8, 134.4, 132.1, 131.8, 131.0, 130.8, 128.6, 128.4, 127.9, 127.3, 125.2, 125.1, 124.4, 123.8, 122.0, 120.8, 120.4, 120.2, 118.2, 107.1, 67.9, 67.6, 67.3, 53.6, 53.3, 47.4, 38.9, 32.2, 32.1, 30.1, 29.8, 29.5, 22.8, 21.8, 15.8, 14.7, 14.2. ^{11}B NMR (160 MHz, CDCl_3) δ -12.26. ^{19}F NMR (376 MHz, CDCl_3) δ -149.36. IR (ν cm^{-1} , CHCl_3) 2922, 2850, 2322, 1900, 1810, 1723, 1601, 1512, 1454, 1378, 1344, 1252, 1181, 1095, 1070, 1017, 758, 712. UV/Vis (Chloroform) ($\lambda_{\text{max}}/\text{nm}$, ϵ $\text{mol}^{-1}\text{dm}^3\text{cm}^{-1}$) 447 (244200), 475 (100200), 592 (83000), 631 (12000), 649 (14400), 705 (32800). Fluorescence (in chloroform) λ_{f} (Φ_{f}) 714 nm (0.159). Calculated mass: $m/z = 1051.3755$, measured mass: $m/z = 1051.3766$ [M^+].

3.5 References

1. Bauer, V. J.; Clive, D. L. J.; Dolphin, D.; Paine, J. B.; Harris, F. L.; King, M. M.; Loder, J.; Wang, S. W. C.; Woodward, R. B., Sapphyrins: novel aromatic pentapyrrolic macrocycles. *J. Am. Chem. Soc.* **1983**, *105*, 6429-6436.
2. Narayanan, S. J.; Sridevi, B.; Chandrashekar, T. K.; Englich, U.; Ruhlandt-Senge, K., Core-Modified Smaragdyrins: First Examples of Stable Meso-Substituted Expanded Corrole. *Org. Lett.* **1999**, *1*, 587-590.
3. Pareek, Y.; Ravikanth, M.; Chandrashekar, T. K., Smaragdyrins: emeralds of expanded porphyrin family. *Acc. Chem. Res.* **2012**, *45*, 1801-16.
4. Chatterjee, T.; Srinivasan, A.; Ravikanth, M.; Chandrashekar, T. K., Smaragdyrins and Sapphyrins Analogues. *Chem. Rev.* **2017**, *117*, 3329-3376.
5. Rajeswara Rao, M.; Ravikanth, M., Boron complexes of oxasmaragdyrin, a core-modified expanded porphyrin. *J. Org. Chem.* **2011**, *76*, 3582-7.
6. Jasat, A.; Dolphin, D., Expanded Porphyrins and Their Heterologs. *Chem. Rev.* **1997**, *97*, 2267-2340.
7. Osuka, A.; Saito, S., Expanded porphyrins and aromaticity. *Chem. Commun.* **2011**, *47*, 4330-4339.
8. Saito, S.; Osuka, A., Expanded Porphyrins: Intriguing Structures, Electronic Properties, and Reactivities. *Angew. Chem. Int. Ed.* **2011**, *50*, 4342-4373.
9. Kuimova, M. K.; Collins, H. A.; Balaz, M.; Dahlstedt, E.; Levitt, J. A.; Sergent, N.; Suhling, K.; Drobizhev, M.; Makarov, N. S.; Rebane, A.; Anderson, H. L.; Phillips, D., Photophysical properties and intracellular imaging of water-soluble porphyrin dimers for two-photon excited photodynamic therapy. *Org. Biomol. Chem.* **2009**, *7*, 889-896.

10. Escobedo, J. O.; Rusin, O.; Lim, S.; Strongin, R. M., NIR dyes for bioimaging applications. *Curr. Opin. Chem. Biol.* **2010**, *14*, 64-70.
11. Ethirajan, M.; Chen, Y.; Joshi, P.; Pandey, R. K., The role of porphyrin chemistry in tumor imaging and photodynamic therapy. *Chem. Soc. Rev.* **2011**, *40*, 340-362.
12. Kobayashi, N.; Furuyama, T.; Satoh, K., Rationally Designed Phthalocyanines Having Their Main Absorption Band beyond 1000 nm. *J. Am. Chem. Soc.* **2011**, *133*, 19642-19645.
13. Brennan, B. J.; Lam, Y. C.; Kim, P. M.; Zhang, X.; Brudvig, G. W., Photoelectrochemical Cells Utilizing Tunable Corroles. *ACS Appl. Mater. Interfaces* **2015**, *7*, 16124-16130.
14. Pham, W.; Cassell, L.; Gillman, A.; Koktysh, D.; Gore, J. C., A near-infrared dye for multichannel imaging. *Chem. Commun.* **2008**, 1895-1897.
15. Fischer, G. M.; Isomäki-Krondahl, M.; Göttker-Schnetmann, I.; Daltrozzo, E.; Zumbusch, A., Pyrrolopyrrole Cyanine Dyes: A New Class of Near-Infrared Dyes and Fluorophores. *Chem. Eur. J.* **2009**, *15*, 4857-4864.
16. Tang, B.; Yu, F.; Li, P.; Tong, L.; Duan, X.; Xie, T.; Wang, X., A Near-Infrared Neutral pH Fluorescent Probe for Monitoring Minor pH Changes: Imaging in Living HepG2 and HL-7702 Cells. *J. Am. Chem. Soc.* **2009**, *131*, 3016-3023.
17. Arunkumar, E.; Forbes, C. C.; Noll, B. C.; Smith, B. D., Squaraine-Derived Rotaxanes: Sterically Protected Fluorescent Near-IR Dyes. *J. Am. Chem. Soc.* **2005**, *127*, 3288-3289.
18. Johnson, J. R.; Fu, N.; Arunkumar, E.; Leevy, W. M.; Gammon, S. T.; Piwnica-Worms, D.; Smith, B. D., Squaraine rotaxanes: superior substitutes for Cy-5 in molecular probes for near-infrared fluorescence cell imaging. *Angew. Chem. Int. Ed.* **2007**, *46*, 5528-5531.
19. Umezawa, K.; Citterio, D.; Suzuki, K., Water-soluble NIR Fluorescent Probes Based on Squaraine and Their Application for Protein Labeling. *Anal. Sci.* **2008**, *24*, 213-217.
20. Fu, N.; Gassensmith, J. J.; Smith, B. D., Effect of Stopper Size on Squaraine Rotaxane Stability. *Supramol. Chem.* **2009**, *21*, 118-124.
21. Loudet, A.; Bandichhor, R.; Burgess, K.; Palma, A.; McDonnell, S. O.; Hall, M. J.; O'Shea, D. F., B,O-Chelated Azadipyrrromethenes as Near-IR Probes. *Org. Lett.* **2008**, *10*, 4771-4774.
22. Umezawa, K.; Nakamura, Y.; Makino, H.; Citterio, D.; Suzuki, K., Bright, Color-Tunable Fluorescent Dyes in the Visible–Near-Infrared Region. *J. Am. Chem. Soc.* **2008**, *130*, 1550-1551.

23. Umezawa, K.; Matsui, A.; Nakamura, Y.; Citterio, D.; Suzuki, K., Bright, Color-Tunable Fluorescent Dyes in the Vis/NIR Region: Establishment of New “Tailor-Made” Multicolor Fluorophores Based on Borondipyrromethene. *Chem. Eur. J.* **2009**, *15*, 1096-1106.
24. Nesterov, E. E.; Skoch, J.; Hyman, B. T.; Klunk, W. E.; Bacskai, B. J.; Swager, T. M., In Vivo Optical Imaging of Amyloid Aggregates in Brain: Design of Fluorescent Markers. *Angew. Chem. Int. Ed.* **2005**, *44*, 5452-5456.
25. Meek, S. T.; Nesterov, E. E.; Swager, T. M., Near-Infrared Fluorophores Containing Benzo[c]heterocycle Subunits. *Org. Lett.* **2008**, *10*, 2991-2993.
26. Yang, Y.; Lowry, M.; Xu, X.; Escobedo, J. O.; Sibrian-Vazquez, M.; Wong, L.; Schowalter, C. M.; Jensen, T. J.; Fronczek, F. R.; Warner, I. M.; Strongin, R. M., Seminaphthofluorones are a family of water-soluble, low molecular weight, NIR-emitting fluorophores. *Proc. Natl. Acad. Sci. U.S.A* **2008**, *105*, 8829.
27. Nesterova, I. V.; Verdree, V. T.; Pakhomov, S.; Strickler, K. L.; Allen, M. W.; Hammer, R. P.; Soper, S. A., Metallo-Phthalocyanine Near-IR Fluorophores: Oligonucleotide Conjugates and Their Applications in PCR Assays. *Bioconjugate Chem.* **2007**, *18*, 2159-2168.
28. Kee, H. L.; Nothdurft, R.; Muthiah, C.; Diers, J. R.; Fan, D.; Ptaszek, M.; Bocian, D. F.; Lindsey, J. S.; Culver, J. P.; Holten, D., Examination of chlorin-bacteriochlorin energy-transfer dyads as prototypes for near-infrared molecular imaging probes. *Photochem. Photobiol.* **2008**, *84*, 1061-1072.
29. Nesterova, I. V.; Erdem, S. S.; Pakhomov, S.; Hammer, R. P.; Soper, S. A., Phthalocyanine Dimerization-Based Molecular Beacons Using Near-IR Fluorescence. *J. Am. Chem. Soc.* **2009**, *131*, 2432-2433.
30. Cowley, A. B.; Kennedy, M. L.; Silchenko, S.; Lukat-Rodgers, G. S.; Rodgers, K. R.; Benson, D. R., Insight into Heme Protein Redox Potential Control and Functional Aspects of Six-Coordinate Ligand-Sensing Heme Proteins from Studies of Synthetic Heme Peptides. *Inorg. Chem.* **2006**, *45*, 9985-10001.
31. Giuntini, F.; Alonso, C. M. A.; Boyle, R. W., Synthetic approaches for the conjugation of porphyrins and related macrocycles to peptides and proteins. *Photochem. Photobiol. Sci.* **2011**, *10*, 759-791.
32. Liu, T. W. B.; Chen, J.; Zheng, G., Peptide-based molecular beacons for cancer imaging and therapy. *Amino Acids* **2011**, *41*, 1123-1134.
33. Waghorn, P. A., Radiolabelled porphyrins in nuclear medicine. *J. Labelled Compd. Radiopharm.* **2014**, *57*, 304-309.

34. Abrahamse, H.; Hamblin, Michael R., New photosensitizers for photodynamic therapy. *Biochem. J* **2016**, 473, 347.
35. Karikis, K.; Georgilis, E.; Charalambidis, G.; Petrou, A.; Vakuliuk, O.; Chatziioannou, T.; Raptaki, I.; Tsovola, S.; Papakyriacou, I.; Mitraki, A.; Gryko, D. T.; Coutsolelos, A. G., Corrole and Porphyrin Amino Acid Conjugates: Synthesis and Physicochemical Properties. *Chem. Eur. J.* **2016**, 22, 11245-11252.
36. Sessler, J. L.; Andrievsky, A., Efficient Transport of Aromatic Amino Acids by Sapphyrin–Lasalocid Conjugates. *Chem. Eur. J.* **1998**, 4, 159-167.
37. Madhu, S.; Basu, S. K.; Jadhav, S.; Ravikanth, M., 3,5-Diformyl-borondipyrromethene for selective detection of cyanide anion. *Analyst* **2013**, 138, 299-306.
38. Lee, P.-Y. H. a. C.-H., Facile Syntheses of Modified Tripyrranes and Their Application to the Syntheses of Regioisomerically Pure Porphyrin Derivatives. *Bull. Korean Chem. Soc.* **1996**, 17, 6.

Chapter 4

Glucosamine conjugated BF₂-oxasmaragdyrin as NIR Fluorescence Imaging Agent

4.1 Introduction

Optical imaging has emerged as a non-invasive diagnostic technique which can be used to visualise cellular functions with high sensitivity, at low cost and less toxicity. Dyes which absorb and fluoresce in visible region has been employed extensively. These dyes have inherent disadvantages to image the mammalian cells/tissues as mammalian cells absorb and auto-fluoresce in this region leading to less signal to noise ratio. As mammalian cells are highly transparent in the region 650–900 nm,¹ dyes which fluoresce in this region are therefore very useful for Near-Infrared Fluorescence (NIRF) imaging and therapy. Hence there is a growing need for dyes that can be easily prepared to absorb and emit strongly in the NIR region. To best of our knowledge, there are only few dyes that are fluorescent in this region; these include cyanine dyes,²⁻⁴ squaraine dyes,⁵⁻⁸ BODIPY analogues,⁹⁻¹¹ benzo[c]heterocycles,¹²⁻¹³ xanthenes,¹⁴ phthalocyanines, and a small section of porphyrin derivatives.¹⁵⁻¹⁸

One such molecule which absorb and emit in NIR region is smaragdyrin which belongs to the class of expanded porphyrins. Smaragdyrins are 22π aromatic expanded pentapyrrolic macrocycles in which the five pyrroles are connected by three *meso* carbons and two direct pyrrole–pyrrole bonds. Until recently, it was believed that the presence of two direct pyrrole–pyrrole bonds makes the smaragdyrin macrocycle highly strained and not very stable for further studies.¹⁹ However, Chandrasekhar and co-workers found a way that the smaragdyrins can be stabilized if one of the pyrrole ring is replaced with a furan ring.²⁰⁻²² The resultant 25-oxasmaragdyrins are stable and show interesting spectral and electrochemical properties. The 25-oxasmaragdyrins absorb and emit in the Vis-NIR region with moderate quantum yields and singlet state lifetimes. The stability and photophysical properties can be further enhanced when the 25-oxasmaragdyrin is complexed with BF₂- unit to form BF₂-oxasmaragdyrins.²³ We have recently reported amino acid conjugated BF₂-oxasmaragdyrins. These molecules have retained the photophysical properties of BF₂-oxasmaragdyrins but didn't show any cellular uptake owing to their hydrophobicity.²⁴

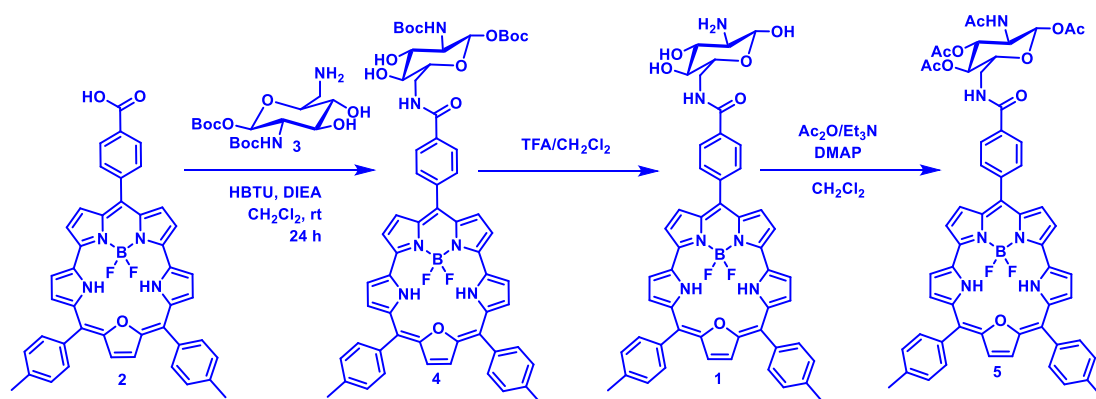
Upon perusal of literature, various targeting molecules have been used to internalise drugs and nanoparticles such as transferrin,²⁵ pluronic,²⁶ folic acid,²⁷ biotin²⁸ and polysaccharides.²⁹ Glucosamine³⁰ is one such molecule which easily permeates through the cell membrane as glucose is essential for the synthesis of highly glycosylated lysosomal proteins. Glunde and coworkers have demonstrated that fluorophore bound at C6 position of glucosamine can be used to optically image lysosomes in cells.³¹ Herein we report the synthesis

and characterisation of stable glucosamine conjugated BF₂-oxasmaragdyrin **1**. Furthermore biocompatibility, cellular internalisation and NIR fluorescence imaging properties of glucosamine conjugated BF₂-oxasmaragdyrin **1** were evaluated in mouse fibroblast L929 cell line as well as human breast cancer MDA-MB-231 cell line.

4.2 Results and Discussions

4.2.1 Synthesis and characterisation

The target BF₂-25-oxasmaragdyrin-glucosamine conjugate **1** was prepared over sequence of two steps as shown in Scheme 4.1. The required precursors, BF₂-25-oxasmaragdyrin **2** containing *p*-carboxyphenyl substituent at *meso* position and 6-amine-6-deoxy-1-O-Boc-2-N-Boc- β -D-glucosamine **3** were synthesized by following reported methods.^{23, 32-33} Compound **2** was reacted with compound **3** in presence of *N,N,N',N'*-tetramethyl-*O*-(1H-benzotriazol-1-yl)uronium hexafluorophosphate (HBTU) and *N,N*-diisopropylethylamine (DIEA) in dichloromethane under inert atmosphere for 8 hours, followed by basic alumina column chromatography to afford compound **4** as a green solid (55% yield). In the subsequent step, removal of solvent under reduced pressure yielded compound **1** as green solid (70% yield) which was used as it is without further purification. All intermediates and the target compound were characterised by ¹H, ¹H-¹H COSY, ¹³C, ¹¹B, ¹⁹F NMR spectroscopy and High Resolution Mass Spectrometry (HRMS). The ¹H NMR of compound **1** in DMSO-D₆ shows clear resonances corresponding to BF₂-25-oxasmaragdyrin but the resonances corresponding to that of the glucosamine were merged with residual water/solvent peak.



Scheme 4.1: Synthesis of glucosamine conjugated BF₂-oxa-smaragdyrin (**1**).

To confirm the presence of intact glucosamine moiety in compound **1**, the acetylation reaction was performed by treating compound **1** in dichloromethane with an excess of acetic

anhydride in presence of triethylamine and catalytic amount of 4-dimethylaminopyridine for 4 hours at room temperature followed by workup and silica gel column chromatography to afford compound **5** as a green solid (70% yield). Compound **5** was characterised in detail by ¹H, ¹H-¹H COSY, ¹³C, ¹¹B, ¹⁹F NMR as and all the resonances were assigned based on their location, integration, coupling constant, and cross-peak connectivity in ¹H-¹H COSY NMR spectroscopy as shown in Figure 4.1. In compound **5**, BF₂-oxasmaragdyrin core protons appear as five signals (four doublets and one singlet) in the region of 9.0 -10.5 ppm hence these peaks were identified as protons *a-e*. Further, Peaks 8.72, 8.36, 8.30, 7.70 ppm were identified as aryl protons *f, g, i, j* respectively by their integration and cross peak correlation in ¹H-¹H COSY. The four acyl protons appeared as four distinct singlets at 2.29, 2.25, 2.18 and 2.00 ppm. The peak at 6.92 ppm appeared as a triplet which was identified as '*k*' proton showed correlation with peaks at 4.05 ppm and 3.77 ppm which were assigned as '*l*' and '*l*' respectively. Further

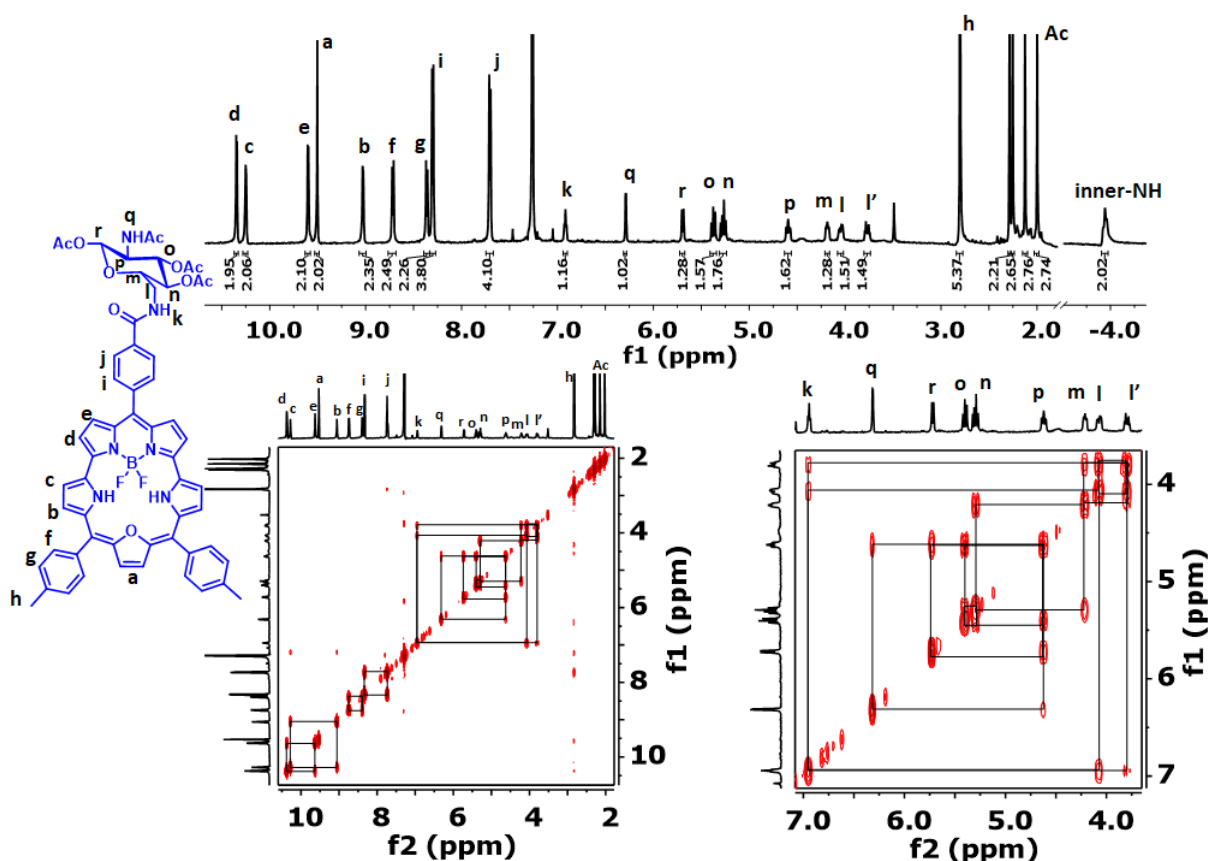


Figure 4.1. ¹H, ¹H-¹H COSY NMR of compound **5**.

proton '*l*' shows a correlation with peak at 4.19 ppm which was designated as proton '*m*'. Proton '*m*' shows a cross peak correlation with peak 5.27 ppm which was identified as proton

'*n*' which in turn showed a cross peak correlation with peak at 5.38 ppm assigned as proton '*o*'. Furthermore, proton '*o*' showed a cross peak correlation with peak at 4.59 ppm identified as proton '*p*' which in turn shows cross peak correlation with peak 6.29 ppm and 5.69 ppm which were assigned as protons '*q*' and '*r*' respectively. Thus, 1D and 2D NMR spectroscopy were very useful in deducing the molecular structure of compound **5**.

4.2.2 Photophysical and Electrochemical properties

The absorption and fluorescence spectra of compounds were recorded, and data are presented in Table 4.1. The absorption and fluorescence studies revealed that the compounds absorb in Vis-NIR region and emit in NIR region. The absorption spectra of compounds **1**, **4** and **5** in DMSO showed that all the molecules have similar absorption features (Figure 4.2a) with subtle differences in extinction coefficients (Table 4.1) since there is not much change in the electronic structure of the compounds. Similarly, the fluorescence spectra of compounds **1**, **4** and **5** in DMSO show that all the compounds have similar fluorescence spectral features (Figure 4.2b) with slight change in quantum yields. Compound **1** has relatively lower quantum yield ($\phi_f = 0.12$) compared to that of compounds **4** and **5** ($\phi_f = 0.19$).

Furthermore, Time-correlated single photon counting (TCSPC) experiments were carried out on compounds **1**, **4** and **5** by exciting the compounds at 440 nm and detecting emission at 710 nm. All the compounds showed single exponential decay profile (Figure 4.2c) with similar excited state lifetime (~ 4.9 ns). The electrochemical properties of compounds **4** and **5** were studied in CH_2Cl_2 by cyclic voltammetry at a scan rate of 50 mV/s by using tetrabutylammonium perchlorate (TBAP) as the supporting electrolyte (Figure 4.2d). Compounds **4** and **5** showed three reversible oxidations and one reversible reduction (Table 4.1) unlike $\text{BF}_2\text{-25-oxasmaragdyrin}$ which shows two reversible oxidations and one reversible reduction. The electrochemical data indicate that these compounds are easier to oxidize and reduce and compounds are stable under electrochemical conditions.

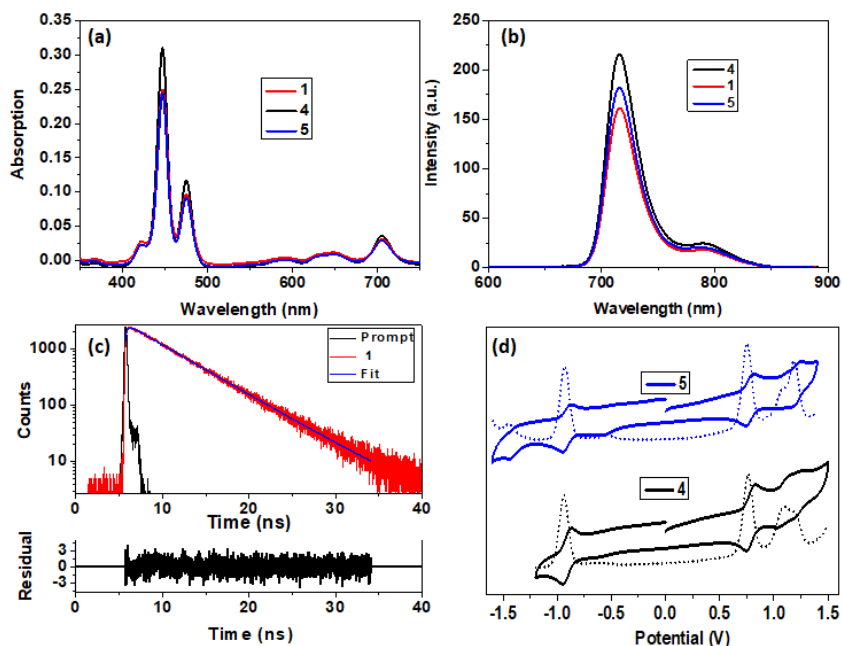


Figure 4.2. Comparison of (a) absorption, (b) fluorescence spectra of compounds **1**, **4** and **5** (conc: 1×10^{-5} M). (c) Fluorescence decay profile and the weighted residuals distribution fit of fluorescence decay of **1** in DMSO. The λ_{ex} used was 440 nm and emission was detected at 710 nm. (d) Comparison of cyclic Voltammograms and Differential Pulse Voltammograms of **4** and **5** in CH₂Cl₂ containing 0.1M TBAP as supporting electrolyte using scan rate of 50 mV/sec.

4.2.3 *In vitro* studies

Biocompatibility: The synthesized material, compound **1** is intended to be used as an imaging agent and evaluation of biocompatibility is a pre-requisite. The compound **1** was evaluated for biocompatibility in L929 cells with varying concentrations, ranging from 10 $\mu\text{g/mL}$ to 150 $\mu\text{g/mL}$ and presented in Figure 4.3. The compound **1** was biocompatible in the evaluated range and the morphology was intact after 24 h exposure and the % cell viability was $>90\%$ with the highest concentration. From this study, it can be concluded that the synthesized material is highly biocompatible and further studies could be evaluated.

Table 1. Photophysical and electrochemical data for compounds **1**, **4** and **5**.

Compounds	Wavelength (nm)						λ_f (nm)	ϕ_f	τ_s (ns)	Reduction (V)	Oxidation (V)		
	$(\epsilon \text{ in } [\text{mol}^{-1} \text{ L cm}^{-1} \times 10^4])$									I	I	II	III
I²³	446	553	591	634	647	703	708	0.15	--	-0.88	0.80	1.22	--
	(2.50)	(1.26)	(0.10)	(0.12)	(0.15)	(0.39)							
1	446	475	590	630	646	704	715	0.12	4.91	--	--	--	--
	(2.51)	(1.00)	(0.05)	(0.09)	(0.12)	(0.31)							
4	446	475	590	630	646	704	715	0.19	4.87	-0.94	0.76	1.09	1.18
	(3.10)	(1.19)	(0.01)	(0.08)	(0.11)	(0.36)							
5	446	475	590	630	646	704	715	0.19	4.87	-0.93	0.75	1.07	1.18
	(2.45)	(0.92)	(0.02)	(0.07)	(0.10)	(0.29)							

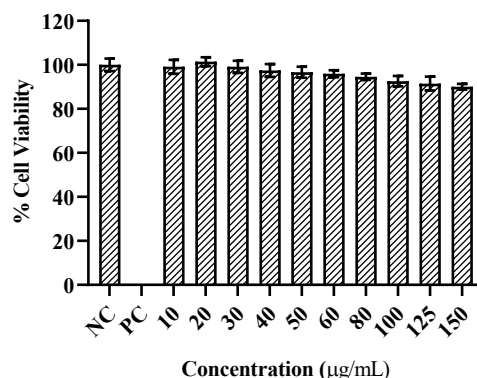


Figure 4.3. Biocompatibility of compound **1** on fibroblasts L929 cells (n = 5).

Cellular uptake: Qualitative in vitro cellular uptake of the compound **1** was performed in L929 and MDA MB 231 cells. It is necessary to evaluate the behaviour of material in the presence of cells i.e. the inherent property of fluorescence. The L929 and MDA MB 231 cells were incubated with compound **1** (10 µg/well) for 24 hours. CLSM data (Figure 4.4 and 4.5) revealed that the compound **1** was internalized in the cells and was able to exhibit strong fluorescence in NIR region. DAPI staining experiments were carried out to understand the localisation of compound **1** in the cells. DAPI staining analysis showed (Figure 4.5) that the compound **1** was localised in cytoplasm of the cells with very good emission in NIR region and not present inside the nucleus. This property of NIR emission could be exploited for the *in vivo* whole-body imaging or site-specific imaging.

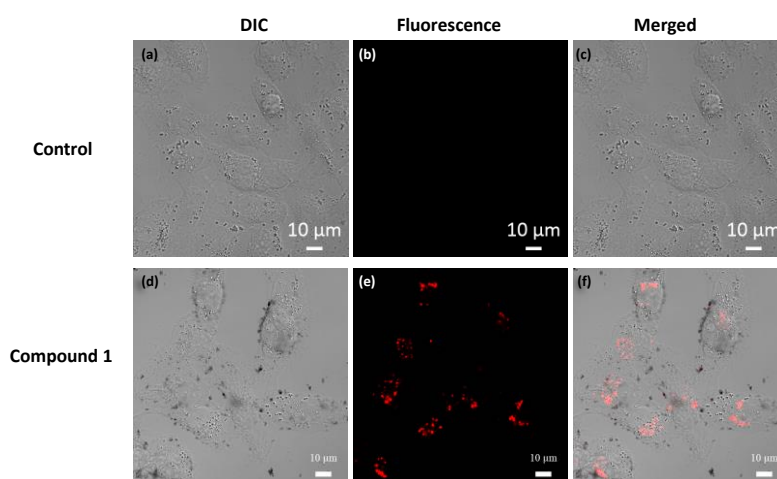


Figure 4.4. CLSM images of controls cells (a) Differential Interference Contrast (DIC) image, (b) Fluorescence channel with 680-730 nm and (c) merged image of all channels and cells treated with compound **1** (d) Differential Interference Contrast (DIC) image, (e) Fluorescence channel with 680-730 nm and (f) merged image of all channels

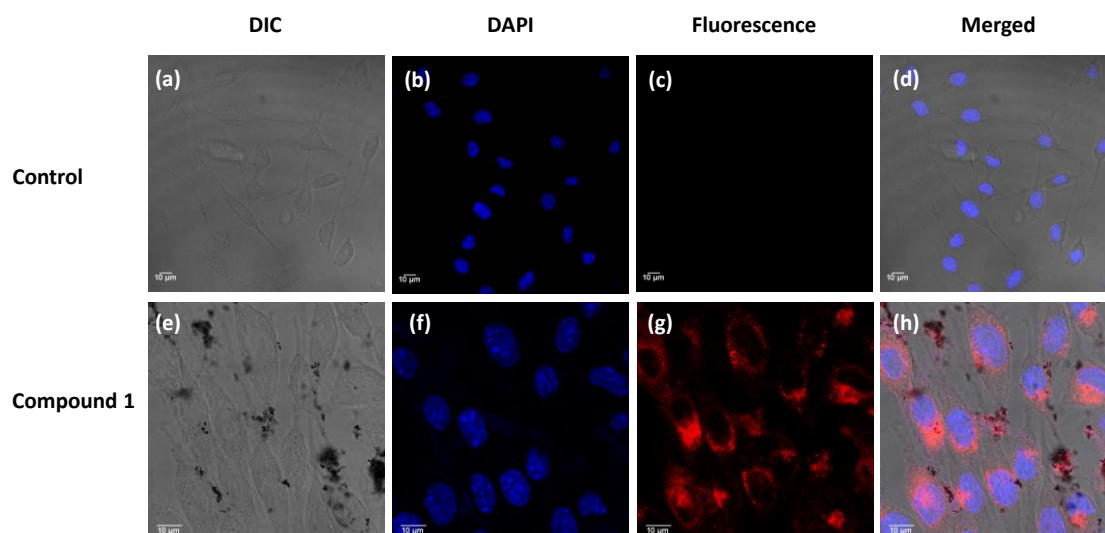


Figure 4.5. CLSM images showing L929 Control cells treated with DAPI (a) Differential Interference Contrast (DIC) image, (b) DAPI channel with 410-454 nm emission filter, (c) Fluorescence channel with 680-730 nm emission filter, (d) merged image of all channels and L929 cells treated with DAPI and compound **1**, (e) Differential Interference Contrast (DIC) image, (f) DAPI channel with 410-454 nm emission filter, (g) Fluorescence channel with 680-732 nm emission filter and (h) merged image of all channels.

4.3 Conclusions

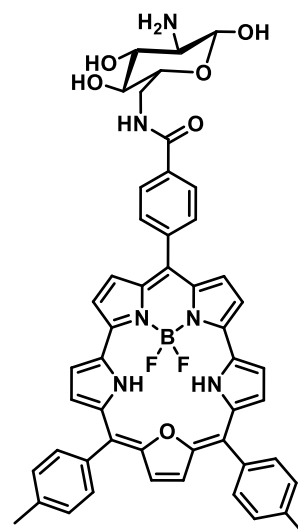
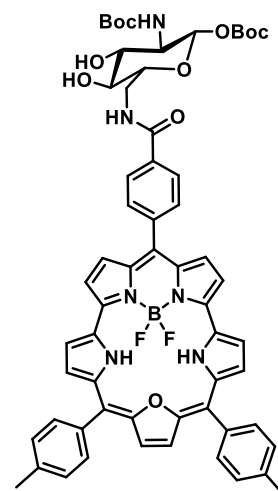
We have successfully synthesised glucosamine conjugated BF₂-oxasmaragdyrins and thoroughly characterised with ¹H, ¹H-¹H COSY, ¹¹B, ¹⁹F and HRMS. We found that the conjugates are stable and have retained the photophysical, electrochemical properties as that of the BF₂-oxasmaragdyrin. Glucosamine conjugated BF₂-oxasmaragdyrins showed excellent biocompatibility (even upto 150 μg/ml) in L929 cells. CLSM experiments also revealed that the glucosamine conjugated BF₂-oxasmaragdyrin **1** was internalised into the L929 and MDA-MB-231 within 24 hours and emitting strong NIR fluorescence within the cells. The DAPI staining experiments revealed that the glucosamine conjugated BF₂-oxasmaragdyrin **1** was internalised into the cytoplasm of the cells. The property of NIR emission could be exploited for the *in vivo* whole-body imaging or site-specific imaging.

4.4 Experimental

4.4.1 Syntheses

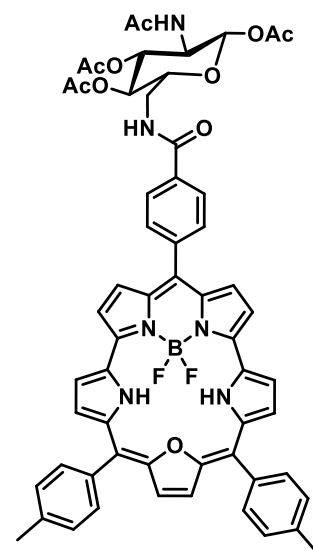
Compound 4: To a solution of amine **3** (31.8 mg, 0.084 mmol), acid **2** (30 mg, 0.042 mmol) and HBTU (15.2 mg, 0.040 mmol) in CH₂Cl₂ (5 mL), DIEA (45 µl, 0.252 mmol) was added under nitrogen atmosphere and stirred for 24 hours at room temperature. The formation of the product was monitored by TLC which showed single less polar spot. After completion of the reaction, the reaction mixture was diluted with CH₂Cl₂ (20 mL) and washed with 1N HCl (2 × 30 mL), 1N NaOH (2 × 30 mL), brine solution (2 × 30 mL). The organic layer was dried on anhydrous sodium sulphate and the solvent was removed under reduced pressure to give crude product. The crude product was purified by neutral alumina column chromatography (CH₂Cl₂/MeOH: 95/5) to obtain pure compound as green solid (35 mg, yield: 78%). ¹H NMR (400 MHz, CDCl₃) δ 10.34 (d, *J* = 4.5 Hz, 2H), 10.24 (dd, *J* = 4.5, 2.0 Hz, 2H), 9.58 (d, *J* = 4.5 Hz, 2H), 9.52 (s, 2H), 9.03 (dd, *J* = 4.4, 1.8 Hz, 2H), 8.72 (d, *J* = 8.2 Hz, 2H), 8.39 (d, *J* = 8.2 Hz, 2H), 8.30 (d, *J* = 7.9 Hz, 4H), 7.70 (d, *J* = 7.7 Hz, 4H), 7.05 (dd, *J* = 8.2, 4.5 Hz, 1H), 6.13 (d, *J* = 3.5 Hz, 1H), 4.85 (s, 1H), 4.59 – 4.40 (m, 1H), 4.07 – 3.83 (m, 2H), 3.57 (q, *J* = 9.6, 8.3 Hz, 2H), 2.80 (s, 6H), 1.49 (s, 9H), 1.26 (s, 9H). ¹³C NMR (101 MHz, CDCl₃) δ 169.8, 152.2, 150.0, 143.5, 139.7, 138.1, 135.2, 134.4, 132.5, 131.6, 131.0, 130.8, 130.6, 128.4, 127.3, 125.1, 124.1, 123.9, 122.3, 121.1, 120.6, 107.2, 94.6, 83.6, 80.5, 73.3, 71.1, 54.3, 40.5, 32.1, 29.8, 28.5, 28.5, 27.9, 27.8, 22.8, 21.8. ¹⁹F NMR (377 MHz, CDCl₃) δ -149.16. ¹¹B NMR (128 MHz, CDCl₃) δ -12.80. HRMS: calcd. for C₆₀H₅₉BF₂N₆O₁₀ [M + H]⁺ 1072.4358; found 1072.4329.

Compound 1: Compound **4** (50 mg, mmol) was dissolved in 3 ml of CH₂Cl₂ /TFA (3:1 v/v) and stirred for 15 min under inert atmosphere. The progress of the reaction was monitored by TLC analysis. The solvent was removed under reduced pressure and the residue was neutralised by methanolic ammonia (10 ml). The solvent was removed on rotary evaporator under reduced vacuo to obtain the compound **1** as green solid which was used without further purification (50 mg, yield: 73.7%) ¹H NMR (400 MHz, DMSO-d₆) δ 10.77 (d, *J* = 4.5 Hz, 2H), 10.69 (s, 2H), 9.70 (s, 2H), 9.57 (s, 2H),



9.01 (s, 2H), 8.76 (d, $J = 7.7$ Hz, 2H), 8.55 (d, $J = 7.6$ Hz, 2H), 8.34 (d, $J = 7.2$ Hz, 4H), 7.79 (d, $J = 7.6$ Hz, 4H), 2.77 (s, 6H), -4.19 (s, 2H). ^{19}F NMR (377 MHz, DMSO- d_6) δ -147.62. ^{11}B NMR (128 MHz, DMSO- d_6) δ -12.54. HRMS: calcd. for $\text{C}_{50}\text{H}_{43}\text{BF}_2\text{N}_6\text{O}_6$ $[\text{M} + \text{H}]^+$ 872.3308; found 872.3292.

Compound 5: To the mixture of triethylamine (0.50 ml, 0.458 mmol), 4-dimethylaminopyridine (1.4 mg, 0.011 mmol) and compound **1** (20 mg, 0.023 mmol) in dichloromethane at 0 °C under inert atmosphere, acetic anhydride (0.23 ml, 0.229 mmol) was added dropwise and stirred for 2 hours. After completion of reaction, the reaction mixture was quenched with 1N NaOH and compound was extracted with CH_2Cl_2 (2×20 mL). The combined organic layers were dried over anhydrous Na_2SO_4 and solvent was evaporated to obtain crude product as green solid. The crude product was further purified by silica gel column chromatography (50% CH_2Cl_2 /petroleum ether) to obtain compound **5** as green solid (18.0



mg, yield: 75%). ^1H NMR (500 MHz, CDCl_3) δ 10.35 (d, $J = 4.4$ Hz, 2H), 10.25 (dd, $J = 4.5$, 2.0 Hz, 2H), 9.60 (d, $J = 4.4$ Hz, 2H), 9.50 (s, 2H), 9.03 (dd, $J = 4.5$, 1.8 Hz, 2H), 8.72 (d, $J = 8.0$ Hz, 2H), 8.36 (d, $J = 7.9$ Hz, 2H), 8.30 (d, $J = 7.5$ Hz, 4H), 7.70 (d, $J = 7.5$ Hz, 4H), 6.92 (t, $J = 5.9$ Hz, 1H), 6.29 (d, $J = 3.6$ Hz, 1H), 5.69 (d, $J = 8.9$ Hz, 1H), 5.41 – 5.35 (m, 1H), 5.31 – 5.24 (m, 1H), 4.59 (ddd, $J = 10.7$, 8.9, 3.7 Hz, 1H), 4.19 (ddd, $J = 9.6$, 6.1, 2.7 Hz, 1H), 4.05 (ddd, $J = 14.2$, 6.4, 2.8 Hz, 1H), 3.86 – 3.72 (m, 1H), 2.80 (s, 6H), 2.29 (s, 3H), 2.25 (s, 3H), 2.13 (s, 3H), 2.00 (s, 3H), -3.95 (t, $J = 5.7$ Hz, 1H). ^{19}F NMR (471 MHz, CDCl_3) δ -149.30. ^{11}B NMR (160 MHz, CDCl_3) δ -12.26. ^{13}C NMR (126 MHz, CDCl_3) δ 172.0, 170.3, 169.9, 169.1, 167.9, 150.0, 142.9, 139.7, 138.1, 135.2, 134.4, 133.6, 131.6, 130.8, 130.7, 129.9, 129.6, 128.9, 128.4, 127.6, 127.1, 125.6, 125.1, 124.2, 123.9, 122.3, 121.0, 120.5, 117.4, 107.2, 91.0, 70.9, 70.9, 70.8, 70.7, 69.3, 68.8, 63.7, 51.6, 39.8, 29.8, 29.5, 23.3, 22.8, 21.8, 21.2, 21.1, 21.0, 20.9, 14.3. HRMS: calcd. for $\text{C}_{58}\text{H}_{51}\text{BF}_2\text{N}_6\text{O}_{10}$ $[\text{M} + \text{H}]^+$ 1040.3732; found 1040.3709.

4.4.2 In vitro

Mouse fibroblast cells (L929) and human breast cancer cell line, MDA MB 231 were procured from National Centre for Cell Sciences, Pune, India. Phosphate buffer saline (PBS), antibiotic-antimycotic solution, Dulbecco's Modified Eagle Medium (DMEM), and fetal bovine serum (FBS) were purchased from HiMedia Laboratories Pvt. Ltd India.

Cell Culture: DMEM supplemented with 10% v/v FBS and 1% v/v antibiotic-antimycotic solution was used for culturing and maintaining L929 and MDA MB 231 cells. The cells were incubated at 37 °C and 5% CO₂ during culture and experimentation.

Biocompatibility Study: *In vitro* biocompatibility assessment of Compound **1** was carried out in L929 cells. Briefly, L929 cells were seeded in a 96 well plate at a density of ~ 6000 cells/well and were incubated for 24 h to adhere and attain morphology. Compound **1** dissolved in DMSO, was diluted in complete media to attain different concentrations in the range 10 to 150 µg/mL. Further, the media was replaced with varying concentrations of compound **1**, positive control (PC) being 1% Triton X-100, negative control (NC) being complete media. The cells were incubated for 24 hours, the contents of wells removed, washed with PBS, followed by addition of alamar blue at a concentration of 10 µg/well. The cells were incubated for 4 h, followed by recording the fluorescence with excitation and emission wavelengths being 560 and 590 nm respectively (TECAN Infinite 200 Pro series). Percentage cell viability was calculated based on the following equation

$$\text{Cell viability (\%)} = \frac{\text{Intensity of treated sample}}{\text{Intensity of negative control}} \times 100$$

Cellular uptake by confocal laser scanning microscopy (CLSM)

CLSM was performed to evaluate the cellular uptake in L929 and MDA MB 231 cells. Briefly, the cells were seeded on sterile coverslips in a 12-well plate at a density of 25000 cells/well and incubated for 24 hours. Compound **1** dissolved in DMSO was diluted appropriately and added to each well such that the final amount of compound in each well is 10 µg/well. The cells were incubated for 24 h, followed by careful washing with PBS and fixation. The fixation was carried out with 4% paraformaldehyde (15 min) at room temperature, followed by PBS wash. CLSM imaging (Olympus (IX 81) & Fluoview 500 and LEICA TCS SP8) was performed on fixed cells by using 488 nm excitation and 680-740 nm emission filter respectively.

DAPI staining: The fixed cells were stained with DAPI (10 µg/well) for 30 seconds and thoroughly washed with PBS. CLSM imaging was performed on fixed cells using 405 nm excitation and 410-454 nm emission filter for DAPI channel; 458 nm excitation and 680-732 nm emission filter for fluorescence channel of compound **1**.

4.5 References:

1. Kobayashi, H.; Ogawa, M.; Alford, R.; Choyke, P. L.; Urano, Y., New Strategies for Fluorescent Probe Design in Medical Diagnostic Imaging. *Chem. Rev.* **2010**, *110*, 2620-2640.
2. Tang, B.; Yu, F.; Li, P.; Tong, L.; Duan, X.; Xie, T.; Wang, X., A Near-Infrared Neutral pH Fluorescent Probe for Monitoring Minor pH Changes: Imaging in Living HepG2 and HL-7702 Cells. *J. Am. Chem. Soc.* **2009**, *131*, 3016-3023.
3. Fischer, G. M.; Isomäki-Krondahl, M.; Göttker-Schnetmann, I.; Daltrozzi, E.; Zumbusch, A., Pyrrolopyrrole Cyanine Dyes: A New Class of Near-Infrared Dyes and Fluorophores. *Chem. Eur. J.* **2009**, *15*, 4857-4864.
4. Pham, W.; Cassell, L.; Gillman, A.; Koktysh, D.; Gore, J. C., A near-infrared dye for multichannel imaging. *Chem. Commun.* **2008**, 1895-1897.
5. Fu, N.; Gassensmith, J. J.; Smith, B. D., Effect of Stopper Size on Squaraine Rotaxane Stability. *Supramol. Chem.* **2009**, *21*, 118-124.
6. Umezawa, K.; Citterio, D.; Suzuki, K., Water-soluble NIR Fluorescent Probes Based on Squaraine and Their Application for Protein Labeling. *Anal. Sci.* **2008**, *24*, 213-217.
7. Johnson, J. R.; Fu, N.; Arunkumar, E.; Leevy, W. M.; Gammon, S. T.; Piwnica-Worms, D.; Smith, B. D., Squaraine rotaxanes: superior substitutes for Cy-5 in molecular probes for near-infrared fluorescence cell imaging. *Angew. Chem. Int. Ed.* **2007**, *46*, 5528-5531.
8. Arunkumar, E.; Forbes, C. C.; Noll, B. C.; Smith, B. D., Squaraine-Derived Rotaxanes: Sterically Protected Fluorescent Near-IR Dyes. *J. Am. Chem. Soc.* **2005**, *127*, 3288-3289.
9. Umezawa, K.; Matsui, A.; Nakamura, Y.; Citterio, D.; Suzuki, K., Bright, Color-Tunable Fluorescent Dyes in the Vis/NIR Region: Establishment of New "Tailor-Made" Multicolor Fluorophores Based on Borondipyrromethene. *Chem. Eur. J.* **2009**, *15*, 1096-1106.
10. Umezawa, K.; Nakamura, Y.; Makino, H.; Citterio, D.; Suzuki, K., Bright, Color-Tunable Fluorescent Dyes in the Visible–Near-Infrared Region. *J. Am. Chem. Soc.* **2008**, *130*, 1550-1551.
11. Loudet, A.; Bandichhor, R.; Burgess, K.; Palma, A.; McDonnell, S. O.; Hall, M. J.; O'Shea, D. F., B,O-Chelated Azadipyrromethenes as Near-IR Probes. *Org. Lett.* **2008**, *10*, 4771-4774.
12. Meek, S. T.; Nesterov, E. E.; Swager, T. M., Near-Infrared Fluorophores Containing Benzo[c]heterocycle Subunits. *Org. Lett.* **2008**, *10*, 2991-2993.

13. Nesterov, E. E.; Skoch, J.; Hyman, B. T.; Klunk, W. E.; Bacskai, B. J.; Swager, T. M., In Vivo Optical Imaging of Amyloid Aggregates in Brain: Design of Fluorescent Markers. *Angew. Chem. Int. Ed.* **2005**, *44*, 5452-5456.
14. Yang, Y.; Lowry, M.; Xu, X.; Escobedo, J. O.; Sibrian-Vazquez, M.; Wong, L.; Schowalter, C. M.; Jensen, T. J.; Fronczek, F. R.; Warner, I. M.; Strongin, R. M., Seminaphthofluorones are a family of water-soluble, low molecular weight, NIR-emitting fluorophores. *Proc. Natl. Acad. Sci. U.S.A* **2008**, *105*, 8829.
15. Nesterova, I. V.; Erdem, S. S.; Pakhomov, S.; Hammer, R. P.; Soper, S. A., Phthalocyanine Dimerization-Based Molecular Beacons Using Near-IR Fluorescence. *J. Am. Chem. Soc.* **2009**, *131*, 2432-2433.
16. Kuimova, M. K.; Collins, H. A.; Balaz, M.; Dahlstedt, E.; Levitt, J. A.; Sergent, N.; Suhling, K.; Drobizhev, M.; Makarov, N. S.; Rebane, A.; Anderson, H. L.; Phillips, D., Photophysical properties and intracellular imaging of water-soluble porphyrin dimers for two-photon excited photodynamic therapy. *Org. Biomol. Chem.* **2009**, *7*, 889-896.
17. Kee, H. L.; Nothdurft, R.; Muthiah, C.; Diers, J. R.; Fan, D.; Ptaszek, M.; Bocian, D. F.; Lindsey, J. S.; Culver, J. P.; Holten, D., Examination of chlorin-bacteriochlorin energy-transfer dyads as prototypes for near-infrared molecular imaging probes. *Photochem. Photobiol.* **2008**, *84*, 1061-1072.
18. Nesterova, I. V.; Verdree, V. T.; Pakhomov, S.; Strickler, K. L.; Allen, M. W.; Hammer, R. P.; Soper, S. A., Metallo-Phthalocyanine Near-IR Fluorophores: Oligonucleotide Conjugates and Their Applications in PCR Assays. *Bioconjugate Chem.* **2007**, *18*, 2159-2168.
19. Xie, D.; Liu, Y.; Rao, Y.; Kim, G.; Zhou, M.; Yu, D.; Xu, L.; Yin, B.; Liu, S.; Tanaka, T.; Aratani, N.; Osuka, A.; Liu, Q.; Kim, D.; Song, J., meso-Triaryl-Substituted Smaragdyrins: Facile Aromaticity Switching. *J. Am. Chem. Soc.* **2018**, *140*, 16553-16559.
20. Chatterjee, T.; Srinivasan, A.; Ravikanth, M.; Chandrashekar, T. K., Smaragdyrins and Sapphyrins Analogues. *Chem. Rev.* **2017**, *117*, 3329-3376.
21. Pareek, Y.; Ravikanth, M.; Chandrashekar, T. K., Smaragdyrins: emeralds of expanded porphyrin family. *Acc. Chem. Res.* **2012**, *45*, 1801-16.
22. Narayanan, S. J.; Sridevi, B.; Chandrashekar, T. K.; Englich, U.; Ruhlandt-Senge, K., Core-Modified Smaragdyrins: First Examples of Stable Meso-Substituted Expanded Corrole. *Org. Lett.* **1999**, *1*, 587-590.
23. Rajeswara Rao, M.; Ravikanth, M., Boron complexes of oxasmaragdyrin, a core-modified expanded porphyrin. *J. Org. Chem.* **2011**, *76*, 3582-7.

24. Laxman, K.; Ravikanth, M., Synthesis of Oxasmaragdyrin-Amino Acid Conjugates. *Eur. J. Org. Chem.* **2017**, 2017, 5884-5891.
25. Ghadiri, M.; Vasheghani-Farahani, E.; Atyabi, F.; Kobarfard, F.; Mohamadyar-Toupkanlou, F.; Hosseinkhani, H., Transferrin-conjugated magnetic dextran-spermine nanoparticles for targeted drug transport across blood-brain barrier. *J. Biomed. Mater. Res. A* **2017**, 105, 2851-2864.
26. Lee, J. H.; Sahu, A.; Jang, C.; Tae, G., The effect of ligand density on in vivo tumor targeting of nanographene oxide. *J. Controlled Release* **2015**, 209, 219-228.
27. Gawde, K. A.; Sau, S.; Tatiparti, K.; Kashaw, S. K.; Mehrmohammadi, M.; Azmi, A. S.; Iyer, A. K., Paclitaxel and di-fluorinated curcumin loaded in albumin nanoparticles for targeted synergistic combination therapy of ovarian and cervical cancers. *Colloids Surf. B. Biointerfaces* **2018**, 167, 8-19.
28. Ren, W. X.; Han, J.; Uhm, S.; Jang, Y. J.; Kang, C.; Kim, J.-H.; Kim, J. S., Recent development of biotin conjugation in biological imaging, sensing, and target delivery. *Chem. Commun.* **2015**, 51, 10403-10418.
29. Tripodo, G.; Trapani, A.; Torre, M. L.; Giammona, G.; Trapani, G.; Mandracchia, D., Hyaluronic acid and its derivatives in drug delivery and imaging: Recent advances and challenges. *Eur. J. Pharm. Biopharm.* **2015**, 97, 400-416.
30. Pawar, S.; Shevalkar, G.; Vavia, P., Glucosamine-anchored doxorubicin-loaded targeted nano-niosomes: pharmacokinetic, toxicity and pharmacodynamic evaluation. *J. Drug Targeting* **2016**, 24, 730-743.
31. Glunde, K.; Foss, C. A.; Takagi, T.; Wildes, F.; Bhujwalla, Z. M., Synthesis of 6'-O-Lissamine-rhodamine B-Glucosamine as a Novel Probe for Fluorescence Imaging of Lysosomes in Breast Tumors. *Bioconjugate Chem.* **2005**, 16, 843-851.
32. Li, C.; Greenwood, T. R.; Bhujwalla, Z. M.; Glunde, K., Synthesis and Characterization of Glucosamine-Bound Near-Infrared Probes for Optical Imaging. *Org. Lett.* **2006**, 8, 3623-3626.
33. Mane, S. B.; Hu, J.-Y.; Chang, Y.-C.; Luo, L.; Diau, E. W.-G.; Hung, C.-H., Novel expanded porphyrin sensitized solar cells using boryl oxasmaragdyrin as the sensitizer. *Chem. Commun.* **2013**, 49, 6882-6884.

Chapter 5

*L,L-Diphenylalanine Conjugated BF₂-oxasmaragdyrin Self-Assemblies
as NIR Photothermal Therapeutic Agents for Cancer Therapy*

5.1 Introduction:

There is a rapid increase in the incidence of cancer and the associated mortalities worldwide. Cancer remains to be the second most leading cause for mortalities, placed only next to noncommunicable diseases, and it remains to be a major barrier to enhanced life expectancy globally¹. The current cancer treatment modalities are often limited to surgery, chemotherapy, radiotherapy and immunotherapy due to the heterogenous nature of cancer. These therapeutic approaches are largely associated with untoward effects and thus fuelling researchers to search for alternatives². One such promising and widely studied approach is photothermal therapy (PTT). PTT remains to be an exciting strategy owing to its minimal invasiveness, ease of operation, rapid treatment and quick recovery³. The success of PTT relies greatly on photothermal agents, that convert light energy to heat and the latter being utilized for tumor ablation. To date, various materials have been screened for their application in PTT and some of these include gold nanoparticles,⁴⁻⁷ graphene and graphene oxide,^{8,9} black phosphorus,^{10,11} palladium,^{12,13} copper sulphide,^{14,15} copper selenide,¹⁶ molybdenum oxide,¹⁷ etc. The non-biodegradability and long-term toxicity of inorganic materials is of grave concern. Though polymer based materials were developed and their photothermal potential was evaluated,¹⁸⁻²⁷ such materials are often encumbered with lengthy synthesis and complicated processing techniques.

To overcome these hurdles and the need to develop efficient photothermal agents has resulted in propelling research towards organic dyes, which fluoresce in the biological window (650-950 nm), where the absorption of light by biological fluids is minimal, possess excellent potential as a Near-Infrared Fluorescence (NIRF) imaging and therapeutic agent²⁸. Hence there is a growing need for dyes that can be easily prepared to absorb and emit strongly in the NIR region. To best of our knowledge, there are limited number of dyes that are fluorescent in this region, which include cyanine dyes,^{29,30} squaraine dyes,³¹⁻³⁴ BODIPY analogues,³⁵⁻³⁷ benzo[c]heterocycles,³⁸ xanthenes,³⁹ phthalocyanines, and a small selection of porphyrin derivatives.⁴⁰⁻⁴²

One such molecule which absorb and emit in NIR region is smaragdyrin which belongs to the class of expanded porphyrins. Smaragdyrins are 22 π aromatic expanded pentapyrrolic macrocycles in which the five pyrroles are connected by three meso carbons and two direct pyrrole-pyrrole bonds.⁴³ Chandrasekhar and co-workers reported the synthesis of stable *meso*-triaryl 25-oxasmaragdyrins in which one of the pyrrole ring of pentaazasmaragdyrin is replaced

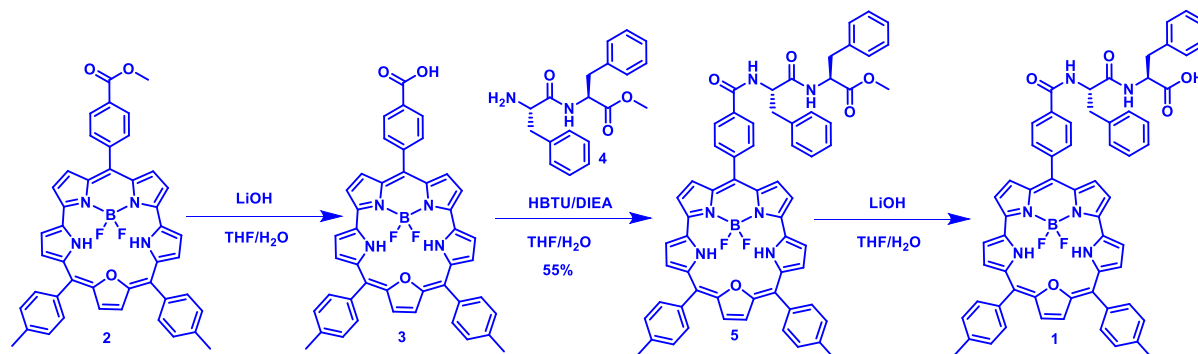
with a furan ring.^{44–46} The 25-oxasmaragdyrins absorb and emit in the Vis-NIR region with moderate quantum yields and singlet state lifetimes. Recently our group reported the synthesis of BF₂- and PO₂- complexes of 25-oxasmaragdyrins which exhibit better photophysical properties compared to that of freebase 25-oxasmaragdyrin.^{47,48}

Recent studies suggest that NIR fluorescent dyes in conjugation with self-assembling small biomolecules would be of great advantage. The simple dipeptide, diphenylalanine is known for its self-assembling properties with varying morphology.⁴⁹ Diphenylalanine in conjunction with porphyrin⁵⁰ and phthalocyanine were recently reported as anticancer agents. Herein, we report the L,L-diphenylalanine conjugated BF₂-oxasmaragdyrin self-assemblies as effective NIR photothermal therapeutic agents with good light to heat conversion with respect to that of the existing materials. *In vitro* studies revealed that the FF-BSC NPs were highly biocompatible with good cellular uptake and excellent anticancer properties under photothermal conditions. *In vivo* studies revealed that the FF-BSC NPs have excellent photothermal efficacy with a single dose intra-tumoral treatment.

5.2 Results and Discussions

5.2.1 Synthesis and characterisation

The target 25-oxasmaragdyrin-diphenylalanine conjugate **1** was prepared over a sequence of four steps as shown in Scheme 1. The starting 25-oxasmaragdyrin **2** containing *p*-carboxymethylphenyl substituent at *meso* position, was synthesized via a reported method.^{47,52} Hydrolysis of ester **2** LiOH in THF/H₂O liberated the carboxylic acid appended at the *meso* position. Compound **3** was reacted with protected L,L-diphenylalanine **4** in presence of *N,N,N',N'*-tetramethyl-*O*-(1*H*-benzotriazol-1-yl)uronium hexafluorophosphate (HBTU) and



Scheme 5.1: Synthesis of L,L-diphenylalanine conjugated BF₂-oxa-smaragdyrin (**1**).

N,N-diisopropylethylamine (DIEA) in dichloromethane under inert atmosphere for 8 hours, followed by basic alumina column chromatography to afford compound **5** as a green solid (55% yield). All intermediates were characterised by ¹H, ¹H-¹H COSY, ¹³C, ¹¹B, ¹⁹F NMR spectroscopy and High-Resolution Mass Spectrometry (HRMS). In the last step, compound **5** was hydrolysed with LiOH to afford the target compound **1** which was characterised by ¹H, ¹H-¹H COSY, ¹³C, ¹¹B, ¹⁹F NMR spectroscopy and HRMS. In compound **1**, BF₂-oxasmaragdyrin core protons appear as five signals (four doublets and one singlet) in the

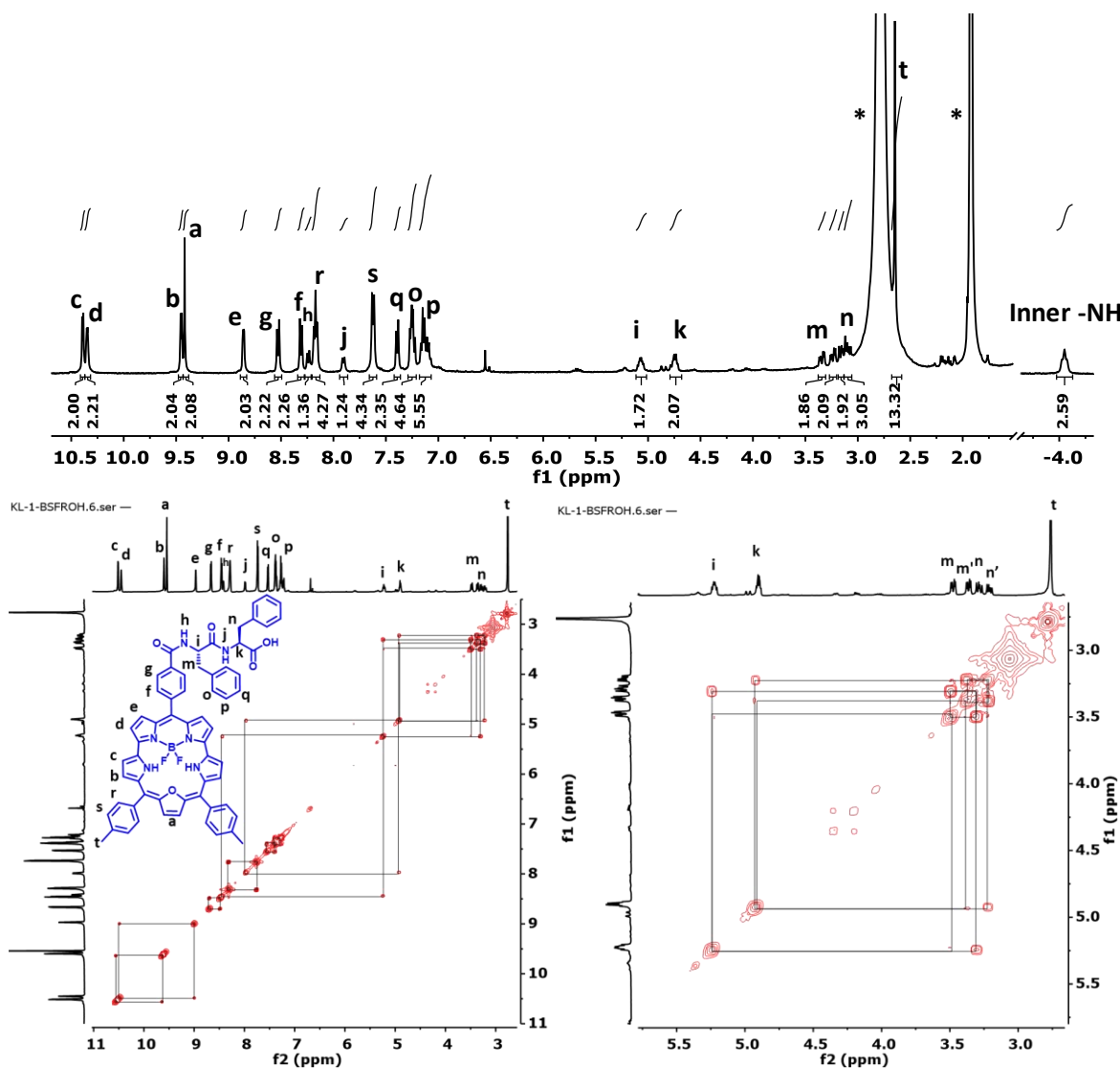


Figure 5.1: ¹H, ¹H-¹H COSY spectra of compound **1**. (* represents residual solvent peaks)

region of 8.7 -10.5 ppm hence these peaks were identified as protons *a-e* as shown in Figure 5.1. Further, Peaks 8.72, 8.36, 8.30, 7.70 ppm were identified as aryl protons *f*, *g*, *s*, *r* respectively by their integration and cross peak correlation in ¹H-¹H COSY. The proton *h* appeared at 8.42 ppm corresponding to amide NH which showed ¹H-¹H COSY correlation with

peak at 5.2 ppm assigned as proton *i*. The proton *i* showed cross peak correlation with protons *m*, *m'* which are diastereotopic protons appearing at 3.35 and 3.51 ppm which appeared as doublet of doublets. Similarly, proton *j* appeared as doublet at 7.80 ppm corresponding to amide NH which showed ^1H - ^1H COSY correlation with peak at 4.7 ppm assigned as proton *k*. The proton *k* showed cross peak correlation with protons *n*, *n'* which are diastereotopic protons appearing at 3.4 and 3.2 ppm. Thus, 1D and 2D NMR spectroscopy were very useful in deducing the molecular structure of compound **1**. A resonance at -12.8 ppm and -148.9 ppm in ^{11}B and ^{19}F NMR confirmed the presence of intact BF_2 - group of the macrocycle. Furthermore, the absorption and fluorescence spectroscopic studies showed that the compound **1** had possessed all the photophysical properties corresponding to the parent molecule **2**.

5.2.2 Formation of self-assemblies

To prepare the spherical self-assemblies, compound **1** was dissolved in different solvents such as acetonitrile, Hexafluoro-2-propanol, acetone and DMSO and was diluted with water. The solvent was removed either by evaporation or dialysis. Particles with various sizes and morphology were formed and aggregated in most of the cases. The acetone-water mixture (1:1 ratio) resulted in monodisperse nanoparticles with controlled spherical morphology (Figure 5.2). The acetone was removed from the above solution under reduced pressure and temperature 55 °C to obtain self-assembled spherical particles of compound **1** (FF-BSC NP). DLS analysis revealed that FF-BSC NP had mean hydrodynamic diameter of 152.1 ± 13.7 nm and polydispersity (PDI) of 0.09 ± 0.05 . Further, FEG-SEM and FEG-TEM analysis of FF-BSC NP revealed spherical and controlled morphology with diameter 123 ± 33 nm as shown in Figure 5.3. The nanoparticles had a zeta potential of -22 ± 5 mV. These results indicate that

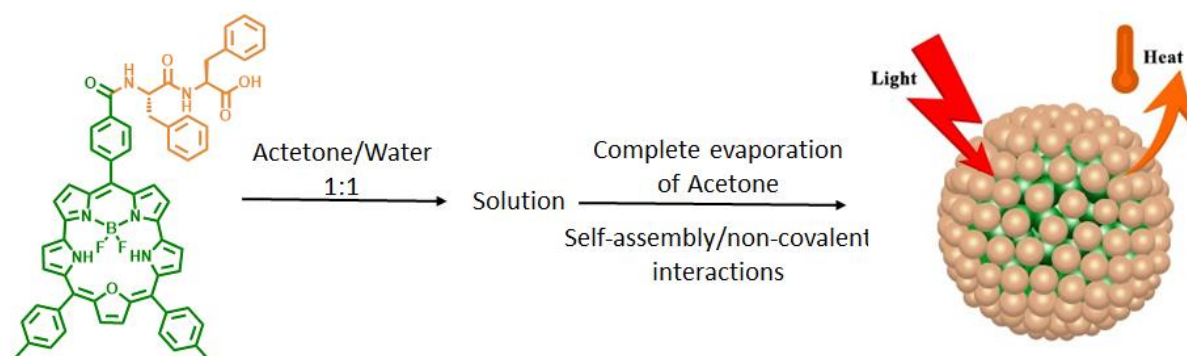


Figure 5.2: Schematic representation for the formation of L,L-diphenylalanine conjugated BF_2 -oxasmaragdyrin **1** self-assemblies (FF-BSC NP).

the FF-BSC NP were monodisperse and exhibited spherical morphology. Significant changes have been observed in absorption and fluorescence properties of compound **1** (Figure 5.3c, 5.3d) after preparation of nanoparticles. The absorption spectrum was broadened, and the corresponding absorption coefficients were reduced. Similarly, there was severe quenching of fluorescence due to aggregation induced quenching phenomena. To assess whether the nanoparticles were formed upon addition of water to the compound **1** in acetone or during the removal of acetone from the acetone/water mixture of compound **1**, the absorption and fluorescence spectra (Figure 5.3c, 5.3d) of compound **1** were analysed in acetone, acetone/water (1:1 v/v) and water (post acetone removal). It was observed that there was no change in absorption and fluorescence spectra in acetone and acetone/water mixture indicating the molecular behaviour of compound **1**. However, significant changes were observed in absorption and fluorescence spectra of compound **1** due to formation of self-assemblies upon removal of acetone from acetone/water mixture.

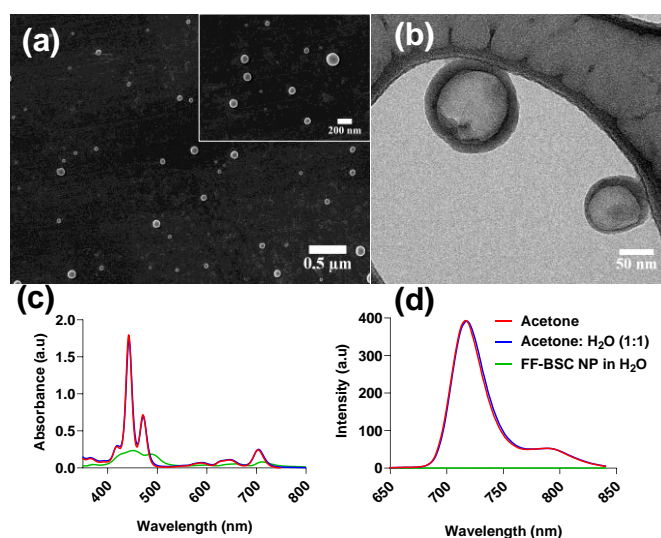


Figure 5.3: (a) FEG-SEM images of FF-BSC NP (Inset indicating the higher magnification image) (b) FEG-TEM image of self-assemblies. Absorption (c) and fluorescence (d) comparison of self-assembled particles to that of the single-molecular entities (1.6×10^{-6} M).

5.2.3 Stability studies

pH stability: The pH stability of the synthesized nanoparticles was evaluated in different pH conditions (5.5, 6.5, and 7.4). The samples were withdrawn at pre-determined intervals and the absorbance and fluorescence of samples recorded at different time points did not exhibit any changes as shown in Figure 5.4. These results indicate that the nanoparticles were not

disassembled and were stable at the studied pH conditions. Furthermore, SEM analysis of the samples post 96 h, revealed spherical morphology, indicating the stability and non-dissociation of FF-BSC NP. and an increase in mean diameter was observed (~ 30 nm) indicated the presence of spherical particles with minor increase in the mean diameter (~ 140 nm \pm 20 nm) even at 6.5 pH.

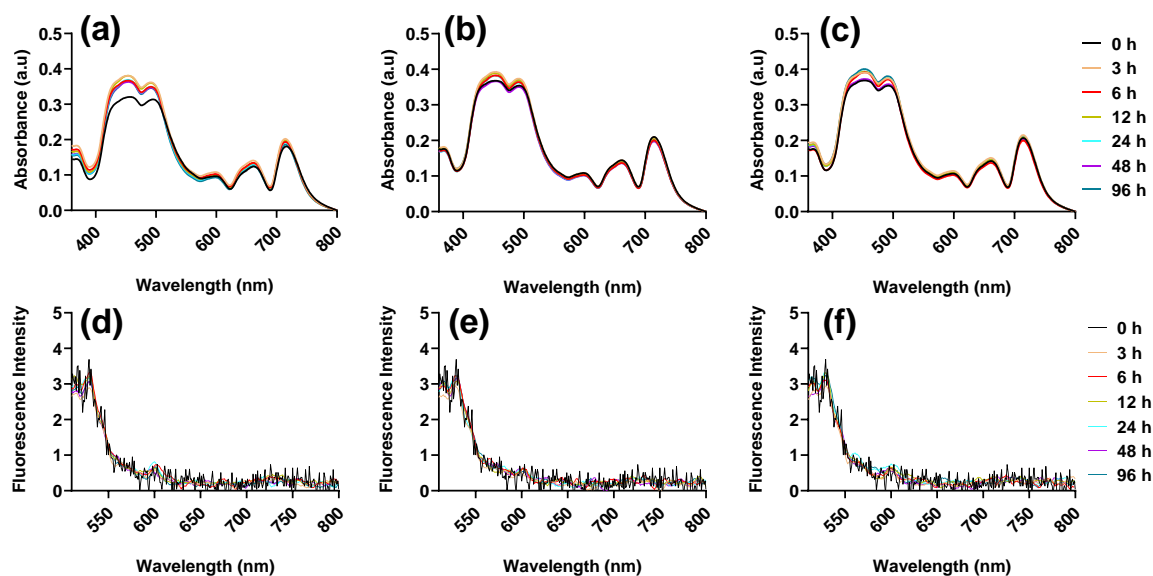


Figure 5.4: Absorbance spectrum of FF-BSC NP maintained at pH (a) 5.5, (b) 6.5, (c) 7.4; Fluorescence spectrum of FF-BSC NP maintained at pH (d) 5.5, (e) 5.6 and (f) 7.4

Lyophilization: To enhance the storage stability of FF-BSC NP, the sample was subjected to lyophilization. Three different cryoprotectants (sucrose, mannose and trehalose) at three different concentrations (1%, 2.5%, 5% w/w) were studied in presence/absence of poloxamer 188 (F-68). It was observed that all the samples containing cryoprotectants were readily reconstituted with milli Q, except the one without any cryoprotectant. The DLS analysis revealed that sucrose and trehalose were effective in mitigating the stress during lyophilization. This effect was more pronounced in presence of F-68, indicating the synergistic effect between the cryoprotectants and F-68⁵³, as shown in Table 5.1. Further, SEM images of sucrose and trehalose lyophilized samples revealed distinct spherical nanoparticles, whereas the sample lyophilized without any cryoprotectant depicted huge aggregates, as shown in Figure 5.5.

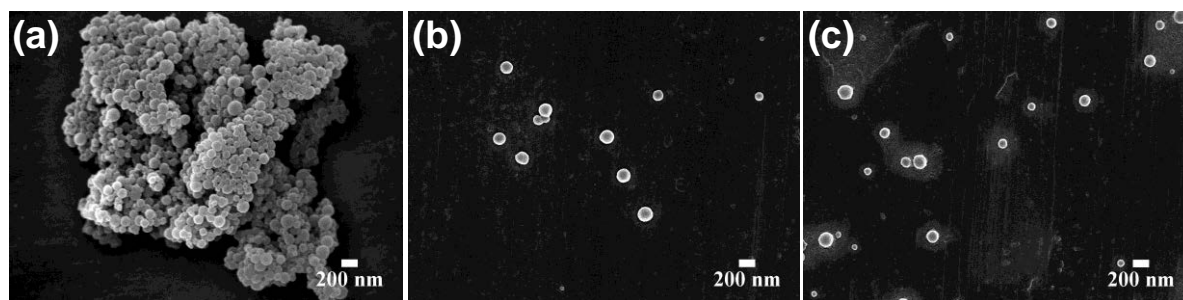


Figure 5.5: SEM images of FF-BSC NP post lyophilization (a) without cryoprotectant (b) F-68 (0.5%) + sucrose (1%) and (c) F-68 (0.5%) + trehalose (1%).

Table 5.1: Mean hydrodynamic diameter (mean HDD) and PDI of FF-BSN NP post lyophilization with various cryoprotectants

S. No	Sample details	Mean HDD (nm)	PDI
1	Before Lyophilization	152.10 ± 13.70	0.09 ± 0.05
2	No cryoprotectant	1415.0	0.707
3	Mannitol 1%	254.7	0.382
4	Mannitol 2.5%	278.4	0.401
5	Mannitol 5%	220.2	0.540
6	Sucrose 1%	428.2	0.782
7	Sucrose 2.5%	314.8	0.235
8	Sucrose 5%	165.5	0.075
9	Trehalose 1%	425.2	0.362
10	Trehalose 2.5%	323	0.251
11	Trehalose 5%	152.3	0.071
12	Pluronic F-68	294.8	0.279
13	F-68 0.5% + Mannitol 1%	171.7	0.382
14	F-68 0.5% + Mannitol 2.5%	237.4	0.404
15	F-68 0.5% + Mannitol 5%	163.9	0.233
16	F-68 0.5% + Sucrose 1%	162.2	0.071
17	F-68 0.5% + Sucrose 2.5%	162.4	0.029
18	F-68 0.5% + Sucrose 5%	167.7	0.024
19	F-68 0.5% + Trehalose 1%	178.4	0.127
20	F-68 0.5% + Trehalose 2.5%	175.7	0.099
21	F-68 0.5% + Trehalose 5%	172.4	0.099

5.2.4 Photo-thermal transduction studies

Photo-thermal transduction: The FF-BSC NP exhibited photo-thermal properties upon irradiation with 750 nm laser. Photo-thermal transduction potential of the nanoparticles was evaluated by constructing central composite design (CCD) with three independent variables, concentration of sample, laser power, and laser irradiation time as OFAT (one factor at a time) approach doesn't necessarily provide the vital interaction among the factors, whereas the same

can be evaluated with CCD. The design layout along with the response is provided in Table 5.2. Quadratic model was selected, based on the p-value of sequential sum of squares and the ANOVA of the selected model revealed the model significant and lack of fit insignificant, as shown in Table 5.4. Further, the diagnostic plots for the selected model did not reveal any abnormalities and the coded equation for the model is provided below.

$$Y = +54.21 + 3.65A + 5.64B + 6.02C + 0.35AB + 0.97AC + 1.87BC + 2.51A^2 - 3.12B^2 + 0.98C^2$$

Where A, B, C and Y represents concentration of sample, laser irradiation time, power of laser irradiation, and temperature respectively. Positive and negative sign indicates synergistic and

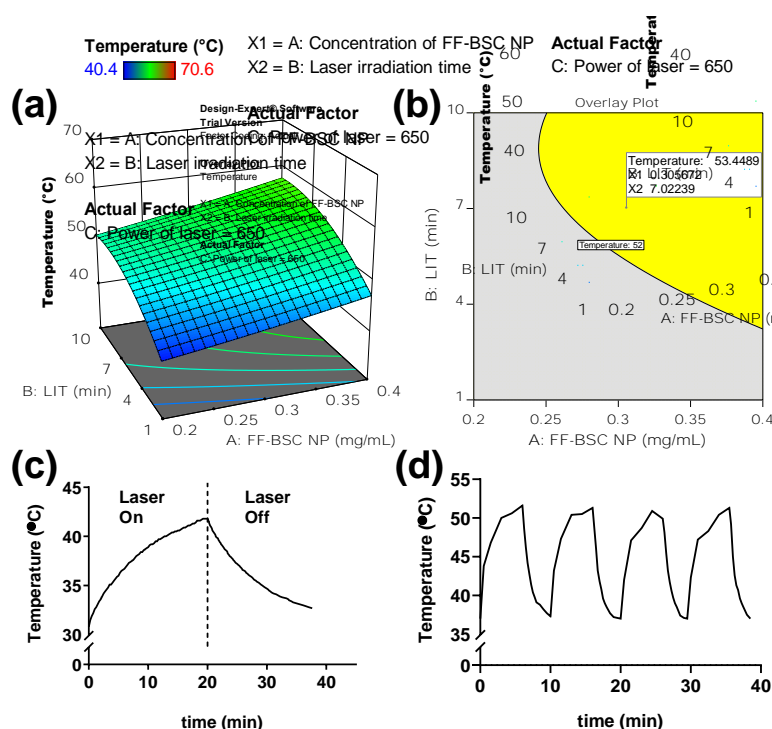


Figure 5.6: (a) 3D plot and (b) Design space for the response, temperature evaluated with CCD; (c) time vs temperature profile of FF-BSC NP (d) multi-cycle temperature changes upon exposure of FF-BSC NP with 750 nm laser.

antagonistic effect on the factors respectively. Coefficients with single factor represent the effect of that factor, whereas coefficients with two factors and second-order represent the effects of interaction among those factors and quadratic nature respectively. The above equation clearly depicts that power of laser has the highest impact followed by irradiation time and concentration of sample on the photothermal transduction potential of FF-BSC NP. 3D plot was constructed by setting the laser power at 750 mW for the response, temperature. Further, numerical and graphical optimization was carried out and the parameters were selected

such the temperature outcome would be in the range 52-60°, as shown in Figure 5.6b. The design space was validated by selecting three random points and the experimental results were within the ranges of predicted ones as shown in Table 5.5. Photothermal conversion efficiency (PCE) denotes the efficacy value for FF-BSC NP in converting absorbed NIR light to heat and is related to the NIR absorption of material. The PCE of FF-BSC NP was evaluated under experimental conditions described and the PCE of FF-BSC NP was found to be 53.61%, and the time vs temperature profiling is given in Figure 5.6c. To evaluate the photo-stability and multicycle photothermal potential of FF-BSC NP, cyclic laser ON/OFF experiments were performed. It was observed that the photothermal potential of material was retained even after 4 laser ON/OFF cycles and the temperature increment was same as that of the first cycle, as shown in Figure 5.6d. Further, absorption and fluorescence spectra did not reveal any changes indicating the stability of the nanomaterial. This is particularly important, as most of the commercially available dyes, including indocyanine green are extremely sensitive to light⁵⁴. The excellent photothermal properties, coupled with high conversion efficiency and excellent photo-stability makes FF-BSC NP an ideal candidate for PTT.

5.2.5 *In vitro*

Biocompatibility: The biocompatibility of a material is one of the most important criteria for any biomaterial and the *in vitro* biocompatibility of FF-BSC NP was carried out in L929 cells. The viable cells convert non-fluorescent blue coloured resazurin to fluorescent red-coloured resorufin and evaluating the intensity of later be used for estimating the % cell viability. It was observed that the FF-BSC NP possessed excellent biocompatibility and the material was

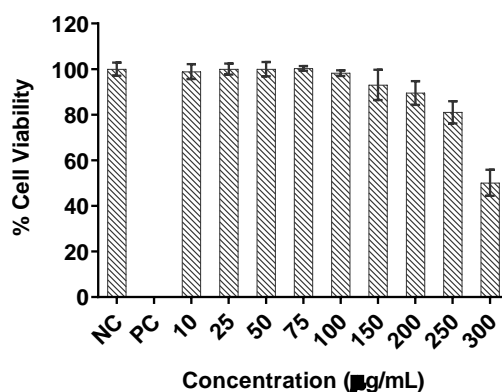


Figure 5.7: *In vitro* biocompatibility of FF-BSC NP in L929 cells

biocompatible up to a concentration of 250 µg/mL, as shown in Figure 5.7.

Cellular uptake: The cellular uptake of FF-BSC NP in 4T1 cells was evaluated with FACS. Flow cytometry enables the evaluation of intensity of fluorescence in cells, thereby providing the fraction of cells with the nanoparticles. The shift in the median of fluorescence peak at various time points in comparison to the negative control indicates the uptake of particles. It can be clearly observed that there is a shift in the median value with increase in incubation time as shown in Figure 5.8a. Further, after 24 hours, internalization was found to be almost 100% in comparison to the control cells.

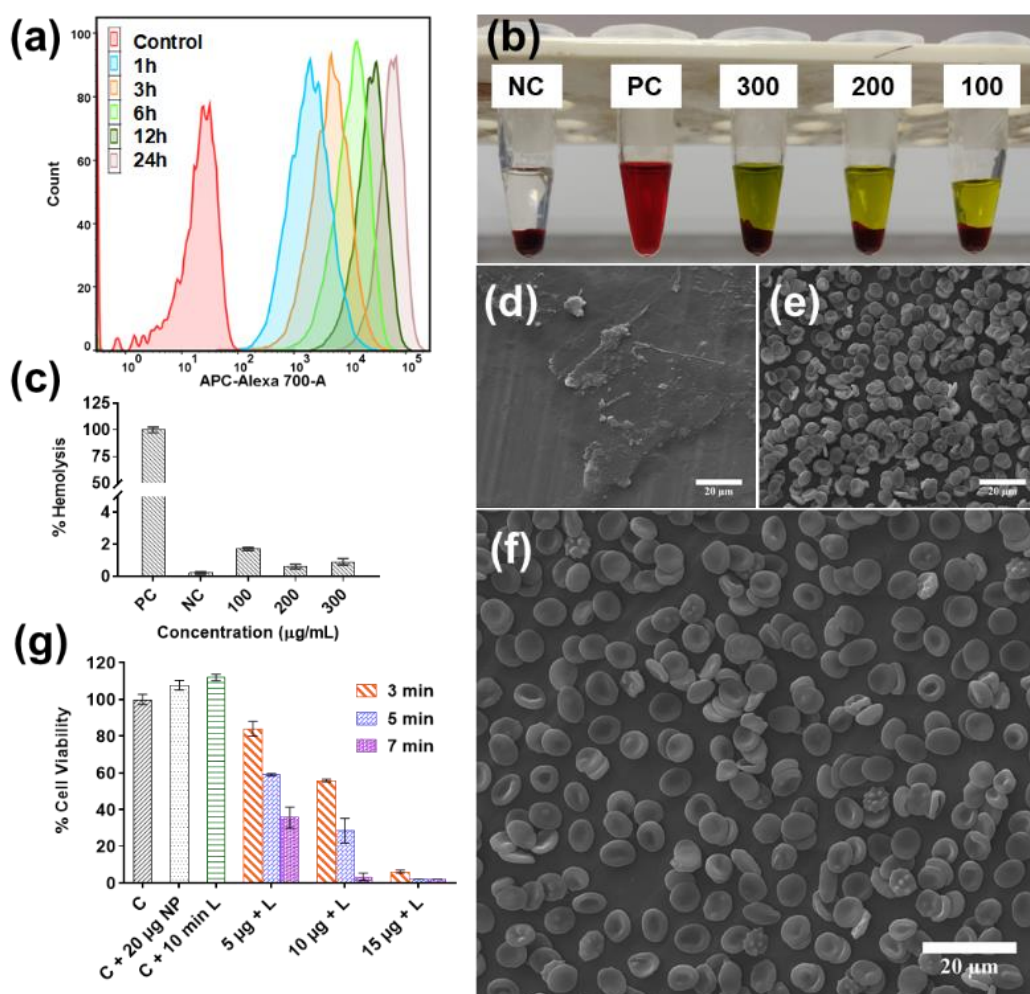


Figure 5.8: (a) uptake of FF-BSC NP in 4T1 cells, (b) digital image of various samples of hemocompatibility study, (c) graph depicting the hemocompatibility study of FF-BSC NP, ESEM images of RBC treated with (d) positive control (triton X-100), (e) negative control (PBS), (f) 300 µg/mL FF-BSC NP, (g) *in vitro* photothermal efficacy in 4T1 cells.

***In vitro* photothermal efficacy:** The *in vitro* photothermal efficacy testing was carried out in 4T1 cells revealed that the material is highly efficient. From the graph it is evident that the cell viability in sample exposed to NIR laser for 7 min with 10µg/well was <5%, whereas the cells

exposed to material and laser alone did not exhibit changes in cell viability. The further increase in FF-BSC NP concentration is quite effective even at lower laser exposure levels, as shown in Figure 5.8g.

Hemocompatibility study: The intended nano-particulate formulation, FF-BSC NP is bound to encounter blood upon intravenous administration, and hemocompatibility is an absolute requirement. Hemo-incompatibility is often influenced by the physicochemical properties of material i.e. size, shape, charge and shape.^{55,56} RBCs treated with varying concentrations of FF-BSC NP did not exhibit hemolysis and the % hemolysis was well below 5%. The sample treated with Triton X-100, resulted in complete hemolysis and no RBC pellet was observed as shown in Figure 5.8b-c. Further, ESEM analysis of FF-BSC NP treated samples revealed that the morphology of RBCs was intact, and no significant difference was observed (Figure 5.8d-f).

5.2.6 *In vivo* studies

Biodistribution and Toxicity Testing: An understanding of the *in vivo* biodistribution of an external agent like nanoparticles is a prerequisite to assess its pharmacodynamics and associated adverse effects. 14 days post intravenous administration of FF-BSC NP, *ex vivo* fluorescence imaging of the vital organs reveal that the majority of the nanoparticles were accumulated in the liver, lung and spleen, followed by kidney and heart suggesting that the major portion of the injected material is taken up by the components of the reticuloendothelial system in the body. Accumulation of a portion of injected material in the kidney also suggest the possibility of renal clearance.

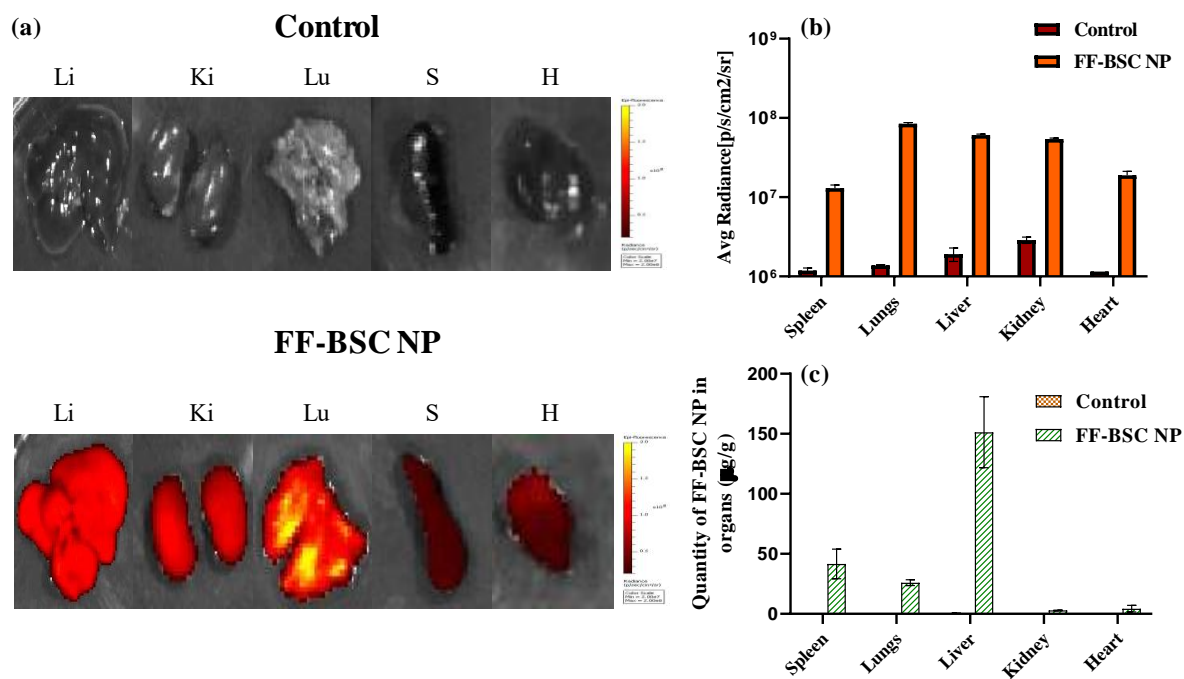


Figure 5.9: (a) *Ex vivo* fluorescence imaging of different vital organs collected from control and FF-BSC NP injected mice on day 14 post material injection (b) Qualitative evaluation of fluorescence output from organ samples of spleen, lungs, liver, kidney and heart from control and treated mice (c) Quantitative estimation of FF-BSC NP from organ samples of spleen, lungs, liver, kidney and heart from control and treated mice.

In vivo photothermal efficacy: The photothermal efficacy testing of FF-BSC NP revealed that the material possesses excellent efficacy *in vivo*. It was observed that there was a dramatic reduction in bioluminescence signal post PTT, indicative of drastic tumor ablation further associated with no signs of weight loss post PTT suggesting no therapy burden. However, the bioluminescence signal of control as well the material control groups showed continuous increase, indicating the non-toxic nature of material and progressive tumor growth. The control groups as well as material control group showed signs of necrosis at day 5, beyond which no further imaging was carried for these animals owing to the ethical concerns and the mice were sacrificed. Treated animals were followed till day 30 post treatment and showed no increase in the bioluminescence signal (signal was equivalent to the background) highlighting effective and complete tumor ablation with no signs of relapse post PTT prolonging the overall survival of the treated mice.

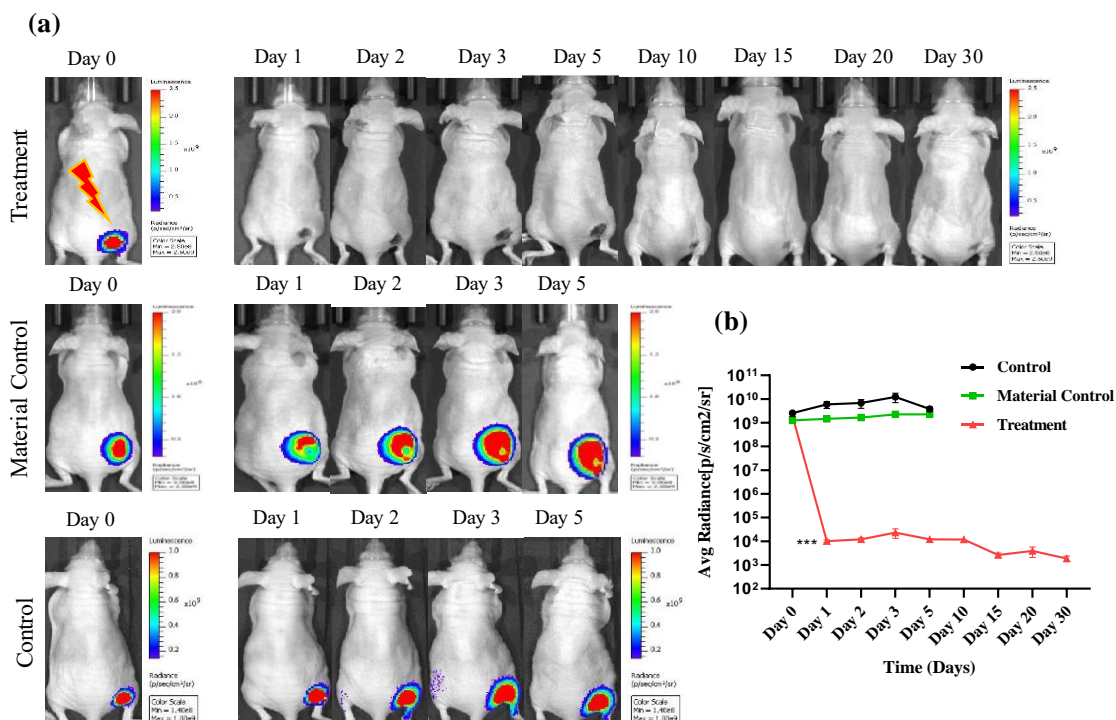


Figure 5.10: *In vivo* photothermal ablation by FF-BSC NP in 4T1 xenograft mouse model: (a) representative *in vivo* bioluminescence images of various treatment groups, (b) quantitative assessment of bioluminescence signal for different groups during the follow-up (***) indicates $P = 0.001$ post third treatment)

5.3 Conclusions

We have successfully synthesised diphenylalanine conjugated BF₂-oxasmaragdyrin and self-assembled into spherical nanoparticles. These self-assemblies have shown excellent photothermal properties when irradiated with 750 nm laser with a photothermal efficacy of 53.61%. *In vitro* studies showed that FF-BSC NP are biocompatible and easily internalised into 4T1 cells within 24 hours. Furthermore, FF-BSC NP showed excellent photothermal efficacy in *in vitro* as well as *in vivo* model for cancer therapy.

5.4 Experimental

All chemicals were used as received unless otherwise noted. All solvents were of at least reagent grade or higher and dried if necessary. The ¹H, ¹¹B, ¹⁹F and ¹³C NMR spectra were recorded in CDCl₃ on Bruker 400 or 500 MHz instrument. The frequency of 101 MHz is used for ¹³C nucleus. Tetramethylsilane [Si(CH₃)₄] was used as an internal standard for ¹H and ¹³C NMR spectra acquisition. Absorption and steady state fluorescence spectra were obtained with Cary series UV-Vis-NIR spectrophotometer and Varian-Cary Eclipse spectrofluorometer.

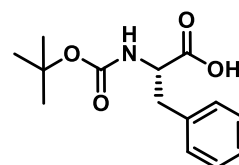
respectively. The fluorescence quantum yield (Φ_f) were estimated from emission and absorption spectra by comparative method at the excitation wavelength of 440 nm using H₂TPP ($\Phi_f = 0.11$) as the standard.⁵⁷ Cyclic voltammetric studies were carried out with BAS electrochemical system utilizing the three electrode configuration consisting of Glassy carbon (working electrode), platinum wire (auxillary electrode) and saturated calomel (reference electrode) electrodes. The experiments were done in dry CH₂Cl₂ using 0.1 M tetrabutylammonium perchlorate (TBAP) as the supporting electrolyte. All the solutions were purged prior to collection of electrochemical and spectral measurements with argon gas. The high resolution mass spectra (HRMS) were recorded with a Bruker maxis Impact and Q-Tof micro mass spectrometer. For UV-vis and fluorescence titrations, the stock solution of all compounds (1×10^{-3} M) were prepared using HPLC grade chloroform solvent. SEM analysis was carried out using a JEOL JSM-7600F Schottky Field Emission Scanning Electron Microscope. TEM analysis was performed using JEOL FEGTEM 200kV.

Material characterization

The mean hydrodynamic diameter was evaluated with Zetasizer Nano ZS (Malvern Instruments, United Kingdom). Zeta potential of material was evaluated with Anton Paar Litesizer™ 500. The UV-Vis and fluorescence spectra were recorded with Perkin Elmer spectrophotometer (Lambda 25, USA) and Agilent's Cary 5000 UV-Vis-NIR spectrophotometer respectively. Field emission gun scanning electron microscope (FEG-SEM, JSM-7600F, Jeol Ltd., Japan) and field emission gun transmission electron microscope (FEG-TEM, JEM-1400 and JSM-2100F, Jeol Ltd., Japan) were employed for morphology characterization. Nuclear magnetic resonance (NMR) was recorded with Bruker 400 and 500 MHz instruments. Environmental scanning electron microscopy (ESEM, Quanta 200, FEI, Austria) was used for observing the morphology of red blood cells (RBCs).

Synthesis of *N*-*tert*-butyl-*L*-phenyl alanine:

Di-*tert*-butyl dicarbonate (0.68 mL, 3 mmol) was added dropwise to a ice cold suspension of *L*-phenyl alanine (0.165 g, 1 mmol), K₂CO₃ (0.28g, 2 mmol) was suspended in 50 mL of dioxane-water (1:1 v/v) until a clear solution is formed. The reaction mixture was stirred overnight at room



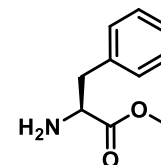
temperature. After completion of reaction, the reaction mixture was extracted with ethylacetate (3 x 50 ml). Combined organic layers were dried on anhydrous Na₂SO₄ and rotary evaporated to give *N*-*tert*-butyl-*L*-phenyl alanine as colourless solid. (200 mg, 75% yield). ¹H NMR (400

MHz, DMSO-*d*₆) δ 7.37 – 7.15 (m, 5H), 7.05 (d, *J* = 8.4 Hz, 1H), 4.16 – 4.02 (m, 1H), 3.01 (dd, *J* = 13.8, 4.6 Hz, 1H), 2.82 (dd, *J* = 13.8, 10.2 Hz, 1H), 1.31 (s, 9H). ¹³C NMR (101 MHz, DMSO-*d*₆) δ 174.0, 155.8, 138.4, 129.5, 128.5, 126.7, 78.5, 55.5, 36.9, 28.6.

L-Phenylalanine Methyl ester:

L-phenylalanine (0.5 g, 3.0 mmol) was dissolved in MeOH (50 mL) and SOCl₂ (2 ml) was added dropwise at 0 °C under inert atmosphere and stirred for 6 hours.

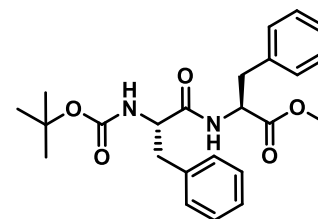
The solvent was evaporated under reduced pressure and the crude product was purified by silica gel column chromatography. (0.4 g, 73% yield) ¹H NMR (500



MHz, D₂O) δ 7.58 – 7.39 (m, 3H), 7.38 – 7.25 (m, 2H), 4.45 (dd, *J* = 7.4, 5.9 Hz, 1H), 3.85 (s, 3H), 3.36 (dd, *J* = 14.6, 5.7 Hz, 1H), 3.25 (dd, *J* = 14.6, 7.6 Hz, 1H). ¹³C NMR (126 MHz, D₂O) δ 170.0, 133.7, 129.43, 129.40, 129.29, 129.24, 128.1, 128.0, 54.1, 53.6, 35.5.

Synthesis of methyl (*tert*-butoxycarbonyl)-L-phenylalanyl-L-phenylalaninate

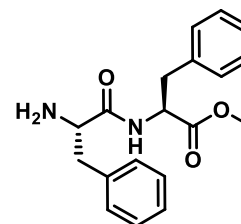
Samples of *N*-(*tert*-butoxycarbonyl)-L-phenylalanine (1.0 g, 5.58 mmol), methyl-L-phenylalaninate (1.47 g, 5.58 mmol), HBTU (2.1 g, 1.5 mmol) were dissolved in 50 ml of dry dichloromethane. To the above solution, *N,N*-diisopropylethylamine (2.3 ml, 3 mmol) was added dropwise at 0 °C under a nitrogen atmosphere. The reaction



mixture was stirred for 6 hours. The progress of the reaction was monitored by TLC which showed the development of a less polar spot correspondent with the desired product. After the completion of reaction, the mixture was diluted with 50 ml of dichloromethane and washed with 1N HCl (3 x 30 ml) followed by saturated Na₂CO₃ solution (3 x 30 ml) and water (2 x 30 ml). The organic layer was dried over Na₂SO₄, filtered and evaporated under reduced pressure to give crude product as off-white semisolid. The crude product was purified by silica gel column chromatography (1:10 EtOAc/petroleum ether) to afford pure product as a colourless solid. (1.66 g, 70% yield). ¹H NMR (400 MHz, CDCl₃) δ 7.34 – 7.24 (m, 2H), 7.27 – 7.15 (m, 6H), 6.98 (dd, *J* = 7.3, 2.2 Hz, 2H), 6.24 (d, *J* = 7.7 Hz, 1H), 4.91 (s, 1H), 4.78 (q, *J* = 6.4 Hz, 1H), 4.32 (d, *J* = 8.1 Hz, 1H), 3.67 (s, 3H), 3.16 – 2.74 (m, 4H), 1.40 (s, 9H). ¹³C NMR (101 MHz, CDCl₃) δ 171.5, 170.70, 170.69, 135.8, 129.5, 129.4, 128.8, 128.7, 127.3, 127.1, 77.4, 53.4, 52.4, 38.4, 38.1, 28.4.

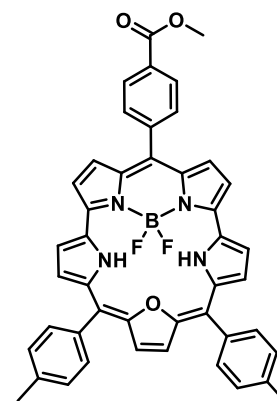
Synthesis of methyl L-phenylalanyl-L-phenylalaninate (4):

A sample of methyl (*tert*-butoxycarbonyl)-L-phenylalanyl-L-phenylalaninate (35 mg, 0.9 mmol) was stirred in mixture of trifluoroacetic acid/dichloromethane (1:1) for 30 minutes under nitrogen atmosphere at room temperature. The solvent was evaporated under reduced pressure and afforded methyl L-phenylalanyl-L-phenylalaninate **4** as colourless solid which was used without further purification.

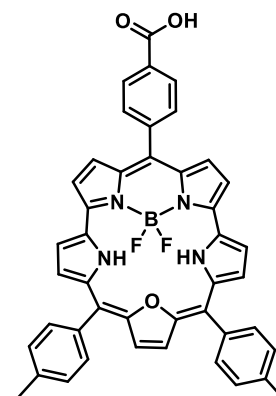
**Synthesis of *meso*-(4-carboxy methyl ester phenyl) BF₂-oxasmaragdyrin (2):**

meso-(4-carboxy methyl ester phenyl) BF₂-oxasmaragdyrin **2** was synthesized by the previously reported method.

¹H NMR (400 MHz, CDCl₃) δ 10.26 (d, *J* = 4.5 Hz, 2H), 10.17 (dd, *J* = 4.5, 2.0 Hz, 2H), 9.50 (d, *J* = 4.4 Hz, 2H), 9.44 (s, 2H), 8.96 (dd, *J* = 4.5, 1.8 Hz, 2H), 8.63 (d, *J* = 8.3 Hz, 2H), 8.57 (d, *J* = 8.3 Hz, 2H), 8.22 (d, *J* = 7.9 Hz, 4H), 7.63 (d, *J* = 7.6 Hz, 4H), 4.09 (s, 3H), 2.72 (s, 6H), -4.04 (t, *J* = 10.2 Hz, 2H). ¹³C NMR (101 MHz, CDCl₃) δ 167.6, 150.0, 144.2, 139.7, 138.1, 135.0, 134.5, 130.9, 129.8, 129.7, 128.5, 125.2, 124.1, 124.0, 122.3, 121.1, 120.6, 107.3, 52.6, 21.8. ¹¹B NMR (128 MHz, CDCl₃) δ -12.6. ¹⁹F NMR (377 MHz, CDCl₃) δ -149.2.

**Synthesis of *meso*-(4-carboxyphenyl) BF₂-oxasmaragdyrin (3):**

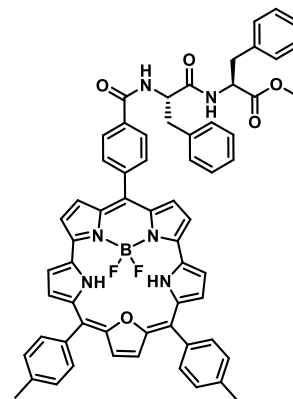
1 N LiOH (15 ml) was added to a solution of *meso*-(4-carboxy methyl ester phenyl) BF₂-oxasmaragdyrin **2** (60 mg, 0.8 mmol) in THF (15 mL). The reaction mixture was stirred for 6 hours before being quenched with 1N HCl and extracted using dichloromethane (50 mL). All the organic extracts were combined, dried over anhydrous Na₂SO₄, filtered and rotary evaporated to afford *meso*-(4-carboxyphenyl) BF₂-oxasmaragdyrin **3** which was used without further purification. (50 mg, 80% yield) ¹H NMR (400 MHz, DMSO-*d*₆) δ 10.78 (d, *J* = 4.5 Hz, 2H), 10.71 (dd, *J* = 4.5, 2.0 Hz, 2H), 9.73 (d, *J* = 4.5 Hz, 2H), 9.59 (s, 2H), 9.02 (dd, *J* = 4.5, 1.8 Hz, 2H), 8.81 (d, *J* = 8.1 Hz, 2H), 8.61 (d, *J* = 8.2 Hz, 2H), 8.42 – 8.31 (m, 4H), 7.79 (d, *J* = 7.5 Hz, 4H), 2.77 (s, 6H), -3.77 – -4.53 (m, 2H). ¹³C NMR (101 MHz, DMSO-*d*₆) δ 168.0, 149.5, 142.9, 139.0, 138.3, 135.4, 134.4, 131.2, 130.9, 130.2, 130.0, 128.9, 126.0, 124.9, 123.9, 123.6, 122.3, 121.4,



117.4, 107.1, 66.3, 34.4, 29.7, 21.7. ¹¹B NMR (128 MHz, DMSO-d₆) δ -12.81. ¹⁹F NMR (377 MHz, DMSO-d₆) δ -147.61.

Synthesis of methyl-L,L-diphenylalaninate conjugated BF₂-oxasmaragdyrin (**5**):

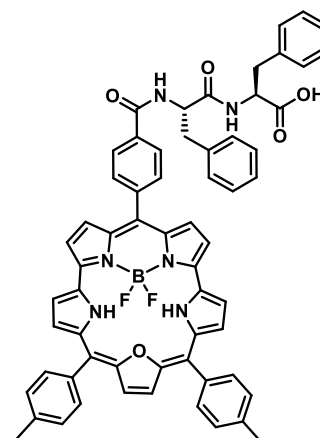
A solution of methyl-L-phenylalanyl-L-phenylalaninate **4** (22 mg, 0.7 mmol), *meso*-(4-carboxyphenyl) BF₂-oxasmaragdyrin **3** (50 mg, 0.7 mmol) and HBTU (40 mg, 1.05 mmol) of dry dichloromethane (15 mL). *N,N*-diisopropylethylamine (30 μL, 2.1 mmol) was added dropwise at 0 °C under nitrogen atmosphere. The reaction mixture was stirred for 6 hours. The progress of the reaction was monitored by TLC. After 6 h, the reaction mixture was diluted with dichloromethane (50 mL) and successively washed with 1N HCl (3 x 30 mL), saturated Na₂CO₃ solution (3 x 30 mL) and water (2 x 30 mL). The organic phase was then dried over anhydrous Na₂SO₄, filtered and rotary evaporated to give a brown semisolid. The crude product was subjected column chromatographic purification (SiO₂; 7:10 dichloromethane/petroleum ether) afforded the target product **5** in 55% yield. (40 mg). ¹H NMR (500 MHz, CDCl₃) δ in ppm: 10.34 (d, J = 4.4 Hz, 2H), 10.25 (d, J = 2.6 Hz, 2H), 9.57 (d, J = 4.3 Hz, 2H), 9.52 (s, 2H), 9.04 (s, 2H), 8.69 (d, J = 7.9 Hz, 2H), 8.30 (d, J = 7.6 Hz, 6H), 7.71 (d, J = 7.6 Hz, 4H), 7.50 – 7.40 (m, 4H), 7.30 (d, J = 6.7 Hz, 2H), 7.13 (dd, J = 13.5, 7.6 Hz, 2H), 6.46 (d, J = 7.5 Hz, 1H), 5.07 (dd, J = 14.0, 7.3 Hz, 1H), 4.91 (dd, J = 13.3, 6.5 Hz, 1H), 3.78 (s, 3H), 3.42 (dd, J = 13.9, 6.2 Hz, 1H), 3.32 (dd, J = 13.9, 7.6 Hz, 1H), 3.23 (dd, J = 13.8, 5.5 Hz, 1H), 3.10 (dd, J = 13.9, 6.6 Hz, 1H), 2.80 (s, 6H), -3.97 (s, 2H). ¹³C NMR (101 MHz, CDCl₃) δ in ppm: 171.4, 170.5, 167.2, 149.8, 139.5, 137.9, 136.5, 135.6, 135.0, 134.3, 130.7, 129.6, 129.3, 128.9, 128.7, 128.3, 127.2, 127.0, 125.0, 123.8, 122.1, 120.9, 120.4, 107.1, 54.8, 53.6, 52.4, 38.3, 38.0, 21.6. ¹¹B NMR (128 MHz, CDCl₃) δ -12.77. ¹⁹F NMR (377 MHz, CDCl₃) δ -149.32.



Synthesis of compound **1**:

1 N LiOH (15 mL) was added to a solution of methyl-L,L-diphenylalaninate conjugated BF₂-oxasmaragdyrin **5** (30 mg, mmol) in THF (15 mL). The reaction mixture was stirred for 6 hours before being quenched with 1N HCl and extracted using ethylacetate (50 mL). All the organic extracts were combined, dried over anhydrous Na₂SO₄, filtered and rotary evaporated to afford compound **1** which was used without further purification. (25 mg, 84% yield) ¹H

NMR (600 MHz, Acetone- d_6) δ 10.51 (d, J = 4.3 Hz, 2H), 10.45 (dd, J = 4.3, 2.0 Hz, 2H), 9.60 (d, J = 4.4 Hz, 2H), 9.54 (s, 2H), 8.97 (dd, J = 4.4, 1.9 Hz, 2H), 8.66 (d, J = 7.9 Hz, 2H), 8.46 (d, J = 8.0 Hz, 2H), 8.42 (d, J = 8.2 Hz, 1H), 8.32 – 8.26 (m, 4H), 7.99 (d, J = 7.9 Hz, 1H), 7.74 (d, J = 7.3 Hz, 4H), 7.53 (d, J = 7.0 Hz, 2H), 7.41 – 7.35 (m, 4H), 7.31 – 7.20 (m, 4H), 5.22 (ddd, J = 9.7, 8.0, 5.1 Hz, 1H), 4.90 (td, J = 7.6, 5.2 Hz, 1H), 3.48 (dd, J = 14.4, 5.0 Hz, 1H), 3.36 (dd, J = 13.8, 5.2 Hz, 1H), 3.29 (dd, J = 14.5, 9.7 Hz, 1H), 3.21 (dd, J = 14.0, 7.5 Hz, 1H), 2.76 (s, 6H), -3.95 (t, J = 10.1 Hz, 2H).



^{13}C NMR (151 MHz, Acetone- d_6) δ 172.7, 171.6, 167.1, 167.0, 150.1, 147.3, 145.4, 142.5, 142.1, 139.5, 139.3, 138.6, 138.5, 137.7, 135.0, 134.4, 134.3, 131.7, 130.9, 130.7, 129.9, 129.8, 129.7, 129.7, 129.1, 128.7, 128.7, 128.5, 127.9, 126.9, 126.8, 125.5, 124.7, 124.0, 123.0, 121.4, 121.2, 118.1, 114.1, 107.3, 78.7, 78.5, 78.3, 78.0, 55.5, 54.3, 37.7, 37.7, 34.7, 33.9, 32.1, 22.8, 21.1, 13.8. ^{11}B NMR (128 MHz, Acetone- d_6) δ -12.77. ^{19}F NMR (377 MHz, Acetone- d_6) δ -148.89.

Cell culture conditions

Mouse fibroblast (L929) cell line was procured from NCL, India and mouse breast cancer (4T1) cell line was procured from ATCC, USA. RPMI-1640 supplemented with 10% FBS, and 1 %v/v was used for culturing 4T1 cells. DMEM, supplemented with 1 %v/v antibiotic, and 10 %v/v FBS was employed for culturing L929 cells, and the incubation condition for both cell lines was 37 °C and 5% CO₂.

Preparation and characterization of FF-BSC NP

The nanoparticle preparation was carried out by dissolving compound **1** in acetone and equal volume of milli Q was added. The acetone was removed from the mixture under reduced pressure at 55 °C, using rotavapor. The pressure was gradually reduced, and acetone was completely removed from the mixture and the remnant was allowed to cool to room temperature. Finally, the volume was adjusted such the final concentration of FF-BSC was 0.1 mg/mL, and characterized. The UV-Vis spectrum was recorded on Cary 5000 UV-Vis-NIR spectrophotometer. The fluorescence spectrum was recorded on Perkin Elmer Spectrofluorometer. Material drop casted on aluminium foil and lacey grids were analysed by FEG-SEM and FEG-TEM for morphological evaluation.

Lyophilization

Cryo-protectant screening for FF-BSC NP lyophilization was carried out with varying concentrations (1, 2.5 and 5% w/w) of mannitol, sucrose and trehalose in the presence/absence of F-68 (0.5%). The selected cryoprotectants were dissolved in the FF-BSC NP suspension to attain the mentioned concentration, and were frozen at -80 °C. The samples were subjected to lyophilization at 50×10^{-3} bar for 48 h (FreeZone 1 liter benchtop lyophilizer, Labconco corporation, USA). The samples were reconstituted with milli Q after lyophilization and characterized.

Photothermal transduction potential evaluation

The photothermal transduction potential of FF-BSC NP was studied using a 750 nm continuous wave (cw) NIR laser. The impact of independent variables on the temperature raise, concentration of nanoparticles, laser power and laser exposure time were evaluated by constructing a face centred central composite design (CCD). CCD comprising of 17 runs and 3 centre points was designed using Design Expert and the levels selected for independent variables is given in Table 5.2. The experiments were carried out in a 96 well plate by irradiating 100 µL nanoparticle suspension with NIR laser, maintaining the experimental conditions as per the design layout provided in Table 5.3.

Table 5.2: Types of variables, levels and selected ranges of factors for constructing the design

Type of variables	Levels		
	Low (-1)	Medium (0)	High (+1)
<i>Independent variable (Factors)</i>			
A = Concentration of FF-BSC NP (mg/mL)	0.2	0.3	0.4
B = Laser irradiation time (min)	1	5.5	10
C = Power of laser (mW)	500	750	1000
<i>Dependent variable (Response)</i>			
R = Temperature (°C)			

The statistical evaluation of the selected model was carried out with Analysis of variance (ANOVA).

Table 5.3: CCD design layout along with recorded response

Run	Concentration of NP (mg/mL)	FF-BSC Laser irradiation time (min)	Power of laser (mW)	Temperature (°C)
1	0.2	10	500	47.1
2	0.3	5.5	500	48.6
3	0.2	10	1000	61
4	0.4	10	1000	70.6
5	0.4	1	1000	55
6	0.4	5.5	750	58.1
7	0.4	1	500	44.7
8	0.3	1	750	45.9
9	0.3	5.5	750	52.9
10	0.3	5.5	1000	61.8
11	0.4	10	500	53.5
12	0.3	5.5	750	54.2
13	0.2	1	500	40.4
14	0.3	5.5	750	55.5
15	0.2	5.5	750	50.8
16	0.2	1	1000	46.1
17	0.3	10	750	56.3

Table 5.4: ANOVA for the response, temperature for the selected quadratic model

Source	Sum Squares	of df	Mean Square	F- value	p-value	
Model	879.65	9	97.74	138.19	< 0.0001	significant
A-Concentration of FF-BSC NP	133.22	1	133.22	188.37	< 0.0001	
B-Laser irradiation time	318.10	1	318.10	449.76	< 0.0001	
C-Power of laser	362.40	1	362.40	512.40	< 0.0001	
AB	0.9800	1	0.9800	1.39	0.2776	
AC	7.60	1	7.60	10.75	0.0135	
BC	28.13	1	28.13	39.77	0.0004	
A ²	0.1421	1	0.1421	0.2009	0.6676	
B ²	26.08	1	26.08	36.87	0.0005	
C ²	2.57	1	2.57	3.64	0.0981	
Residual	4.95	7	0.7073			
Lack of Fit	1.57	5	0.3142	0.1859	0.9433	not significant
Pure Error	3.38	2	1.69			
Cor Total	884.60	16				

Table 5.5: Confirmatory trials for the obtained design space

Trial No	Concentration of FF-BSC NP (mg/mL)	Laser irradiation time (min)	Power of laser (mW)	95% prediction interval low	Observed value	95% prediction interval high
1	0.3	3	850	50.08	52.8	54.44
2	0.3	5	850	53.86	56.3	58.19
3	0.3	7	850	56.40	58.3	60.72

Photothermal conversion efficiency study

Photothermal conversion (η) efficiency for FF-BSC NP was carried as per the reported procedure, using the following equation.

$$\eta = \frac{hS(T_{\text{Max}} - T_{\text{Surr}}) - Q_{\text{Dis}}}{I(1 - 10^{-A_{750}})} \quad (1)$$

Where h indicates heat transfer coefficient, S indicates sample well surface area, T_{Max} is the steady state maximum temperature attained by FF-BSC NP, T_{Surr} is the room temperature, Q_{Dis} is baseline energy input, I indicate the laser power, and A_{750} is the absorbance of FF-BSC NP at 750 nm. FF-BSC NP suspension, dispensed in quartz cuvette was subjected to NIR laser irradiation and the temperature raise was recorded. Laser exposure was carried out till saturation was attained and the drop was recorded and plotted. Further, milli Q was exposed to NIR laser and the laser was turned off once equilibrium was attained and photothermal conversion efficiency was calculated¹.

Photo-stability and multi cycle PTT

The photo-stability and repetitive photothermal potential of FF-BSC NP was carried out by exposing nanoparticles to NIR laser for extended period of time and the temperature changes were monitored. 100 μL nanoparticle suspension was dispensed in 96 well plate and irradiated with 750 nm laser for 6 min at 650 mW and temperature was monitored at regular intervals. The sample was allowed to cool to room temperature and was subjected to NIR laser with same experimental conditions and the cycle was repeated for 3 times. Temperature was recorded during each cycle and the graph; temperature vs time was plotted.

Biocompatibility Study

In vitro biocompatibility of FF-BSC NP was determined in exponentially growing L929 cells with alamar blue assay. The cells were trypsinized and seeded in a 96 well plate at a density of $\sim 6 \times 10^3$ cells/well and incubated for 24 h. After 24 h, the components of the wells were replaced with media containing varying concentration of FF-BSC NP, ranging from 10 $\mu\text{g/mL}$ to 300 $\mu\text{g/mL}$. Complete media and 1% triton X-100 were employed as negative and positive controls respectively and were incubated for 24 h. The components of wells were carefully removed and washed with PBS, followed by addition of alamar blue (10 $\mu\text{g/well}$) and incubated for 4 hours. The fluorescence was recorded with excitation and emission wavelengths being

560 nm and 590 nm respectively, using a microplate reader (TECAN Infinite 200 PRO series). The percentage cell viability was calculated using the following equation

$$\text{Cell viability (\%)} = \frac{\text{Fluorescence intensity of treated sample}}{\text{Fluorescence intensity of control sample}} \times 100$$

Intensity of sample indicates the intensity of samples treated with varying concentrations of FF-BSC NP and control reflects intensity of negative control.

Cell internalization

Cell internalization of FF-BSC NP was carried out in 4T1 cells. Briefly, cells were seeded at a density of 1×10^6 cells per 60 mm dish and incubated for 24 hours under humidified conditions. Freshly prepared sample (10 $\mu\text{g/mL}$) was incubated with cells for different time periods i.e. 1h, 3h, 6h, 12h and 24h. After the incubation period, the contents of the dish were removed, washed with PBS, and trypsinized. Cells were centrifuged and redispersed in 0.5 mL PBS and internalization was quantified using flow cytometer. The excitation wavelength was 488 nm (blue) laser and emission was captured employing APC-Alexa 700-A channel and minimum of 10000 events were recorded. Gating was carried out to remove any debris, free nanoparticles, or dead cells and the data was analysed with FlowJo.

***In vitro* photothermal efficacy testing**

The *in vitro* photothermal efficacy evaluation was carried out in 4T1 cells. Briefly, cells were trypsinized and seeded in a 96 well plate at a density of $\sim 6 \times 10^3$ cells/well and incubated for 24 h. After 24 h, the components of the wells were replaced with media containing varying concentrations of FF-BSC NP (5, 10 and 15 $\mu\text{g/well}$). The cells were exposed with 750 nm NIR laser at 650 mW for three different time periods, 3, 5 and 7 min. Negative control, material control and laser control were employed during experimentation and after 12h of treatment, alamar blue was added to each well (10 $\mu\text{g/well}$). The cells were incubated for 4 h and the fluorescence was recorded, % cell viability calculated as mentioned above.

Hemocompatibility assessment

Hemocompatibility study for FF-BSC NP was performed with blood withdrawn from healthy volunteers after proper consent and in accordance with ethical guidelines. Whole blood withdrawn in EDTA coated tubes was centrifuged at 1000 rpm for 5 min, pellet resuspended in PBS to separate RBC and this is repeated multiple times. Hemocompatibility was evaluated

by adding varying concentrations of nanoparticle suspension i.e. 100, 200 and 300 µg/mL to RBS suspension, and incubated at 37 °C for 3 h. Triton X-100 and PBS were used as positive and negative controls, respectively. After 3h, the samples were centrifuged for 5 min at 4000 rpm and the supernatant was carefully removed and dispensed in 96 well plate. The absorbance was recorded at 540 nm using plate reader (TECAN Infinite 200 PRO series), and the percentage hemolysis was calculated using the following equation

$$\text{Hemolysis (\%)} = \frac{(\text{Absorbance of test sample} - \text{Absorbance of negative control})}{(\text{Absorbance of positive control} - \text{Absorbance of negative control})} \times 100$$

Test sample indicates the samples treated with varying concentrations of FF-BSC NP and the pelleted RBCs were fixed overnight under cold conditions with 2% glutaraldehyde. Further, the suspension was centrifuged at 4000 rpm for 5 min and ESEM analysis was carried out to evaluate the morphology of RBCs.

Biodistribution and Single dose toxicity testing of FF-BSC NP

Biodistribution and single dose toxicity testing of FF-BSC NP was carried out in healthy female swiss bare mice, post approval by Institute Animal Ethics Committee (IAEC), at ACTREC. The animals were housed in 12 hrs light and dark cycle as per the Committee for the Purpose of Control and Supervision on Experiments in Animals (CPCSEA) guidelines during the experimentation. Briefly, the mice were divided in two groups: control and test (n=5 each), the control group was administered with PBS, while the test group with 300µg of FF-BSC NP through tail vein. The mice were monitored for changes in body weight for 14 days and at the end of 14th day, the mice were sacrificed, blood and major organs i.e. liver, kidney, lungs, heart and spleen were harvested. Blood was centrifuged at 2500 rpm and the supernatant containing serum was further processed for serum biochemical analysis. A small part of the harvested organs were fixed in formaldehyde, paraffin blocks were made and haematoxylin & eosin staining was performed in order to identify associated toxicity of the materials to these vital organs, if any. *Ex vivo* fluorescence imaging of different organs harvested was performed by recording the spectra at an excitation and emission wavelength of 465 and 720 nm respectively, using IVIS spectrum imaging system, Caliper life sciences, USA. Qualitative assessment of the amount of FF-BSC NP accumulated, was done by comparing the fluorescence output from harvested organs of FF-BSC NP injected mice with that of control mice. For further quantification the organs were snap freezed in liquid nitrogen, followed by grinding and extraction with DMSO. The absolute quantification was done by comparing the fluorescence

of the extracted lysate from different organs to that of the standard curve and total nanoparticles accumulated in different organs was represented in terms of μg of compound/gram of the tissue.

***In vivo* photothermal efficacy and bioluminescence imaging for FF-BSC NP**

The *in vivo* photothermal efficacy testing of FF-BSC NP was carried out in CD1 nude mice. Tumor was induced by implanting 1×10^6 4T1 fl2 cells subcutaneously on the right flank of CD1 nude mice. Mice were randomly segregated into control, material control and treatment groups ($n=5$ for each group) as the desired tumor volume was attained (70 to 80 mm^3). The tumor growth was monitored through live animal imaging by administering $100 \mu\text{L}$ of D-luciferin (3 mg/ml) intraperitoneally. Bioluminescence imaging was done in IVIS Lumina II imaging system, Caliper life sciences, USA by keeping F stop 8, at a time interval of 1 min till the peak signal is attained. Briefly, control animals were administered with PBS while material control and treatment groups with $300 \mu\text{g}$ of FF-BSC NP intra-tumorally. The treatment group was further subjected to 750 nm fixed wavelength laser irradiation for 5 min (750 mW), whereas the control and material control groups were devoid of laser irradiation. Bioluminescence signal was recorded for all the groups at regular intervals till day 30 post PTT to understand the effectiveness of FF-BSC NP for PTT mediated tumor ablation. Living image v4.4 software was used to acquire the images, quantify the signal and the signal output was reported in terms of average radiance ($\text{p/sec/cm}^2/\text{sr}$).

5.5 References

- (1) Bray, F.; Ferlay, J.; Soerjomataram, I.; Siegel, R. L.; Torre, L. A.; Jemal, A. Global Cancer Statistics 2018: GLOBOCAN Estimates of Incidence and Mortality Worldwide for 36 Cancers in 185 Countries. *CA. Cancer J. Clin.* **2018**, *68*, 394–424.
- (2) Vines, J. B.; Yoon, J. H.; Ryu, N. E.; Lim, D. J.; Park, H. Gold Nanoparticles for Photothermal Cancer Therapy. *Front. Chem.* **2019**, *7*, 167.
- (3) Lal, S.; Clare, S. E.; Halas, N. J. Nanoshell-Enabled Photothermal Cancer Therapy: Impending Clinical Impact. *Acc. Chem. Res.* **2008**, *41*, 1842–1851.
- (4) Dickerson, E. B.; Dreaden, E. C.; Huang, X.; El-Sayed, I. H.; Chu, H.; Pushpanketh, S.; McDonald, J. F.; El-Sayed, M. A. Gold Nanorod Assisted Near-Infrared Plasmonic Photothermal Therapy (PPTT) of Squamous Cell Carcinoma in Mice. *Cancer Lett.* **2008**, *269*, 57–66.

- (5) Gao, L.; Fei, J.; Zhao, J.; Li, H.; Cui, Y.; Li, J. Hypocrellin-Loaded Gold Nanocages with High Two-Photon Efficiency for Photothermal/Photodynamic Cancer Therapy in Vitro. *ACS Nano* **2012**, *6*, 8030–8040.
- (6) Qin, C.; Fei, J.; Wang, A.; Yang, Y.; Li, J. Rational Assembly of a Biointerfaced Core@shell Nanocomplex towards Selective and Highly Efficient Synergistic Photothermal/Photodynamic Therapy. *Nanoscale* **2015**, *7*, 20197–20210.
- (7) Abadeer, N. S.; Murphy, C. J. Recent Progress in Cancer Thermal Therapy Using Gold Nanoparticles. *J. Phys. Chem. C* **2016**, *120*, 4691–4716.
- (8) Yang, K.; Zhang, S.; Zhang, G.; Sun, X.; Lee, S. T.; Liu, Z. Graphene in Mice: Ultrahigh in Vivo Tumor Uptake and Efficient Photothermal Therapy. *Nano Lett.* **2010**, *10*, 3318–3323.
- (9) Robinson, J. T.; Tabakman, S. M.; Liang, Y.; Wang, H.; Sanchez Casalongue, H.; Vinh, D.; Dai, H. Ultrasmall Reduced Graphene Oxide with High Near-Infrared Absorbance for Photothermal Therapy. *J. Am. Chem. Soc.* **2011**, *133*, 6825–6831.
- (10) Sun, Z.; Xie, H.; Tang, S.; Yu, X. F.; Guo, Z.; Shao, J.; Zhang, H.; Huang, H.; Wang, H.; Chu, P. K. Ultrasmall Black Phosphorus Quantum Dots: Synthesis and Use as Photothermal Agents. *Angew. Chem. Int. Ed.* **2015**, *54*, 11526–11530.
- (11) Tao, W.; Zhu, X.; Yu, X.; Zeng, X.; Xiao, Q.; Zhang, X.; Ji, X.; Wang, X.; Shi, J.; Zhang, H.; et al. Black Phosphorus Nanosheets as a Robust Delivery Platform for Cancer Theranostics. *Adv. Mater.* **2017**, *29*.
- (12) Zhao, Z.; Shi, S.; Huang, Y.; Tang, S.; Chen, X. Simultaneous Photodynamic and Photothermal Therapy Using Photosensitizer-Functionalized Pd Nanosheets by Single Continuous Wave Laser. *ACS Appl. Mater. Interfaces* **2014**, *6*, 8878–8885.
- (13) Shi, S.; Huang, Y.; Chen, X.; Weng, J.; Zheng, N. Optimization of Surface Coating on Small Pd Nanosheets for in Vivo Near-Infrared Photothermal Therapy of Tumor. *ACS Appl. Mater. Interfaces* **2015**, *7*, 14369–14375.
- (14) Tian, Q.; Jiang, F.; Zou, R.; Liu, Q.; Chen, Z.; Zhu, M.; Yang, S.; Wang, J.; Wang, J.; Hu, J. Hydrophilic Cu₉S₅ Nanocrystals: A Photothermal Agent with a 25.7% Heat Conversion Efficiency for Photothermal Ablation of Cancer Cells in Vivo. *ACS Nano* **2011**, *5*, 9761–9771.

- (15) Zhou, M.; Li, J.; Liang, S.; Sood, A. K.; Liang, D.; Li, C. CuS Nanodots with Ultrahigh Efficient Renal Clearance for Positron Emission Tomography Imaging and Image-Guided Photothermal Therapy. *ACS Nano* **2015**, *9*, 7085–7096.
- (16) Hessel, C. M.; P. Pattani, V.; Rasch, M.; Panthani, M. G.; Koo, B.; Tunnell, J. W.; Korgel, B. A. Copper Selenide Nanocrystals for Photothermal Therapy. *Nano Lett.* **2011**, *11*, 2560–2566.
- (17) Song, G.; Shen, J.; Jiang, F.; Hu, R.; Li, W.; An, L.; Zou, R.; Chen, Z.; Qin, Z.; Hu, J. Hydrophilic Molybdenum Oxide Nanomaterials with Controlled Morphology and Strong Plasmonic Absorption for Photothermal Ablation of Cancer Cells. *ACS Appl. Mater. Interfaces* **2014**, *6*, 3915–3922.
- (18) Yang, J.; Choi, J.; Bang, D.; Kim, E.; Lim, E.-K.; Park, H.; Suh, J.-S.; Lee, K.; Yoo, K.-H.; Kim, E.-K.; et al. Convertible Organic Nanoparticles for Near-Infrared Photothermal Ablation of Cancer Cells. *Angew. Chem. Int. Ed.* **2010**, *50*, 441–444.
- (19) Yu, J.; Javier, D.; Yaseen, M. A.; Nitin, N.; Richards-Kortum, R.; Anvari, B.; Wong, M. S. Self-Assembly Synthesis, Tumor Cell Targeting, and Photothermal Capabilities of Antibody-Coated Indocyanine Green Nanocapsules. *J. Am. Chem. Soc.* **2010**, *132*, 1929–1938.
- (20) Chen, M.; Fang, X.; Tang, S.; Zheng, N. Polypyrrole Nanoparticles for High-Performance in Vivo near-Infrared Photothermal Cancer Therapy. *Chem. Commun.* **2012**, *48*, 8934–8936.
- (21) Zhou, J.; Lu, Z.; Zhu, X.; Wang, X.; Liao, Y.; Ma, Z.; Li, F. NIR Photothermal Therapy Using Polyaniline Nanoparticles. *Biomaterials* **2013**, *34*, 9584–9592.
- (22) Geng, J.; Sun, C.; Liu, J.; Liao, L. De; Yuan, Y.; Thakor, N.; Wang, J.; Liu, B. Biocompatible Conjugated Polymer Nanoparticles for Efficient Photothermal Tumor Therapy. *Small* **2015**, *11*, 1603–1610.
- (23) Xu, L.; Cheng, L.; Wang, C.; Peng, R.; Liu, Z. Conjugated Polymers for Photothermal Therapy of Cancer. *Polym. Chem.* **2014**, *5*, 1573–1580.
- (24) Cheng, L.; Wang, C.; Feng, L.; Yang, K.; Liu, Z. Functional Nanomaterials for Phototherapies of Cancer. *Chem. Rev.* **2014**, *114*, 10869–10939.

- (25) Feng, G.; Liu, J.; Geng, J.; Liu, B. Conjugated Polymer Microparticles for Selective Cancer Cell Image-Guided Photothermal Therapy. *J. Mater. Chem. B* **2015**, *3*, 1135–1141.
- (26) Song, X.; Chen, Q.; Liu, Z. Recent Advances in the Development of Organic Photothermal Nano-Agents. *Nano Res.* **2015**, *8*, 340–354.
- (27) Feng, G.; Mai, C. K.; Zhan, R.; Bazan, G. C.; Liu, B. Narrow Band Gap Conjugated Polyelectrolytes for Photothermal Killing of Bacteria. *J. Mater. Chem. B* **2015**, *3*, 7340–7346.
- (28) Kobayashi, H.; Ogawa, M.; Alford, R.; Choyke, P. L.; Urano, Y. New Strategies for Fluorescent Probe Design in Medical Diagnostic Imaging. *Chem. Rev.* **2010**, *110*, 2620–2640.
- (29) Pham, W.; Cassell, L.; Gillman, A.; Koktysh, D.; Gore, J. C. A Near-Infrared Dye for Multichannel Imaging. *Chem. Commun.* **2008**, No. 16, 1895–1897.
- (30) Fischer, G. M.; Isomäki-Krondahl, M.; Göttker-Schnetmann, I.; Daltrozzo, E.; Zumbusch, A. Pyrrolopyrrole Cyanine Dyes: A New Class of Near-Infrared Dyes and Fluorophores. *Chem. – A Eur. J.* **2009**, *15*, 4857–4864.
- (31) Arunkumar, E.; Forbes, C. C.; Noll, B. C.; Smith, B. D. Squaraine-Derived Rotaxanes: Sterically Protected Fluorescent near-IR Dyes. *J. Am. Chem. Soc.* **2005**, *127*, 3288–3289.
- (32) Johnson, J. R.; Fu, N.; Arunkumar, E.; Leevy, W. M.; Gammon, S. T.; Piwnicka-Worms, D.; Smith, B. D. Squaraine Rotaxanes: Superior Substitutes for Cy-5 in Molecular Probes for near-Infrared Fluorescence Cell Imaging. *Angew. Chem. Int. Ed.* **2007**, *46*, 5528–5531.
- (33) Umezawa, K.; Citterio, D.; Suzuki, K. Water-Soluble NIR Fluorescent Probes Based on Squaraine and Their Application for Protein Labeling. *Anal. Sci.* **2008**, *24*, 213–217.
- (34) Fu, N.; Gassensmith, J. J.; Smith, B. D. Effect of Stopper Size on Squaraine Rotaxane Stability. *Supramol. Chem.* **2009**, *21*, 118–124.
- (35) Loudet, A.; Bandichhor, R.; Burgess, K.; Palma, A.; McDonnell, S. O.; Hall, M. J.; O’Shea, D. F. B. O-Chelated Azadipyrrromethenes as near-IR Probes. *Org. Lett.* **2008**,

- 10, 4771–4774.
- (36) Umezawa, K.; Nakamura, Y.; Makino, H.; Citterio, D.; Suzuki, K. Bright, Color-Tunable Fluorescent Dyes in the Visible–Near-Infrared Region. *J. Am. Chem. Soc.* **2008**, *130*, 1550–1551.
- (37) Umezawa, K.; Matsui, A.; Nakamura, Y.; Citterio, D.; Suzuki, K. Bright, Color-Tunable Fluorescent Dyes in the Vis/NIR Region: Establishment of New “Tailor-Made” Multicolor Fluorophores Based on Borondipyrromethene. *Chem. – A Eur. J.* **2009**, *15*, 1096–1106.
- (38) Meek, S. T.; Nesterov, E. E.; Swager, T. M. Near-Infrared Fluorophores Containing Benzo[c]Heterocycle Subunits. *Org. Lett.* **2008**, *10*, 2991–2993.
- (39) Yang, Y.; Lowry, M.; Xu, X.; Escobedo, J. O.; Sibrian-Vazquez, M.; Wong, L.; Schowalter, C. M.; Jensen, T. J.; Fronczek, F. R.; Warner, I. M.; et al. Seminaphthofluorones Are a Family of Water-Soluble, Low Molecular Weight, NIR-Emitting Fluorophores. *Proc. Natl. Acad. Sci. U. S. A.* **2008**, *105*, 8829–8834.
- (40) Nesterova, I. V.; Verdree, V. T.; Pakhomov, S.; Strickler, K. L.; Allen, M. W.; Hammer, R. P.; Soper, S. A. Metallo-Phthalocyanine near-IR Fluorophores: Oligonucleotide Conjugates and Their Applications in PCR Assays. *Bioconjug. Chem.* **2007**, *18*, 2159–2168.
- (41) Kee, H. L.; Nothdurft, R.; Muthiah, C.; Diers, J. R.; Fan, D.; Ptaszek, M.; Bocian, D. F.; Lindsey, J. S.; Culver, J. P.; Holten, D. Examination of Chlorin-Bacteriochlorin Energy-Transfer Dyads as Prototypes for near-Infrared Molecular Imaging Probes. *Photochem. Photobiol.* **2008**, *84*, 1061–1072.
- (42) Kuimova, M. K.; Collins, H. A.; Balaz, M.; Dahlstedt, E.; Levitt, J. A.; Sergent, N.; Suhling, K.; Drobizhev, M.; Makarov, N. S.; Rebane, A.; et al. Photophysical Properties and Intracellular Imaging of Water-Soluble Porphyrin Dimers for Two-Photon Excited Photodynamic Therapy. *Org. Biomol. Chem.* **2009**, *7*, 889–896.
- (43) Xie, D.; Liu, Y.; Rao, Y.; Kim, G.; Zhou, M.; Yu, D.; Xu, L.; Yin, B.; Liu, S.; Tanaka, T.; et al. Meso-Triaryl-Substituted Smaragdyrins: Facile Aromaticity Switching. *J. Am. Chem. Soc.* **2018**, *140*, 16553–16559.
- (44) Narayanan, S. J.; Sridevi, B.; Chandrashekar, T. K.; Englich, U.; Ruhlandt-Senge, K.

- Core-Modified Smaragdyrins: First Examples of Stable Meso-Substituted Expanded Corrole. *Org. Lett.* **1999**, *1*, 587–590.
- (45) Pareek, Y.; Ravikanth, M.; Chandrashekar, T. K. Smaragdyrins: Emeralds of Expanded Porphyrin Family. *Acc. Chem. Res.* **2012**, *45*, 1801–1816.
- (46) Chatterjee, T.; Srinivasan, A.; Ravikanth, M.; Chandrashekar, T. K. Smaragdyrins and Sapphyrins Analogues. *Chem. Rev.* **2017**, *117*, 3329–3376.
- (47) Rajeswara Rao, M.; Ravikanth, M. Boron Complexes of Oxasmaragdyrin, a Core-Modified Expanded Porphyrin. *J. Org. Chem.* **2011**, *76*, 3582–3587.
- (48) Kalita, H.; Lee, W.-Z.; Ravikanth, M. Phosphorus Complexes of Meso-Triaryl-25-Oxasmaragdyrins. *Inorg. Chem.* **2014**, *53*, 9431–9438.
- (49) Yan, X.; Zhu, P.; Li, J. Self-Assembly and Application of Diphenylalanine-Based Nanostructures. *Chem. Soc. Rev.* **2010**, *39*, 1877–1890.
- (50) Zou, Q.; Abbas, M.; Zhao, L.; Li, S.; Shen, G.; Yan, X. Biological Photothermal Nanodots Based on Self-Assembly of Peptide-Porphyrin Conjugates for Antitumor Therapy. *J. Am. Chem. Soc.* **2017**, *139*, 1921–1927.
- (51) Souza, M. I.; Prieto, T.; Rodrigues, T.; Ferreira, F. F.; Nascimento, F. B.; Ribeiro, A. O.; Silva, E. R.; Giuntini, F.; Alves, W. A. Conjugation with L,L-Diphenylalanine Self-Assemblies Enhances in Vitro Antitumor Activity of Phthalocyanine Photosensitizer. *Sci. Rep.* **2017**, *7*, 13166.
- (52) Mane, S. B.; Hu, J.-Y.; Chang, Y.-C.; Luo, L.; Diao, E. W.-G.; Hung, C.-H. Novel Expanded Porphyrin Sensitized Solar Cells Using Boryl Oxasmaragdyrin as the Sensitizer. *Chem. Commun.* **2013**, *49*, 6882–6884.
- (53) Yu, J.; Anchordoquy, T. J. Synergistic Effects of Surfactants and Sugars on Lipoplex Stability during Freeze-Drying and Rehydration. *J. Pharm. Sci.* **2009**, *98*, 3319–3328.
- (54) te Velde, E. A.; Veerman, T.; Subramaniam, V.; Ruers, T. The Use of Fluorescent Dyes and Probes in Surgical Oncology. *European Journal of Surgical Oncology*. 2010, pp 6–15.
- (55) Luyts, K.; Napierska, D.; Nemery, B.; Hoet, P. H. M. How Physico-Chemical Characteristics of Nanoparticles Cause Their Toxicity: Complex and Unresolved

- Interrelations. *Environmental Sciences: Processes and Impacts*. 2013, pp 23–38.
- (56) Gatoo, M. A.; Naseem, S.; Arfat, M. Y.; Mahmood Dar, A.; Qasim, K.; Zubair, S. Physicochemical Properties of Nanomaterials: Implication in Associated Toxic Manifestations. *BioMed Research International*. Hindawi Publishing Corporation 2014.
- (57) Gouterman, M. Electronic Spectra. *The Porphyrins* **1978**, 3, 1–156.

Chapter 6

*BF₂-Oxasmaragdyrin based Quantum Dots as
theragnostic agent for cancer therapy*

6.1 Introduction

A rapid increase in cancer and associated mortalities observed in recent years ensued cancer to be the second most leading cause for mortalities, placed only next to noncommunicable diseases.¹ The current cancer therapeutic modalities are limited to surgery, chemotherapy, radiotherapy and immunotherapy. Due to the heterogeneity of cancers, these therapeutic approaches are often limited to specific types of cancers and serious side effects, propelling the researchers to search for alternative therapeutic approaches.² Photothermal therapy (PTT) is one such evolving therapeutic strategy, possessing excellent potential due to its minimal invasiveness, ease of operation, rapid treatment and quick recovery.³ In recent years various materials have been screened for PTT such as gold nanoparticles,^{4–7} graphene and graphene oxide,^{8,9} black phosphorus,^{10,11} palladium,^{12,13} copper sulphide,^{14,15} copper selenide,¹⁶ molybdenum oxide,¹⁷ organic nanoparticles^{18–25} and various quantum dots.

“Quantum dots (QDs)” was the term first coined by Mark Reed referring to the semiconductor nanoparticles which are quantum confined i.e., the particle size is less than that of the exciton bohr radius of the constituent material.²⁶ Over the years, various types of quantum dots have been reported such as Semiconductor QDs (SQDs),^{27–31} Graphene QDs (GQDs)^{32–35} which are perfectly crystalline in structures. Quantum dots possess distinct properties such as large surface area, resistance to photobleaching, good photostability and opto-electronic properties compared to that of their corresponding bulk counterparts which have found themselves useful in various applications.^{35,36} Another class of nanomaterials with carbogenic core analogous to GQDs are Carbon quantum dots (CQDs)/Cdots which are nanomaterial quasi-spherical particles typically with size below 10 nm.^{36–39} CQDs consists of amorphous to nanocrystalline core with predominantly sp^2 carbon and terminated by oxygenic functionalities such as alcohols, aldehydes, carboxylic acids on their surface which enhances aqueous solubility, biocompatibility, and potential for additional functionalization compared to other carbon nanomaterial structures (GQDs, carbon nanotubes and fullerenes). CQDs have exploitable electronic and photophysical properties which have been used in the fields of medicine, chemical sensors, biosensors, dye sensitized solar cells (DSSCs), supercapacitors, etc.³⁸ In the recent past various synthetic strategies towards N, S, P doped Cdots^{40–45}, and rhodamines,⁴⁶ porphyrins,⁴⁷ phthalocyanines^{48–52} conjugated Cdots have been developed to tune the electronic and photophysical properties of Cdots. Synthesis of NIR fluorescent Cdots^{53–56} has gained a lot of attention as the autofluorescence from the tissues in the window of 650-950 is minimal.⁵⁷ A NIR dye conjugated Cdots were synthesized by Xie and coworkers in the form of cyanine carbon dots (CyCDs) and evaluated their potential for fluorescence

imaging and photothermal cancer therapy.⁵⁸ One such NIR absorbing expanded porphyrin dye is BF₂-oxasmaragdyrin which is a 22 π electronic aromatic macrocycle, absorbs in visible-NIR (~ 400-700 nm) and emits in NIR (~710 nm) region.^{59–61} Though dye based Cdots have been reported, they have been mostly either covalently/noncovalently conjugated with dye.^{40–45} There are very few reports in which the dye is conjugated to precursor molecules to incorporate dye into the nanomaterial structures but there are no reports in which the dye molecules are quantum confined.

Herein we present our first report of the BF₂-oxasmaragdyrin based quantum dots (TBSQDs) which were synthesized by subjecting BF₂-oxasmaragdyrin to moderate pressures of ~800 bar using high pressure homogenizer at room temperature, employing lipid to stabilize the same. Direct evidence of formation of quantum dots was obtained by Surface-Enhanced Raman Scattering (SERS) and Transmission Electron Microscopy (TEM). TBSQDs have interesting photophysical properties with good absorption in Vis-NIR region and fluorescence in NIR region with decent quantum yield. Further, TBSQDs exhibited excellent photothermal properties with good conversion efficiency and the same was evaluated *in vitro* and *in vivo*.

6.2 Results and Discussions

6.2.1 Synthesis and characterization of TBSQDs

meso-Tritolyl-BF₂-oxasmaragdyrin (TBS) was synthesized using previously reported method. TBSQDs were prepared by thin film hydration followed by high pressure homogenization. Chloroform was removed from TBS and lipoid S 75 solubilized mixture under reduced pressure, and the obtained thin film was hydrated at 45°C for 1 hour, followed by high pressure homogenization at 800 bar for 10 passes. The obtained TBSQDs were characterized by Raman spectroscopy, TEM, and absorption and fluorescence spectroscopy.

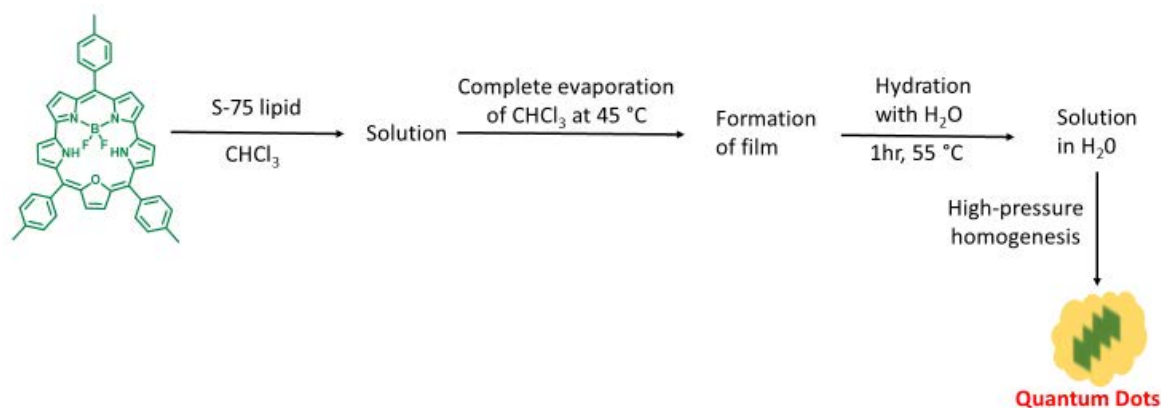


Figure 6.1: Schematic presentation for synthesis of TBSQDs.

The indication of quantum confinement of TBS was clearly evaluated through SERS by physical mixture of TBSQDs solution and Ag colloidal solution. The sample of QDs were excited on the surface of Ag colloidal particles with 532 nm Laser to minimize the effect of fluorescence on weak Raman signals. We observed the sharper Raman signals from TBSQDs compared to that of the TBS (Figure 2a) with about 40-60% decrease (Table 6.1) in full width half maximum (FWHM) values from TBS to TBSQDs suggesting that the obtained material was quantum confined. Further, TEM analysis of the sample has shown that the TBSQDs were amorphous/polycrystalline in nature with particle size of 7.1 ± 2.1 nm (Figure 6.2b-d) which is less than the calculated bohr radius ($a_0 \approx 15$ nm) for the material. The formation of quantum dots may be attributed to the π -stacking of TBS under high pressure and stabilization of hydrophobic self-assembly in water by lipid encapsulation. Absence of lipid in the above process did not yield the TBS quantum dots. Hence, S-75 lipid plays vital role in homogenizing hydrophobic TBS in water and stabilizing the formed hydrophobic TBS quantum dots in water medium.

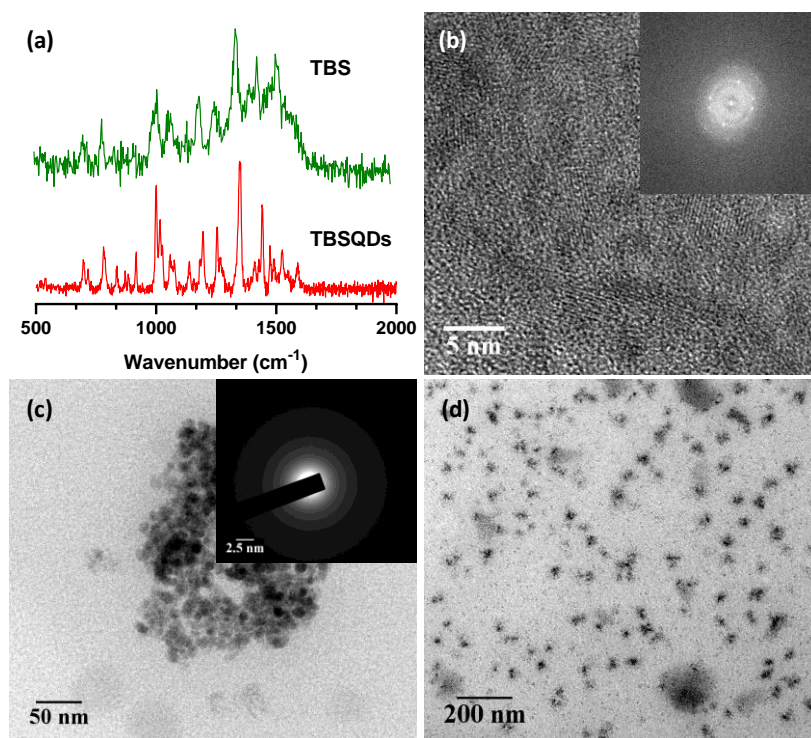


Figure 6.2: (a) Comparison of Raman scattering for TBS and TBSQDs on Ag nanoparticles. (b-d) TEM Images [(b) HRTEM of TBSQDs (Inset shows FFT) (c) TEM image of TBSQDs (inset shows the Selected Area Electron Diffraction (SAED))]

Table 6.1: Full width half maximas of selected Surface Enhanced Raman (SER) signals.

Frequency (cm ⁻¹)	FWHM (cm ⁻¹)		% decrease from TBS to TBSQDs
	TBS	TBSQDs	
1525	22.9	11.4	50.3
1440	18.4	7.5	59.3
1348	26.7	15.3	42.7
1256	23.4	11.4	51.3
1193	22.9	11.4	50.3
998	15.9	7.7	51.5
780	19.1	11.4	40.1

6.2.2 Photophysical properties

The absorption and emission characterizations were carried out on the synthesized TBSQDs. The absorption spectra of the TBSQDs has a similar pattern as that of TBS with 2 sorlet bands, four Q-bands which are severely broadened (Figure 6.3a) and a reduction of 10 times in absorbance of the sorlet was observed from TBS to TBSQDs due to aggregation of TBS and formation of TBSQDs (Table 6.2). Further, a bathochromic shift of 30 nm in the last Q-band absorption was observed for TBSQDs compared to that of the TBS suggesting the strongly coupled electronic states of individual building block TBS in the formed TBSQDs.

Table 6.2: Photophysical characterisation data for TBSQDs

Compound	Absorption						Fluorescence		
	Wavelength [nm]						λ_f	Φ_f	τ
	(Absorbance)						(nm)		
TBS	446	474	589	627	648	703	713	0.15	4.15
	(2.03)	(0.90)	(0.09)	(0.11)	(0.14)	(0.30)			
TBS-QDs	446	475	593	652	708	730	708	0.09	5.86
	(0.19)	(0.14)	(0.04)	(0.04)	(0.05)	(0.07)			

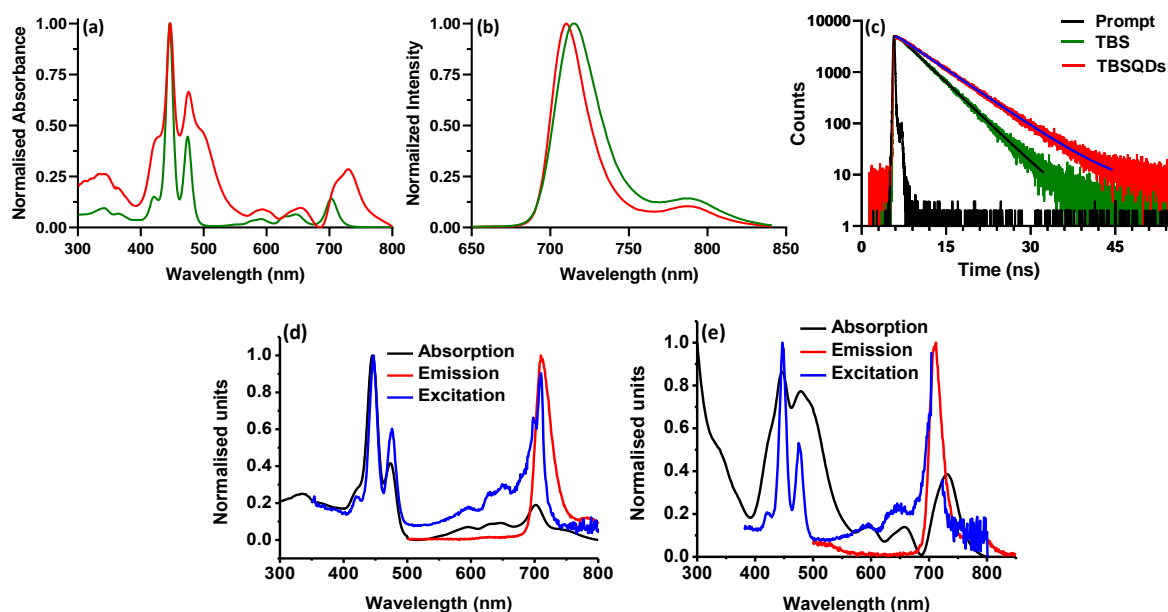


Figure 6.3: Comparison of (a) Normalized Absorption, (b) Normalized fluorescence, (c) Fluorescence decay profile of TBSQDs with TBS and Overlay of Absorption, Emission and Excitation spectra of TBS (d) and TBSQD (e).

Strangely the fluorescence emission wavelength was observed to be 4 nm blue shifted compared to that of the TBS (Figure 6.3b) though the bathochromic shift was observed in the absorption spectrum (Figure 6.3a). Excitation spectra for TBS and TBSQDs (Figure 6.3d and 6.3e) was recorded to understand the fluorescence behavior, and found that the excitation spectra of TBSQDs looks more like an absorption spectrum of TBS. This suggests that the fluorescence of individual TBS in TBSQDs was mostly quenched by the formation of quantum dots and the fluorescence observed is only from the peripheral TBS present on TBSQDs. No fluorescence was observed when the TBSQDs were excited at 730 nm suggesting that the absorption at 730 nm is leading to the nonradiative decay. The fluorescence lifetime of 4.5 ns, 5.8 ns (Figure 6.3c, Table 6.2) was observed for TBS, TBSQDs respectively. Increase in fluorescence lifetime of TBSQDs to that of TBS could be attributed to the local hydrophobic environment created by the lipid stabilizes the electronically excited state in TBSQDs. The reduction in fluorescence quantum yield from 0.15 to 0.09 (Table 6.2) from TBS to TBS QDs suggests that there is an increase in amount of nonradiative decay from excited state upon formation of TBSQDs which we observed as thermal energy.

6.2.3 Photothermal properties

TBSQDs exhibited excellent photo-thermal properties, upon exposure with NIR laser (750 nm). The factors that plays an important role in the photo-thermal transduction are concentration of TBSQDs, laser exposure time and power of laser. Employing an OFAT (one factor at a time) approach doesn't reveal interaction among the factors, whereas the same can be evaluated using response surface methodology (RSM), and CCD was employed. The constructed design along with the obtained results are given in Table 6.5. The p-value for quadratic model was found to be significant ($p=0.0215$), and the same was selected. The ANOVA revealed that the selected model was significant ($p < 0.0001$), and the lack of fit insignificant ($p < 0.2797$), as provided in Table 6.6. The diagnostic tests didn't reveal any anomalies, and the impact of various factors on response is provided in Equation (1)

$$Y = +58.33 + 8.69A + 8.23B + 7.36C + 1.67AC + 4.45BC - 3.72B^2 \quad (1)$$

Where A, B, C and Y represents concentration of TBSQDs, laser exposure time, laser power, and temperature respectively. The synergistic and antagonistic effects of factors is indicated by positive and negative signs respectively. Coefficients of single, two factors, and second-order represents effects of individual, interaction and quadratic nature respectively. Equation 1 clearly indicates concentration of TBSQDs has highest impact on photo-thermal transduction, followed by laser exposure time and laser power.

The impact of various factors was studied with 3D plot, and Figure 6.3a represents the 3D plot constructed by freezing laser irradiation time to 5 min. The numerical and graphical optimizations were carried out by setting the ranges of various parameters such that the response outcome would be in the range 52-65 °C. The design space was evaluated by randomly selecting 5 points, experiments carried out and it was observed that the results were well within the predicted ranges, as shown in a Table 6.7.

The photothermal conversion efficiency (PCE) of material indicates the efficacy of material in converting the absorbed light to heat and is primarily influenced by the material absorption properties. The PCE of TBSQDs was evaluated in accordance with the reported procedure and the PCE of TBSQDs was found to be 43.65%. The time vs temperature profiling of TBSQDs and Milli-Q is given in Figure 6.3c and 6.3e respectively.

The stability of a photothermal agent is an essential requirement and organic dyes are more prone to photo-bleaching. To evaluate the stability of TBSQDs, the material was subjected to NIR laser exposure for multiple times and it was observed that the material has retained its photo-thermal properties even after 4 cycles of NIR laser exposure (5 min each), as

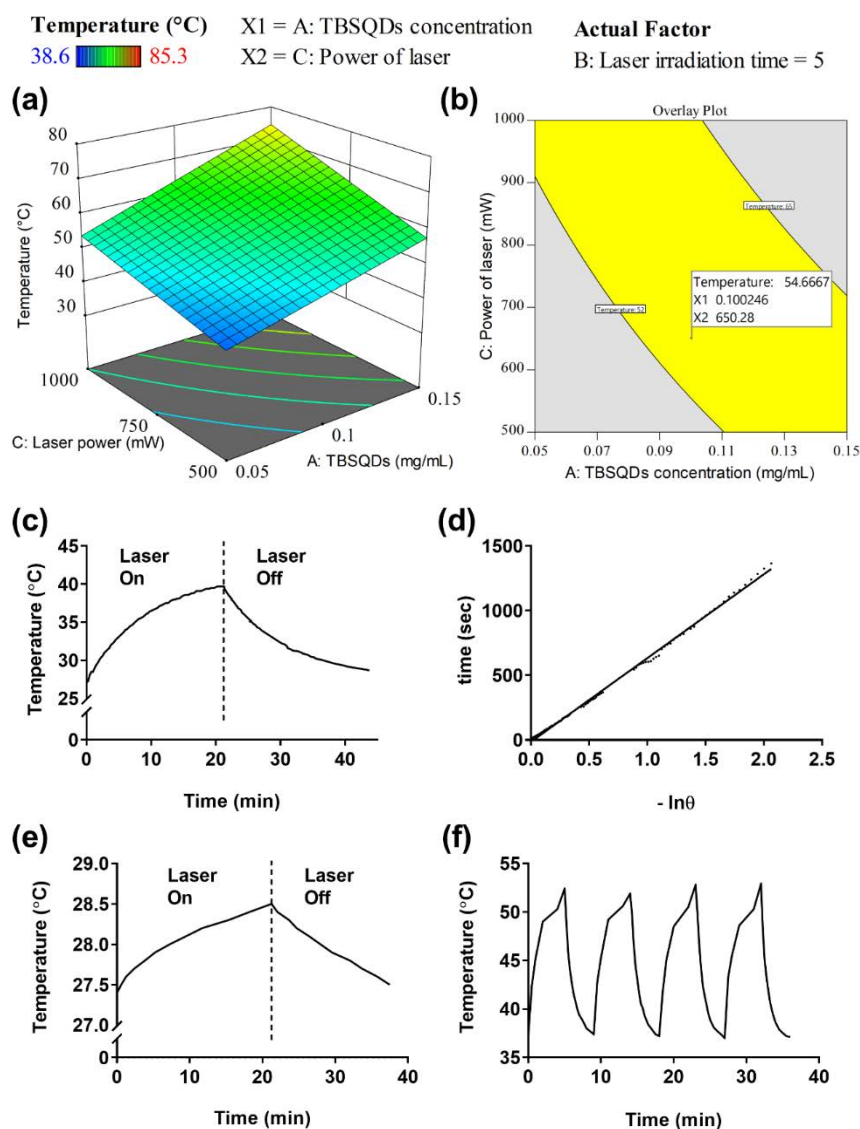


Figure 6.4. (a) 3D plot, (b) design space for the response-temperature, (c) temperature change corresponding to laser ON and OFF of TBSQDs, (d) time versus negative logarithm of temperature (θ) from the cooling stage of TBSQDs, (e) time vs temperature profile of Milli-Q, and (f) multi-cycle temperature changes upon exposure of FF-BSC NP with 750 nm laser.

shown in Figure 6.4f. To further evaluate the stability, the absorbance and fluorescence spectrum were recorded, and no spectral differences were observed. These studies indicate that the material has excellent photothermal properties, conversion efficiency and photo-stability. The phot-stability is of particular interest, as most of the organic dyes are prone to photo-bleaching. These properties make TBSQDs an ideal candidate for cancer theragnostic.

6.2.4 In-vitro studies

Biocompatibility: The *in vitro* biocompatibility of TBSQDs was carried out in mouse fibroblast L929 cells. The viable cells convert non-fluorescent blue colored resazurin to fluorescent red-colored resofurin and the intensity of later was evaluated for estimating the % cell viability. It was observed that the TBSQDs possessed excellent biocompatibility even up to a concentration of 150 $\mu\text{g/mL}$, as shown in Figure 6.5a.

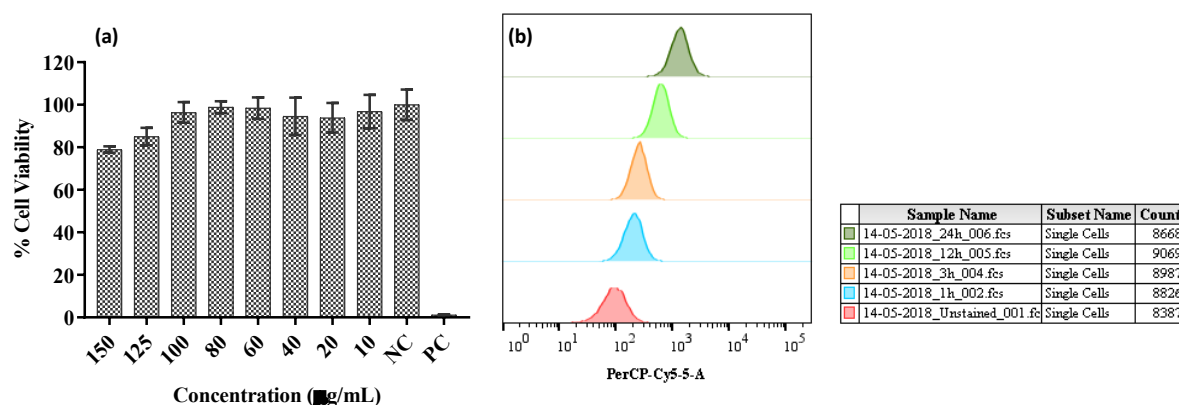


Figure 6.5: (a) Biocompatibility of TBSQDs in L929 cells at various concentrations. (b) Cellular uptake of TBSQDs in 4T1 cells at different time points by FACS.

Cellular uptake: The cellular uptake of TBSQDs in 4T1 cells was evaluated by FACS and CLSM. Flow cytometry enables the evaluation of intensity of fluorescence in cells, thereby providing the fraction of cells with the nanoparticles. The shift in the median of fluorescence peak at various time points in comparison to the negative control indicates the uptake of particles. It is clear from the Figure 6.5b that there is a shift in the median value with increase in incubation time. Further, after 24 hours, internalization was found to be almost 100% in comparison to the control cells. Furthermore, qualitative *in vitro* cellular uptake of the TBSQDs was performed in 4T1 cells. The 4T1 cells were incubated with TBSQDs (10 $\mu\text{g/well}$) for 24 hours. CLSM data (Figure 6.6) revealed that the TBSQDs were internalized in the cells and was able to exhibit strong fluorescence in NIR region (680-740 nm). DAPI staining experiments were carried out to understand the localisation of TBSQDs in the cells showed (Figure 6.6) that the TBSQDs were localised in cytoplasm of the cells with very good emission in NIR region and not present inside the nucleus.

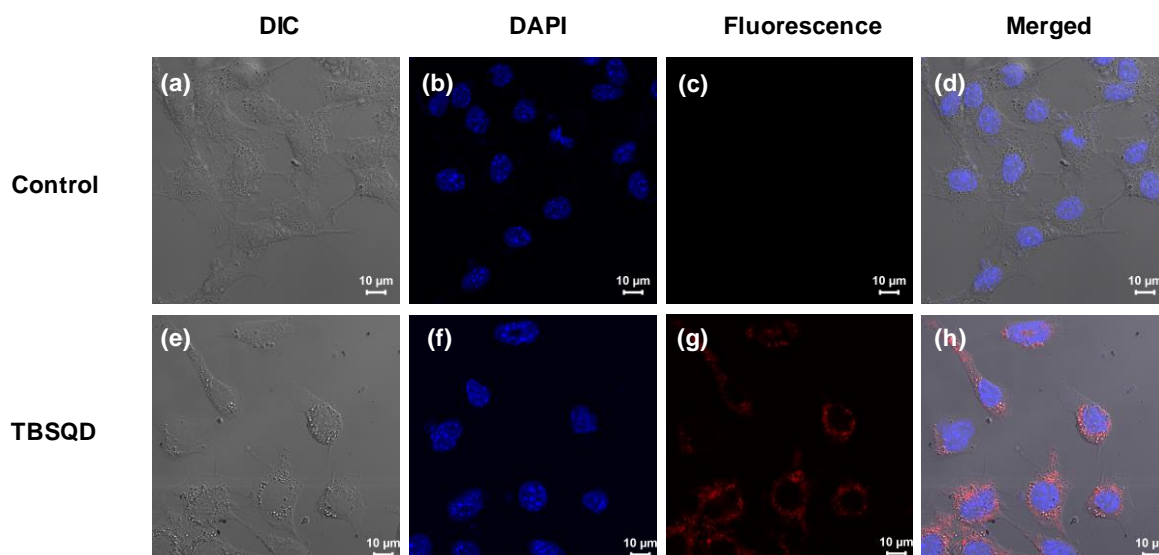


Figure 6.6. CLSM images showing 4T1 Control cells treated with DAPI (a) Differential Interference Contrast (DIC) image, (b) DAPI channel with 410-454 nm emission filter, (c) Fluorescence channel with 680-730 nm emission filter, (d) merged image of all channels and 4T1 cells treated with DAPI and TBSQD, (e) Differential Interference Contrast (DIC) image, (f) DAPI channel with 410-454 nm emission filter, (g) Fluorescence channel with 680-730 nm emission filter and (h) merged image of all channels.

In vitro photothermal efficacy: The *in vitro* photothermal efficacy testing carried out in 4T1 cells revealed that the material is highly efficient. As shown in the Figure 6.7a, at 10 $\mu\text{g/mL}$ with 650 mW laser power for 7 min, the cell viability was less than 5%, while at 10 $\mu\text{g/mL}$ for 5 min laser power, the viability was around 10%, and the cell exposed to only laser and only TBSQDs had viability greater than 95%, thus suggesting the effective photothermal potential of TBSQDs with low laser power exposure.

Hemocompatibility: Hemocompatibility is an important assay after biocompatibility assay for all materials that are designed to be administered in the body. Surface charge, morphology, and size of the designed material strongly affects its interactions with RBCs, and hemolysis occurs if haemoglobin is released due to this interaction. The TBSQDs showed less than 5% hemolysis at various concentrations till 200 $\mu\text{g/mL}$ and can be considered as hemocompatible. The positive control showed 100% hemolysis in comparison to the negative control. ESEM imaging was employed to examine the morphology of the treated RBCs, where no significant variation was observed in the biconcave morphology in the treated sample with respect to untreated negative control, shown in Figure 6.7f.

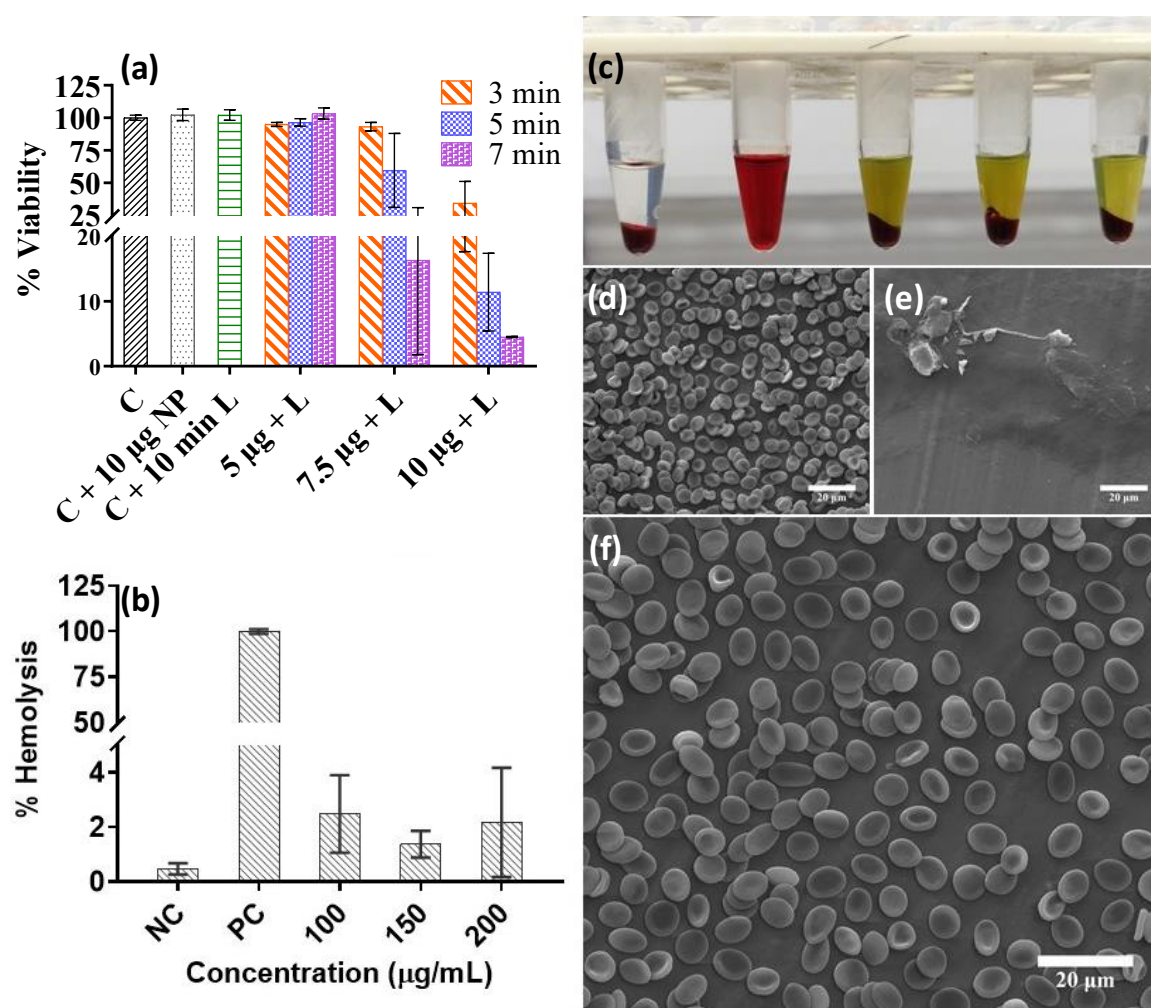


Figure 6.7: (a) *in vitro* photothermal efficacy in 4T1 cells, (b) graph depicting the hemocompatibility of TBSQD (c) digital image of various samples of hemocompatibility study, ESEM images of RBC treated with (d) negative control (PBS), (e) positive control (triton X-100), (f) 200 µg/mL TBSQD.

6.2.5 *In-vivo* studies

Biodistribution and Toxicity Testing TBSQDs: An understanding of the *in vivo* biodistribution of an external agent like nanoparticles is a prerequisite to assess its pharmacodynamics and associated adverse effects. 14 days post intravenous administration of TBSQDs, *ex vivo* fluorescence imaging of the vital organs revealed that majority of the nanoparticles were accumulated in the liver, lung and spleen, followed by kidney and heart suggesting that the major portion of the injected material is taken up by the components of the reticuloendothelial system in the body (Figure 6.8). Accumulation of a portion of injected material in the kidney also suggest the possibility of renal clearance.

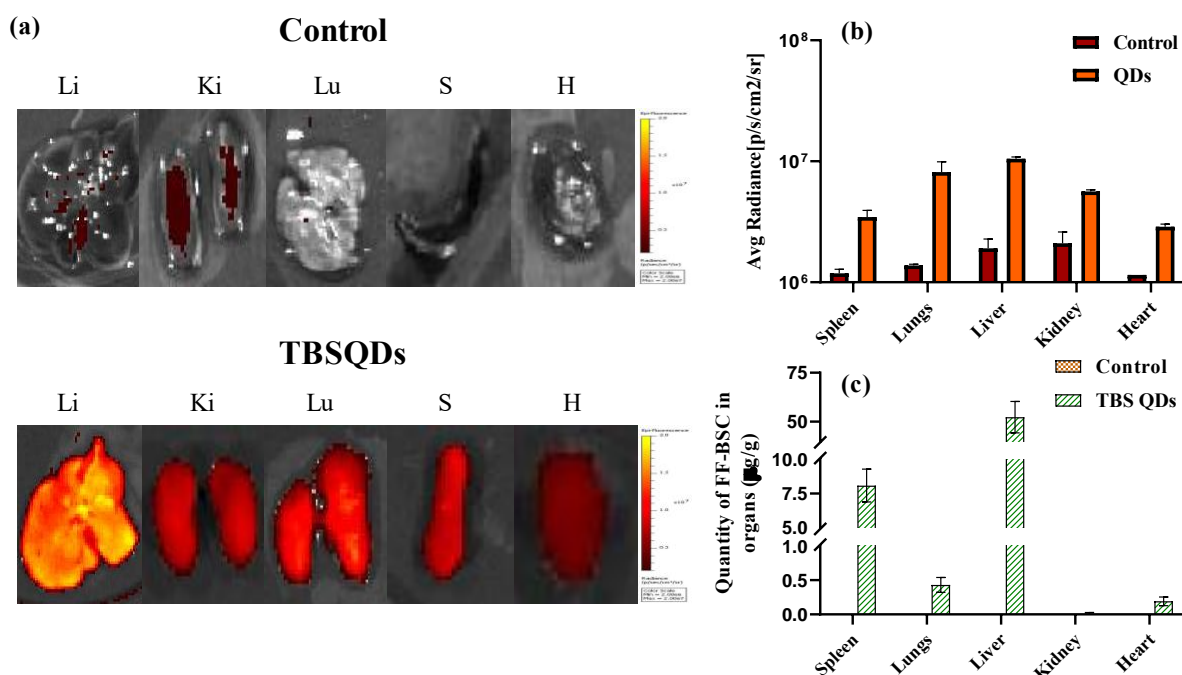


Figure 6.8: (a) *Ex vivo* fluorescence imaging of different vital organs collected from control and TBS QDs injected mice on day 14 post material injection (b) Qualitative evaluation of fluorescence output from organ samples of spleen, lungs, liver, kidney and heart from control and treated mice (c) Quantitative estimation of TBSQDs from organ samples of spleen, lungs, liver, kidney and heart from control and treated mice.

In vivo photothermal efficacy TBS QDs: The photothermal efficacy testing of TBS QDs revealed that the material possesses excellent efficacy *in vivo*. It was observed that there was a dramatic reduction in bioluminescence signal post first and second treatment, indicative of drastic tumor ablation. However, presence of residual tumor at the treatment site suggest the necessity of third treatment. Third photothermal treatment to this group imparts complete tumor ablation (bioluminescence signal post third treatment was equivalent to the background signal). This was further associated with no signs of weight loss post PTT suggesting no therapy burden. The bioluminescence signal of control as well the material control groups showed continuous increase, indicating the non-toxic nature of material and progressive tumor growth. The control groups as well as material control group showed signs of necrosis at day 5, beyond which no further imaging was carried for these animals owing to the ethical concerns and the mice were sacrificed. Treated animals were followed till day 30 post treatment and showed no increase in the bioluminescence signal, highlighting effective and complete tumor ablation with no signs of relapse post PTT prolonging the overall survival of the treated mice.

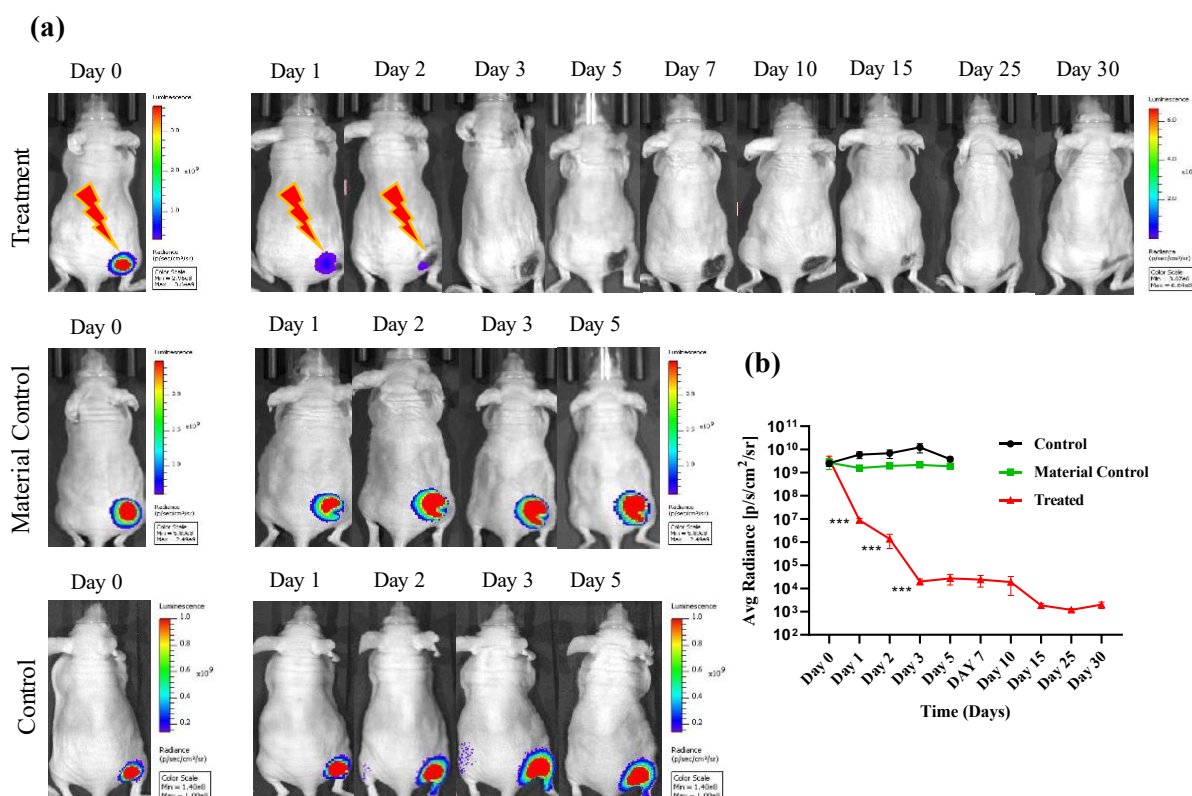


Figure 6.9: In vivo photothermal ablation by TBS QDs in 4T1 xenograft mouse model: (a) representative in vivo bioluminescence images of various treatment groups, (b) quantitative assessment of bioluminescence signal for different groups during the follow-up (***) indicates $P = 0.001$ post third treatment)

6.3 Conclusion

We have successfully synthesized BF_2 -oxasmaragdyrin based quantum dots (TBSQDs) by subjecting BF_2 -oxasmaragdyrin to moderate pressures of ~ 800 bar using high pressure homogenizer at room temperature, employing lipid to stabilize the same. Direct evidence of formation of quantum dots was obtained by Surface-Enhanced Raman Scattering (SERS) and Transmission Electron Microscopy (TEM). TBSQDs have interesting photophysical properties with good absorption in Vis-NIR region and fluorescence in NIR region with decent quantum yield. Invitro studies showed that the TBSQDs was biocompatible and easily internalized into 4T1 cells with good emission in NIR region. Further, TBSQDs exhibited excellent photothermal properties with good conversion efficiency and the same was evaluated *in vitro* and *in vivo*. NIR Fluorescence and Photothermal properties of TBSQDs makes it an excellent choice as a theragnostic agent.

6.4 Experimental

All chemicals were procured from Aldrich and used as received unless otherwise noted. All solvents were of at least reagent grade and dried if necessary. Sucrose, D-(+)-trehalose dihydrate, D(-)-mannitol and resazurin sodium salt were purchased from Merck Life Science Pvt. Ltd. (India). Roswell park memorial institute media (RPMI-1640), fetal bovine serum (FBS), dulbecco's modified eagle media (DMEM), phosphate-buffered saline (PBS), and antibiotic-antimycotic were purchased from HiMedia Laboratories Pvt. Ltd. (India). Pluronic F-68 was generously provided by BASF, India. The ¹H, ¹¹B, ¹⁹F, and ¹³C NMR spectra were recorded in CDCl₃ with a Bruker 400 or 500 MHz instrument. The frequency of 101 and 126 MHz is used for ¹³C nucleus. Tetramethylsilane [Si(CH₃)₄] was used as an internal standard for ¹H and ¹³C NMR spectroscopy, tetrafluorotoluene as an external standard for ¹⁹F NMR, and boric acid as an external standard for ¹¹B NMR spectroscopy. Absorption and steady state fluorescence spectra were obtained with a Cary series UV/Vis-NIR spectrophotometer and a Varian-Cary Eclipse spectrofluorometer, respectively. The fluorescence quantum yields (Φ_f) were estimated from emission and absorption spectra by comparative method at the excitation wavelength of 440 nm by using H2TTP ($\Phi_f = 0.11$) as the standard. The time-resolved fluorescence decay measurements were carried out at the magic angle using a picosecond-diode-laser-based, time-correlated, single-photon-counting (TCSPC) fluorescence spectrometer from IBH, UK. All the decays were fitted to single exponential unless specified. All solutions were purged prior to spectral measurements with argon gas. High-resolution mass spectra (HRMS) were recorded with a Bruker maxis Impact and Q-ToF micro mass spectrometer. For UV/Vis and fluorescence the stock solutions of all compounds (1×10^{-3} M) were prepared by using HPLC grade chloroform solvent and Milli-Q water. Field emission gun transmission electron microscope (FEG-TEM, JEM-1400 and JSM-2100F, Jeol Ltd., Japan) were employed for morphology characterization. Nuclear magnetic resonance (NMR) was recorded with Bruker 400 and 500 MHz instruments. Environmental scanning electron microscopy (ESEM, Quanta 200, FEI, Austria) was used for observing the morphology of red blood cells (RBCs). Confocal Laser Scanning Microscopy (CLSM) experiments were carried on Olympus (IX 81) & Fluoview 500.

Synthesis of *meso*-Tritolyl-BF₂-oxasmaragdyrin (TBS)⁵⁹

A sample of 25-oxasmaragdyrin (0.157 mmol) was taken in CH₂Cl₂ (30 mL) and triethylamine (6.28 mmol) was added at room temperature. After 5 min BF₃·Et₂O (7.85 mmol) was added, and stirring was continued at room temperature for 30 min. The reaction mixture was diluted

with CH₂Cl₂ and washed thoroughly with 0.1 M NaOH solution and water. The organic layers were combined, dried over Na₂SO₄, and filtered, and solvent was removed on a rotary evaporator under vacuum. The resulting crude product was purified by column chromatography on alumina, using petroleum ether/dichloromethane (70:30), and afforded pure compound TBS as a green powder. Yield: 81 mg, 76%; mp >300 °C; ¹H NMR (400 MHz, CDCl₃, δ in ppm): 3.60 (t, 2H; NH), 2.76 (s, 9H; Tol), 7.66 (d, 4H, 3J(H,H) = 7.0 Hz; Ar), 7.75 (d, 2H, 3J(H,H) = 7.0 Hz; Ar), 8.26 (d, 4H, 3J(H,H) = 6.7 Hz; Ar), 8.46 (d, 2H, 3J(H,H) = 6.7 Hz; Ar), 8.92 (dd, 2H, 3J(H,H) = 4.4 Hz, 4J(H,H) = 1.4 Hz; Py), 9.41 (s, 2H; Fur), 9.52 (d, 2H, 3J(H,H) = 7.0 Hz; Py), 10.15 (dd, 2H, 3J(H,H) = 4.4 Hz, 4J(H,H) = 1.4 Hz; Py), 10.20 (d, 2H, 3J(H,H) = 7.0 Hz; Py); ¹⁹F NMR (282.2 MHz, CDCl₃, δ in ppm): 149.6 (bs); ¹¹B NMR (96.3 MHz, CDCl₃, δ in ppm): 12.04 (bs); ¹³C NMR (100 MHz, CDCl₃, δ in ppm): 21.7, 21.8, 107.0, 120.1, 120.5, 121.7, 123.7, 124.8, 125.0, 128.4, 129.4, 130.7, 131.1, 132.0, 134.4, 134.8, 136.2, 138.0, 138.1, 139.7, 149.9; HRMS (ESI) *m/z*: [M + H]⁺ calculated for C₄₄H₃₃BF₂N₄O 682.2715; found, 682.2682.

Synthesis of TBSQDs

The synthesis of TBSQDs was carried out by thin-film hydration followed by high pressure homogenization. Briefly, TBS and lipid S-75 were dissolved in chloroform and the solvent was removed under reduced pressure at 45 °C, till a thin film was formed. The film was hydrated at 55 °C, and 150 rpm for 1 hour. the suspension was subjected to high shear homogenization (T-25, IKA) at 10000 rpm for 5 min. Further, the suspension was subjected to high pressure homogenization at 800 bar (Emulsiflex B15, Avestin) for 10 passes. The suspension was stored at 5 ± 3 °C, for further evaluation.

Photothermal transduction studies

The photothermal transduction potential of TBSQDs was studied using a 750 nm continuous wave (CW) NIR laser. The impact of independent variables on the temperature raise, concentration of nanoparticles, laser power and laser exposure time were evaluated by constructing a face centred central composite design (CCD). CCD comprising of 17 runs and 3 centre points was designed using Design Expert and the levels selected for independent variables is given in Table 6.3. The experiments were carried out in a 96 well plate by irradiating 100 μL nanoparticle suspension with NIR laser, maintaining the experimental conditions as per the design layout provided in Table 6.4.

Table 6.3: Types of variables, levels and selected ranges of factors for constructing the design

Type of variables	Levels		
	Low (-1)	Medium (0)	High (+1)
<i>Independent variable (Factors)</i>			
A = Concentration of TBSQDs (mg/mL)	0.05	0.1	0.15
B = Laser irradiation time (min)	1	5.5	10
C = Power of laser (mW)	500	750	1000
<i>Dependent variable (Response)</i>			
R = Temperature (°C)			

The statistical evaluation of the selected model was carried out with Analysis of variance (ANOVA).

Table 6.4: CCD layout along with experimental results

	Factor 1	Factor 2	Factor 3	Response 1
Run	A: TBSQDs concentration (mg/mL)	B: Laser irradiation time (min)	C: Power of laser (mW)	Temperature (°C)
1	0.15	10	1000	85.3
2	0.15	5.5	750	67.6
3	0.1	10	750	63.3
4	0.1	5.5	500	49.5
5	0.1	5.5	750	58
6	0.15	10	500	58.8
7	0.1	5.5	1000	66.5
8	0.05	1	500	38.6
9	0.05	10	500	43.6
10	0.05	5.5	750	46.9
11	0.15	1	500	49.8
12	0.1	5.5	750	59.8
13	0.1	1	750	44.6
14	0.15	1	1000	58.3
15	0.05	10	1000	63.2
16	0.1	5.5	750	60
17	0.05	1	1000	40.6

Table 6.5: Sequential model sum of squares

Source	Sum of Squares	df	Mean Square	F-value	p-value	
Mean vs Total	53581.14	1	53581.14			
Linear vs Mean	1974.19	3	658.06	31.85	< 0.0001	
2FI vs Linear	189.68	3	63.23	8.01	0.0052	
Quadratic vs 2FI	57.50	3	19.17	6.26	0.0215	Suggested
Cubic vs Quadratic	13.29	4	3.32	1.23	0.4514	Aliased
Residual	8.13	3	2.71			
Total	55823.94	17	3283.76			

Table 6.6: ANOVA for the response, temperature for quadratic model

Source	Sum of Squares	df	Mean Square	F-value	p-value	
Model	2211.99	6	368.66	119.65	< 0.0001	significant
A-TBSQDs concentration	755.16	1	755.16	245.08	< 0.0001	
B-Laser irradiation time	677.33	1	677.33	219.82	< 0.0001	
C-Power of laser	541.70	1	541.70	175.81	< 0.0001	
AC	22.44	1	22.44	7.28	0.0224	
BC	158.42	1	158.42	51.41	< 0.0001	
B ²	56.94	1	56.94	18.48	0.0016	
Residual	30.81	10	3.08			
Lack of Fit	28.39	8	3.55	2.92	0.2797	not significant
Pure Error	2.43	2	1.21			
Cor Total	2242.80	16				

Table 6.7: Confirmatory trials to evaluate the design space

Trial No.	TBSQDs (mg/mL)	Laser exposure time (min)	Laser power (mW)	95% PI low	Data Mean	95% PI high
1	0.1	1	650	40.8678	42.8	49.5642
2	0.1	2	650	43.9288	45.6	52.308
3	0.1	3	650	46.4944	48.9	54.8127
4	0.1	4	650	48.6391	51.4	57.0037
5	0.1	5	650	50.4153	54.9	58.8287

Photothermal conversion efficiency study

Photothermal conversion (η) efficiency for TBSQDs was carried as per the reported procedure, using the following equation.

$$\eta = \frac{hS(T_{\text{Max}} - T_{\text{Surr}}) - Q_{\text{Dis}}}{I(1 - 10^{-A_{750}})} \quad (1)$$

Where h indicates heat transfer coefficient, S indicates sample well surface area, T_{Max} is the steady state maximum temperature attained by TBSQDs, T_{Surr} is the room temperature, Q_{Dis} is baseline energy input, I indicate the laser power, and A_{750} is the absorbance of TBSQDs at 750 nm. TBSQDs suspension, dispensed in quartz cuvette was subjected to NIR laser irradiation and the temperature raise was recorded. Laser exposure was carried out till saturation was attained and the drop was recorded and plotted. Further, milli Q was exposed to NIR laser and the laser was turned off once equilibrium was attained and photothermal conversion efficiency was calculated.⁶²

Photo-stability and multi cycle PTT

The photo-stability and repetitive photothermal potential of TBSQDs was carried out by exposing nanoparticles to NIR laser for extended period and the temperature changes were monitored. 100 μL nanoparticle suspension was dispensed in 96 well plate and irradiated with 750 nm laser for 6 min at 650 mW and temperature was monitored at regular intervals. The sample was allowed to cool to room temperature and was subjected to NIR laser with same experimental conditions and the cycle was repeated for 3 times. Temperature was recorded during each cycle and the graph; temperature vs time was plotted.

Cell culture

Mouse fibroblast (L929) cell line was procured from NCL, India and mouse breast cancer (4T1) cell line was procured from ATCC, USA. RPMI-1640 supplemented with 10% FBS, and 1% v/v was used for culturing 4T1 cells. DMEM, supplemented with 1% v/v antibiotic, and 10% v/v FBS was employed for culturing L929 cells, and the incubation condition for both cell lines was 37 °C and 5% CO₂.

Biocompatibility Study

In vitro biocompatibility of TBSQDs was determined by exponentially growing L929 cells with alamar blue assay. The cells were trypsinized and seeded in a 96 well plate at a density of $\sim 6 \times 10^3$ cells/well and incubated for 24 h. After 24 h, the components of the wells were replaced with media containing varying concentration of TBSQDs, ranging from 10 µg/mL to 300 µg/mL. Complete media and 1% triton X-100 were employed as negative and positive controls respectively and were incubated for 24 h. The components of wells were carefully removed and washed with PBS, followed by addition of alamar blue (10 µg/well) and incubated for 4 hours. The fluorescence was recorded with excitation and emission wavelengths being 560 nm and 590 nm respectively, using a microplate reader (TECAN Infinite 200 PRO series). The percentage cell viability was calculated using the following equation

$$\text{Cell viability (\%)} = \frac{\text{Fluorescence intensity of treated sample}}{\text{Fluorescence intensity of control sample}} \times 100$$

Intensity of sample indicates the intensity of samples treated with varying concentrations of TBSQDs and control reflects intensity of negative control.

Cellular uptake

FACS

Cell internalization of TBSQDs was carried out in 4T1 cells. Briefly, cells were seeded at a density of 1×10^6 cells per 60 mm dish and incubated for 24 hours under humidified conditions. Freshly prepared sample (10 µg/mL) was incubated with cells for different time periods i.e. 1h, 3h, 6h, 12h and 24h. After the incubation period, the contents of the dish were removed, washed with PBS, and trypsinized. Cells were centrifuged and redispersed in 0.5 mL PBS and internalization was quantified using flow cytometer. The excitation wavelength was 488 nm

(blue) laser and emission was captured employing APC-Alexa 700-A channel and minimum of 10000 events were recorded. Gating was carried out to remove any debris, free nanoparticles, or dead cells and the data was analysed with FlowJo.

Confocal Laser Scanning Microscopy (CLSM)

CLSM was performed to evaluate the cellular uptake in 4T1 cells. Briefly, the cells were seeded on sterile coverslips in a 12-well plate at a density of 25000 cells/well and incubated for 24 hours. The solution of TBSQDs was diluted appropriately and added to each well such that the final amount of compound in each well is 10 µg/well. The cells were incubated for 24 h, followed careful washing with PBS and fixation. The fixation was carried out with 4% paraformaldehyde (15 min) at room temperature, followed by PBS wash. CLSM imaging (Olympus (IX 81) & Fluoview 500 and LEICA TCS SP8) was performed on fixed cells by using 488 nm excitation and 680-740 nm emission filter respectively.

DAPI staining: The fixed cells were stained with DAPI (10 µg/well) for 30 seconds and thoroughly washed with PBS. CLSM imaging was performed on fixed cells using 405 nm excitation and 410-454 nm emission filter for DAPI channel; 458 nm excitation and 680-732 nm emission filter for fluorescence channel of TBSQDs.

Biodistribution and Single dose toxicity testing of TBSQDs

Biodistribution and single dose toxicity testing of TBSQD was carried out in healthy female swiss bare mice, post approval by Institute Animal Ethics Committee (IAEC), at ACTREC. The animals were housed in 12 hrs light and dark cycle as per the Committee for the Purpose of Control and Supervision on Experiments in Animals (CPCSEA) guidelines during the experimentation. Briefly, the mice were divided in two groups: control and test (n=5 each), the control group was administered with PBS, while the test group with 200 µg of TBSQDs through tail vein. The mice were monitored for changes in body weight for 14 days and at the end of 14th day, the mice were sacrificed, blood and major organs i.e. liver, kidney, lungs, heart and spleen were harvested. Blood was centrifuged at 2500 rpm and the supernatant containing serum was further processed for serum biochemical analysis. A small part of the harvested organs were fixed in formaldehyde, paraffin blocks were made and haematoxylin & eosin staining was performed in order to identify associated toxicity of the materials to these vital organs, if any. Ex vivo fluorescence imaging of harvested organs was performed by recording the spectra at an excitation and emission wavelength of 465 and 720 nm respectively, using IVIS spectrum imaging system, Caliper life sciences, USA. Qualitative assessment of

the amount of TBSQDs accumulated, was done by comparing the fluorescence output from harvested organs of material injected mice with that of the control mice. For further quantification the organs were snap frozen in liquid nitrogen, followed by grinding and extraction with DMSO. The absolute quantification was done by comparing the fluorescence of the extracted lysate from different organs to that of the standard curve and total nanoparticles accumulated in different organs was represented in terms of μg of compound/gram of the tissue.

***In vivo* photothermal efficacy and bioluminescence imaging for TBSQDs**

The *in vivo* photothermal efficacy testing of TBSQDs was carried out in CD1 nude mice. Tumor was induced by implanting 1×10^6 4T1 fl2 cells subcutaneously on the right flank of CD1 nude mice. Mice were randomly segregated into control, material control and treatment groups ($n=5$ for each group) as the desired tumor volume was attained (70 to 80 mm^3). The tumor growth was monitored through live animal imaging by administering 100 μL of D-luciferin (3 mg/ml) intraperitoneally. Bioluminescence imaging was done in IVIS Lumina II imaging system, Caliper life sciences, USA by keeping F stop 8, at a time interval of 1 min till the peak signal is attained. Briefly, control animals were administered with PBS while material control and treatment groups with 100 μg of TBSQDs intra-tumorally. The control and material control groups were devoid of laser irradiation. However, the treatment group was further subjected to 750 nm fixed wavelength laser irradiation for 5 min (650 mW) and this treatment cycle was given simultaneously for 3 days. Bioluminescence signal was recorded for all the groups at regular intervals till day 30 post PTT to understand the effectiveness of TBSQDs for PTT mediated tumor ablation. Living image v4.4 software was used to acquire the images, quantify the signal and the signal output was reported in terms of average radiance ($\text{p/sec/cm}^2/\text{sr}$).

6.5 References

- (1) Bray, F.; Ferlay, J.; Soerjomataram, I.; Siegel, R. L.; Torre, L. A.; Jemal, A. Global Cancer Statistics 2018: GLOBOCAN Estimates of Incidence and Mortality Worldwide for 36 Cancers in 185 Countries. *CA. Cancer J. Clin.* **2018**, *68*, 394–424.
- (2) Vines, J. B.; Yoon, J. H.; Ryu, N. E.; Lim, D. J.; Park, H. Gold Nanoparticles for Photothermal Cancer Therapy. *Front. Chem.* **2019**, *7*, 167–182.
- (3) Lal, S.; Clare, S. E.; Halas, N. J. Nanoshell-Enabled Photothermal Cancer Therapy: Impending Clinical Impact. *Acc. Chem. Res.* **2008**, *41*, 1842–1851.

- (4) Dickerson, E. B.; Dreaden, E. C.; Huang, X.; El-Sayed, I. H.; Chu, H.; Pushpanketh, S.; McDonald, J. F.; El-Sayed, M. A. Gold Nanorod Assisted Near-Infrared Plasmonic Photothermal Therapy (PPTT) of Squamous Cell Carcinoma in Mice. *Cancer Lett.* **2008**, *269*, 57–66.
- (5) Gao, L.; Fei, J.; Zhao, J.; Li, H.; Cui, Y.; Li, J. Hypocrellin-Loaded Gold Nanocages with High Two-Photon Efficiency for Photothermal/Photodynamic Cancer Therapy in Vitro. *ACS Nano* **2012**, *6*, 8030–8040.
- (6) Qin, C.; Fei, J.; Wang, A.; Yang, Y.; Li, J. Rational Assembly of a Biointerfaced Core@shell Nanocomplex towards Selective and Highly Efficient Synergistic Photothermal/Photodynamic Therapy. *Nanoscale* **2015**, *7*, 20197–20210.
- (7) Abadeer, N. S.; Murphy, C. J. Recent Progress in Cancer Thermal Therapy Using Gold Nanoparticles. *J. Phys. Chem. C* **2016**, *120*, 4691–4716.
- (8) Yang, K.; Zhang, S.; Zhang, G.; Sun, X.; Lee, S.-T.; Liu, Z. Graphene in Mice: Ultrahigh In Vivo Tumor Uptake and Efficient Photothermal Therapy. *Nano Lett.* **2010**, *10*, 3318–3323.
- (9) Robinson, J. T.; Tabakman, S. M.; Liang, Y.; Wang, H.; Sanchez Casalongue, H.; Vinh, D.; Dai, H. Ultrasmall Reduced Graphene Oxide with High Near-Infrared Absorbance for Photothermal Therapy. *J. Am. Chem. Soc.* **2011**, *133*, 6825–6831.
- (10) Sun, Z.; Xie, H.; Tang, S.; Yu, X. F.; Guo, Z.; Shao, J.; Zhang, H.; Huang, H.; Wang, H.; Chu, P. K. Ultrasmall Black Phosphorus Quantum Dots: Synthesis and Use as Photothermal Agents. *Angew. Chem. Int. Ed.* **2015**, *54*, 11526–11530.
- (11) Tao, W.; Zhu, X.; Yu, X.; Zeng, X.; Xiao, Q.; Zhang, X.; Ji, X.; Wang, X.; Shi, J.; Zhang, H.; et al. Black Phosphorus Nanosheets as a Robust Delivery Platform for Cancer Theranostics. *Adv. Mater.* **2017**, *29*, 1603276–1603284.
- (12) Zhao, Z.; Shi, S.; Huang, Y.; Tang, S.; Chen, X. Simultaneous Photodynamic and Photothermal Therapy Using Photosensitizer-Functionalized Pd Nanosheets by Single Continuous Wave Laser. *ACS Appl. Mater. Interfaces* **2014**, *6*, 8878–8885.
- (13) Shi, S.; Huang, Y.; Chen, X.; Weng, J.; Zheng, N. Optimization of Surface Coating on Small Pd Nanosheets for in Vivo Near-Infrared Photothermal Therapy of Tumor. *ACS Appl. Mater. Interfaces* **2015**, *7*, 14369–14375.
- (14) Tian, Q.; Jiang, F.; Zou, R.; Liu, Q.; Chen, Z.; Zhu, M.; Yang, S.; Wang, J.; Wang, J.; Hu, J. Hydrophilic Cu₉S₅ Nanocrystals: A Photothermal Agent with a 25.7% Heat Conversion Efficiency for Photothermal Ablation of Cancer Cells in Vivo. *ACS Nano* **2011**, *5*, 9761–9771.

- (15) Zhou, M.; Li, J.; Liang, S.; Sood, A. K.; Liang, D.; Li, C. CuS Nanodots with Ultrahigh Efficient Renal Clearance for Positron Emission Tomography Imaging and Image-Guided Photothermal Therapy. *ACS Nano* **2015**, *9*, 7085–7096.
- (16) Hessel, C. M.; Pattani, V. P.; Rasch, M.; Panthani, M. G.; Koo, B.; Tunnell, J. W.; Korgel, B. A. Copper Selenide Nanocrystals for Photothermal Therapy. *Nano Lett.* **2011**, *11*, 2560–2566.
- (17) Song, G.; Shen, J.; Jiang, F.; Hu, R.; Li, W.; An, L.; Zou, R.; Chen, Z.; Qin, Z.; Hu, J. Hydrophilic Molybdenum Oxide Nanomaterials with Controlled Morphology and Strong Plasmonic Absorption for Photothermal Ablation of Cancer Cells. *ACS Appl. Mater. Interfaces* **2014**, *6*, 3915–3922.
- (18) Zhou, J.; Lu, Z.; Zhu, X.; Wang, X.; Liao, Y.; Ma, Z.; Li, F. NIR Photothermal Therapy Using Polyaniline Nanoparticles. *Biomaterials* **2013**, *34*, 9584–9592.
- (19) Yang, J.; Choi, J.; Bang, D.; Kim, E.; Lim, E.-K.; Park, H.; Suh, J.-S.; Lee, K.; Yoo, K.-H.; Kim, E.-K.; et al. Convertible Organic Nanoparticles for Near-Infrared Photothermal Ablation of Cancer Cells. *Angew. Chem. Int. Ed.* **2010**, *50*, 441–444.
- (20) Xu, L.; Cheng, L.; Wang, C.; Peng, R.; Liu, Z. Conjugated Polymers for Photothermal Therapy of Cancer. *Polym. Chem.* **2014**, *5*, 1573–1580.
- (21) Geng, J.; Sun, C.; Liu, J.; Liao, L.-D.; Yuan, Y.; Thakor, N.; Wang, J.; Liu, B. Biocompatible Conjugated Polymer Nanoparticles for Efficient Photothermal Tumor Therapy. *Small* **2014**, *11*, 1603–1610.
- (22) Feng, G.; Liu, J.; Geng, J.; Liu, B. Conjugated Polymer Microparticles for Selective Cancer Cell Image-Guided Photothermal Therapy. *J. Mater. Chem. B* **2015**, *3*, 1135–1141.
- (23) Cheng, L.; Wang, C.; Feng, L.; Yang, K.; Liu, Z. Functional Nanomaterials for Phototherapies of Cancer. *Chem. Rev.* **2014**, *114*, 10869–10939.
- (24) Chen, M.; Fang, X.; Tang, S.; Zheng, N. Polypyrrole Nanoparticles for High-Performance in Vivo near-Infrared Photothermal Cancer Therapy. *Chem. Commun.* **2012**, *48*, 8934–8936.
- (25) Song, X.; Chen, Q.; Liu, Z. Recent Advances in the Development of Organic Photothermal Nano-Agents. *Nano Research*. Tsinghua University Press 2015, pp 340–354.
- (26) Reed, M. A. Quantum Dots. *Sci. Am.* **1993**, *268*, 118–123.
- (27) Bera, D.; Qian, L.; Tseng, T.-K.; Holloway, P. H. Quantum Dots and Their Multimodal Applications: A Review. *Materials (Basel)*. **2010**, *3*, 2260–2345.

- (28) Jing, L.; Kershaw, S. V.; Li, Y.; Huang, X.; Li, Y.; Rogach, A. L.; Gao, M. Aqueous Based Semiconductor Nanocrystals. *Chemical Reviews*. American Chemical Society September 28, 2016, pp 10623–10730.
- (29) Pietryga, J. M.; Park, Y. S.; Lim, J.; Fidler, A. F.; Bae, W. K.; Brovelli, S.; Klimov, V. I. Spectroscopic and Device Aspects of Nanocrystal Quantum Dots. *Chemical Reviews*. American Chemical Society September 28, 2016, pp 10513–10622.
- (30) Burda, C.; Chen, X.; Narayanan, R.; El-Sayed, M. A. Chemistry and Properties of Nanocrystals of Different Shapes. *Chemical Reviews*. April 2005, pp 1025–1102.
- (31) Carey, G. H.; Abdelhady, A. L.; Ning, Z.; Thon, S. M.; Bakr, O. M.; Sargent, E. H. Colloidal Quantum Dot Solar Cells. *Chemical Reviews*. American Chemical Society 2015, pp 12732–12763.
- (32) Kumawat, M. K.; Thakur, M.; Gurung, R. B.; Srivastava, R. Graphene Quantum Dots for Cell Proliferation, Nucleus Imaging, and Photoluminescent Sensing Applications. *Sci. Rep.* **2017**, 7, 15858.
- (33) Gupta, V.; Chaudhary, N.; Srivastava, R.; Sharma, G. D.; Bhardwaj, R.; Chand, S. Luminescent Graphene Quantum Dots for Organic Photovoltaic Devices. *J. Am. Chem. Soc.* **2011**, 133, 9960–9963.
- (34) Wang, L.; Wang, Y.; Xu, T.; Liao, H.; Yao, C.; Liu, Y.; Li, Z.; Chen, Z.; Pan, D.; Sun, L.; et al. Gram-Scale Synthesis of Single-Crystalline Graphene Quantum Dots with Superior Optical Properties. *Nat Commun* **2014**, 5, 5357–5365.
- (35) Kozák, O.; Sudolská, M.; Pramanik, G.; Cígler, P.; Otyepka, M.; Zbořil, R. Photoluminescent Carbon Nanostructures. *Chem. Mater.* **2016**, 28, 4085–4128.
- (36) Lim, S. Y.; Shen, W.; Gao, Z. Carbon Quantum Dots and Their Applications. *Chem. Soc. Rev.* **2015**, 44, 362–381.
- (37) Wang, R.; Lu, K.-Q.; Tang, Z.-R.; Xu, Y.-J. Recent Progress in Carbon Quantum Dots: Synthesis, Properties and Applications in Photocatalysis. *J. Mater. Chem. A* **2017**, 5, 3717–3734.
- (38) Wang, Y.; Hu, A. Carbon Quantum Dots: Synthesis, Properties and Applications. *J. Mater. Chem. C* **2014**, 2, 6921–6939.
- (39) Zhang, J.; Yu, S.-H. Carbon Dots: Large-Scale Synthesis, Sensing and Bioimaging. *Mater. Today* **2016**, 19, 382–393.
- (40) Zhu, S.; Meng, Q.; Wang, L.; Zhang, J.; Song, Y.; Jin, H.; Zhang, K.; Sun, H.; Wang, H.; Yang, B. Highly Photoluminescent Carbon Dots for Multicolor Patterning, Sensors, and Bioimaging. *Angew. Chem. Int. Ed.* **2013**, 52, 3953–3957.

- (41) Yang, Y.; Cui, J.; Zheng, M.; Hu, C.; Tan, S.; Xiao, Y.; Yang, Q.; Liu, Y. One-Step Synthesis of Amino-Functionalized Fluorescent Carbon Nanoparticles by Hydrothermal Carbonization of Chitosan. *Chem. Commun.* **2012**, 48, 380–382.
- (42) Xu, Y.; Wu, M.; Liu, Y.; Feng, X.-Z.; Yin, X.-B.; He, X.-W.; Zhang, Y.-K. Nitrogen-Doped Carbon Dots: A Facile and General Preparation Method, Photoluminescence Investigation, and Imaging Applications. *Chem. - A Eur. J.* **2013**, 19, 2276–2283.
- (43) Sun, D.; Ban, R.; Zhang, P. H.; Wu, G. H.; Zhang, J. R.; Zhu, J. J. Hair Fiber as a Precursor for Synthesizing of Sulfur- and Nitrogen-Co-Doped Carbon Dots with Tunable Luminescence Properties. *Carbon N. Y.* **2013**, 64, 424–434.
- (44) Chandra, S.; Patra, P.; Pathan, S. H.; Roy, S.; Mitra, S.; Layek, A.; Bhar, R.; Pramanik, P.; Goswami, A. Luminescent S-Doped Carbon Dots: An Emergent Architecture for Multimodal Applications. *J. Mater. Chem. B* **2013**, 1, 2375–2382.
- (45) Wang, D.; Chen, J.-F.; Dai, L. Recent Advances in Graphene Quantum Dots for Fluorescence Bioimaging from Cells through Tissues to Animals. *Part. Part. Syst. Charact.* **2015**, 32, 515–523.
- (46) Diac, A.; Focsan, M.; Socaci, C.; Gabudean, A. M.; Farcau, C.; Maniu, D.; Vasile, E.; Terec, A.; Veca, L. M.; Astilean, S. Covalent Conjugation of Carbon Dots with Rhodamine B and Assessment of Their Photophysical Properties. *RSC Adv.* **2015**, 5, 77662–77669.
- (47) Wu, F.; Su, H.; Cai, Y.; Wong, W.-K.; Jiang, W.; Zhu, X. Porphyrin-Implanted Carbon Nanodots for Photoacoustic Imaging and in Vivo Breast Cancer Ablation. *ACS Appl. Bio Mater.* **2018**, 1, 110–117.
- (48) Barman, M. K.; Jana, B.; Bhattacharyya, S.; Patra, A. Photophysical Properties of Doped Carbon Dots (N, P, and B) and Their Influence on Electron/Hole Transfer in Carbon Dots–Nickel (II) Phthalocyanine Conjugates. *J. Phys. Chem. C* **2014**, 118, 20034–20041.
- (49) Koh, K. H.; Noh, S. H.; Kim, T. H.; Lee, W. J.; Yi, S. C.; Han, T. H. A Graphene Quantum Dot/Phthalocyanine Conjugate: A Synergistic Catalyst for the Oxygen Reduction Reaction. *RSC Adv.* **2017**, 7, 26113–26119.
- (50) Nwahara, N.; Nkhahle, R.; Ngoy, B. P.; Mack, J.; Nyokong, T. Synthesis and Photophysical Properties of BODIPY-Decorated Graphene Quantum Dot-Phthalocyanine Conjugates. *New J. Chem.* **2018**, 42, 6051–6061.
- (51) Nene, L. C.; Managa, M.; Nyokong, T. Photo-Physicochemical Properties and in Vitro Photodynamic Therapy Activity of Morpholine-Substituted Zinc(II)-Phthalocyanines π - π Stacked on Biotinylated Graphene Quantum Dots. *Dye. Pigment.* **2019**, 165, 488–498.

- (52) Xu, T.; Wang, D.; Dong, L.; Shen, H.; Lu, W.; Chen, W. Graphitic Carbon Nitride Co-Modified by Zinc Phthalocyanine and Graphene Quantum Dots for the Efficient Photocatalytic Degradation of Refractory Contaminants. *Appl. Catal. B Environ.* **2019**, *244*, 96–106.
- (53) Ding, H.; Zhou, X.; Qin, B.; Zhou, Z.; Zhao, Y. Highly Fluorescent Near-Infrared Emitting Carbon Dots Derived from Lemon Juice and Its Bioimaging Application. *J. Lumin.* **2019**, *211*, 298–304.
- (54) Tao, H.; Yang, K.; Ma, Z.; Wan, J.; Zhang, Y.; Kang, Z.; Liu, Z. In Vivo NIR Fluorescence Imaging, Biodistribution, and Toxicology of Photoluminescent Carbon Dots Produced from Carbon Nanotubes and Graphite. *Small* **2012**, *8*, 281–290.
- (55) Li, L.; Zhang, R.; Lu, C.; Sun, J.; Wang, L.; Qu, B.; Li, T.; Liu, Y.; Li, S. In Situ Synthesis of NIR-Light Emitting Carbon Dots Derived from Spinach for Bio-Imaging Applications. *J. Mater. Chem. B* **2017**, *5*, 7328–7334.
- (56) Sun, Y. P.; Wang, P.; Lu, Z.; Yang, F.; Mezziani, M. J.; LeCroy, G. E.; Liu, Y.; Qian, H. Host-Guest Carbon Dots for Enhanced Optical Properties and Beyond. *Sci. Rep.* **2015**, *5*, 12354–12359.
- (57) Kobayashi, H.; Ogawa, M.; Alford, R.; Choyke, P. L.; Urano, Y. New Strategies for Fluorescent Probe Design in Medical Diagnostic Imaging. *Chem. Rev.* **2010**, *110*, 2620–2640.
- (58) Zheng, M.; Li, Y.; Liu, S.; Wang, W.; Xie, Z.; Jing, X. One-Pot To Synthesize Multifunctional Carbon Dots for Near Infrared Fluorescence Imaging and Photothermal Cancer Therapy. *ACS Appl. Mater. Interfaces* **2016**, *8*, 23533–23541.
- (59) Rajeswara Rao, M.; Ravikanth, M. Boron Complexes of Oxasmaragdyrin, a Core-Modified Expanded Porphyrin. *J. Org. Chem.* **2011**, *76*, 3582–3587.
- (60) Chatterjee, T.; Srinivasan, A.; Ravikanth, M.; Chandrashekar, T. K. Smaragdyrins and Sapphyrins Analogues. *Chem. Rev.* **2017**, *117*, 3329–3376.
- (61) Pareek, Y.; Ravikanth, M.; Chandrashekar, T. K. Smaragdyrins: Emeralds of Expanded Porphyrin Family. *Acc. Chem. Res.* **2012**, *45*, 1801–1816.
- (62) Roper, D. K.; Ahn, W.; Hoepfner, M. Microscale Heat Transfer Transduced by Surface Plasmon Resonant Gold Nanoparticles. *J. Phys. Chem. C* **2007**, *111*, 3636–3641.

Chapter 7

*Cell Penetrating Peptide Conjugated BF₂-Oxasmaragdyrin As NIR
Imaging and Photothermal Therapeutic Agents*

7.1 Introduction

Near-Infra Red Fluorescence (NIRF) imaging has attracted a lot of attention in recent years as an alternative and sophisticated tool for non-invasive imaging and diagnostic techniques for *in vitro* as well as *in vivo* applications over the existing imaging techniques. It is partly owing to relatively more transparency of mammalian cells in NIR region (650-900 nm, 1100-1300 nm) leading to the higher penetrating ability of NIR light into live tissues and better signal to noise ratio in fluorescence signal.¹ Furthermore, Photothermal therapy (PTT) has emerged as a useful tool for cancer therapy for its advantages in easy administration and less time for treatment.¹ These materials can also be used for photoacoustic (PA) imaging² of tissues to provide higher resolutions than optical microscopic techniques. To date, few inorganic nanoparticles,^{3, 4} black phosphorus quantum dots,⁵ organic polymer based materials^{6, 7} have been used as PTT agents.

Hence there is a growing demand for new dyes which absorb and emit strongly in the NIR region. Upon perusal of literature, there are only few dye molecules such as cyanine dyes,⁸⁻¹⁰ xanthenes,¹¹ squaraine dyes,¹²⁻¹⁵ benzo[c]heterocycles,^{16, 17} BODIPY analogs,¹⁸⁻²⁰ phthalocyanines and a small selection of porphyrin derivatives²¹⁻²⁴ which absorb and emit in the NIR region. One such molecule belongs to expanded porphyrins, which absorb and emit in the NIR region is pentaazasmaragdyrin **I**. Pentaazasmaragdyrin **I** is a pentapyrrolic macrocycle in which five pyrroles are connected by three methene bridges and two pyrrole-pyrrole direct bonds. Though pentaazasmaragdyrin **I** was discovered in the 1960s, its synthesis was elusive until recently owing to its unstable nature in its free base.²⁵ Chandrasekhar and co-workers were successful in synthesizing stable *meso* triaryl 25-oxasmaragdyrins **II** in which one of the pyrrole rings of pentaazasmaragdyrin was replaced with a furan ring.²⁶⁻²⁸ The 25-oxasmaragdyrins absorb and emit in the Vis-NIR region with moderate quantum yields and singlet state lifetimes. Recently, our group reported the synthesis of BF₂- (**III**) and PO₂- (**IV**) complexes of 25-oxasmaragdyrins which are much more stable and exhibit much better photophysical properties compared to that of freebase 25-oxasmaragdyrin **III**.^{29, 30} Though BF₂- and PO₂- complexes of 25-oxasmaragdyrins have excellent photophysical properties, their potential for biological applications was least explored owing to its hydrophobicity.³¹

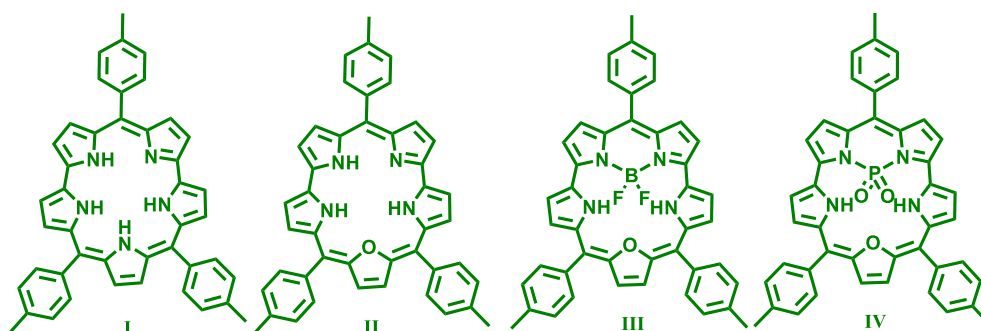


Chart 7.1: Structures of smaragdyrin analogues.

Various targeting molecules have been used to internalize hydrophobic drugs and nanoparticles such as transferrin,³² pluronic,³³ folic acid,³⁴ biotin,³⁵ and polysaccharides.³⁶ Alternatively, cell penetrating peptides (CPPs) can also be used to deliver the hydrophobic dyes/drugs into the cells by either covalent/noncovalent conjugation of CPPs with the target cargo.³⁷ CPPs have numerous advantages over other materials such as low toxicity, biodegradability, specifically targeting receptors, etc. Garcion and coworkers have shown that the functionalized micelles of CRGDK could be used for delivering anticancer drugs (Doxorubicin) in cancer cell lines (Breast MDA-MB-231, Prostatic PC3 cancer cell lines).³⁸ Similarly, Matsushita and co-workers have shown that the polyarginine (R₉) is novel CPPs targeting human glioblastoma cell lines.^{39, 40}

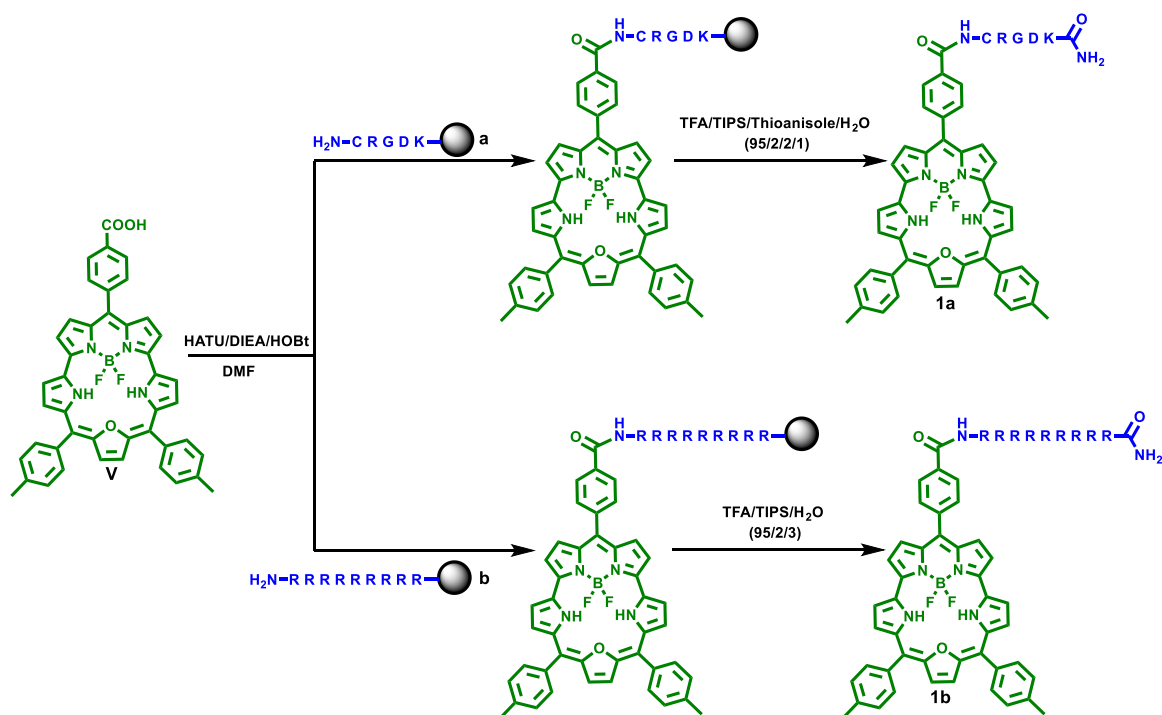
Herein, we report the synthesis of CPPs such as CRGDK and R₉ peptide conjugated BF₂-oxasmaragdyrin molecules by solid phase peptide synthesis, purification by RP-HPLC and their use as NIR fluorescence imaging agents. Furthermore, R₉-conjugated BF₂-oxasmaragdyrin behaves as an active photothermal agent with good light to heat conversion with respect to that of the existing materials when irradiated with 750 nm laser. The R₉-conjugated BF₂-oxasmaragdyrin can be used as a dual agent as both NIR Fluorescence imaging as well as photothermal therapeutic (PTT) agent as shown in this work.

7.2 Results and Discussions

7.2.1 Synthesis and characterization

The target CRGDK conjugated BF₂-25-oxasmaragdyrin **1a** and R₉ conjugated BF₂-25-oxasmaragdyrin **1b** were prepared over a sequence of steps, as shown in Scheme 7.1. The starting BF₂-25-oxasmaragdyrin **V** containing *p*-carboxymethylphenyl substituent at *meso* position was synthesized by a reported method.³⁰ Solid supported (Rink amide) peptides with free *N*-terminal **a**, **b** were prepared by standard automated microwave-accelerated solid-phase

peptide synthesis procedure with *fmoc*-protected amino acid precursors. The formation of desired sequence was determined by sample cleavage of resin (30 mg) with TFA/TIPS/H₂O (3 mL, 95:3:2) followed by evaporation of solvent, precipitation of peptide by cold Et₂O (3 mL) and analysis of crude precipitate by analytical Reverse Phase HPLC (RP-HPLC) and mass spectrometry. To obtain solid supported BF₂-oxasmaragdyrin-peptide conjugates, corresponding solid supported (Rink amide) peptides with free *N*-terminal was treated with the mixture containing BF₂-25-oxasmaragdyrin **V**, HATU, HOBt and DIEA in DMF (3 mL) and shaken for 24 hours. After completion of the reaction, the resin was thoroughly washed with DMF (20 × 5 mL) and CH₂Cl₂ (20 × 5 mL). Respective resins were cleaved with corresponding cleavage mixtures (20 mL) for 3 hours followed by evaporation of the solvent, precipitation by cold Et₂O (20 mL). The precipitate was centrifuged, and the supernatant was removed to give crude compounds **1a** and **1b** as green solids. In order to purify the compounds **1a** and **1b**, RP-HPLC analysis was performed on Agilent 1200 series instruments



Scheme 7.1: Synthesis of CRGDK and R₉ conjugated BF₂-oxasmaragdyrin **1a** and **1b**.

by dissolving the crude solids in corresponding solvent mixtures (**1a** in 2:1:7 DMSO/ACN/H₂O and **1b** in 1:1:8 DMSO/ACN/H₂O) at a concentrations of 2-3 mg/mL and injecting 50 μL onto Vydac C18 (4.6 × 250 mm, 5 μm) analytical column and using a linear gradient of 0.1% TFA at a flow rate of 1.5 mL/min. The RP-HPLC analysis of crude residues

of compounds **1a** and **1b** showed that the residues contain some impurities along with the desired compound identified by mass spectrometry. To obtain pure compounds, preparative RP-HPLC was performed on compounds **1a**, **1b** using C4, C18 columns respectively with a

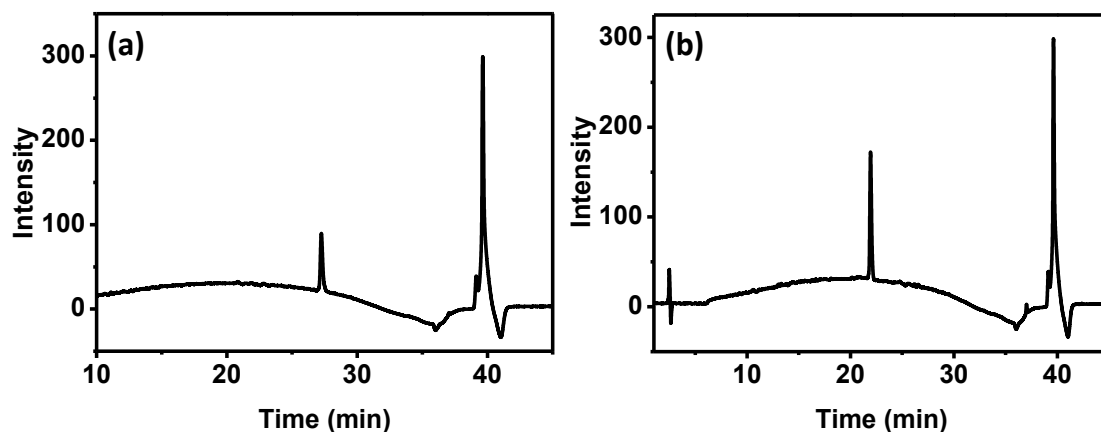


Figure 7.1: HPLC traces for pure compounds **1a** and **1b**.

flow rate of 10 mL min⁻¹ under linear gradients of 0.1% TFA in MeCN. The fractions corresponding to the desired products were identified, combined together and lyophilized to give pure compounds **1a** and **1b** as green foamy solids in 11.0% and 5.2% yields respectively. The compounds **1a-b** were characterised by mass spectrometry which showed peak corresponding to molecular ion ($[M+H]^+$) and analytical RP-HPLC showed that the compounds **1a-b** as a single peak with >95% purity (Figure 7.1).

7.2.2 Photophysical characterization

The absorption and fluorescence studies were performed on compounds **1a-b** and the data are tabulated in Table 7.1. Compound **1a** absorbs in the visible region and emits in the NIR region (~717 nm) with moderate quantum yield ($\phi_f = 0.23$) and an excited state lifetime of 4.74 ns (figure 7.2a-c). Compound **1a** aggregates in the presence of H₂O leading to red shift with a significant broadening in absorption spectra (Figure 2a) and complete quenching of fluorescence (Figure 7.2b). Similarly, compound **1b** also absorbs in the visible region and emits in NIR region (~719 nm) with a moderate quantum yield ($\phi_f = 0.24$) and an excited state lifetime of 5.23 ns (Figure 7.2d-f). Compound **1b** also aggregates in H₂O which was observed as broadening of absorption spectra with a slight redshift. The quenching of fluorescence of compound **1b** (Figure 7.2e) with a decrease in quantum yield in H₂O ($\phi_f = 0.04$) was observed compared to that of DMSO ($\phi_f = 0.24$). A decrease in an excited state

lifetime was also observed for compound **1b** in H₂O ($\tau_s = 3.32$ ns) compared to that of the DMSO ($\tau_s = 5.23$ ns).

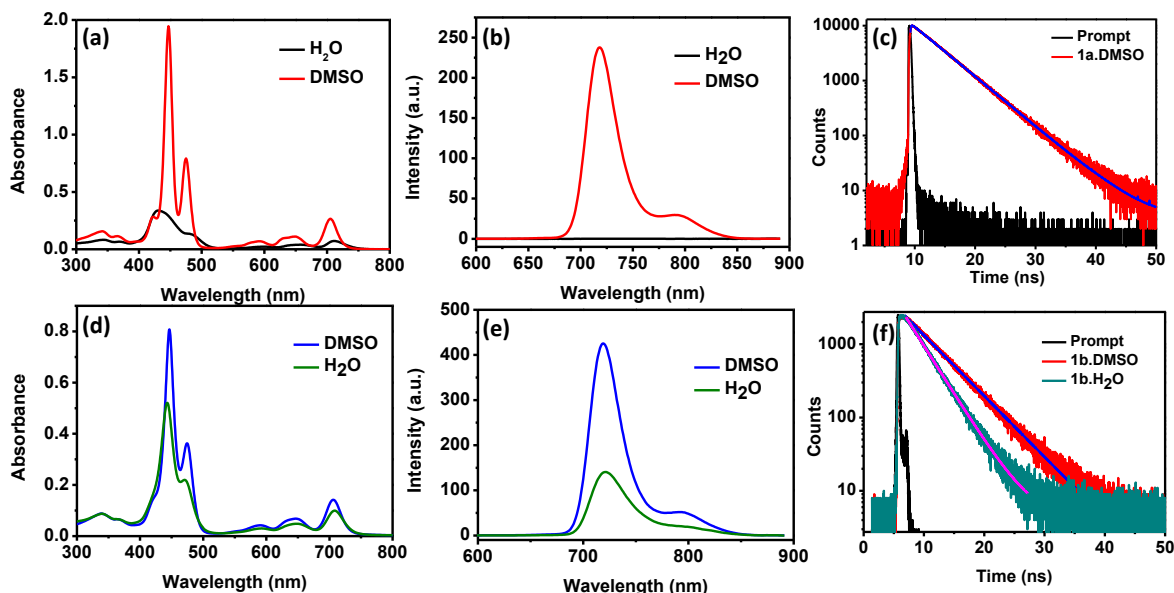


Figure 7.2: (a) Absorption (b) fluorescence (c) TCSPC of compound **1a** in different solvents. (d) Absorption (e) fluorescence (f) TCSPC of compound **1b** in different solvents.

Table 7.1: Photophysical data for compounds **1a** and **1b**.

Compounds		Wavelength (nm) (ϵ in [$\text{mol}^{-1} \text{L cm}^{-1} \times 10^5$])					λ_f (nm)	ϕ_f	τ_s (ns)
I		446 (2.50)	553 (1.26)	591 (0.10)	634 (0.12)	647 (0.15)	703 (0.39)	708	0.15 --
1a.DMSO		446 (1.96)	475 (0.79)	590 (0.08)	630 (0.10)	646 (0.12)	704 (0.27)	717	0.23 4.74
1a.H₂O		446 (0.34)	475 (0.14)	590 (0.02)	--	656 (0.04)	711 (0.07)	--	-- --
1b.DMSO		447 (5.1)	475 (2.27)	591 (0.23)	632 (0.33)	650 (0.36)	706 (0.81)	719	0.24 5.23
1b.H₂O		446 (1.52)	475 (0.64)	593 (0.14)	--	652 (0.19)	708 (0.31)	721	0.04 3.32

7.2.3 In vitro studies

Biocompatibility: The synthesized compounds **1a-b** is intended to be used as imaging agents and evaluation of biocompatibility is a pre-requisite. The compound **1a** was evaluated for biocompatibility in L929 cells with varying concentrations, ranging from 10 $\mu\text{g/mL}$ to 150

$\mu\text{g/mL}$ and presented in Figure 7.3. The compound **1a** was biocompatible in the evaluated range and the morphology was intact after 24 h exposure and the % cell viability was $>80\%$ with the highest concentration making compound **1a** as highly biocompatible and could be used to evaluate further studies.

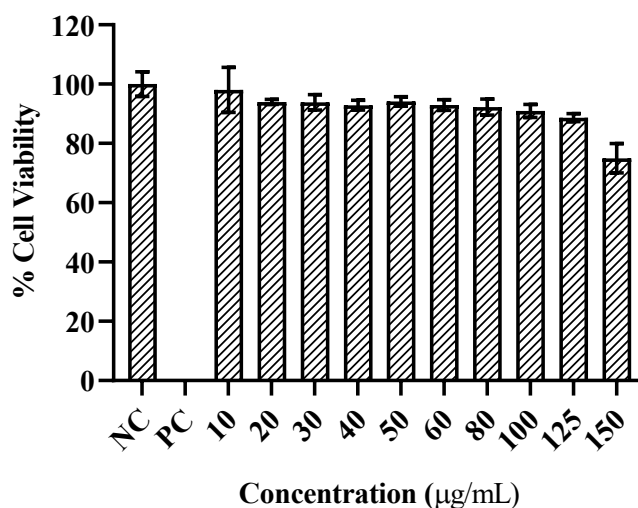


Figure 7.3: Cell viability studies of compound **1a** on L929 cells.

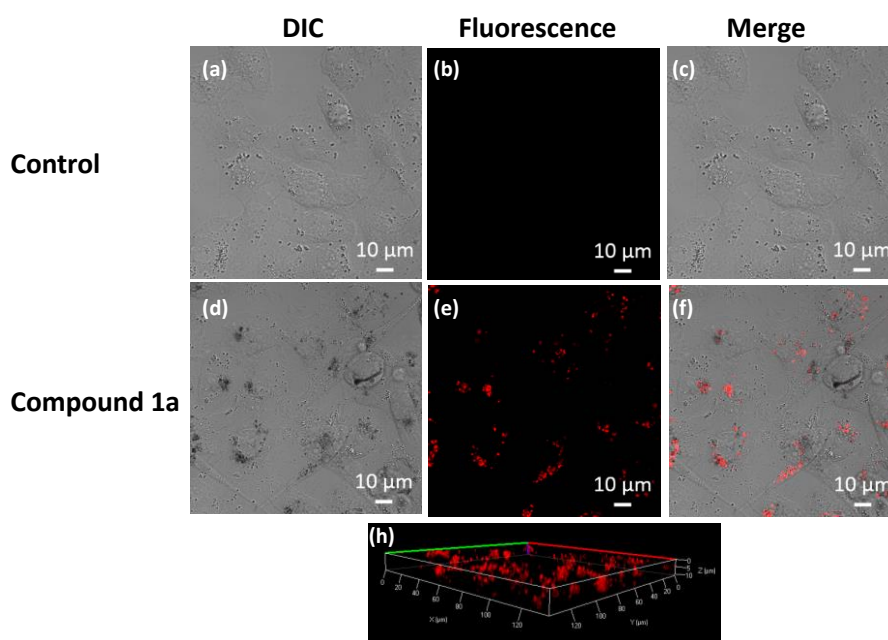


Figure 7.4: CLSM images of control cells (a) Differential Interference Contrast (DIC) channel, (b) fluorescence channel (c) merged image of all channels, cells treated with compound **1a** (d) DIC channel, (e) fluorescence channel, (f) merged image of all channels. cells treated with compound **1a** (h) 3D view of compound **1a** localization in MDA-MB-231 cells. Fluorescence channel was recorded with 680-740 nm emission filter.

Cellular uptake: To evaluate the behaviour of material in the presence of cells i.e., the inherent property of fluorescence, qualitative invitro cellular uptake of the compounds **1a-b**

was performed in MDA MB 231 cells. CLSM data (Figure 7.4 and 7.5) revealed that the material was internalized in the cells within 24 hours of incubation and was able to exhibit strong fluorescence in NIR region, which could be exploited for the *in vivo* whole body imaging or site specific imaging.

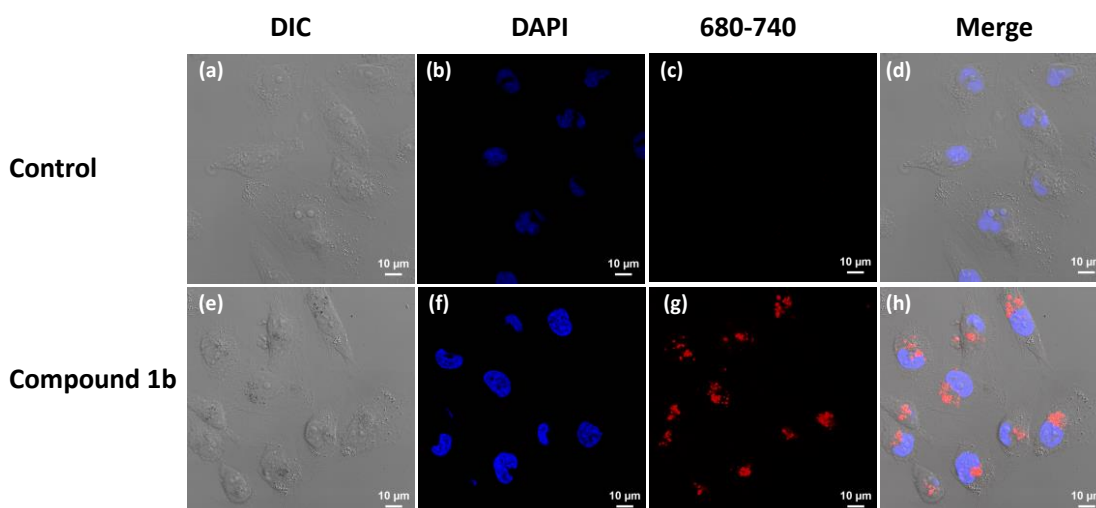


Figure 7.5: CLSM images of control cells (a) Differential Interference Contrast (DIC) channel, (b) DAPI channel (c) fluorescence channel (d) merged image of all channels, cells treated with compound **1b** (e) DIC channel, (f) DAPI channel, (g) fluorescence channel, (h) merged image of all channels. Fluorescence channel was recorded with 680-740 nm emission filter.

7.2.4 Photothermal properties

Photothermal transduction studies: Photothermal transduction studies were performed to evaluate the photothermal efficacy of compound **1b**. The factors that plays an important role in the photothermal transduction of a material are concentration of sample used, laser power used and the time period of exposure of laser. By constructing a CCD design, it was possible to evaluate the impact of individual and interaction factors over the selected response. The design layout along with the experimental results are presented in Table 7.3 and Table 7.4. Quadratic model was selected since the p-value was less than 0.05, based on sequential sum of squares as shown in Table 7.5. ANOVA of the selected indicated that the chosen model was with lack of fit insignificant, as shown in Table 7.6. It can be clearly observed that the model was significant ($p < 0.0001$), and the lack of fit insignificant ($p > 0.05$). Further, R^2 of the selected model was 0.951 and the difference between the adjusted and predicted R^2 was less than 0.2, indicating the selected model could be used for evaluation of design space. The

equation, used for evaluating the relative impact of various factors on response is given in equation 1.

$$\text{Temperature} = +51.77 + 5.54A + 4.21B + 8.26C + 2.11AC + -6.87C^2 \quad (1)$$

From this equation, it can be understood that the factor C has the highest impact on response, followed by A and B. Further, diagnostics revealed no anomalies with the selected model and the contour as well as 3D plots are presented in Figure 7.6a-b, which could be used to evaluate the impact of individual factors. Design space (yellow region) for the selected model was constructed by setting the response value in the range, 52-65 °C, as shown in Figure 4c. The design space was evaluated by selecting three random points and the results are presented in Table 7.7. From the results, it can be concluded that the design space was evaluated and the material possess excellent photothermal properties. These properties could be utilized for photothermal cancer therapy.

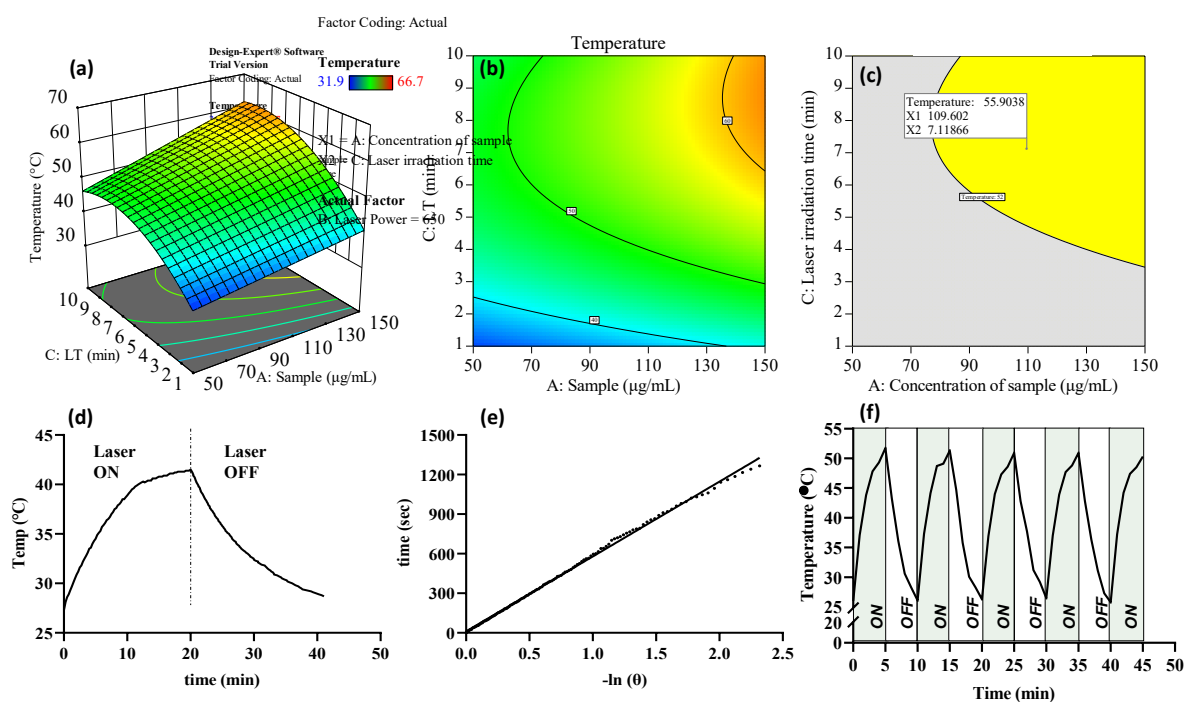


Figure 7.6: (a) 2D contour plot, (b) 3D response surface plot, and (c) graphical optimization plot (Design Space) for the selected response, temperature (LT indicates laser irradiation time). (d) temperature change corresponding to laser ON and OFF of compound **1b**, (e) time versus natural logarithm of temperature (θ) from the cooling stage of polyarginine-BSC and (f) multi-cycle photothermal transduction potential of compound **1b** upon NIR laser irradiation (ON indicates laser on and OFF indicates laser was off during that period).

Photothermal conversion efficiency: Photothermal conversion efficiency of the material was calculated by the equation 2 mentioned in experimental section. The sample was irradiated with NIR laser and the temperature increment and decrement was recorded and plotted as

shown in figure 7.6d-e. Based on the calculations, the photothermal conversion efficiency of compound **1b** was found to be 72.29%. From this study, it can be concluded that the compound **1b** possesses excellent photothermal properties and conversion efficiency, which could be exploited for its application in photothermal cancer therapy.

Multi-cycle photothermal transduction potential: Most of the organic dyes are extremely sensitive to light and possess very less thermal stability, thus inhibiting their usage for multi-cycle PTT. The multi-cycle photothermal transduction potential of compound **1b** was evaluated by irradiating the same sample with 750 nm for multiple times and evaluating the temperature increment. Compound **1b** was able to show the temperature increment even after four cycles of exposure (5 min cycle each) as shown in figure 7.6f, indicating excellent stability. Photobleaching results in loss of fluorescence and photothermal transduction potential of organic compounds and compound **1b** exhibited no signs of photobleaching.

7.3 Conclusions:

We have successfully synthesized CPPs CRGDK and R₉ conjugated BF₂-oxasmaragdyrin conjugates by following the automated SPPS method. The synthesized compounds were purified by RP-HPLC and characterized by mass spectrometry. The photophysical properties of synthesized compounds were thoroughly evaluated and found that both the conjugates were stable, absorb in the UV-Vis and emit in the NIR region with moderate quantum yields and singlet state lifetimes. CLSM experiments also revealed that the conjugates **1a** and **1b** were internalized into the MDA-MB-231 within 24 hours and emitting strong NIR fluorescence from within the cells. The property of NIR emission could be exploited for the *in vivo* whole-body or site-specific imaging. Furthermore, R₉ conjugated BF₂-oxasmaragdyrin **1b** has photothermal property when irradiated with 750 nm laser with a photothermal efficiency of 72.3% and highly stable under irradiation conditions with no bleaching observed from the multi-cycle photothermal transduction potential studies. Compound **1b** could be used as NIR imaging and photothermal therapeutic dual agents for *in vivo* whole-body or site-specific imaging as well as therapy.

7.4 Experimental

All chemicals were used as received unless otherwise noted. All solvents were of at least reagent grade or higher and dried if necessary. The ¹H, ¹¹B, ¹⁹F, and ¹³C NMR spectra were recorded in CDCl₃ on Bruker 400 or 500 MHz instruments. The frequency of 101 MHz is

used for the ^{13}C nucleus. Tetramethylsilane [$\text{Si}(\text{CH}_3)_4$] was used as an internal standard for ^1H and ^{13}C NMR spectra acquisition. Absorption and steady state fluorescence spectra were obtained with Cary series UV-Vis-NIR spectrophotometer and Varian-Cary Eclipse spectrofluorometer respectively. The fluorescence quantum yield (Φ_f) were estimated from emission and absorption spectra by comparative method at the excitation wavelength of 440 nm using H_2TTP ($\Phi_f = 0.11$) as the standard.⁴¹ Cyclic voltammetric studies were carried out with BAS electrochemical system utilizing the three electrode configuration consisting of Glassy carbon (working electrode), platinum wire (auxiliary electrode), and saturated calomel (reference electrode) electrodes. The experiments were done in dry CH_2Cl_2 using 0.1 M tetrabutylammonium perchlorate (TBAP) as the supporting electrolyte. All the solutions were purged prior to collection of electrochemical and spectral measurements with argon gas. The high resolution mass spectra (HRMS) were recorded with a Bruker maxis Impact and Q-Tof micro mass spectrometer. For UV-vis and fluorescence titrations, the stock solution of all compounds (1×10^{-3} M) was prepared using HPLC grade chloroform solvent.

Reverse phase high performance liquid chromatography (RP-HPLC) was performed on Agilent 1200 series instruments. For analytical experiments, the instrument was equipped with photodiode array (PDA) detection (controlled by ChemStation software) and a manual injection port (100 μL loop volume). In preparative examples, instruments used multivariable wavelength (MVW) detection (controlled by ChemStation software) and an Agilent unit injector (2 mL loop volume). The solvent system used throughout this study (except where specified) was buffer A: 0.1% aqueous TFA; buffer B: 0.1% TFA in MeCN. Analytical experiments were performed on Vydac C18 (4.6 x 250 mm, 5 μm) analytical columns, at a flow rate of 1.5 mL min⁻¹. Preparative RP-HPLC was performed on Vydac C18 (22 x 250 mm, 10 μm) and Vydac C4 (22 x 250 mm, 10 μm) preparative columns, at a flow rate of 10 mL min⁻¹. Linear gradients of 0.1% TFA in MeCN were employed as specified.

Automated microwave-accelerated solid-phase peptide synthesis (SPPS) was performed with a CEM Liberty-Discover system. Unless indicated otherwise, all peptides were synthesized on a 0.1 mmol scale on Rink amide resin at 0.61 mmol/g loading (164 mg resin). Manual SPPS was performed in polypropylene Terumo syringes (5 or 10 mL) fitted with a polyethylene porous (20 μm) filter. Resin wash and filtering steps were aided by the use of a Visprep™ SPE DL 24-port model vacuum manifold. Coupling reactions and cleavage mixtures were shaken on a KS125 basic KA elliptical shaker at 400 revolutions per minute

(rpm). Cleaved peptides were collected by centrifugation at a speed of 6,000 rpm, on a Hermle Z200A centrifuge or at a speed of 6,000 rpm on a TMC-1 mini centrifuge.

7.4.1 General automated SPPS procedure

The required amount of rink amide resin (164 mg, 0.1 mmol, 0.61 mmol/g) was added to a 50 mL centrifuge tube and suspended in approximately 10 mL of CH₂Cl₂:DMF (1:1) for approximately 60 minutes. The required Fmoc-protected amino acids (0.2 M in DMF), activator reagents (e.g. HATU, 0.5 M in DMF), activator base (DIPEA, 2 M in NMP) and deprotection reagent (piperidine, 20% v/v in DMF) were made up in the appropriate amounts as determined by the CEM PepDriver program immediately prior to the commencement of the synthesis. The conditions for each automated synthesis step involving most amino acids were as follows:

Table 7.2: Parameters for automated SPPS reactions

Synthetic step	Temperature	Microwave power	Time
initial deprotection	37°C	36 W	2 min
deprotection	75°C	45 W	10 min
pre-activation	25°C	0 W	2 min
coupling	75°C	25 W	10 min

Compound **a**: The desired free *N*-terminal solid supported peptide was prepared by automated microwave-accelerated solid-phase peptide synthesis as described above. The formation of the desired product was confirmed by performing a sample cleavage of the solid supported peptide (30mg) by TFA/TIPS/H₂O (95:3:2) followed by precipitating the peptide by cold Et₂O (2 mL). The precipitate was centrifuged and the residue was analyzed by analytical HPLC with a gradient of 0-100% buffer B/buffer A in 40 min. A single peak at 9.9 min retention time. LRMS C₂₁H₃₉N₉O₈S Mass Calculated: 577.264 [M+H]⁺ Mass Observed: 577.3.

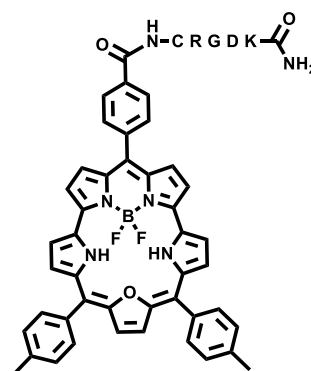


Compound **b**: The desired free *N*-terminal solid supported peptide was prepared by automated microwave-accelerated



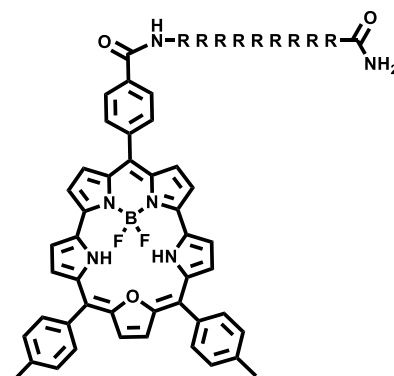
solid-phase peptide synthesis as described above with minor modification. The coupling was carried out at room temperature for 40 min followed by a 25W microwave burst at 75°C for 10 minutes. The formation of the desired product was confirmed by performing a sample cleavage of the solid supported peptide (30mg) by TFA/H₂O (97:3) followed by precipitating the peptide by cold Et₂O (2 mL). The precipitate was centrifuged and the residue was analyzed by analytical HPLC with a gradient of 0-40% buffer B/buffer A in 40 min. A single peak at 13.1 min retention time. LRMS C₅₄H₁₁₁N₃₇O₉ Mass Calculated: 1054 [(M+H+6CF₃COOH)/2]⁺ Mass Observed: 1054.1.

Compound **1a**: To the free *N*-terminal solid supported peptide **a**, mixture of compound **I** (107 mg, 0.15 mmol), HATU (56.7 mg, 0.145 mmol), HOBT (20 mg, 0.145 mmol) and DIEA (80 µL, 0.45 mmol) in DMF (3 mL) was added. The mixture was shaken at room temperature for 24 hours and the solvent was filtered under vacuum. The residue was washed with DMF (8 × 10 mL), CH₂Cl₂ (8 × 10 mL) and dried under vacuum. The crude compound **1a** was



obtained by cleavage of resin by 10 mL of TFA/TIPS/H₂O (95:3:2) followed by precipitating the crude compound **1a** by cold Et₂O (20 mL). The precipitate was centrifuged and the residue was analyzed by analytical HPLC on C4 column with a gradient of 10-100% Buffer A/Buffer B in 30 min. The desired compound **1a** was eluted at 27.2 min which was confirmed by mass spectrometry. The compound **1a** was purified by preparative HPLC on C4 column and the desired fractions were lyophilized to give compound **1a** as green solid. (14 mg, yield: 11.0%). HRMS C₆₅H₇₀BF₂N₁₄O₉S Calculated mass: 1271.5237 [M+H]⁺ Measured Mass: 1271.5101.

Compound **1b**: To the free *N*-terminal solid supported peptide **a**, mixture of compound **I** (107 mg, 0.15 mmol), HATU (56.7 mg, 0.145 mmol), HOBT (20 mg, 0.145 mmol) and DIEA (80 µL, 0.45 mmol) in DMF (3 mL) was added. The mixture was shaken at room temperature for 24 hours and the solvent was filtered under vacuum. The residue was



washed with DMF (8 × 10 mL), CH₂Cl₂ (8 × 10 mL) and dried under vacuum. The crude compound **1b** was obtained by cleavage of resin by 10 mL of TFA/TIPS/H₂O (95:3:2) followed by precipitating the crude compound **1b** by cold Et₂O (20 mL). The precipitate was centrifuged and the residue was analyzed by analytical HPLC on C18 column with a gradient

of 0-100% Buffer A/Buffer B in 45 min. The desired compound **1b** was eluted at 23.6 min which was confirmed by mass spectrometry. The compound **1b** was purified by preparative HPLC on C18 column and the desired fractions were lyophilized to give compound **1b** as green solid. (11 mg, yield: 5.19 %). HRMS C₉₈H₁₄₀BF₂N₄₁O₁₁ Calculated mass: 706.7343 [(M+3H)/3]⁺ Measured Mass: 706.7313.

7.4.2 Photothermal studies:

Photothermal transduction studies: The photothermal transduction potential of polyarginine-BSC was evaluated using 750 nm NIR laser. This experimentation was carried out by constructing a central composite design (CCD): factors and response listed in table 3. The CCD with 17 runs was constructed using Design Expert software (Design Expert 11.0.4.0). Briefly, each run was performed by exposing 100 µL of varying concentrations of the sample with 750 nm NIR laser, at specified power and time as per the constructed design. Post exposure, the temperature was recorded immediately, and statistical analysis (analysis of variance: ANOVA) was carried out to evaluate the model.

Table 7.3: Types of variables, levels and selected ranges of factors for constructing the design

Type of variables	Levels		
	Low (-1)	Medium (0)	High (+1)
<i>Independent variable (Factors)</i>			
A = Concentration of Compound 1b (µg/mL)	50	100	150
B = Laser irradiation power (mW)	500	625	750
C = Laser irradiation time (min)	1	5.5	10
<i>Dependent variable (Response)</i>			
R = Temperature (°C)			

Table 7.4: Design matrix with experimental results

Run Number	Concentration of polyarginine-BSC ($\mu\text{g/mL}$)	Power of laser (mW)	Laser irradiation time (min)	Temperature ($^{\circ}\text{C}$)
1	100	500	5.5	43.2
2	150	750	1	42
3	50	750	1	34.9
4	100	625	1	37.1
5	100	625	5.5	51.1
6	150	625	5.5	57.8
7	100	625	5.5	53.2
8	50	625	5.5	44.3
9	50	500	10	42.2
10	100	625	10	53.6
11	100	750	5.5	58
12	100	625	5.5	54.8
13	50	500	1	31.9
14	150	750	10	66.7
15	50	750	10	49.2
16	150	500	1	37.3
17	150	500	10	54.1

Table 7.5: Sequential model sum of squares

Source	Sum of Squares	df	Mean Square	F-value	p-value	
Mean vs Total	38727.64	1	38727.64			
Linear vs Mean	1166.43	3	388.81	16.77	< 0.0001	
2FI vs Linear	60.06	3	20.02	0.8295	0.5074	
Quadratic vs 2FI	198.47	3	66.16	10.79	0.0051	Suggested
Cubic vs Quadratic	31.00	4	7.75	1.95	0.3046	Aliased
Residual	11.91	3	3.97			
Total	40195.52	17	2364.44			

Table 7.6: ANOVA for reduced quadratic model for response, temperature

Source	Sum of Squares	df	Mean Square	F-value	p-value	
Model	1396.56	5	279.31	43.08	< 0.0001	significant
A-Concentration of sample	306.92	1	306.92	47.34	< 0.0001	
B-Laser Power	177.24	1	177.24	27.34	0.0003	
C-Laser irradiation time	682.28	1	682.28	105.23	< 0.0001	
AC	35.70	1	35.70	5.51	0.0387	
C ²	194.42	1	194.42	29.99	0.0002	
Residual	71.32	11	6.48			
Lack of Fit	64.43	9	7.16	2.08	0.3668	not significant
Pure Error	6.89	2	3.44			
Cor Total	1467.88	16				

Table 7.7: Confirmation trials for the evaluation of design space

Trial No	Concentration of polyarginine (µg/mL)	Laser irradiation time (min)	Power of laser (mW)	95% prediction interval low	Observed value	95% prediction interval high
1	100	4	650	43.14	48.7	55.05
2	100	4.5	650	44.46	50.3	56.42
3	100	5	650	45.61	52.3	57.61

Photothermal conversion efficiency: Photothermal conversion efficiency of compound **1b** was evaluated by exposing 3 mL of 0.2 mg/mL to 750 nm NIR laser (650 mW). The sample was loaded in a quartz cuvette, exposed to NIR laser from a distance of 15 cm and the temperature was recorded using a thermocouple. The temperature increment was recorded at regular intervals, and once the saturation was attained, the laser was turned off and then drop was recorded. The same was carried out for Milli Q, which was used as a control, and the photothermal conversion efficiency was calculated using the following equation

$$\eta = \frac{hS(T_{\max} - T_{\text{surr}}) - Q_{\text{dis}}}{I(1 - 10^{-A_{750}})} \quad (2)$$

Where η , h , S , T_{\max} , T_{surr} , I , Q_{dis} , A_{750} , indicate photothermal conversion efficiency, heat transfer coefficient, surface area of sample well, steady state maximum temperature attained by compound **1b** could be used as NIR imaging and photothermal therapeutic dual agents for *in vivo* whole-body or site-specific imaging as well as therapy, surrounding room temperature, laser power, baseline energy input, and A_{750} is the absorbance of compound **1b** could be used as NIR imaging and photothermal therapeutic dual agents for *in vivo* whole-body or site-specific imaging as well as therapy. at 750 nm respectively.

Multi-cycle photothermal transduction: The stability of compound **1b** could be used as NIR imaging and photothermal therapeutic dual agents for *in vivo* whole-body or site-specific imaging as well as therapy. and the ability of compound **1b** could be used as NIR imaging and photothermal therapeutic dual agents for *in vivo* whole-body or site-specific imaging as well as therapy to exhibit multi-cycle photothermal transduction was evaluated by irradiating the sample for a prolonged time. Briefly, the sample was dispensed in a 96 well plate and was exposed to 750 NIR laser at 650 mW and the temperature was recorded at different time intervals. The same sample was irradiated multiple times, the temperature recorded and graph was plotted.

7.4.3 *In vitro* Studies

Mouse fibroblast cells (L929) and human breast cancer cell line, MDA MB 231 were procured from National Centre for Cell Sciences, Pune, India. Phosphate buffer saline (PBS), antibiotic-antimycotic solution, Dulbecco's Modified Eagle Medium (DMEM), and fetal bovine serum (FBS) were purchased from HiMedia Laboratories Pvt. Ltd India.

Cell Culture: DMEM supplemented with 10% v/v FBS and 1% v/v antibiotic-antimycotic solution was used for culturing and maintaining L929 and MDA MB 231 cells. The cells were incubated at 37 °C and 5% CO₂ during culture and experimentation.

Biocompatibility Study: *In vitro* biocompatibility assessment of Compound **1a** was carried out in L929 cells. Briefly, L929 cells were seeded in a 96 well plate at a density of ~ 6000 cells/well and were incubated for 24 h to adhere and attain morphology. Compound **1a** dissolved in DMSO was diluted in complete media to attain different concentrations in the range 10 to 150 µg/mL. Further, the media was replaced with varying concentrations of compound **1a**, positive control being 1 % Triton X-100, negative control being complete

media. The cells were incubated for 24 hours, the contents of wells removed, washed with PBS, followed by addition of Alamar blue at a concentration of 10 µg/well. The cells were incubated for 4 h, followed by recording the fluorescence with excitation and emission wavelengths being 560 and 590 nm respectively (TECAN Infinite 200 Pro series). Percentage cell viability was calculated based on the following equation

$$\text{Cell viability (\%)} = \frac{\text{Intensity of treated sample}}{\text{Intensity of negative control}} \times 100$$

Cellular uptake by confocal laser scanning microscopy (CLSM): CLSM was performed to evaluate the cellular uptake in MDA MB 231 cells. Briefly, the cells were seeded on sterile coverslips in a 12-well plate at a density of 25000 cells/well and incubated for 24 hours. Compound **1a-b** were dissolved in DMSO and were diluted appropriately and added to each well such that the final amount of compound in each well is 10 µg/well. The cells were incubated for 24 h, followed by careful washing with PBS and fixation. The fixation was carried out with 4% paraformaldehyde (15 min) at room temperature, followed by PBS wash. CLSM imaging was performed on fixed cells by using 488 nm excitation and 680-740 nm emission filter respectively.

7.5 References:

1. Boca, S. C.; Potara, M.; Gabudean, A. M.; Juhem, A.; Baldeck, P. L.; Astilean, S., Chitosan-coated triangular silver nanoparticles as a novel class of biocompatible, highly effective photothermal transducers for in vitro cancer cell therapy. *Cancer Lett.* **2011**, *311*, 131-40.
2. Kim, J.-W.; Galanzha, E. I.; Shashkov, E. V.; Moon, H.-M.; Zharov, V. P., Golden carbon nanotubes as multimodal photoacoustic and photothermal high-contrast molecular agents. *Nat. Nanotechnol.* **2009**, *4*, 688.
3. Yang, K.; Zhang, S.; Zhang, G.; Sun, X.; Lee, S.-T.; Liu, Z., Graphene in Mice: Ultrahigh In Vivo Tumor Uptake and Efficient Photothermal Therapy. *Nano Lett.* **2010**, *10*, 3318-3323.
4. Gao, L.; Fei, J.; Zhao, J.; Li, H.; Cui, Y.; Li, J., Hypocrellin-Loaded Gold Nanocages with High Two-Photon Efficiency for Photothermal/Photodynamic Cancer Therapy in Vitro. *ACS Nano* **2012**, *6*, 8030-8040.

5. Sun, Z.; Xie, H.; Tang, S.; Yu, X. F.; Guo, Z.; Shao, J.; Zhang, H.; Huang, H.; Wang, H.; Chu, P. K., Ultrasmall Black Phosphorus Quantum Dots: Synthesis and Use as Photothermal Agents. *Angew. Chem. Int. Ed. Engl.* **2015**, *54*, 11526-30.
6. Yu, J.; Javier, D.; Yaseen, M. A.; Nitin, N.; Richards-Kortum, R.; Anvari, B.; Wong, M. S., Self-Assembly Synthesis, Tumor Cell Targeting, and Photothermal Capabilities of Antibody-Coated Indocyanine Green Nanocapsules. *J. Am. Chem. Soc.* **2010**, *132*, 1929-1938.
7. Cheng, L.; Wang, C.; Feng, L.; Yang, K.; Liu, Z., Functional Nanomaterials for Phototherapies of Cancer. *Chem. Rev.* **2014**, *114*, 10869-10939.
8. Fischer, G. M.; Isomäki-Krondahl, M.; Göttker-Schnetmann, I.; Daltrozzi, E.; Zumbusch, A., Pyrrolopyrrole Cyanine Dyes: A New Class of Near-Infrared Dyes and Fluorophores. *Chem. Eur. J.* **2009**, *15*, 4857-4864.
9. Tang, B.; Yu, F.; Li, P.; Tong, L.; Duan, X.; Xie, T.; Wang, X., A Near-Infrared Neutral pH Fluorescent Probe for Monitoring Minor pH Changes: Imaging in Living HepG2 and HL-7702 Cells. *J. Am. Chem. Soc.* **2009**, *131*, 3016-3023.
10. Pham, W.; Cassell, L.; Gillman, A.; Koktysh, D.; Gore, J. C., A near-infrared dye for multichannel imaging. *Chem. Commun.* **2008**, 1895-1897.
11. Yang, Y.; Lowry, M.; Xu, X.; Escobedo, J. O.; Sibrian-Vazquez, M.; Wong, L.; Schowalter, C. M.; Jensen, T. J.; Fronczek, F. R.; Warner, I. M.; Strongin, R. M., Seminaphthofluorones are a family of water-soluble, low molecular weight, NIR-emitting fluorophores. *Proc. Natl. Acad. Sci. U.S.A* **2008**, *105*, 8829.
12. Johnson, J. R.; Fu, N.; Arunkumar, E.; Leevy, W. M.; Gammon, S. T.; Piwnicka-Worms, D.; Smith, B. D., Squaraine rotaxanes: superior substitutes for Cy-5 in molecular probes for near-infrared fluorescence cell imaging. *Angew. Chem. Int. Ed.* **2007**, *46*, 5528-5531.
13. Fu, N.; Gassensmith, J. J.; Smith, B. D., Effect of Stopper Size on Squaraine Rotaxane Stability. *Supramol. Chem.* **2009**, *21*, 118-124.
14. Arunkumar, E.; Forbes, C. C.; Noll, B. C.; Smith, B. D., Squaraine-Derived Rotaxanes: Sterically Protected Fluorescent Near-IR Dyes. *J. Am. Chem. Soc.* **2005**, *127*, 3288-3289.
15. Umezawa, K.; Citterio, D.; Suzuki, K., Water-soluble NIR Fluorescent Probes Based on Squaraine and Their Application for Protein Labeling. *Anal. Sci.* **2008**, *24*, 213-217.

16. Nesterov, E. E.; Skoch, J.; Hyman, B. T.; Klunk, W. E.; Bacskai, B. J.; Swager, T. M., In Vivo Optical Imaging of Amyloid Aggregates in Brain: Design of Fluorescent Markers. *Angew. Chem. Int. Ed.* **2005**, *44*, 5452-5456.
17. Meek, S. T.; Nesterov, E. E.; Swager, T. M., Near-Infrared Fluorophores Containing Benzo[c]heterocycle Subunits. *Org. Lett.* **2008**, *10*, 2991-2993.
18. Umezawa, K.; Matsui, A.; Nakamura, Y.; Citterio, D.; Suzuki, K., Bright, Color-Tunable Fluorescent Dyes in the Vis/NIR Region: Establishment of New “Tailor-Made” Multicolor Fluorophores Based on Borondipyrromethene. *Chem. Eur. J.* **2009**, *15*, 1096-1106.
19. Loudet, A.; Bandichhor, R.; Burgess, K.; Palma, A.; McDonnell, S. O.; Hall, M. J.; O’Shea, D. F., B,O-Chelated Azadipyrromethenes as Near-IR Probes. *Org. Lett.* **2008**, *10*, 4771-4774.
20. Umezawa, K.; Nakamura, Y.; Makino, H.; Citterio, D.; Suzuki, K., Bright, Color-Tunable Fluorescent Dyes in the Visible–Near-Infrared Region. *J. Am. Chem. Soc.* **2008**, *130*, 1550-1551.
21. Nesterova, I. V.; Erdem, S. S.; Pakhomov, S.; Hammer, R. P.; Soper, S. A., Phthalocyanine Dimerization-Based Molecular Beacons Using Near-IR Fluorescence. *J. Am. Chem. Soc.* **2009**, *131*, 2432-2433.
22. Kuimova, M. K.; Collins, H. A.; Balaz, M.; Dahlstedt, E.; Levitt, J. A.; Sergent, N.; Suhling, K.; Drobizhev, M.; Makarov, N. S.; Rebane, A.; Anderson, H. L.; Phillips, D., Photophysical properties and intracellular imaging of water-soluble porphyrin dimers for two-photon excited photodynamic therapy. *Org. Biomol. Chem.* **2009**, *7*, 889-896.
23. Kee, H. L.; Nothdurft, R.; Muthiah, C.; Diers, J. R.; Fan, D.; Ptaszek, M.; Bocian, D. F.; Lindsey, J. S.; Culver, J. P.; Holten, D., Examination of chlorin-bacteriochlorin energy-transfer dyads as prototypes for near-infrared molecular imaging probes. *Photochem. Photobiol.* **2008**, *84*, 1061-1072.
24. Nesterova, I. V.; Verdree, V. T.; Pakhomov, S.; Strickler, K. L.; Allen, M. W.; Hammer, R. P.; Soper, S. A., Metallo-Phthalocyanine Near-IR Fluorophores: Oligonucleotide Conjugates and Their Applications in PCR Assays. *Bioconjugate Chem.* **2007**, *18*, 2159-2168.
25. Xie, D.; Liu, Y.; Rao, Y.; Kim, G.; Zhou, M.; Yu, D.; Xu, L.; Yin, B.; Liu, S.; Tanaka, T.; Aratani, N.; Osuka, A.; Liu, Q.; Kim, D.; Song, J., meso-Triaryl-Substituted Smaragdyrins: Facile Aromaticity Switching. *J. Am. Chem. Soc.* **2018**, *140*, 16553-16559.

26. Narayanan, S. J.; Sridevi, B.; Chandrashekar, T. K.; Englich, U.; Ruhlandt-Senge, K., Core-Modified Smaragdyrins: First Examples of Stable Meso-Substituted Expanded Corrole. *Org. Lett.* **1999**, *1*, 587-590.
27. Chatterjee, T.; Srinivasan, A.; Ravikanth, M.; Chandrashekar, T. K., Smaragdyrins and Sapphyrins Analogues. *Chem. Rev.* **2017**, *117*, 3329-3376.
28. Pareek, Y.; Ravikanth, M.; Chandrashekar, T. K., Smaragdyrins: emeralds of expanded porphyrin family. *Acc. Chem. Res.* **2012**, *45*, 1801-16.
29. Kalita, H.; Lee, W.-Z.; Ravikanth, M., Phosphorus Complexes of meso-Triaryl-25-oxasmaragdyrins. *Inorg. Chem.* **2014**, *53*, 9431-9438.
30. Rajeswara Rao, M.; Ravikanth, M., Boron complexes of oxasmaragdyrin, a core-modified expanded porphyrin. *J. Org. Chem.* **2011**, *76*, 3582-7.
31. Laxman, K.; Ravikanth, M., Synthesis of Oxasmaragdyrin-Amino Acid Conjugates. *Eur. J. Org. Chem.* **2017**, *2017*, 5884-5891.
32. Ghadiri, M.; Vasheghani-Farahani, E.; Atyabi, F.; Kobarfard, F.; Mohamadyar-Toupkanlou, F.; Hosseinkhani, H., Transferrin-conjugated magnetic dextran-spermine nanoparticles for targeted drug transport across blood-brain barrier. *J. Biomed. Mater. Res. A* **2017**, *105*, 2851-2864.
33. Lee, J. H.; Sahu, A.; Jang, C.; Tae, G., The effect of ligand density on in vivo tumor targeting of nanographene oxide. *J. Controlled Release* **2015**, *209*, 219-228.
34. Gawde, K. A.; Sau, S.; Tatiparti, K.; Kashaw, S. K.; Mehrmohammadi, M.; Azmi, A. S.; Iyer, A. K., Paclitaxel and di-fluorinated curcumin loaded in albumin nanoparticles for targeted synergistic combination therapy of ovarian and cervical cancers. *Colloids Surf. B. Biointerfaces* **2018**, *167*, 8-19.
35. Ren, W. X.; Han, J.; Uhm, S.; Jang, Y. J.; Kang, C.; Kim, J.-H.; Kim, J. S., Recent development of biotin conjugation in biological imaging, sensing, and target delivery. *Chem. Commun.* **2015**, *51*, 10403-10418.
36. Tripodo, G.; Trapani, A.; Torre, M. L.; Giammona, G.; Trapani, G.; Mandracchia, D., Hyaluronic acid and its derivatives in drug delivery and imaging: Recent advances and challenges. *Eur. J. Pharm. Biopharm.* **2015**, *97*, 400-416.
37. Borrelli, A.; Tornesello, L. A.; Tornesello, L. M.; Buonaguro, M. F., Cell Penetrating Peptides as Molecular Carriers for Anti-Cancer Agents. *Molecules* **2018**, *23*, 28.
38. Weyland, M.; Griveau, A.; Bejaud, J.; Benoit, J. P.; Coursaget, P.; Garcion, E., Lipid nanocapsule functionalization by lipopeptides derived from human papillomavirus type-16 capsid for nucleic acid delivery into cancer cells. *Int. J. Pharm.* **2013**, *454*, 756-764.

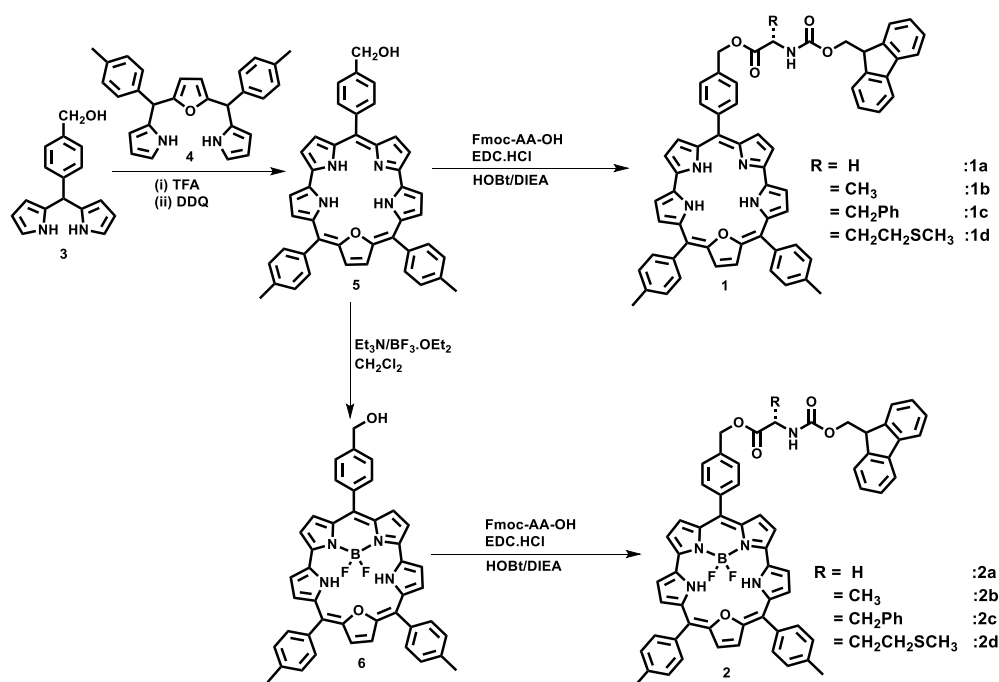
39. Higa, M.; Katagiri, C.; Shimizu-Okabe, C.; Tsumuraya, T.; Sunagawa, M.; Nakamura, M.; Ishiuchi, S.; Takayama, C.; Kondo, E.; Matsushita, M., Identification of a novel cell-penetrating peptide targeting human glioblastoma cell lines as a cancer-homing transporter. *Biochem. Biophys. Res. Commun.* **2015**, *457*, 206-212.
40. Wender, P. A.; Mitchell, D. J.; Pattabiraman, K.; Pelkey, E. T.; Steinman, L.; Rothbard, J. B., The design, synthesis, and evaluation of molecules that enable or enhance cellular uptake: Peptoid molecular transporters. *Proc. Natl. Acad. Sci. U.S.A* **2000**, *97*, 13003.
41. Gouterman, M., Electronic spectra. *The Porphyrins* **1978**, *3*, 1-156.

Chapter 8

Summary

Near Infra-Red Fluorescence (NIRF) is gaining a lot of attention in recent years as mammalian cells are found to be more transparent in the window of 700-900 nm (designated as NIR I region) and 1000-1700 nm (designated as NIR II region). Hence dyes which absorb and emit in these regions are very advantageous as lower tissue auto-fluorescence and less fluorescence extinction enhance deep tissue penetration with minimal background interference.¹⁻³ NIR light is known to travel at least 10 cm through breast tissue and 4 cm through skull/brain tissue and deep muscle tissue by usage of microwatt laser sources (FDA class 1).⁴ Though Near-IR Fluorescence (NIRF) imaging is advantageous, there are only handful of dyes that fluoresce in this region such as cyanine dyes,^{5,6} xanthenes/rhodamines,⁷ squaraine dyes,⁸⁻¹¹ benzo[c]heterocycles,¹² BODIPY analogs,¹³⁻¹⁶ phthalocyanines and a small selection of porphyrin derivatives.¹⁷⁻¹⁹

In Chapter 1, a detailed discussion on advantages of NIR Fluorescence imaging and dye molecules available in literature which have been used for the same purpose was presented. Furthermore, the photophysical properties of expanded porphyrins such as sapphyrins and oxasmaragdyrins were discussed along with the prospects of NIR-Fluorescence imaging. On the other hand, different types of cancer and treatment methodologies were also discussed with hyperthermia as one of the viable modalities for cancer therapy and how NIR fluorophores have become part of it. In Chapter 2, we describe the materials, methods and synthesis of the reported precursors along with various analytical, *in vitro* and *in vivo* studies which have been incorporated in this thesis. In Chapter 3, we described the synthesis of amino acid conjugated oxasmaragdyrin and its BF₂-complexes **1/2** by following scheme 8.1. To realise the amino acid conjugation, the precursor molecule 4-(*p*-hydroxymethyl)benzaldehyde was prepared by selectively reducing 1,4-terephthalaldehyde by NaBH₄ in CH₃OH. The 4-(*p*-hydroxymethyl)benzaldehyde was reacted with excess of pyrrole in the presence of catalytic amount of TFA in CH₂Cl₂ followed by work-up and column chromatographic purification afforded *meso*(4-hydroxymethyl)phenyl dipyrromethane **3** as white solid. The 25-oxasmaragdyrin **5** containing benzylhydroxyl group at one of the *meso* position was synthesized by condensing one equivalent of dipyrromethane **3** with one equivalent of 16-oxatripyrrane **4** in CH₂Cl₂ in the presence of catalytic amount of TFA for 1 h under inert atmosphere followed by oxidation with DDQ in open air for additional 1 h followed by column chromatographic purification to give *meso*-(*p*-methylhydroxy phenyl) oxasmaragdyrin as green solid.



Scheme 8.1: Synthesis oxasmaragdyrin-amino acid conjugates **1a-d** and BF₂ complex of oxasmaragdyrin-amino acid conjugates **2a-d**.

The compound **5** was treated with excess BF₃·OEt₂ in CH₂Cl₂ in the presence of triethylamine for 15 min and purified the crude compound by basic alumina column chromatography to afford pure BF₂ complex of functionalized 25-oxasmaragdyrin **6** as green crystalline solid in 80% yield. The oxasmaragdyrin **5** or its BF₂ complex **6** was reacted with appropriate Fluorenylmethyloxycarbonyl-protected amino acid (Fmoc-AA) in CH₂Cl₂ in the presence of 1 equivalent of 1-Ethyl-3-(3-dimethylaminopropyl)carbodiimide Hydrochloride (EDC·HCl), 0.1 equivalent HOBt (Hydroxybenzotriazole) and 1 equivalent *N,N*-diisopropylethylamine (DIEA) at room temperature for 3 h. All the conjugates were thoroughly characterised by 1D, 2D NMR and HRMS. The covalently linked smaragdyrin-amino acid conjugates showed five sets of resonances for 10 protons corresponding to eight pyrrole and two furan protons in the region of 9 – 10.5 ppm which were identified by their location, integration, coupling constant and cross-peak connectivity in COSY NMR. The protons corresponding to amino acid moiety appeared in the region of 1.5 – 6 ppm which were also easily identified based on their cross-peak correlations in COSY spectra. The inner NH protons of BF₂-smaragdyrin-amino acid conjugates **2** were appeared at upfield region of -3.5 ppm which were not observed in smaragdyrin-amino acid conjugates due to their involvement in rapid tautomerism. The absorption, fluorescence and electrochemical properties of free base/BF₂-smaragdyrin-amino acid conjugates **1/2** were studied and the comparison is shown in

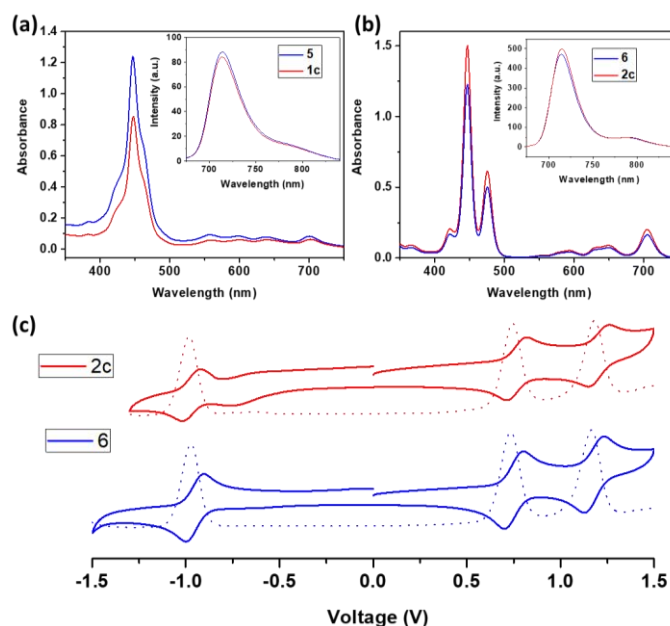
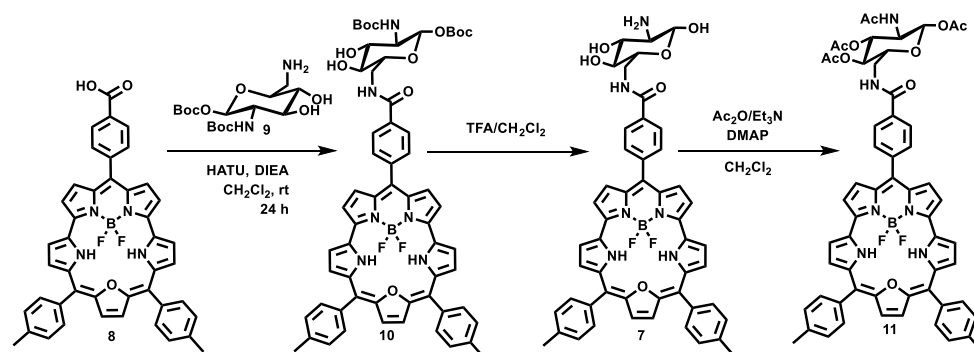


Figure 8.1: (a) Comparison of absorption and fluorescence (inset) spectra of **1c** and **5** recorded in CHCl₃; (b) Comparison of absorption and fluorescence (inset) spectra of **2c** and **6** recorded in CHCl₃; (c) Comparison of cyclic Voltammograms and Differential Pulse Voltammograms of **2c** and **6** in CH₂Cl₂ containing 0.1M TBAP as supporting electrolyte using scan rate of 50 mV/sec.

Figure 8.1. These conjugates showed similar absorption features like smaragdyrin precursors **5** & **6** with almost no shifts in their peak maxima. The conjugates **1** and **2** also showed two reversible oxidations and one or two reversible/irreversible reduction(s) like their precursor smaragdyrin **5** and BF₂-smaragdyrin **6** with negligible shifts in their peak potentials indicating that the rich redox chemistry of smaragdyrin/BF₂-smaragdyrin did not alter significantly by linking them with various amino acids. The spectral and electrochemical properties indicated that the conjugates showed similar rich spectral and redox properties like unconjugated smaragdyrins/BF₂-smaragdyrins without significant alteration which are very useful for their potential applications as NIR fluorescent probes in biology and medicine.

In chapter 4, we discussed the synthesis of BF₂-oxasmaragdyrin-glucosamine conjugate **7** and its use as a NIR Fluorescence imaging agent. The target BF₂-oxasmaragdyrin-glucosamine conjugate **7** was prepared over sequence of two steps as shown in Scheme 8.2. The required precursors, BF₂-25-oxasmaragdyrin **8** containing *p*-carboxyphenyl substituent at *meso* position and 6-amine-6-deoxy-1-O-Boc-2-N-Boc- β -D-glucosamine **9** were synthesized by following reported methods.^{20,21} Compound **8** was reacted with compound **9** in presence of *N,N,N',N'*-tetramethyl-*O*-(1H-benzotriazol-1-yl)uronium hexafluorophosphate (HBTU) and



Scheme 8.2: Synthesis of glucosamine conjugated BF₂-oxa-smaragdyrin (**1**).

N,N-diisopropylethylamine (DIEA) in dichloromethane under inert atmosphere for 24 hours, followed by basic alumina column chromatography to afford compound **10** as a green solid (55% yield). In the subsequent step, treatment of compound with TFA/CH₂Cl₂ for 15 min followed by removal of solvent under reduced pressure yielded compound **7** as green solid (70% yield). All intermediates and the target compound were characterised by 1D, 2D NMR spectroscopy and High Resolution Mass Spectrometry (HRMS).

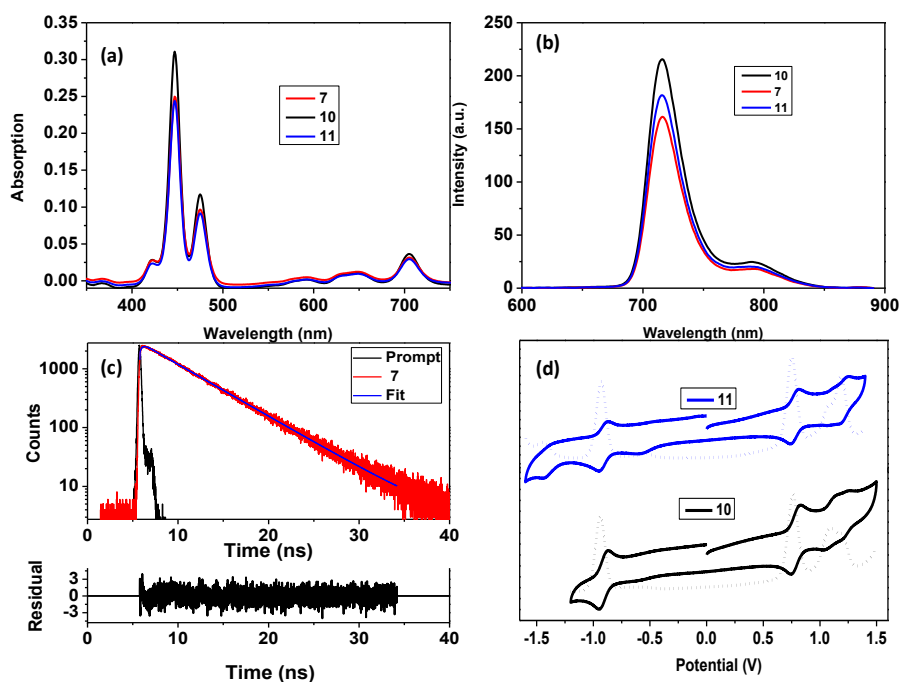


Figure 8.2: Comparison of (a) absorption, (b) fluorescence spectra of compounds **7**, **10** and **11** (conc: 1×10^{-5} M). (c) Fluorescence decay profile and the weighted residuals distribution fit of fluorescence decay of **7** in DMSO. The λ_{ex} used was 440 nm and emission were detected at 710 nm. (d) Comparison of cyclic Voltammograms and Differential Pulse Voltammograms of **10** and **11** in CH₂Cl₂ containing 0.1M TBAP as supporting electrolyte using scan rate of 50 mV/sec.

The absorption and fluorescence studies revealed that the compounds absorb in Vis-NIR region and emit in NIR region. The absorption and fluorescence spectra of compounds **7**, **10** and **11** in DMSO showed that all the molecules have similar absorption and fluorescence spectral features (Figure 8.2) with slight change in quantum yields. Compound **7** has relatively lower quantum yield ($\phi_f = 0.12$) compared to that of compounds **10** and **11** ($\phi_f = 0.19$). Furthermore, Time-correlated single photon counting (TCSPC) experiment was carried out on compounds **7**, **10** and **11** by exciting the compounds at 440 nm and detecting emission at 710 nm. All the compounds showed single exponential decay profile (Figure 4.2c) with similar singlet excited state lifetime (~ 4.9 ns). Compounds **10** and **11** showed three reversible oxidations and one reversible reduction unlike BF₂-25-oxasmaragdyrin which shows two reversible oxidations and one reversible reduction. The electrochemical data indicate that these compounds are easier to oxidize and reduce and are stable under electrochemical conditions.

Qualitative *in vitro* cellular uptake of the compound **7** was performed in L929 and MDA MB 231 cells. The L929 and MDA MB 231 cells were incubated with compound **7** (10 μ g/well) for 24 hours. CLSM data revealed that the compound **7** was internalized in the cells and was able to exhibit strong fluorescence in NIR region (Figure 8.3). DAPI staining experiments were carried out to understand the localisation of compound **7** in the cells. DAPI staining analysis

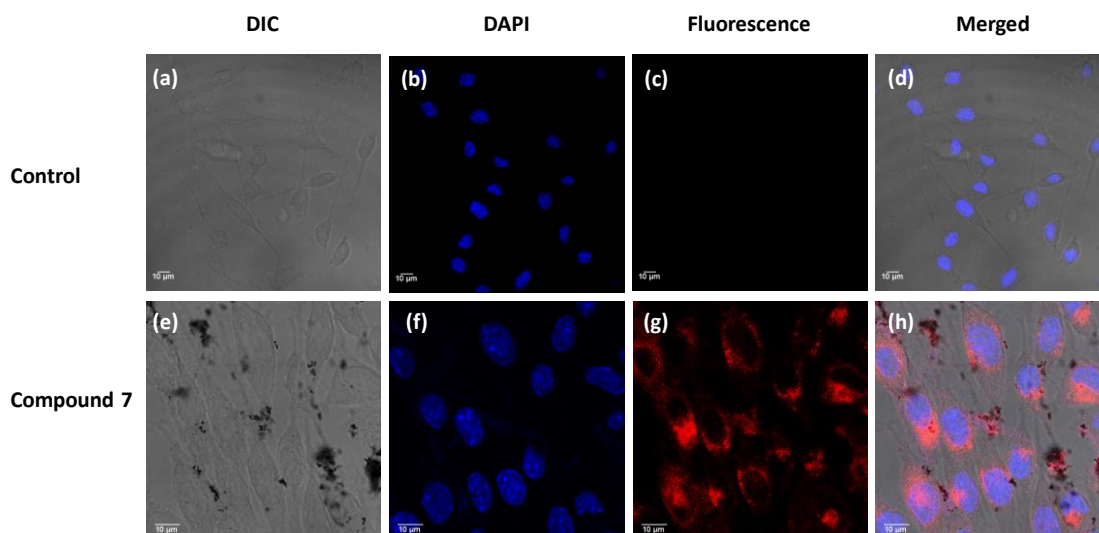
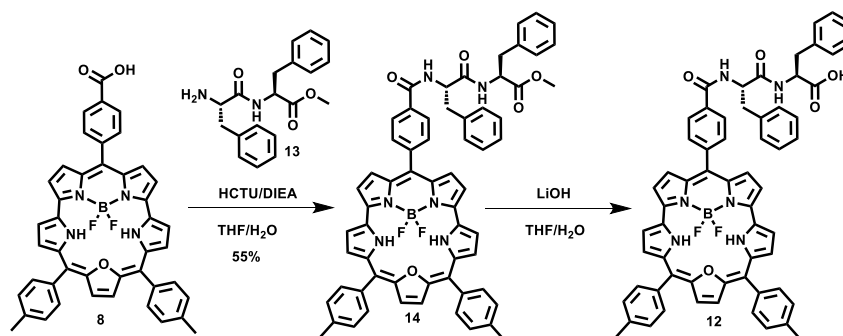


Figure 8.3: CLSM images showing L929 Control cells treated with DAPI (a) Differential Interference Contrast (DIC) image, (b) DAPI channel with 410-454 nm emission filter, (c) Fluorescence channel with 680-730 nm emission filter, (d) merged image of all channels and L929 cells treated with DAPI and compound **1**, (e) Differential Interference Contrast (DIC) image, (f) DAPI channel with 410-454 nm emission filter, (g) Fluorescence channel with 680-732 nm emission filter and (h) merged image of all channels.

showed that the compound **7** was localised in cytoplasm of the cells with very good emission in NIR region. This property of NIR emission could be exploited for the *in vivo* whole-body imaging or site-specific imaging.

In chapter 5, we discussed the synthesis of L,L-diphenylalanine conjugated BF₂-oxasmaragdyrin self-assemblies and its use as photothermal therapeutic agent. The target 25-oxasmaragdyrin-diphenylalanine conjugate **12** was prepared over a sequence of two steps as shown in Scheme 8.3. The starting 25-oxasmaragdyrin **8** containing *p*-carboxyphenyl substituent at *meso* position, was synthesized via a reported method. Compound **8** was reacted with protected L,L-diphenylalanine **13** in presence of *N,N,N',N'*-tetramethyl-*O*-(1*H*-benzotriazol-1-yl)uronium hexafluorophosphate (HBTU) and *N,N*-diisopropylethylamine (DIEA) in dichloromethane under inert atmosphere for 8 hours, followed by basic alumina column chromatography to afford compound **14** as a green solid (55% yield). All intermediates were characterised by ¹H, ¹H-¹H COSY, ¹³C, ¹¹B, ¹⁹F NMR spectroscopy and High-Resolution Mass Spectrometry (HRMS). In the last step, compound **14** was hydrolysed with LiOH to afford the target compound **12** which was characterised by ¹H, ¹H-¹H COSY, ¹³C, ¹¹B, ¹⁹F NMR spectroscopy and HRMS.



Scheme 8.3: Synthesis of L,L-diphenylalanine conjugated BF₂-oxa-smaragdyrin (**12**).

To prepare the spherical self-assemblies, compound **12** was dissolved in different solvents such as acetonitrile, Hexafluoro-2-propanol, acetone and DMSO and was diluted with water. The organic solvent was removed either by evaporation or dialysis. Particles with various sizes and morphology were formed and aggregated in most of the cases. The acetone-water mixture (1:1 ratio) resulted in monodisperse nanoparticles with controlled spherical morphology (Figure 8.4). The acetone was removed from the above solution under reduced pressure and temperature 55 °C to obtain self-assembled spherical particles (FF-BSC NP). The nanoparticles were characterised by DLS, FEGSEM, FEGTEM and Zeta potential and found that the FF-BSC NP were spherical having a controlled morphology with diameter of 123 ± 33 nm and a zeta potential of -22 ± 5 mV. Significant changes have been observed in absorption

and fluorescence properties of compound **12** (Figure 5.3c, 5.3d) after preparation of nanoparticles. The absorption spectrum was broadened, and the corresponding absorption coefficients were reduced (figure 8.4c). Similarly, there was severe quenching of fluorescence (figure 8.4d) due to aggregation induced quenching phenomena. Furthermore, pH stability studies at different pH (5.5, 6.5, 7.5) were carried out and found that the FF-BSC NPs were stable at these pHs with minimal changes in absorption, fluorescence and FEGSEM data. Lyophilization studies were also carried out on the FF-BSC NPs using various cryoprotectants and found that the best results were obtained when pluronic F-68 is used with sugars such as sucrose and trehalose.

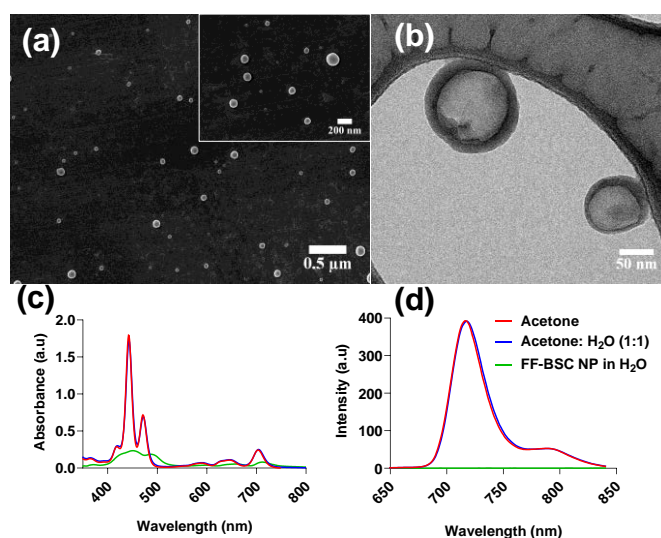


Figure 8.4: (a) FEG-SEM images of FF-BSC NP (Inset indicating the higher magnification image) (b) FEG-TEM image of self-assemblies. Absorption (c) and fluorescence (d) comparison of self-assembled particles to that of the single-molecular entities (1.6×10^{-6} M).

The FF-BSC NP exhibited photo-thermal properties upon irradiation with 750 nm laser. Photo-thermal transduction potential of the nanoparticles was evaluated by constructing central composite design (CCD) with three independent variables, concentration of sample, laser power, and laser irradiation time and found that the optimal conditions to attain a temperature range of 52-60 °C was 750 mW laser power with 0.3 mg/ml concentration and 5 minutes of irradiation time. The Photothermal Conversion Efficacy (PCE) of FF-BSC NP was evaluated and found that the PCE of FF-BSC NP was 53.61%, and the time vs temperature profiling is given in Figure 8.5c. Furthermore, FF-BSC NP were found to be highly stable and with negligible loss in photothermal properties even after four cycles (Figure 8.5d).

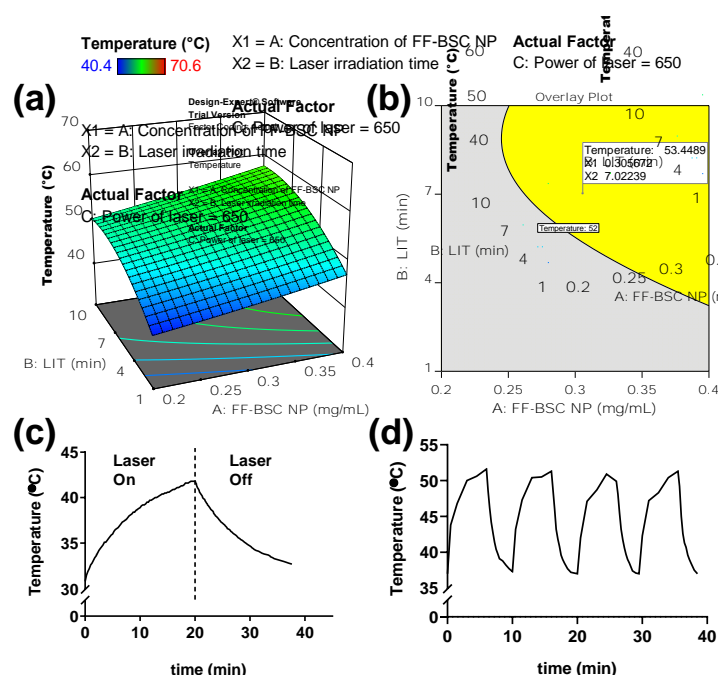


Figure 8.5: (a) 3D plot and (b) Design space for the response, temperature evaluated with CCD; (c) time vs temperature profile of FF-BSC NP (d) multi-cycle temperature changes upon exposure of FF-BSC NP with 750 nm laser.

The biocompatibility studies for the FF-BSC NPs carried out in L929 cells revealed that the material was highly biocompatible upto 250 $\mu\text{g}/\text{mL}$. The cellular uptake of FF-BSC NP in 4T1 cells was evaluated with FACS and found that the material was internalised into the

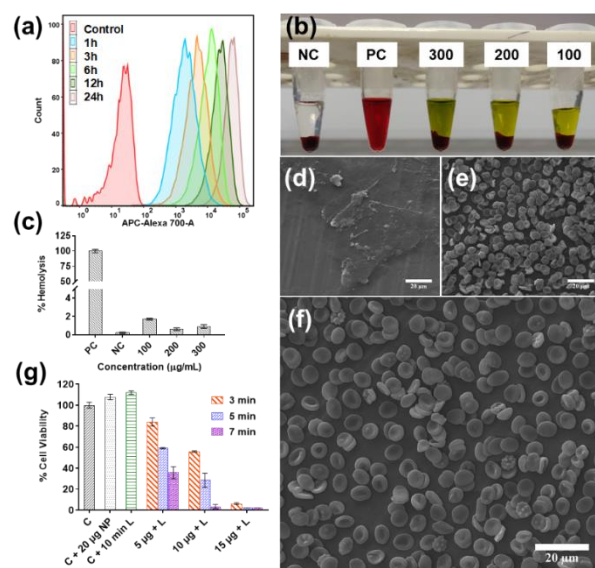


Figure 8.6: (a) uptake of FF-BSC NP in 4T1 cells, (b) digital image of various samples of hemocompatibility study, (c) graph depicting the hemocompatibility study of FF-BSC NP, ESEM images of RBC treated with (d) positive control (triton X-100), (e) negative control (PBS), (f) 300 $\mu\text{g}/\text{mL}$ FF-BSC NP, (g) *in vitro* photothermal efficacy in 4T1 cells

cells within 24 hours (Figure 8.6a). *In vitro* photothermal efficacy testing was carried out in 4T1 cells revealed that the material is highly efficient. From the graph it is evident that the cell viability in sample exposed to NIR laser for 7 min with $10\mu\text{g}/\text{well}$ was $<5\%$, whereas the cells exposed to material and laser alone did not exhibit changes in cell viability (Figure 8.6g). Hemocompatibility studies on FF-BSC NPs revealed that FF-BSC NP did not exhibit hemolysis and the % hemolysis was well below 5%. The sample treated with Triton X-100, resulted in complete hemolysis and no RBC pellet was observed as shown in Figure 8.6b-c. Further, ESEM analysis of FF-BSC NP treated samples revealed that the morphology of RBCs was intact, and no significant difference was observed (Figure 8.6d-f).

To understand of the *in vivo* biodistribution of FF-BSC NP, *ex vivo* fluorescence imaging studies were carried out 14 days post intravenous administration of FF-BSC NP. The *ex vivo* fluorescence imaging of the vital organs revealed that the majority of the nanoparticles were accumulated in the liver, lung and spleen, followed by kidney and heart suggesting that the major portion of the injected material is taken up by the components of the reticuloendothelial system in the body. Accumulation of a portion of injected material in the

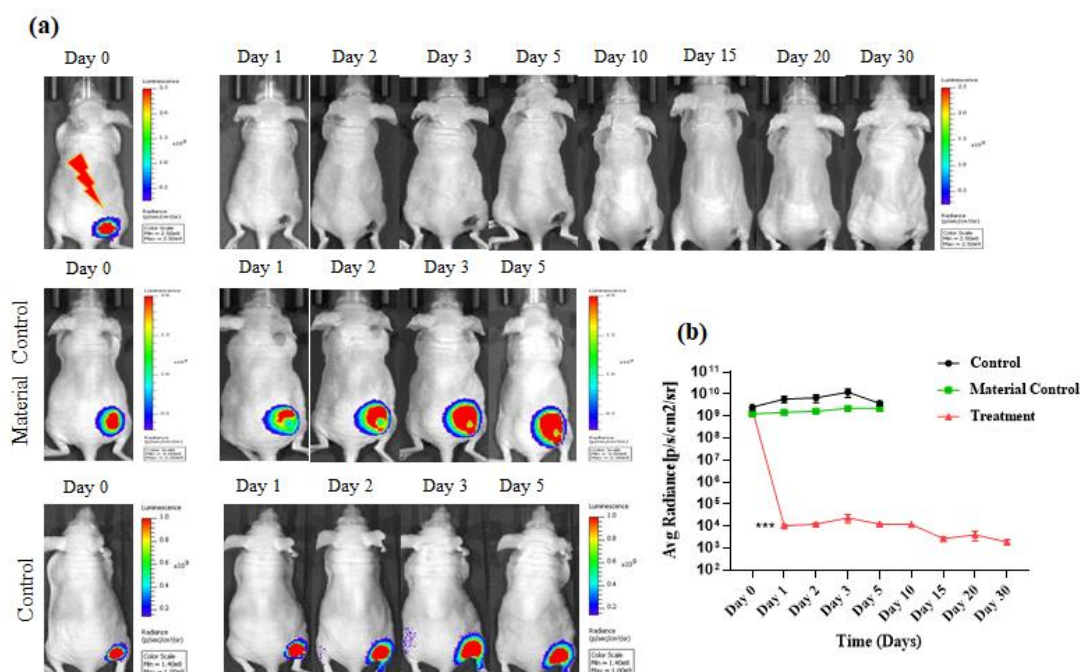


Figure 8.7: *In vivo* photothermal ablation by FF-BSC NP in 4T1 xenograft mouse model: (a) representative *in vivo* bioluminescence images of various treatment groups, (b) quantitative assessment of bioluminescence signal for different groups during the follow-up (***) indicates $P = 0.001$ post third treatment)

kidney also suggest the possibility of renal clearance. The photothermal efficacy testing of FF-BSC NP revealed that the material possesses excellent efficacy *in vivo*. It was observed that there was a dramatic reduction in bioluminescence signal post PTT, indicative of drastic tumor ablation associated with no signs of weight loss post PTT suggests that there is no therapeutic burden (Figure 8.7) on mice. However, the bioluminescence signal of control as well the material control groups showed continuous increase, indicating the non-toxic nature of material and progressive tumor growth. The control group as well as material control group showed signs of necrosis at day 5, beyond which no further imaging was carried for these animals owing to the ethical concerns and the mice were sacrificed. Treated animals were followed till day 30 post treatment and showed no increase in the bioluminescence signal (signal was equivalent to the background) highlighting the effective and complete tumor ablation with no signs of relapse post PTT prolonging the overall survival of the treated mice.

In chapter 6, we discussed the synthesis of *meso*-trititolyl-BF₂-oxasmaragdyrin based quantum dots (TBSQDs) and its use as theragnostic agent for cancer therapy. TBSQDs were prepared by thin film hydration followed by high pressure homogenization (Figure 8.8). Chloroform was removed from TBS and lipoid S 75 solubilized mixture under reduced pressure, and the obtained thin film was hydrated at 45°C for 1 hour, followed by high pressure homogenization at 800 bar for 10 passes. The obtained TBSQDs were characterized by Raman spectroscopy, TEM, absorption and fluorescence spectroscopy. The indication of quantum

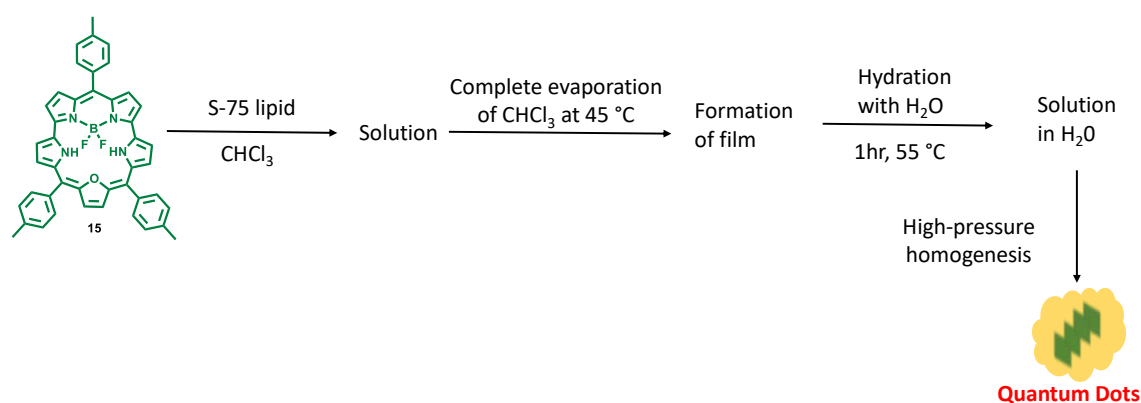


Figure 8.8: Schematic representation for synthesis of TBSQDs.

confinement of TBS was clearly evaluated through SERS by physical mixture of TBSQDs solution and Ag colloidal solution. The sample of QDs were excited on the surface of Ag colloidal particles with 532 nm Laser to minimize the effect of fluorescence on weak Raman signals. We observed the sharper Raman signals from TBSQDs compared to that of the TBS (Figure 8.9a) with about 40-60% decrease in full width half maximum (FWHM) values from

TBS to TBSQDs suggesting that the obtained material was quantum confined. Further, TEM analysis of the sample has shown that the TBSQDs were amorphous/polycrystalline in nature with particle size of 7.1 ± 2.1 nm (Figure 8.9b-d) which is less than the calculated bohr radius ($a_0 \approx 15$ nm) for the material. The formation of quantum dots may be attributed to the π -stacking of TBS under high pressure and stabilization of hydrophobic self-assembly in water by lipid encapsulation. Absence of lipid in the above process did not yield the TBS quantum dots. Hence, S-75 lipid plays vital role in homogenizing hydrophobic TBS in water and stabilizing the formed hydrophobic TBS quantum dots in water medium.

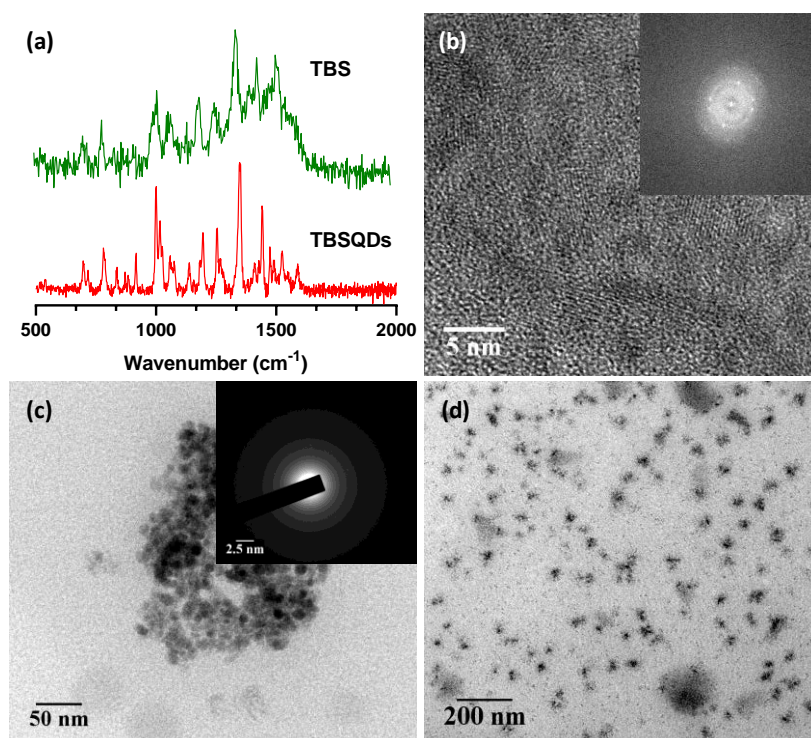


Figure 8.9: (a) Comparison of Raman scattering for TBS and TBSQDs on Ag nanoparticles. (b-d) TEM Images [(b) HRTEM of TBSQDs (Inset shows FFT) (c) TEM image of TBSQDs (inset shows the Selected Area Electron Diffraction (SAED))]

The absorption and emission studies were carried out on the synthesized TBSQDs. The absorption spectra of the TBSQDs has a similar pattern as that of TBS with 2 Soret bands, four Q-bands which are severely broadened (Figure 8.10a) with a reduction of absorbance from TBS to TBSQDs due to aggregation of TBS and formation of TBSQDs. Further, a bathochromic shift of 30 nm in the last Q-band absorption was observed for TBSQDs compared to that of the TBS suggesting the strongly coupled electronic states of individual TBS in the formed TBSQDs. The fluorescence emission was observed to be 4 nm blue shifted compared to that of the TBS (Figure 8.10b) though the bathochromic shift was observed in the absorption

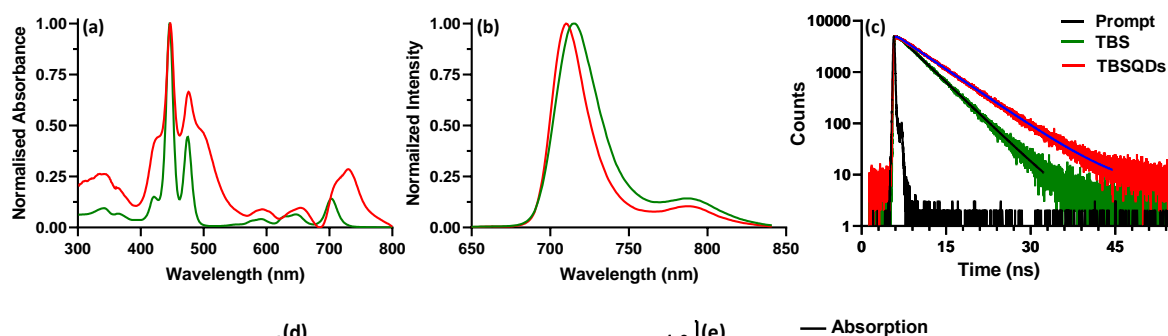


Figure 8.10: Comparison of (a) Normalized Absorption, (b) Normalized fluorescence, (c) Fluorescence decay profile.

spectrum (Figure 8.10a). The fluorescence lifetime of 4.5 ns, 5.8 ns (Figure 8.10c) was observed for TBS, TBSQDs respectively. Increase in fluorescence lifetime of TBSQDs to that of TBS could be attributed to the local hydrophobic environment created by the lipid stabilizes the electronically excited state in TBSQDs. The reduction in fluorescence quantum yield from 0.15 to 0.09 from TBS to TBSQDs suggests that there is an increase in amount of nonradiative decay from excited state upon formation of TBSQDs which we observed as thermal energy.

The TBSQDs exhibited photo-thermal properties upon irradiation with 750 nm laser. Photo-thermal transduction potential of the nanoparticles was evaluated by constructing central composite design (CCD) with three independent variables, concentration of sample, laser power, and laser irradiation time and found that the optimal conditions to attain a temperature range of 52-65 °C was 750 mW laser power with 0.1 mg/ml concentration and 5 minutes of irradiation time with a Photothermal Conversion Efficacy (PCE) of 43.65% for TBSQDs. Furthermore, TBSQDs were found to be highly stable with negligible loss in photothermal properties even after four cycles.

The biocompatibility studies for the TBSQDs carried out in L929 cells revealed that the material was highly biocompatible upto 150 µg/ml. The cellular uptake of TBSQDs in 4T1 cells was evaluated with FACS and found that the material was internalised into the cells within 24 hours. Furthermore, qualitative *in vitro* cellular uptake of the TBSQDs was performed in 4T1 cells by incubating cells with TBSQDs (10 µg/well) for 24 hours. CLSM data (Figure 8.11) revealed that the TBSQDs were internalized in the cells and was able to exhibit strong fluorescence in NIR region (680-740 nm). DAPI staining experiments were carried out to understand the localisation of TBSQDs in the cells showed (Figure 8.11) that the TBSQDs were localised in cytoplasm of the cells with very good emission in NIR region.

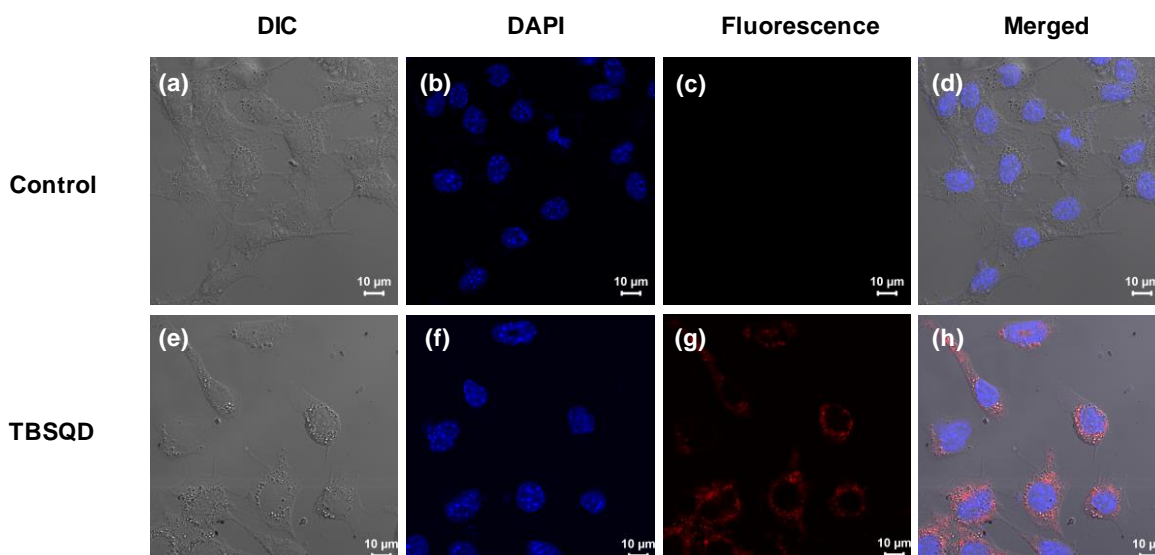


Figure 8.11: CLSM images showing 4T1 Control cells treated with DAPI (a) Differential Interference Contrast (DIC) image, (b) DAPI channel with 410-454 nm emission filter, (c) Fluorescence channel with 680-730 nm emission filter, (d) merged image of all channels and 4T1 cells treated with DAPI and TBSQD, (e) Differential Interference Contrast (DIC) image, (f) DAPI channel with 410-454 nm emission filter, (g) Fluorescence channel with 680-730 nm emission filter and (h) merged image of all channels.

In vitro photothermal efficacy testing was carried out in 4T1 cells revealed that the material is highly efficient and cell viability in sample exposed to NIR laser for 7 min with 10 μ g/well was <5%, whereas the cells exposed to material and laser alone did not exhibit changes in cell viability (Figure 8.12a). Hemocompatibility studies on TBSQDs revealed that TBSQDs did not exhibit hemolysis and the % hemolysis was well below 5% (Figure 8.12b). The sample treated with Triton X-100, resulted in complete hemolysis and no RBC pellet was observed. Further, ESEM analysis of TBSQDs treated samples revealed that the morphology of RBCs was intact, and no significant difference was observed (Figure 8.12d-f).

An understanding of the *in vivo* biodistribution of an external agent like nanoparticles is a prerequisite to assess its pharmacodynamics and associated adverse effects. The *ex vivo* fluorescence imaging studies were carried out 14 days post intravenous administration of TBS QDs. The *ex vivo* fluorescence imaging of the vital organs revealed that the majority of the nanoparticles were accumulated in the liver, lung and spleen, followed by kidney and heart suggesting that the major portion of the injected material is taken up by the components of the reticuloendothelial system in the body. Accumulation of a portion of injected material in the

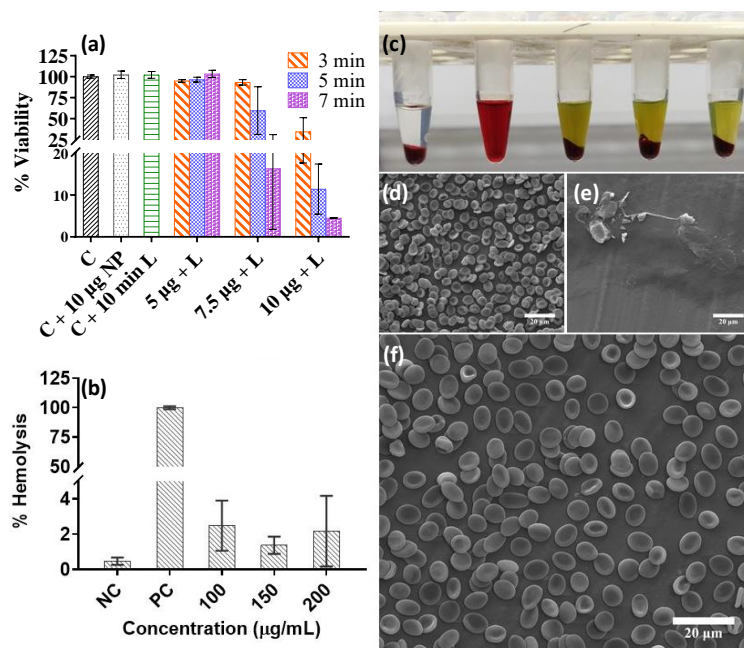


Figure 8.12: (a) *in vitro* photothermal efficacy in 4T1 cells, (b) graph depicting the hemocompatibility of TBSQD (c) digital image of various samples of hemocompatibility study, ESEM images of RBC treated with (d) negative control (PBS), (e) positive control (triton X-100), (f) 200 µg/mL TBSQD.

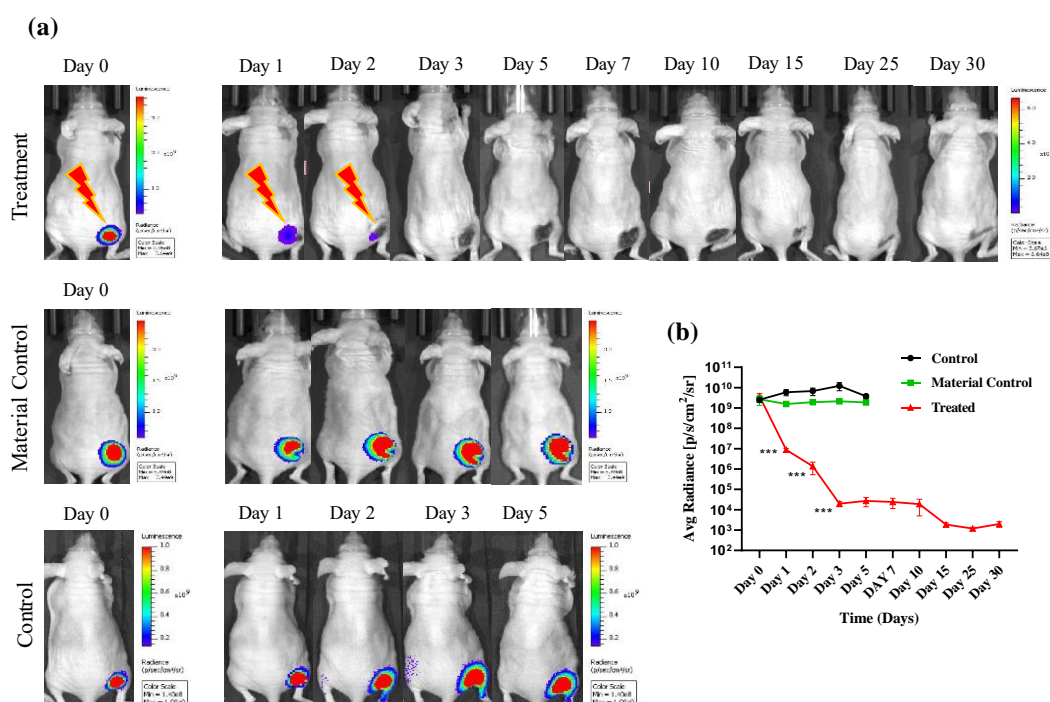
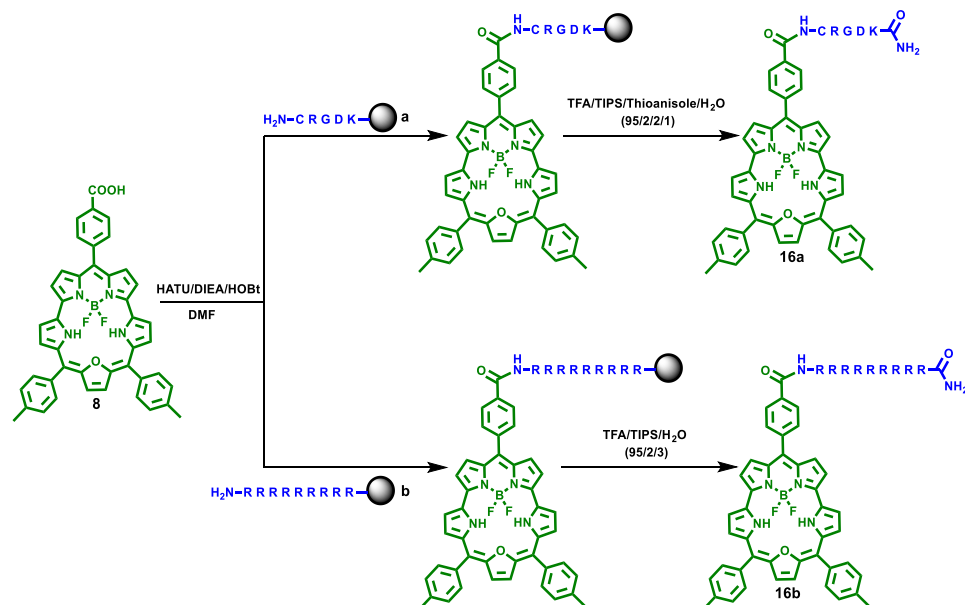


Figure 8.13: In vivo photothermal ablation by TBS QDs in 4T1 xenograft mouse model: (a) representative in vivo bioluminescence images of various treatment groups, (b) quantitative assessment of bioluminescence signal for different groups during the follow-up (***) indicates $P = 0.001$ post third treatment)

kidney also suggest the possibility of renal clearance. The photothermal efficacy testing of TBSQDs revealed that the material possesses excellent efficacy *in vivo* (Figure 8.13). It was observed that there was a dramatic reduction in bioluminescence signal post first and second treatment, indicative of drastic tumor ablation. However, presence of residual tumor at the treatment site suggests the necessity of third treatment. Third photothermal treatment to this group imparts complete tumor ablation (bioluminescence signal post third treatment was equivalent to the background signal). This was further associated with no signs of weight loss in animals post PTT suggesting absence of therapeutic burden on mice. The bioluminescence signal of control as well the material control groups showed continuous increase, indicating the non-toxic nature of material and progressive tumor growth. The control groups as well as material control group showed signs of necrosis at day 5, beyond which no further imaging was carried for these animals owing to the ethical concerns and the mice were sacrificed. Treated animals were followed till day 30 post treatment and showed no increase in the bioluminescence signal, highlighting effective and complete tumor ablation with no signs of relapse post PTT prolonging the overall survival of the treated mice.

In chapter 7, we discussed the synthesis of cell penetrating peptides (CRGDK and R₉) conjugated BF₂-oxasmaragdyrin on solid phase and their use as NIR fluorescence imaging as well as photothermal therapeutic agent. The target CRGDK conjugated BF₂-25-oxasmaragdyrin **16a** and R₉ conjugated BF₂-25-oxasmaragdyrin **16b** were prepared over a sequence of steps, as shown in Scheme 8.4. The starting BF₂-25-oxasmaragdyrin **8** containing *p*-carboxyphenyl substituent at *meso* position was synthesized by a reported method.²⁰ Solid supported (Rink amide) peptides with free *N*-terminal **a**, **b** were prepared by standard automated microwave-accelerated solid-phase peptide synthesis procedure with *fmoc*-protected amino acid precursors. To obtain solid supported BF₂-oxasmaragdyrin-peptide conjugates, corresponding solid supported (Rink amide) peptides with free *N*-terminal was treated with the mixture containing BF₂-25-oxasmaragdyrin **8**, HATU, HOBt and DIEA in DMF (3 mL) and shaken for 24 hours. After completion of the reaction, the resin was thoroughly washed with DMF (20 × 5 mL) and CH₂Cl₂ (20 × 5 mL). Respective resins were cleaved with corresponding cleavage mixtures (20 mL) for 3 hours followed by evaporation of the solvent, precipitation by cold Et₂O (20 mL). The precipitate was centrifuged, and the supernatant was removed to give crude compounds **16a** and **16b** as green solids. RP-HPLC analysis of crude compounds **16a** and **16b** was performed on Agilent 1200 series instruments by dissolving the crude solids in corresponding solvent mixtures (**1a** in 2:1:7

DMSO/ACN/H₂O and **1b** in 1:1:8 DMSO/ACN/H₂O) at a concentrations of 2-3 mg/mL and injecting 50 μ L onto Vydac C18 (4.6 x 250 mm, 5 μ m) analytical column and using a linear



Scheme 8.4: Synthesis of CRGDK and R₉ conjugated BF₂-oxasmaragdyrin **16a** and **16b**.

gradient of 0.1% TFA at a flow rate of 1.5 mL/min. The RP-HPLC analysis of crude residues of compounds **16a** and **16b** showed that the residues contain some impurities along with the desired compound identified by mass spectrometry. To obtain pure compounds, preparative RP-HPLC was performed on compounds **16a**, **16b** using C4, C18 columns respectively with a flow rate of 10 mL min⁻¹ under linear gradients of 0.1% TFA in MeCN. The fractions corresponding to the desired products were identified, combined together and lyophilized to give pure compounds **16a** and **16b** as green foamy solids in 11.0% and 5.2% yields respectively. The compounds **16a-b** were characterised by mass spectrometry which showed peak corresponding to molecular ion ([M+H]⁺) and analytical RP-HPLC showed that the compounds **1a-b** as a single peak with >95% purity (Figure 8.14).

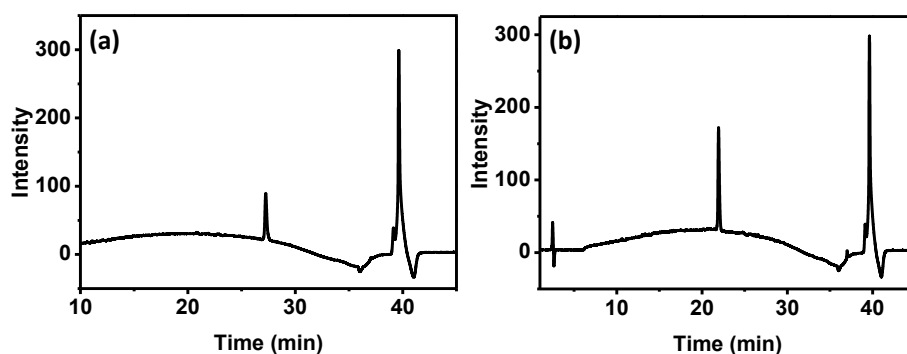


Figure 8.14: HPLC traces for pure compounds **1a** and **1b**.

The absorption and fluorescence studies were performed on compounds **16a-b**. Compound **16a** absorbs in the visible region and emits in the NIR region (~ 717 nm) with moderate quantum yield ($\phi_f = 0.23$) and an excited state lifetime of 4.74 ns (Figure 8.15a-c). Compound **16a** aggregates in the presence of H₂O leading to red shift with a significant broadening in absorption spectra (Figure 8.15a) and complete quenching of fluorescence (Figure 8.15b). Similarly, compound **16b** also absorbs in the visible region and emits in NIR

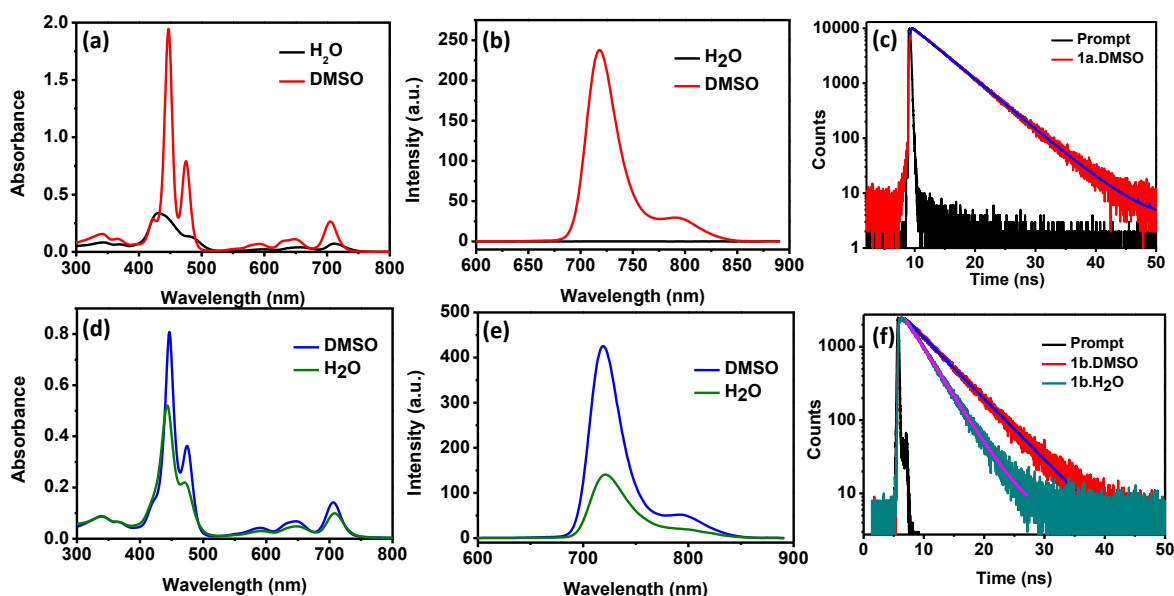


Figure 8.15: (a) Absorption (b) fluorescence (c) TCSPC of compound **16a** in different solvents. (d) Absorption (e) fluorescence (f) TCSPC of compound **16b** in different solvents.

region (~ 719 nm) with a moderate quantum yield ($\phi_f = 0.24$) and an excited state lifetime of 5.23 ns (Figure 8.15d-f). Compound **16b** also aggregates in H₂O which was observed as broadening of absorption spectra with a slight redshift. The quenching of fluorescence of compound **16b** (Figure 8.15e) with a decrease in quantum yield in H₂O ($\phi_f = 0.04$) was observed compared to that of DMSO ($\phi_f = 0.24$). A decrease in an excited state lifetime was also observed for compound **16b** in H₂O ($\tau_s = 3.32$ ns) compared to that of the DMSO ($\tau_s = 5.23$ ns).

To evaluate the behaviour of material in the presence of cells i.e., the inherent property of fluorescence, qualitative invitro cellular uptake of the compounds **16a-b** was performed in MDA MB 231 cells. CLSM data revealed that the material was internalized in the cells within 24 hours of incubation and was able to exhibit strong fluorescence in NIR region (Figure 8.16). Furthermore, Photothermal transduction studies were performed on compound **16b** and found that the material was photothermally active with a conversion efficiency of 72.29% and highly

stable even after several heating and cooling cycles which could be exploited for photothermal therapy.

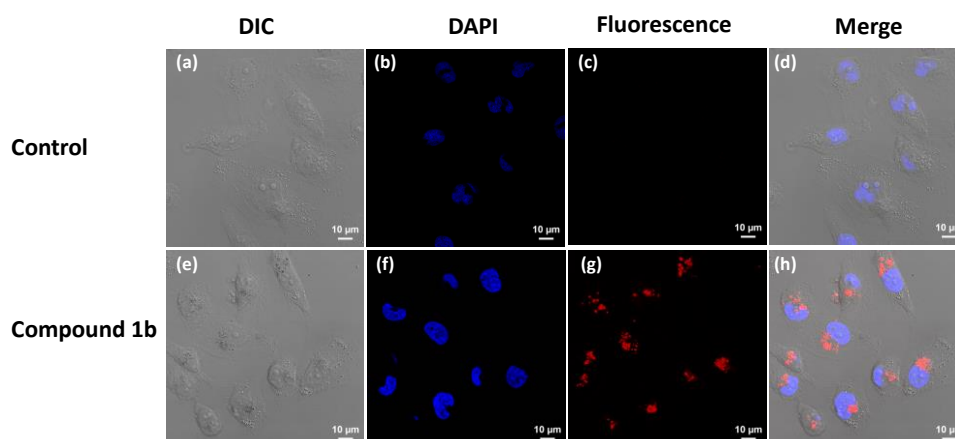


Figure 8.16: CLSM images of controls cells (a) Differential Interference Contrast (DIC) channel, (b) DAPI channel (c) fluorescence channel (d) merged image of all channels, cells treated with compound **16b** (e) DIC channel, (f) DAPI channel, (g) fluorescence channel (h) merged image of all channels. Fluorescence was recorded with 680-740 nm emission filter.

In summary, in this thesis we described the synthesis of various BF₂-oxamsmaragdyrin based systems such as covalent conjugates of BF₂-oxamsmaragdyrin from amino acids, glucosamine, peptides and BF₂-oxamsmaragdyrin based quantum dots (TBSQDs) as shown in figure 8.17. All the materials were characterised with appropriate analytical and spectroscopic techniques. Most of the materials were evaluated for biocompatibility and *in vitro* studies for uptake as well as NIR Fluorescence Imaging studies. Simultaneously, L,L-diphenylalanine and TBSQDs were evaluated as *in vivo* photothermal therapeutic agents and studies showed that both the materials are highly compatible and shows good photothermal therapeutic behaviour with good efficacy. Furthermore, the properties of BF₂-oxamsmaragdyrin based materials is tabulated in Table 1. The amino acid conjugated BF₂-oxamsmaragdyrin has given us the insights about the photophysical properties but was neither useful for NIR imaging nor for PTT due to highly hydrophobic nature of the conjugates. Glucosamine conjugated BF₂-oxamsmaragdyrin wasevaluated for NIR fluorescence imaging and the results showed that the conjugate internalised into the cytoplasm of the cells with good NIR fluorescence from the cells. Polyarginine conjugated BF₂-oxamsmaragdyrin and TBSQDs were also evaluated of NIR fluorescence imaging and similar results were observed.

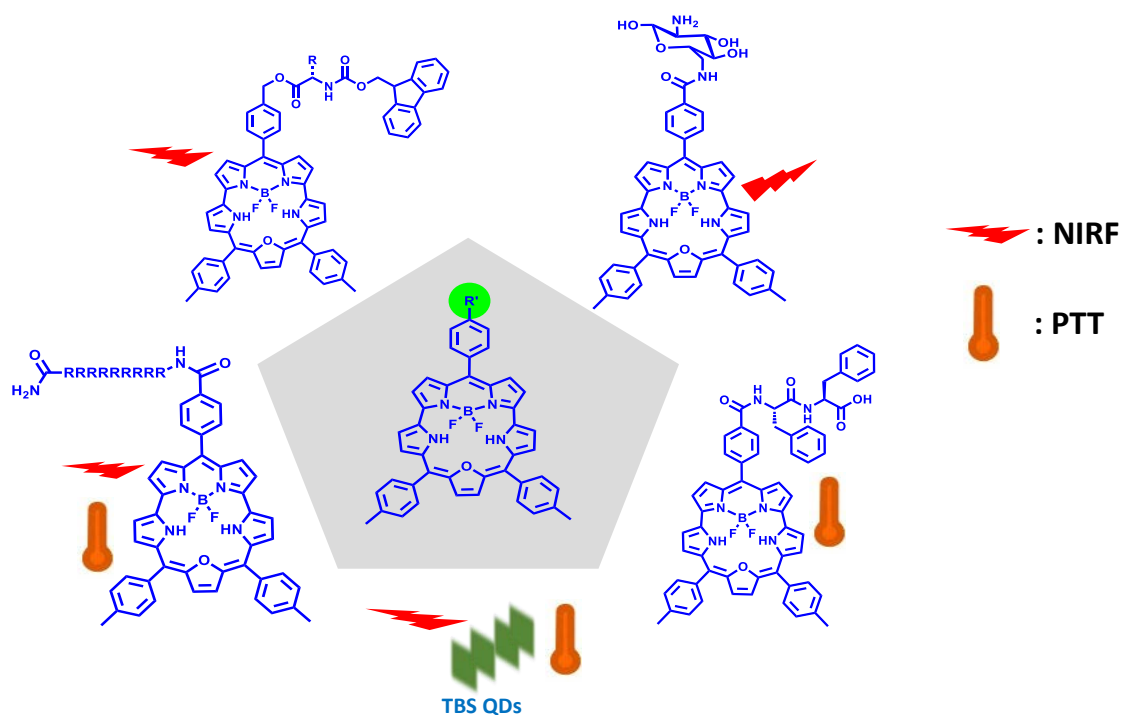


Figure 8.17: various conjugates of BF₂-oxamsmaragdyrin for NIR Imaging and Photothermal therapy.

Table 1. BF₂-oxamsmaragdyrin based systems for NIR Fluorescence and Photothermal therapy.

Compound (conjugates)/Material	Amino acid	Glucosamine	FF-BSC NPs	TBSQD	R ₉
<i>In vitro/in vivo</i> NIRF	--	Yes	--	Yes	Yes
Conc. reqd. for PTT (mg/mL)	--	--	0.3	0.1	0.1
Conc. reqd. for PTT μM	--	--	300	146	47.2
Effective dye Conc. (μg/mL)	--	--	200	90-100	30
PTT efficacy	--	--	53.6%	43%	72.3%

Furthermore, TBSQDs, L,L-diphenylalanine conjugated BF₂-oxamsmaragdyrin NPs, and polyarginine conjugated BF₂-oxamsmaragdyrin were evaluated for photothermal properties. All the materials were photothermally active and have a photothermal efficiency of 43%, 53.6% and 72.3% respectively. Polyarginine conjugated BF₂-oxamsmaragdyrin was found to be best photothermal agent with a photothermal efficacy of 72.3% and low concentration of 47 μ M to reach a temperature of 52 °C within 5 minutes of irradiation with 650 mW/cm² power by 750 nm Laser.

Thus, the results described in this thesis demonstrated the use of expanded porphyrin; BF₂-oxamsmaragdyrin as a fluorophore for NIR fluorescence imaging and NIR photothermal agent *in vitro* as well as *in vivo* using various methodologies ranging from covalent conjugation to nanoparticle formation. We hope this work could trigger many more studies in terms of increasing the efficacy of this material as well as other expanded porphyrins for similar applications.

References:

- (1) Zhao, J.; Zhong, D.; Zhou, S. NIR-I-to-NIR-II Fluorescent Nanomaterials for Biomedical Imaging and Cancer Therapy. *J. Mater. Chem. B* **2018**, *6*, 349–365.
- (2) Yi, X.; Wang, F.; Qin, W.; Yang, X.; Yuan, J. Near-Infrared Fluorescent Probes in Cancer Imaging and Therapy: An Emerging Field. *Int J Nanomedicine* **2014**, *9*, 1347–1365.
- (3) Escobedo, J. O.; Rusin, O.; Lim, S.; Strongin, R. M. NIR Dyes for Bioimaging Applications. *Current Opinion in Chemical Biology*. **2010**, 64–70.
- (4) Khot, M. I.; Andrew, H.; Svavarsdottir, H. S.; Armstrong, G.; Quyn, A. J.; Jayne, D. G. A Review on the Scope of Photothermal Therapy–Based Nanomedicines in Preclinical Models of Colorectal Cancer. *Clinical Colorectal Cancer*. **2019**, e200–e209.
- (5) Pham, W.; Cassell, L.; Gillman, A.; Koktysh, D.; Gore, J. C. A Near-Infrared Dye for Multichannel Imaging. *Chem. Commun.* **2008**, *16*, 1895–1897.
- (6) Fischer, G. M.; Isomäki-Krondahl, M.; Göttker-Schnetmann, I.; Daltrozzo, E.; Zumbusch, A. Pyrrolopyrrole Cyanine Dyes: A New Class of Near-Infrared Dyes and Fluorophores. *Chem. – A Eur. J.* **2009**, *15*, 4857–4864.

-
-
- (7) Yang, Y.; Lowry, M.; Xu, X.; Escobedo, J. O.; Sibrian-Vazquez, M.; Wong, L.; Schowalter, C. M.; Jensen, T. J.; Fronczek, F. R.; Warner, I. M.; et al. Seminaphthofluorones Are a Family of Water-Soluble, Low Molecular Weight, NIR-Emitting Fluorophores. *Proc. Natl. Acad. Sci.* **2008**, *105*, 8829.
 - (8) Arunkumar, E.; Forbes, C. C.; Noll, B. C.; Smith, B. D. Squaraine-Derived Rotaxanes: Sterically Protected Fluorescent Near-IR Dyes. *J. Am. Chem. Soc.* **2005**, *127*, 3288–3289.
 - (9) Johnson, J. R.; Fu, N.; Arunkumar, E.; Leevy, W. M.; Gammon, S. T.; Piwnica-Worms, D.; Smith, B. D. Squaraine Rotaxanes: Superior Substitutes for Cy-5 in Molecular Probes for near-Infrared Fluorescence Cell Imaging. *Angew. Chem. Int. Ed.* **2007**, *46*, 5528–5531.
 - (10) Umezawa, K.; Citterio, D.; Suzuki, K. Water-Soluble NIR Fluorescent Probes Based on Squaraine and Their Application for Protein Labeling. *Anal. Sci.* **2008**, *24*, 213–217.
 - (11) Fu, N.; Gassensmith, J. J.; Smith, B. D. Effect of Stopper Size on Squaraine Rotaxane Stability. *Supramol. Chem.* **2009**, *21*, 118–124.
 - (12) Meek, S. T.; Nesterov, E. E.; Swager, T. M. Near-Infrared Fluorophores Containing Benzo[c]Heterocycle Subunits. *Org. Lett.* **2008**, *10*, 2991–2993.
 - (13) Feng, G.; Liu, J.; Geng, J.; Liu, B. Conjugated Polymer Microparticles for Selective Cancer Cell Image-Guided Photothermal Therapy. *J. Mater. Chem. B* **2015**, *3*, 1135–1141.
 - (14) Loudet, A.; Bandichhor, R.; Burgess, K.; Palma, A.; McDonnell, S. O.; Hall, M. J.; O'Shea, D. F. B,O-Chelated Azadipyrromethenes as Near-IR Probes. *Org. Lett.* **2008**, *10*, 4771–4774.
 - (15) Umezawa, K.; Nakamura, Y.; Makino, H.; Citterio, D.; Suzuki, K. Bright, Color-Tunable Fluorescent Dyes in the Visible–Near-Infrared Region. *J. Am. Chem. Soc.* **2008**, *130*, 1550–1551.
 - (16) Umezawa, K.; Matsui, A.; Nakamura, Y.; Citterio, D.; Suzuki, K. Bright, Color-Tunable Fluorescent Dyes in the Vis/NIR Region: Establishment of New “Tailor-Made” Multicolor Fluorophores Based on Borondipyrromethene. *Chem. – A Eur. J.* **2009**, *15*, 1096–1106.

- (17) Nesterova, I. V.; Verdree, V. T.; Pakhomov, S.; Strickler, K. L.; Allen, M. W.; Hammer, R. P.; Soper, S. A. Metallo-Phthalocyanine Near-IR Fluorophores: Oligonucleotide Conjugates and Their Applications in PCR Assays. *Bioconjug. Chem.* **2007**, *18*, 2159–2168.
- (18) Kee, H. L.; Nothdurft, R.; Muthiah, C.; Diers, J. R.; Fan, D.; Ptaszek, M.; Bocian, D. F.; Lindsey, J. S.; Culver, J. P.; Holten, D. Examination of Chlorin-Bacteriochlorin Energy-Transfer Dyads as Prototypes for near-Infrared Molecular Imaging Probes. *Photochem. Photobiol.* **2008**, *84*, 1061–1072.
- (19) Kuimova, M. K.; Collins, H. A.; Balaz, M.; Dahlstedt, E.; Levitt, J. A.; Sergent, N.; Suhling, K.; Drobizhev, M.; Makarov, N. S.; Rebane, A.; et al. Photophysical Properties and Intracellular Imaging of Water-Soluble Porphyrin Dimers for Two-Photon Excited Photodynamic Therapy. *Org. Biomol. Chem.* **2009**, *7*, 889–896.
- (20) Mane, S. B.; Hu, J.-Y.; Chang, Y.-C.; Luo, L.; Diao, E. W.-G.; Hung, C.-H. Novel Expanded Porphyrin Sensitized Solar Cells Using Boryl Oxasmaragdyrin as the Sensitizer. *Chem. Commun.* **2013**, *49*, 6882–6884.
- (21) Li, C.; Greenwood, T. R.; Bhujwalla, Z. M.; Glunde, K. Synthesis and Characterization of Glucosamine-Bound Near-Infrared Probes for Optical Imaging. *Org. Lett.* **2006**, *8*, 3623–3626.

List of Publications

1. One pot synthesis of unusual meso-dipyrinyl corrole.
Laxman, K.; Kaur, T.; Ravikanth, M. *RSC Adv.*, **2017**, 7, 19878-19884.
2. Synthesis of Oxasmaragdyrin–Amino Acid Conjugates.
Laxman, K.; Ravikanth, M. *Eur. J. Org. Chem.* **2017**, 5884–5891.
3. Antiaromatic Carbaporphyrinoids: Fluorene as fused motif toward synthesis of *meso*-Fused Heterobenziporphyrins.
Kumar, A.; **Laxman, K.;** Ravikanth, M. *Org. Lett.* **2019**, 21, 8726-8730.
4. Synthesis and Studies of Glucosamine Conjugated BF₂-Oxasmaragdyrin.
Laxman, K.; Reddy, B. P. K; Robinson, A.; Srivastava, R.; Ravikanth, M. *ChemistrySelect*, **2020**, 5, 938 -943.
5. Polycyclic Aromatic Hydrocarbons/Heterocycles Embedded Porphyrinoids
Laxman, K.; Kumar, A.; Ravikanth, M. *Asian J. Org. Chem.* **2020**, 9, 162-180.
6. L,L-Diphenylalanine Conjugated BF₂-Oxasmaragdyrin Self-Assemblies as NIR Photo-Thermal Therapeutic Agents For Cancer Therapy.
Laxman, K.; Reddy, B. P. K; Mishra, S. K.; Robinson, A.; De, A.; Srivastava, R.; Ravikanth, M. (*Manuscript Submitted*).
7. BF₂-Oxasmaragdyrin based Quantum Dots as NIR imaging and Photothermal Agents for Cancer Therapy.
Laxman, K.; Reddy, B. P. K; Mishra, S. K.; Robinson, A.; De, A.; Srivastava, R.; Ravikanth, M. (*Manuscript Submitted*).
8. Cell Penetrating Peptide Conjugated BF₂-Oxasmaragdyrin As NIR Imaging and Photo-Thermal Therapeutic Agents.
Laxman, K.; Reddy, B. P. K; Robinson, A.; Srivastava, R.; Ravikanth, M. (*Manuscript Submitted*).
9. Unexpected Trifluoroacetic Acid Triggered Visible to NIR Switching of Ketoenamine-substituted Triphenylamines.
Laxman, K.; Perepichka D. F.; Rao, M. R. (*Manuscript Submitted*)
10. Synthesis of Crowned pyrrolo-(1,2- α)indole fluorophore macrocycles and their stable cation radicals.
Ojha, B.; **Laxman, K.;** Ravikanth, M. (*Manuscript prepared*)

List of Patents

1. CONJUGATES OF BF₂-OXASMARAGDYRIN (TEMP/E-1/42435/2019-MUM)

Kandala Laxman, B. Pradeep K. Reddy, Mangalampalli Ravikanth, Rohit Srivastava,
Andrea Robinson, Abhijit De

2. SYNTHESIS OF MESO-TRITOLYL-BF₂- OXASMARAGDYRIN BASED QUANTUM
DOTS (TEMP/E-1/42476/2019- MUM)

Kandala Laxman, B. Pradeep K. Reddy, Mangalampalli Ravikanth, Rohit Srivastava,
Andrea Robinson, Abhijit De

Acknowledgements

Firstly, I would like to express my deep gratitude and profound thanks to my IIT Bombay supervisor **Prof. M. Ravikanth**, for his guidance, encouragement, continuous support and freedom given to me in carrying out research. He is always approachable and helpful. His guidance helped me in all the time of research and writing of this thesis. I would also like to express by gratitude to my Monash supervisor **Prof. Andrea Robinson**, who took over as a supervisor from **Prof. Patrick Perlmutter** halfway through my Ph. D. with great ease. Her encouragement as well as continuous support for my Ph. D. along with her cordial behaviour during my Monash stay helped me focus on my work. I could not have imagined having better supervisors for my Ph.D. study.

I would like to acknowledge the IITB-Monash Research Academy for providing financial assistance in the form Research Fellowship. I would also like to acknowledge Department of Chemistry, IIT Bombay and School of Chemistry, Monash University Clayton for providing very good infrastructure to carry out my research. I would like to thank my ‘Research Progress Committee’ members, **Prof. Nandita Madhavan** and **Prof. Mibel Aguilar** for valuable and constructive suggestions to improve my research work. I would also like to take this opportunity to thank Prof. Patrick Perlmutter without whom this work would have not started.

I am grateful to **Prof. Rohit Srivastava**, Department of Biosciences and Bioengineering (BSBE), IIT Bombay and **Prof. Abhijit De**, Tata Memorial Centre Advanced Centre for Treatment, Research and Education in Cancer (ACTREC) for generous collaboration and input towards *in vitro* and *in vivo* studies of synthesised material as part of my Ph. D. I would like to thank Mr. B. Pradeep Kumar Reddy (student under Prof. Rohit Srivastava) and Mr. Sumit Mishra (student under Prof. Abhijit De) for their valuable help in realising the *in vitro* and *in vivo* applications. Discussions with them helped me in understanding the strategies for research towards pre-clinical studies.

I thank the entire staff of the Department of Chemistry, Mrs. Shweta, Mr. Amol and Niteen for teaching me NMR spectroscopy, Mr. Rajesh for Mass, Mr. Bharat for fixing glassware, Mr. Darshan for X-ray and Mr. Ratish Sekhar for their kind help and cooperation throughout my research period. I would extend my thanks to entire staff of School of

Chemistry, Monash University, Prof. Toby Bell for cell culture and ultrafast dynamics, Prof. David Turner, Dr. Georg Beilharz, Dr. Peter Nichols for NMR, and Dr. Boujemaa Moubaraki for their support during my Monash stay. I would also like to thank entire staff of IITB-Monash Research Academy, Prof. Murali Shastri, Dr. K. S. Nagabhushana, Mrs. Laya Vijayan, Mrs. Jayashree Thattayath, Mr. Kiran More, Mrs. Beena Pillai, Mrs. Nancy Sowho and support staff Mr. Rahul Ingle, Mr. Bharat Ingle, Chhaya Sonawane without whose help Ph. D. would have been not possible.

I am very happy to acknowledge my seniors and labmates from IIT Bombay, Dr. M. Rajeswara Rao, Dr. Hemanta Kalita, Dr. Avanish Dvivedi, Dr. Ganapathi Emandi, Dr. Tejinder Kaur, Dr. Ritambhara Sharma, Dr. Tamal Chatterjee, Dr. Sunit Kumar, Dr. Kishor, Dr. Angira, Dr. Karunesh Keshav, Dr. Dijo, Dr. Umasekher, Dr. Ankit Kumar, Prosenjit, Alka, Rima, Sabari, K. N. Panda, Bela, Nisha, Avishikta, Bharti, Diksha, Gurpreet and Monash labmates Dr. Troy Attard, Dr. Alessia Begi, Dr. Andrew Wright, Lauren Blakeley, Szabolcs Solyom, Adam Kennedy, John Burton, Ben Husselbee, for their cooperation and providing a friendly and supportive environment. I am grateful to my all-time go to person Dr. Ankit Kumar for talk from chemistry to politics without whom my stay at IIT Bombay would have been a void. I would also like to thank my friends Balagopal and Abhishek who have been with me in thick and thin days of my Ph. D. making “The Three Musketeers”.

I would also like to thank my friends and batch mates, especially Dr. Nageshwar Rao, Dr. Anand Podilapu, Dr. Someshwara Sanpala, Dr. Chandan Singh, Radhakrishna, Shakti, Naveen, Arup, Sanjib, Mihir, Kaushik, Dr. Ketav, Gopal, Anchal, Palak, Bhavesh, Laxman, for their valuable help and support.

This journey would not have been possible without the support of my family, a big thank you for encouraging me in all my pursuits and inspiring me to follow my dreams.

Laxman Kandala